UNIVERSITÀ DEGLI STUDI DI PADOVA
DIPARTIMENTO DI FISICA ED ASTRONOMIA
SCUOLA DI DOTTORATO DI RICERCA IN FISICA
CICLO XXIX

BLAZAR FLARING PATTERNS (B-FLAP)

CLASSIFYING BLAZARS OF UNCERTAIN TYPE DETECTED BY FERMI GAMMA-RAY SPACE TELESCOPE

THESIS PRESENTED BY

GRAZIANO CHIARO

Submitted to the Graduate School in Physics in
Fulfillment of the Requirements for the Degree of

DOCTOR OF PHILOSOPHY IN PHYSICS

DIRECTOR OF THE
DOCTORAL SCHOOL

SANTO LUNARDI

SUPERVISORS

DENIS BASTIERI
DAVID J. THOMPSON

To my wife, Lorena.

Contents

Table of contents **i**

Introduction **v**

1 The gamma-ray Universe **1**
1.1 Gamma-ray astronomy 1
1.1.1 Ground-Based Telescopes 3
1.1.2 The satellite telescopes before Fermi LAT 6
1.2 The Fermi Gamma-ray Space Telescope 11
1.2.1 Overview of the Large Area Telescope 13
1.3 Gamma rays from the sky 15
1.3.1 Diffuse gamma-ray emission 16
1.3.2 Gamma-ray Pulsars and Pulsar Wind Nebulae 18
1.3.3 Supernova Remnants 21
1.3.4 Gamma-Ray Bursts 22
1.3.5 Solar flares 24
1.3.6 Dark Matter 25
1.3.7 Unidentified Sources 27

2 The Active Galactic Nuclei **31**
2.1 The Active Galactic Nuclei and Blazars 31
2.1.1 Current Model 32
2.1.2 Classification 34
2.1.3 Spectra 35
2.1.4 Synchrotron Self-Compton Emission Model 36
2.1.5 External Compton Emission Model 37
2.1.6 Variability 38
2.1.7 High Synchrotron Peak Blazars 39

3 The Fermi-LAT Source Catalogs **41**
3.1 Onboard the Fermi - LAT . . . 41
3.1.1 Construction of a Fermi- LAT catalog . . . 43
3.1.2 The procedure . . . 44
3.1.3 Source identification and association . . . 47
3.2 The Third FERMI/LAT Source Catalog . . . 48
3.2.1 Instrument response functions. Improvement respect to the 2FGL catalog . . . 49

4 Classifying blazar of uncertain type **53**
4.1 Blazar Flaring Patterns (B-FlaP) . . . 54
4.2 The method . . . 55
4.2.1 Empirical Cumulative Distribution Function . . . 55
4.2.2 ECDF for BCUs . . . 56
4.2.3 ECDF for HSP blazars . . . 59
4.2.4 Usefulness of the max-flux parameter . . . 60

5 Classification using Artificial Neural Networks (ANN) **67**
5.1 Architecture of the ANN . . . 68
5.2 Training session . . . 69
5.3 Source sample and predictor parameters . . . 72
5.4 Optimization of the algorithm and classification thresholds . . . 75
5.5 Selecting the most promising HSP candidates . . . 78
5.6 ANN Results and validation . . . 78

6 B-FlaP Classification List **87**
6.1 The List . . . 87
6.2 HSP candidates for Cherenkov telescopes . . . 88

7 Radio Analysis **95**
7.1 Radio flux density distribution . . . 95
7.2 Radio S_r distribution versus BFlaP . . . 96

8 Optical analysis **101**
8.1 Quasar and Blazar in the optical . . . 101
8.1.1 Optical emission in blazars . . . 102
8.2 Optical spectroscopy . . . 102
8.3 Optical results . . . 104
8.3.1 Optical spectra and ECDF comparison for HSP classification . . . 105
8.3.2 Notes on bright sources . . . 106

9 Conclusion **113**
9.1 In this study . . . 113
9.2 Collaboration . . . 114

10 Follow On Results **117**
10.1 MAGN hunting by B-FlaP . . . 117
10.2 Hidden Seyfert galaxies and B-FlaP . . . 122

11 Appendix A **129**
11.1 3FGL BCU Classification List . . . 129

12 Appendix B **147**
12.1 Optical spectra . . . 147

13 Appendix C **155**
13.1 The FERMI LAT Telescope . . . 155
13.2 The Tracker . . . 155
13.3 The Calorimeter . . . 158
13.3.1 The AntiCoincidence Detector . . . 159
13.4 The Data Acquisition System and Trigger . . . 161
13.4.1 Trigger and background rejection . . . 161
13.5 Overview of the Gamma-ray Burst Monitor . . . 162

14 Appendix D **165**
14.1 The Asiago Observatory . . . 165
14.1.1 The telescopes . . . 165

15 Appendix E **169**
15.1 Artificial Neural Networks . . . 169
15.1.1 The multilayer perceptron . . . 170
15.1.2 The propagation rule . . . 171
15.1.3 Back-propagation of the error . . . 171
15.1.4 The training technique . . . 173

Bibliography **175**

Acknowledgements **190**

Introduction

The study of cosmic γ-ray sources is one of the most recent and exciting fields of research in modern astrophysics. The emission of γ rays is related to the most violent and powerful phenomena in the Universe and provides a unique way to probe extreme physical environments but astrophysical sources of high-energy γ- rays have been hard to identify for a long time. Only four of the 25 γ-ray sources in the second COS-B catalog (1981) had identifications, and over half the 271 sources in the third Egret catalog (1999) had no associations with known objects at other wavelengths. The difficulty of finding counterparts of high-energy γ-ray sources was due the large positional errors in their measured locations, a result of the limited photon statistics and of poor angular resolution of the γ-ray instruments as well as the bright diffuse γ-ray emission from the Milky Way.
A major step forward for detection and identification of high-energy γ- ray sources came when the Fermi Gamma-ray Space Telescope (FERMI) was launched on 2008 June 11. It carries on board the *Large Area Telescope* (LAT), a pair conversion telescope based on advanced detectors for High Energy Physics
The optimal performances of the LAT in terms of angular resolution and sensitivity allow studying the 100 MeV to 300 GeV γ-ray sky with unprecedented detail. During its first four years of operation from 2008 August 4 (MJD 54682) to 2012 July 31 (MJD 56139) FERMI discovered more than three thousands of γ-ray sources above 4 σ significance, several orders of magnitude larger than those detected by Egret during its 9 years of activity. The FERMI LAT 4-year Point Source Catalog (3FGL) includes 1740 sources associated with AGN (58% of all 3FGL sources) of which 1144 are clear classified blazars, 573 are unclassified candidate blazers (BCUs), 15 are radio galaxies, 5 are Seifert galaxies and 3 are other AGN.

The aim of this study is to investigate the possibility of finding a simple estimator of the probability that the source under investigation is a blazar and, where is possible, an High Synchrotron Peaked BL Lac blazar (HSP). The present generation of atmospheric Cherenkov telescopes (VERITAS, H.E.S.S., MAGIC) has opened the realm of ground-based γ-ray astronomy in the energy

Table 1: Blazars detections by FERMI from the beginning of the mission

	1FGL	2FGL	3FGL
BL Lac	295	436	660
FSRQ	278	370	484
BCU	92	257	573
Total	665	1063	1717

range above ∼100 GeV. The Cherenkov Telescope Array (CTA) will explore our Universe in depth in Very High Energy (E >100 GeV) γ rays. Blazars and the HSP subclass are the most numerous class of TeV sources therefore the ability to correctly identify these objects will be very important for the the ground-based TeV community in the determination of the observative targets, in order to increase the rate of detections, since Imaging Atmospheric (or Air) Cherenkov Telescope (IACTs) have a small field of view. The fraction of BCUs in 3FGL increased notably (28%)in comparison with the 2FGL release of the catalog. As it was also highlighted in the 3FGL paper, is mainly due to the lower probability to have high quality optical spectrum available for these faint sources, but because of these faint BCUs account for almost the 50% of the classified blazars it justify the reasons that supported this study.
In comparison to existing methods of classification for the active galaxies , the novelty of the present approach is that the estimator relies exclusively on data collected at γ-ray energies where FERMI / LAT, the most important investigator of the gamma-ray sky, is most sensitive (0.1 – 100 GeV). We followed the steps of a Kolmogorov-Smirnov test and computed the Empirical Cumulative Distribution Function (ECDF) of the light curves, then compared the ECDFs of blazar candidates of unknown type (BCUs) to the ECDFs of AGNs whose class is already established. Because of variability is one of the defining characteristics of blazars and a key parameter of our study, we call this method B-FLAP as an acronym for Blazar Flaring Patterns.
Aiming to improve the ECDF results obtained in the first step of the study, we produce an original Artificial Neural Network (ANN) algorithm. Applying our optimized ANN algorithm to BCUs 3FGL we studied the distribution of the likelihood of membership class of BCUs and we obtain a Classification List where 342 BCUs are classified as BL Lac , while 154 as FSRQ. The remaining 77 sources remain unclassified. This result reduces the percentage od BCUs versus classified blazar from 50% to 6.7%. and it significantly increases the availability of new objects for target screening Cherenkov.
For each BCU was also calculated the likelihood relative to a SED HSP type and 53 BCU have shown a likelihood higher than 80%. This result for HSP,

only partly meets the expectations of this study due to contamination of the results by the blazars SED in class LSP and ISP , as described in detail in this study.
When a confident identification of the low-energy counterpart of a γ-ray source was possible, we confirmed B-FLAP with the results of multiwavelength analysis by direct optical and radio observations. EDFC and ANN likelihood results confirm very well the direct observation as we expect for a well-built classification algorithm. Although a statistical method cannot replace confirmed and rigorous techniques for active galaxies classification, B-FLAP might be configured, when detailed observational data are not yet available, as a powerful additional approach for the preliminary identification of blazars and a sufficient grader of HSP objects. This result satisfies the aim of the research.

This thesis is organized as follows.

- Chapter 1. A brief review of then main issues regarding γ-ray astronomy, focusing on the γ-ray Universe and satellite telescopes before the launch of FERMI LAT
- Chaper 2. An overiview of the Active Galactic Nuclei and blazars, the emission models and their spectra
- Chapter 3. The procedure developed by the FERMI collaboration to construct the FERMI LAT source catalogs and an overview of the the Third Fermi LAT Source Catalog
- Chapter 4. B-FLaP step 1 or the original contribution of this study for the 3FGL BCUs screening by Empirical Cumulative Distribution Function
- Chapter 5. B-FlaP step 2 or the classification of 3FGL BCUs using the Artificial Neural Networks (ANNs). By this advanced machine learning technique we produce a Classification List for 573 BCUs. We present the architecture of the algoritm , our optimization and classification thersholds used in the analysis. Then we discuss the classification results
- Chapter 6. The radio analysis as counterpart of B-FlaP. We study the radio flux density distribution of 3FGL blazars and we define two clean area where to classify blazars and to compare the radio S_r distribution versus BFlaP for a matching classification of the two methods
- Chapter 7. We present the results of the optical campain at Asiago Observatory telescopes where we carried out spettroscopic analysis of a

sample of 3FGL BCUs classified by our ANN algorithm. Spettroscopic notes on peculiar sources are included.

The Conclusions section summarizes the main results and provides persperctive future developments.
Appendix A contains the 3FGL BCU Classification List as main result of this study Appendix B contains the full collection of BCU spectra collected during the optical campaign at Asiago Obeservatory Appendix C describes the FERMI LAT telescope and the Data Acquisition System Appendix D gives an overview of the Asiago optical telescopes used for the spettroscopy analysis in this study Appendix E describes in detail the theory of machine learning algorithms we have implemented and applied to classify γ-ray 3FGL BCUs sources.

Questo studio è rivolto alle galassie attive o Nuclei Galattici Attivi (AGN) considerate come le più luminose tra le fonti persistenti di radiazione elettromagnetica nell'universo. L'obiettivo primario dello studio è la ricerca di un estimatore, che permetta, nei casi in cui i dati osservativi dettagliati non siano ancora disponibili, di identificare la sorgente in esame come un blazar e, dove sia possibile, evidenziare l'appartenenza alla sottoclasse dei High Synchrotron Peaked blazar (HSP). L'interesse verso questo tipo di sorgenti (Blazar HSP) è giustificata dal fatto che l'attuale generazione di telescopi atmosferici Cherenkov (VERITAS, HESS, MAGIC) ha aperto nuove frontiere nella γ - astronomia nelle alte energie al di sopra dei $\sim$ 100 GeV fino al TeV. Il prossimo Cherenkov Telescope Array (CTA) esplorerà il nostro Universo in modo approfondito proprio in queste altissime energie gamma (E $>$ 0.1 TeV). I blazar e la sottoclasse HSP rappresentano la classe più numerosa di sorgenti a tali energie e quindi la capacità di identificare correttamente questi oggetti è molto importante per la comunità scientifica TeV nella determinazione degli target osservativi, al fine di aumentare il numero dei rilevamenti, oggi reso più difficoltoso a causa del ridotto campo di vista degli Imaging Atmospheric (or Air) Cherenkov Telescope (IACTs).
Il satellite FERMI / LAT, è il più importante ricercatore del cielo gamma oggi disponibile ed il Terzo Catalogo FERMI /LAT(3FGL) raccoglie le sorgenti rilevate dal LAT nei primi quattro anni di missione [2008-2012] dove 1740 sorgenti vengono classificate come AGN (58% di tutte le sorgenti catalogate in 3FGL) delle quali 1144 sono identificate come blazar, 573 come Blazar non-classificati (BCUs) , 15 come radiogalassie, 5 galassie di Seyfert ed altre 3 sorgenti AGN di diversa natura. Rispetto ai metodi di classificazione delle galassie attive oggi esistenti basati su dati multifrequenza, la novità dell'approccio adottato

in questo studio è nella ricerca di un estimatore basato *esclusivamente* su dati di variabilità raccolti alle γ - energie dove il satellite FERMI / LAT, è maggiormente sensibile (0,1 - - 100 GeV). Con riferimento a questa caratteristica dei Blazar abbiamo chiamato questo nostro metodo B-FLAP come acronimo di *Blazar Flaring Pattens*.
La ricerca si è inizialmente sviluppata valutando i risultati calcolati analizzando la funzione di distribuzione empirica cumulativa (ECDF) per le curve di luce degli AGN presenti nel catalogo 3FGL , confrontando poi le ECDFs dei BCUs con ECDFs dei blazars la cui classe era già stata catalogata. Dalla prima fase dell' analisi è emerso che il massimo γ - flusso (max-flux) considerato negli intervalli temporali disponibili nel 3FGL (bin mensili) risulta essere un parametro interessante per gli scopi di questo lavoro di ordinamento dei BCU.
Con l'obiettivo di migliorare ed approfondire i primi risultati ECDF abbiamo successivamente usato le reti neurali,(Artificial Neural Network (ANN)), sviluppando un algoritmo originale ed abbiamo istruito la rete e successivamente analizzato le sorgenti BCUs utilizzando esclusivamente i dati di *flux history* presenti nel 3FGL . L'obiettivo era la classificazione quantitativa dei BCus attraverso una selezione operata attraverso il dato statistico di verosimiglianza (likelihood).
Applicando il nostro algoritmo ANN ottimizzato per tutte le 573 BCU del catalogo 3FGL e studiando la distribuzione della likelihood , abbiamo quindi ottenuto una Lista di Classificazione dove 342 BCU sono risultati classificabili come BL Lac, 154 come Flat Spectrum Radio Quasar (FSRQ), mentre restanti 77 sorgenti rimangono come non classificate. Questo risultato riduce la percentuale di BCU presenti inizialmente nel catalogo 3FGL dal 50% al 7%.
Per ogni BCU è stata sucessivamente calcolata la likelihood relativa ad una SED di tipo HSP e 53 BCU hanno mostrato una likelihood HSP superiore all' 80%. Questo risultato soddisfa solo parzialmente le aspettative della ricerca a causa della contaminazione significativa delle sorgenti ISP ed LSP nell'analisi degli HSP, ma tuttavia si rivela un interessante risultato in grado di incrementare notevolmente la disponibilità di nuovi oggetti per le screening survey ai telescopi Cherenkov, come viene descritto in dettaglio in questo studio. Quando le condizioni sperimentali l'hanno reso possibile abbiamo validato il nostro metodo B-FLAP attraverso un'identificazione delle sorgenti rigorosa e certa, realizzata con le controparti a bassa energia ottiche e radio. I risultati osservativi ottenuti confermano la classificazione B-FLAP prodotta con il dato statistico ANN/ECDF come altamente attendibile. Questo risultato conferma la bontà dell'algoritmo usato.
Sebbene un metodo statistico non può sostituire tecniche di classificazione confermate e rigorose, B-FLAP si può quindi considerare come un ulteriore solido

approccio alla classificazione dei blazars e all' individuazione *preliminare* della sottoclasse HSP quando non siano disponibili dati osservativi dettagliati.
I risultati ottenuti soddisfano così l'obiettivo primario di questa ricerca.

Chapter 1

The gamma-ray Universe

The emission of γ - rays is related to the most violent and powerful phenomena in the Universe and provides a unique way to probe extreme physical environment characterized by the presence of intense magnetic fields and high energy particles. The γ-ray energy band extends from 100 keV up to multi TeV energies, making it the most energetic portion of the electromagnetic spectrum. Because Earth's atmosphere absorbs γ - rays it is necessary to put detectors at high altitude using balloons or satellites such as Fermi Gamma-ray Space Telescope. At energies above 100 GeV it is possible to use the atmosphere itself as a detector to study the electromagnetic showers of the Very High Energy (VHE) γ - rays from the ground. This is the basic concept of the ground γ-ray Cherenkov telescopes like MAGIC, HESS, VERITAS or large arrays like MILAGRO.

Gamma rays are extremely useful messengers since they are neutral, so that they are not deflected by cosmic magnetic fields (as happens e.g. for cosmic rays), and extremely energetic, so that they are unlikely absorbed by cosmic matter (as happens for photons of lower energy). The Universe is largely transparent to γ - rays and each γ-ray points directly back to its source. Thanks to these characteristic γ - rays permit to observe and study high energy cosmic sources extremely distant, up to $z \sim 5$, that act as natural engines accelerating particles up to extremely high energy.

1.1 Gamma-ray astronomy

The development of the γ-ray astronomy have been carried mainly in the last decades, when the techniques to observe the high-energy Universe was developed. Three important facts explain why it was so hard develop specific techniques to observe the γ-ray sky:

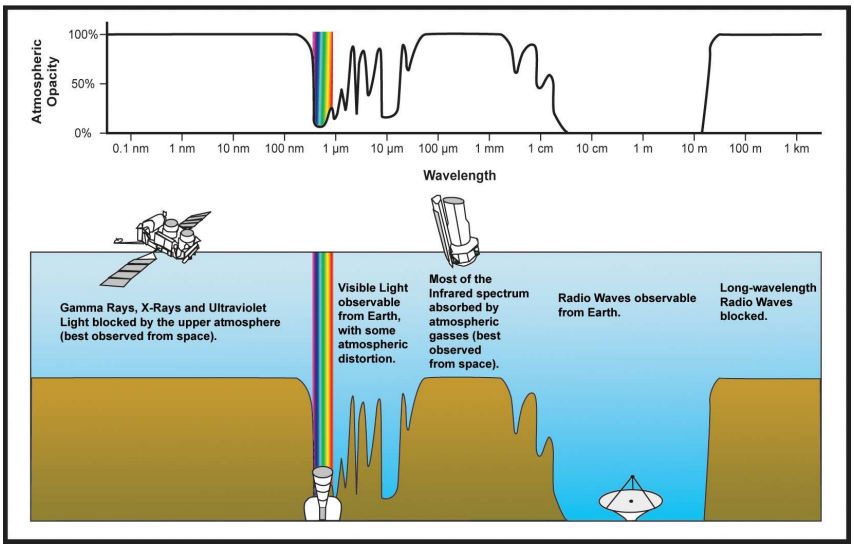

Figure 1.1: Representation of the atmosphere opacity for different wavelengths.

- As shown in Figure 1.1, the Earth's atmosphere is opaque to high-energy photons. At sea level, the atmosphere is 1033 g/cm^2 thick, this implies that an high-energy photon incident from the zenith can reach ground level without interacting electromagnetically with a probability of $\sim 10^{-10}$. Even at mountain altitudes, where the atmosphere is thinner, the probability that an high-energy photon can survive to ground is negligible. Only a detector above the atmosphere (satellite or balloon) can detect primary cosmic γ rays.

- The flux of γ rays from astrophysical sources is quite low and decrease rapidly with increasing energy. This implies that a critical problem to detect a γ-ray source is the sensitivity, we need detectors with a large effective area. A satellite-based detector is too small to detect enough photons above about 100 GeV, this implies VHE γ-ray astronomy can be performed using only ground-based detectors, which reconstruct the energy and the direction of γ rays from the study of their electromagnetic showers in the atmosphere.

- The flux of high-energy is 3 orders of magnitude more in cosmic rays than γ - rays at GeV energies. This large cosmic-ray background has to be rejected in order to study the γ-ray sources. Therefore, detectors have to be able to distinguish efficiently cosmic rays from γ rays.

Two detection techniques are available: the *ground-based techniques*, which is the detection strategy of the *Air Cerenkov Telescopes* (ACTs) and of the

Extended Arraw Shower Detectors (EASDs) and the *satellite-based techniques*. Satellite experiments can operate until ∼300 GeV, otherwise ground-based experiments until ∼50 TeV.

1.1.1 Ground-Based Telescopes

The *Air Čerenkov Telescopes* (ACTs) investigate the upper part of the γ-ray spectrum by looking at the electromagnetic showers created when a high-energy γ ray (E > 100 GeV) enters the atmosphere. The predominant radiation-matter interaction at these energies is pair production. When a high-energy γ ray enters the atmosphere it produces a pair formed by an electron and a positron, they propagate and produce photons via *Bremsstrahlung* initiating an electromagnetic shower. The resulting electromagnetic cascade grows nearly exponentially as it propagates through the atmosphere. The primary photon energy is distributed among more and more particles until electrons and positron approach to their critical energy (∼80 MeV in air). At this point the ionization energy-loss mechanism, that does not produce additional particles, becomes more important then *Bremsstrahlung*. As a consequence, energy is lost from the shower and the number of particles decreases as the shower continue to propagate.In order to improve imaging capability and background rejection more telescope are arranged in arrays working in *stereoscopic mode*. This is for example the case of HESS, CANGAROO, VERITAS and MAGIC. The *Extensive Air Shower Detectors* (EADs) are large arrays that directly detect the secondary particles from the showers induced in the atmosphere by the interaction between high-energy γ rays and air molecules. Examples of EADs are CYGNUS, CASA or HAWC.

The Cherenkov effect. It occurs when a charged particle travels into a dielectric medium of refractive index n, with a speed exceeding the light speed in the medium c/n (Fig. 1.2). When a charge moves in a dielectric medium, a polarisation occurs.When the particle velocity is superluminal v>c/n, the particle is moving faster than the electromagnetic information which induce the polarisation. A coherent wave-front appears at an angle θ , and the emitted radiation is called Cherenkov Light (Fig. 1.4)

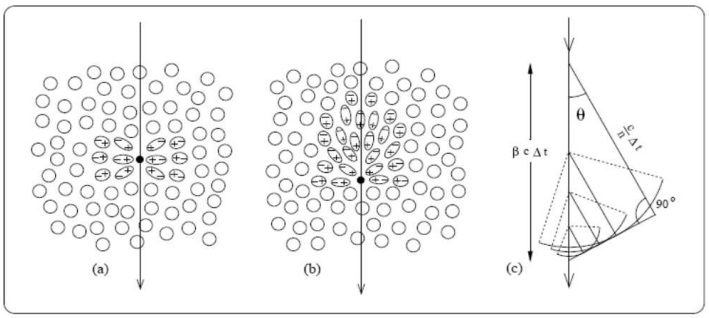

Figure 1.2: The Cherenkov effect

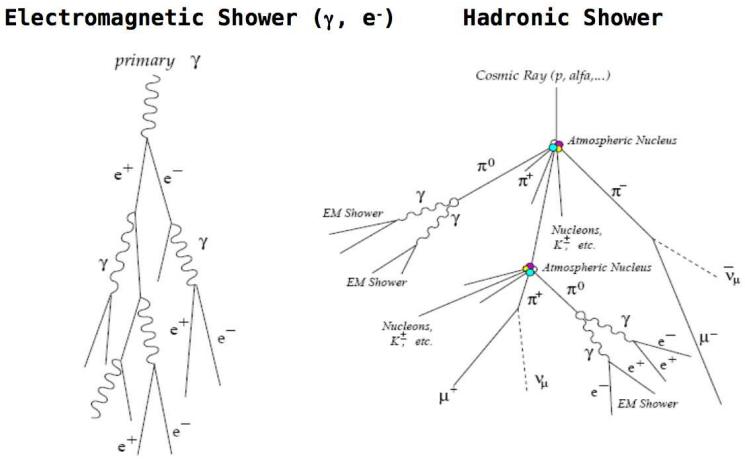

Figure 1.3: Electromagnetic and hadronic pair and photons production

The future of the ATCs is the *Čerenkov Telescope Array* (CTA). CTA will be a large array of mid-size telescopes. Two stations of several telescopes will be installed, one in the southern hemisphere and the other in the northern one.[1]

Ground-Based Telescopes can detect only the upper part of the γ-ray spectrum (E $>$ 100 GeV). To date, it has been discovered more than 150 high energy sources, belonging to the classes of pulsars and their nebulae, supernova remnants, γ-ray binary systems, star forming regions, starbursts and active galaxies. Moreover, about 18% of the detected high-energy sources have not a clear association with objects known in other wavelengths.

[1]CTA website at https://portal.cta-observatory.org

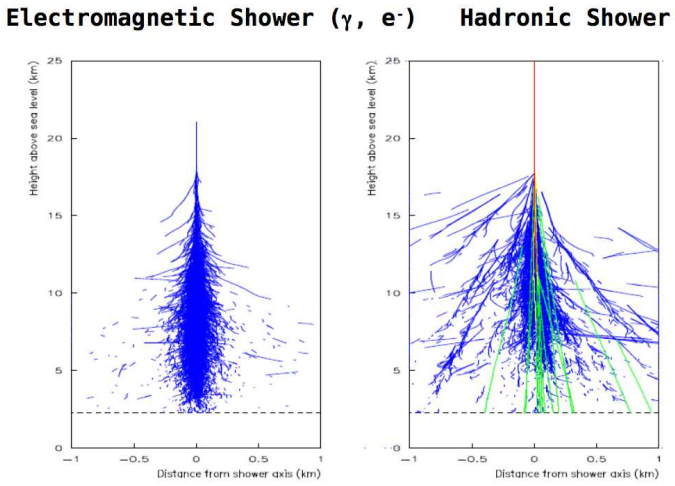

Figure 1.4: Cherenkov showers in γ -ray ground observations

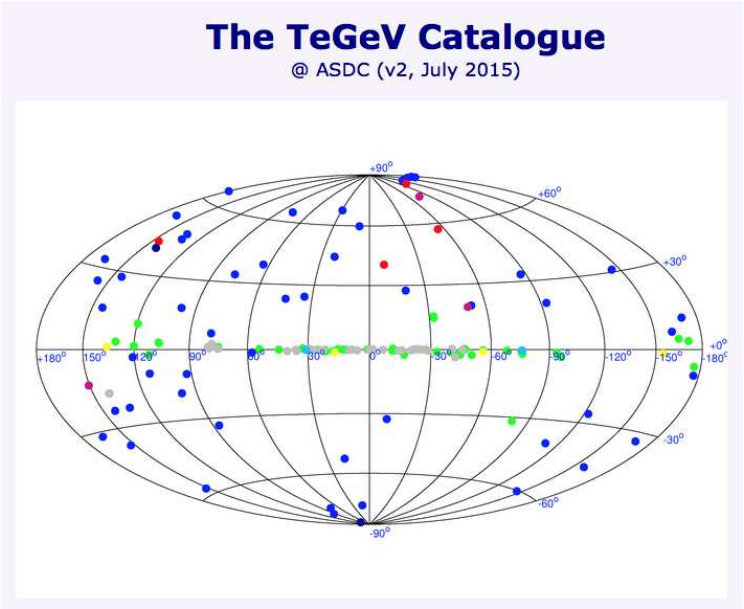

Figure 1.5: TeV sky from ASDC 2015 catalog

A connection between the results obtained by satellite-based and ground-based telescopes is very important to study in detail the nature of the high-energy emission of the most energetic sources in the Universe.

1.1.2 The satellite telescopes before Fermi LAT

In the 1950s, works by Hayakawa [36], Hutchinson [40] and especially by Morrison [60] had led scientists to believe that a number of processes occurring in the Universe would result in γ-ray emission. These processes included cosmic ray interactions with interstellar medium, supernova explosions and interactions of energetic charged particles with intense magnetic fields. However, only in the 1960s the first cosmic γ rays were detected.

Since the interaction of photons with an energy above 10 MeV is dominated by the pair production, all satellite-based telescope detections use a spark chamber or layers of tracker/converter made with high atomic numeber (Z) foil to estimate the incoming direction of the photons, a calorimeter to measure their energy and an anticoincidence shield to reduce the background due to charged particles. The following is a brief review of γ-ray space missions.

Explorer XI (April 1961 - September 1961). The first γ-ray space mission was *Explorer XI* in 1961 [45] and it detected less than 100 photons uniformly distributed in the sky implying the presence of a sort of uniform "γ-ray background". Such a background would be expected from the interaction of cosmic rays with the interstellar medium. The next important step was the NASA *Orbiting Space Observatory III* (OSO III) mission in 1968 [46]. It detected about 600 photons concentrated on the Galactic plane attributable to the γ-ray production in the Milky Way. The main detector used scintillators and Čerenkov detectors and was able to detect photons above 50 MeV.

Vela observatories (1969 -1970).In 1969 and 1970 U.S. Air Force launched the Vela series spacecraft to detect X rays and γ rays coming from the Earth or the Moon in order to determine if Soviets were complying with the nuclear test ban treaty. While no atmospheric γ rays were detected, they serendipitously discovered transient flashes of radiation lasting in average of 10 ms to 10 s in random direction on the sky named Gamma-Ray Bursts (GRBs) [42].

The SAS-2 observatory. (1972 -1973) The first satellite exclusively designed for a γ-ray mission was the second *Small Astronomy Satellite* (SAS-2), launched in the 1972 [43]. SAS-2 carried a single telescope with a 32-level wire spark-chamber covering the energy range from 20 MeV to 1 GeV and with an effective area of 100 cm^2. SAS-2 provided the first detailed information about the γ-ray sky revealing a strong correlation between the diffuse radiation coming from the Galactic plane and and the Galactic structural features and it was the first satellite to detect the isotropic, apparently extragalactic, γ-ray emission.

Moreover, SAS-2 resolved the first point sources detecting a pulsed γ-ray emission from 3 sources, the *Crab* and *Vela* pulsars and *Geminga*, identified as a pulsar more years later.

The COS-B observatory.(1975 - 1982) In 1975 the *European Space*

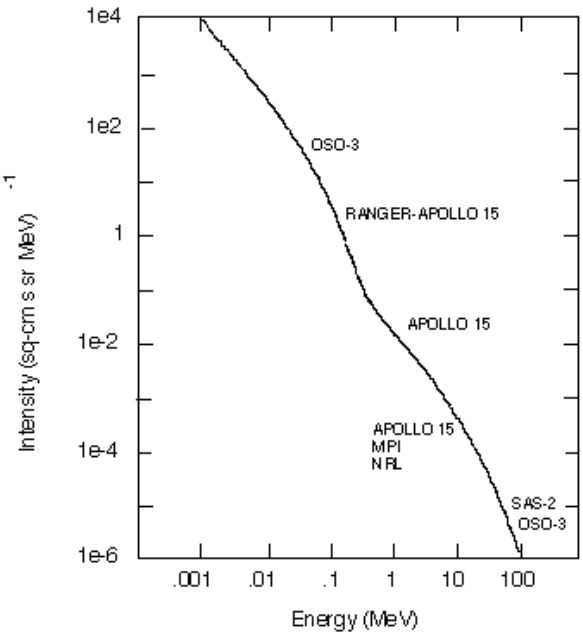

Figure 1.6: The spectrum of the diffuse gamma-ray background detected by SAS-2 in the 0.001 - 100 MeV energy range (*Nasa Heasarc*)

Agency (ESA) launched COS-B [78]. As SAS-2, COS-B carried a wire spark-chamber that recorded the direction of the electron-positron pair created in thin Tungsten plates and a CsI calorimeter that measured the energy of the charged particles. The upper part of the instrument was surrounded by an anticoincidence counter to assure that only neutral particles triggered the instrument. COS-B was able to detect photons in the energy range between 30 MeV and 5 GeV. The major result of the COS-B experiment was the creation of the first γ-ray catalog [17] that contained about 25 γ-ray sources from the observation made during the first three years of activity. The catalog included the *Crab* and *Vela* pulsars, the molecular cloud ρ-Oph and the first extragalactic γ-ray object, the Active Galactic Nucleus (AGN) 3C 273.

The CGRO observatory.(1991 -2000) After a stop of about 15 years because of the *Space Shuttle Challenger* disaster occurred in 1986, the NASA mission *Compton Gamma Ray Observatory* (CGRO) revolutionized our understanding of the γ-ray sky because of the improved sensitivity with respect to previous missions. The CGRO satellite was launched in 1991 and it carried four instruments, OSSE, COMPTEL, BATSE and EGRET, that covered an energy range between 20 MeV and 30 GeV. The *Oriented Scintillation Spectrometer Experiment* (OSSE) consisted of four NaI scintillation crystals and its main objective was spectroscopy of cosmic γ-ray sources and solar flares in

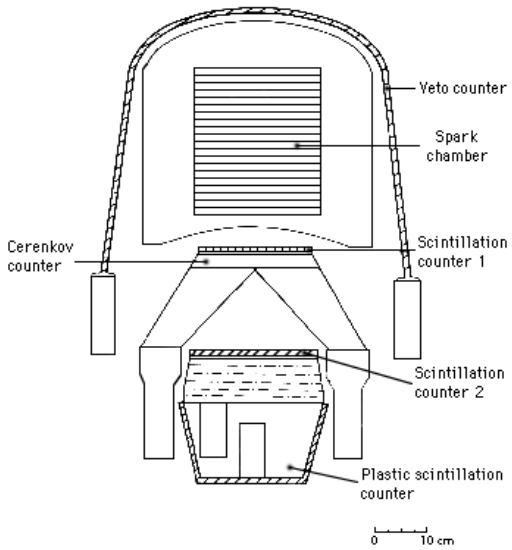

Figure 1.7: Diagram of the gamma-ray detector on COS-B (*NASA Heasarc*)

the energy range from 50 keV to about 10 MeV. OSSE measured the distribution of the energy emitted from a number of γ-ray objects, studied nuclear lines in solar flares, radioactive decay of nuclei in supernova remnants and matter-antimatter annihilation taking place near the center of our Galaxy [41]. The *imaging COMpton TELescope* (COMPTEL) was an imaging detector, its main objective was to study active galaxies, supernova remnants and diffuse γ-ray emission from giant molecular clouds in the energy range between 1 and 30 MeV [41]. The *Burst and Transient Source Experiment* (BATSE) was the smallest instrument onboard CGRO. It was dedicated to monitor the full celestial sphere for transient γ-ray phenomena such as Gamma-Ray Bursts (GRBs) and bursts from other cosmic sources (including solar flares from the sun) all over the sky in the energy range from 20 keV to 1 GeV [41].

EGRET observatory.The *Energetic Gamma-Ray Experiment Telescope* (EGRET) was the main instrument onboard CGRO and it was devoted to the highest energy ever observed from the space, reaching the upper limit of E $\sim$30 GeV. EGRET was a pair-conversion telescope, the conversion of the high-energy photons into electron-positron pairs occurred in an upper stack of 28 Tantalum conversion foils of an average thickness of 90 μm interleaved with spark chamber modules. The direction of the radiation was determined by a time of flight coincidence below the conversion chamber. The mission lasted for nine years and it revolutionized our understanding of the γ-ray sky because of its better performances with respect to the previous ones. During all the mission EGRET detected about 2 millions of photon with E $>$ 100 MeV,

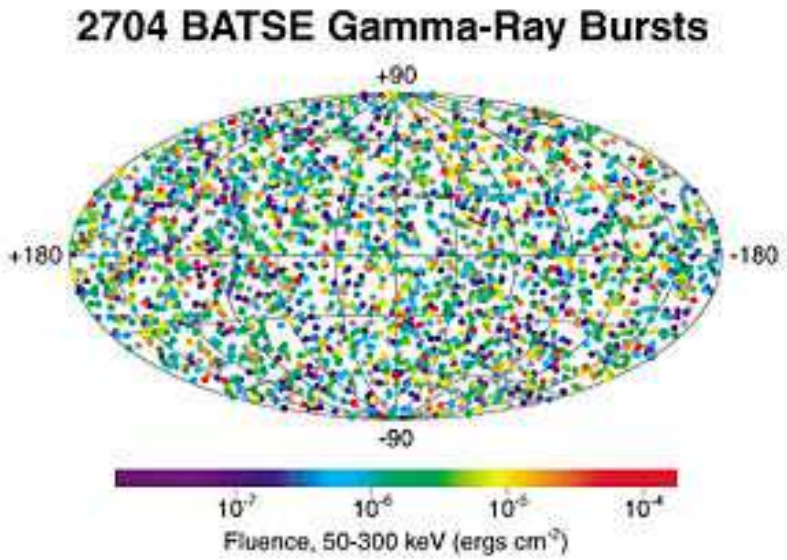

Figure 1.8: Gamma Ray Burst sky detected by BATSE.(*NASA Heasarc*)

allowing a detailed study of the Galactic and extragalactic diffuse emission and of the point-like γ-ray sources.

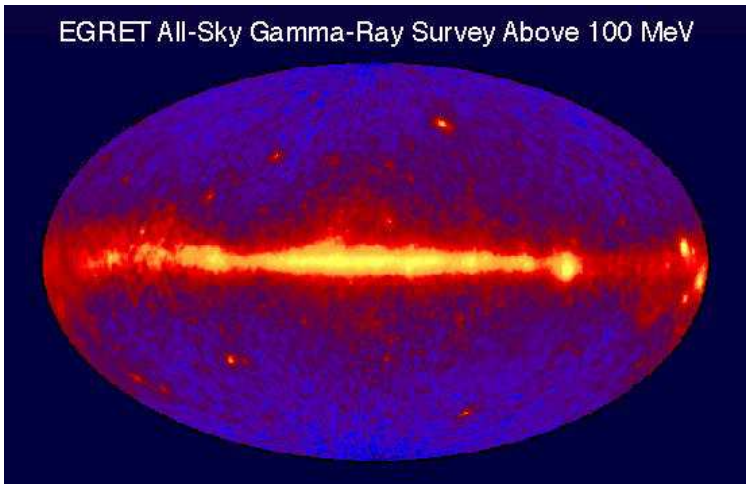

Figure 1.9: EGRET All-Sky Gamma Ray Survey above 100 MeV(*NASA Heasarc*)

The last EGRET Catalog (3EG) [34] consisted of 271 sources (with E > 100 MeV): 6 pulsars (high-energy pulsed emission from *Geminga* was detected [19] , 93 blazars (a subclass of AGNs discovered to be a new class of γ-ray

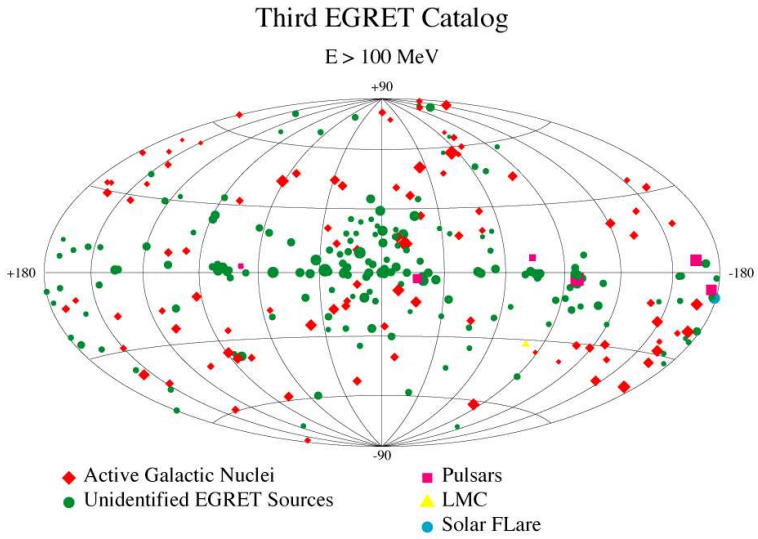

Figure 1.10: The Third EGRET source catalog shown in Galactic coordinates.

emitters [34]), one normal galaxy (the Large Magellanic Cloud) and a solar flare (the single 1991 solar flare). 170 γ-ray sources detected by EGRET, about 60%, had not a clear association with a class of objects known in a different wavelength. Since the association of a γ-ray object with a source known in other wavelengths is primarily based on a positional coincidence, the large number of unidentified sources in the 3EG was related to the bad angular resolution of the γ-ray telescope.

The AGILE observatory (2007 - ...) On April 23, 2007 it has been launched the AGILE mission by the Indian PSLV-C8 rocket from the Satish Dhawan Space Center SHAR, Sriharikota. AGILE (*Astrorivelatore Gamma ad Immagini LEggero*) is a completely italian high-energy astrophysics mission supported by the Italian Space Agency (ASI) with scientific and programmatic participation by INAF (Istituto Nazionale di AstroFisica), INFN (Istituto Nazionale di Fisica Nucleare) and several italian universities. The main scientific goal of AGILE is to explore the γ-ray Universe with a very innovative instrument combining a γ-ray imager (sensitive in the energy range of 30 MeV and 50 GeV) and a hard X-ray imager (sensitive in a energy range between 15 and 45 keV) [79]. The AGILE scientific payload is a small satellite composed by three detectors combined into one integrated instrument.

The first detector is the *Gamma-Ray Imaging Detector* (GRID) that is sensitive in the energy range between 30 MeV and 50 GeV and it has a sensitivity compared to EGRET. All the AGILE detectors are completely surrounded by

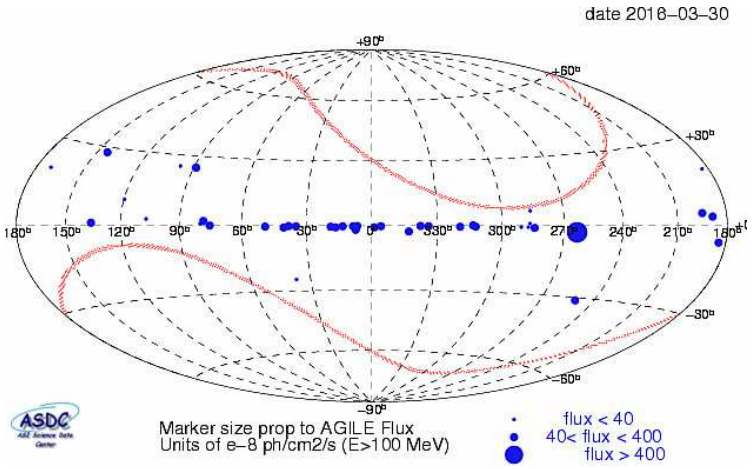

Figure 1.11: AGILE spinning sky view

an AntiCoincidence (AC) System with the aim of rejecting charged particles. It is constitutes by three plastic scintillator layers and the signal is read by photomultiplier placed externally to the AC System.[79]

This detector is aimed at simultaneous X-ray and γ-ray detection of high energy cosmic sources with excellent imaging capabilities.

The third detector is the Cesium-Iodide Mini-Calorimeter (MCAL). It is capable of independently detecting GRBs and other transient sources in the energy range between 300 keV and 100 MeV with optimal time capabilities.

To date, AGILE has been detecting more than ten million of photons giving the opportunity to study in detail a lot of Active Galactic Nuclei, Gamma-Ray Bursts and other transient objects on the Galactic plane, γ-ray pulsars and some Pulsar Wind Nebulae. One of the main important results of the AGILE mission is the discovery of the γ-ray emission from accreting binary systems, which was already supposed but never observed.

1.2 The Fermi Gamma-ray Space Telescope

The *Fermi Gamma-ray Space Telescope* is the space observatory used in this study and data from its catalogs are the core of this research. Fermi is an international and multi-agency observatory class mission that is exploring the Universe in the energy range from 10 keV up to more than 300 GeV, an energy band that has never been observed by a space telescope. Fermi is a product of a collaboration between NASA, the Department of Energy of the United Sates and other institutions in Italy, France, Germany, Sweden, Japan and United States.

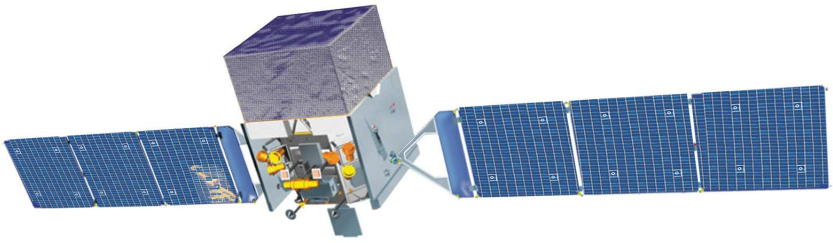

Figure 1.12: *Fermi* LAT spacecraft .

FERMI , whose original name before the launch was GLAST (*Gamma-ray Large Area Space Telescope*), was successfully launched on June 11, 2008 from the launch pad 17-B at Kennedy Space Flight Center (Florida, USA), into an initial orbit at about 565 km altitude with a 25.3° inclination and an eccentricity lower than 0.01. During its normal operations FERMI orbits around Earth with a period of 95 minutes and scans the sky with a rocking angle of about 35°. Figure 1.12 shows a schematic view of the Fermi spacecraft with its two instruments: the *Large Area Telescope* (LAT) and the *Gamma-ray Burst Monitor* (GBM) formerly *GLAST Burst Monitor*).

The LAT, the main FERMI instrument, is a pair-conversion telescope based on high-precision detectors from High Energy Physics technology The LAT is the successor of the EGRET telescope aboard the CGRO but its excellent performances in terms of effective area, angular resolution, energy resolution, Field-of-View (FoV) and dead-time provide a factor greater than 50 in sensitivity compared to EGRET [81].

The GBM is entirely devoted to the study of the transient γ-ray sources, such as Gamma-Ray Bursts and solar flares. It is made up by two kind of detectors based on scintilling materials, which together cover an energy range from 8 keV up to about 30 MeV. This energy range guarantee an energy overlap with the LAT.

FERMI represents the new generation of γ-ray telescopes, its performances are much better than those of the previous missions. The FERMI mission is contributing in a decisive way in several topics of modern understanding of the γ-ray Universe, from the study of Galactic objects, such as pulsars, PWNe and SNRs, and extragalactic objects, such as blazars, to the detailed investigation on the nature of diffuse emission and transient sources.

1.2.1 Overview of the Large Area Telescope

Pair production is the dominant mechanism of interaction between radiation and matter at the energies studied by the *Fermi Large Area Telescope* [13]. This process is the basis to measure the directions, the energies and the arrival times of the γ-ray photons entering the detector, while rejecting background from charged particles. For this reason a pair conversion telescope is made basically by a tracking system, a calorimeter and an anticoincidence system, as shown in Figure 1.13. The EGRET experiment aboard CGRO and previous instruments aboard SAS-2 and COS-B missions shared the same detecting strategy.

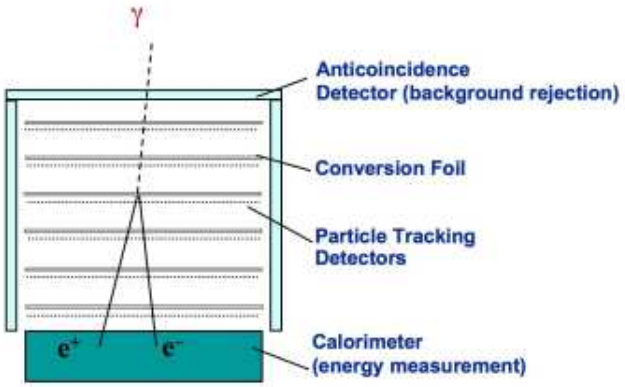

Figure 1.13: Schematic view of a pair conversion telescope like the LAT. Credit: *Fermi*-LAT Team.

A γ ray entering the LAT creates an electron-positron pair, whose energies and directions are reconstructed by the LAT subsystems. From these information it is possible to determine the energy, the arrival time and direction of the incoming photon using the conservation of four-momentum.

The tracks of the electrons and the positrons produced by a γ ray are measured by the tracking system. In order to maximize the conversion probability in the detector, detecting planes are interleaved with *conversion foils* of particular tickness. Since the conversion probability increases with the atomic number (Z) as Z^2, the conversion foils are usually made by high Z material, EGRET used Tantalum (Ta) foils while LAT uses Tungsten (W) foils. In the calorimeter the electron-positron pair creates an electromagnetic shower, from the measurement of the shower the calorimeter determines the energy of the pair. The measurements gathered by the tracking system and by the calorimeter are then used to reconstruct the energy of the incoming γ ray.

The orbit environment is extremely rich of charged particles that enter the detector with rates of the order of about 10^5 times the rate of γ rays. For this reason an anticoincidence detector is used to reject the charged particles background. The anticoincidence shield surrounds the detector and it is usually made by plastic scintillator. Since charged particles give a signal when crossing the scintillators while γ rays do not, the anticoincidence shield reduce the charged particles background with high efficiency.

The *Fermi Large Area Telescope* (LAT) follows the same base principles but is based on a new generation γ-ray detectors developed for High Energy Physics. The main LAT subsystems are the *Tracker* (TKR), the *Calorimeter* (CAL), the *AntiCoincidence Detector* (ACD) and the *Data Acquisition System* (DAQ). The TKR is made up of alternated layers of converters, made up of Tungsten foils that allows the conversion of γ rays, and trackers, made up of silicon microstrip detectors that allow the reconstruction of the electron positron tracks. The CAL is located below the TKR and measures the energy of the pair. The ACD covers the LAT in order to reduce the background due to charged particles discriminating their from γ-rays. The DAQ manages the main subsystems function, e.g. the reading procedure and the trigger control.

The LAT is made of an array of 4×4 identical *towers* each one made by a Tracker module, a Calorimeter module and a DAQ module; the 16 towers are surrounded by an outer segmented AntiCoincidence Detector. The main mechanical structure is a 16 cell aluminum grid that hold both the trackers towers and the calorimeter modules and all the electronic boxes are placed below the grid. The outside dimensions of the LAT are approximately 1.8 m $\times$ 1.8 m $\times$ 1 m and its mass is $\sim$3000 kg. The overall aspect ratio of the LAT tracker (height/width) is 0.4, allowing a large Field-of-View and ensuring that nearly all pair-conversion events initiated in the tracker pass into the calorimeter for energy measurement.

The LAT offer higher performances with respect to its predecessor EGRET thanks to the new design strategy and the new detecting technologies.

The main innovation of the LAT is the introduction of the TKR based on solid-state detectors instead of spark chambers used for the EGRET tracker. These detectors have many advantages. First of all they provide a spatial resolution about 10 times better than spark chambers without many complications during fabrication. Additionally they offer a lower dead time of about 20 μs, with respect to the dead time of 100 ms of the EGRET spark chambers. Moreover, the silicon detectors used for the LAT Tracker are radiation hard and does not contain consumables, while EGRET used spark chambers for the tracking system and the gas deteriorated with time.

The LAT CAL is made by scintillation bars, in order to better reconstruct the electromagnetic shower development, while the EGRET calorimeter was

based on a monolithic scintillating detector.

The segmented ACD detector is also another big LAT innovation, since the EGRET anticoincidence detector was made by a single scintillator panel. This segmentation will provide an higher detecting efficiency at energies greater than 10 GeV. At these energies the *self-veto* problem becomes important, because a particle from the electromagnetic shower can backscatter in the ACD producing a spurious signal. For this reason in the LAT the ACD is segmented, making possible to know roughly which ACD panel gave a signal, in order to determine if the panel has undergone a backsplash or not. In this way it is possible to avoid efficiency loss at high energies as was for the EGRET telescope.

In order to achieve its scientific goals the LAT must reject most of the background due to various contributions. The main contribution is due to cosmic rays that enter the detectors producing spurious signals. Another contribution comes from the albedo γ rays from the Earth, that can be removed mainly by considering the position of the spacecraft with respect to our planet.

A comparison between the LAT performances and those of EGRET is shown in Table 1.1.

Quantity	**LAT**	**EGRET**
Energy Range	20 MeV - 300 GeV	10 MeV - 30 GeV
Peak Effective Area	~ 8000 cm^2	1500 cm^2
Field Of View	~ 2.4 sr	0.5 sr
Angular Resolution	$< 3°.5$ (100 MeV)	$5°.8$ (100 MeV)
(single photon)	$\sim 0°.6$ (1 GeV)	$\sim 1°.7$ (1 GeV)
(68% containment)	$< 0°.15$ (> 10 GeV)	
Energy Resolution	$< 10\%$	10%
Deadtime per Event	< 100 μsec	100 msec
Source Localization	$< 0'.5$	$15'$
Point Source Sensitivity	$< 6 \times 10^{-9}$ cm^{-2} sec^{-1}	$\sim 10^{-7}$ cm^{-2} sec^{-1}

Table 1.1: LAT specifications and performances compared with EGRET. Quoted sensitivity for the LAT is referred to sources out of the Galactic plane and E $>$ 100 MeV.

1.3 Gamma rays from the sky

The knowledge of γ-ray sources before the launch of the *Fermi Gamma-Ray Space Telescope* (2008) came mainly from the experience of the CGRO experiment and in particular from the results of the Third EGRET Catalog [34].

Galactic γ-ray sources are mainly compact objects, such as neutron stars and their nebula or accreting black holes [74]. Supernova remnants (SNRs) are cosmic objects which may be related to the cosmic ray acceleration. Structures like shells that interact with Interstellar Medium (ISM) have been observed with high resolution telescopes in the X-ray band and these sites have been associated with shocks. The main sources of extragalactic radiation are the Active Galactic Nuclei (AGN), and in particular blazars, a subclass of AGN whose jet is aligned with the line of sight. In the extragalactic Universe an important role is played by transient sources like GRBs, that are shining flashes of radiation. In addition, a diffuse γ-ray emission given by the contribution of two different components, Galactic and extragalactic, dominates the entire high-energy Universe. The Galactic one is thought to be related to the interaction between cosmic rays and the matter in the Galactic disk; other side the extragalactic one is probably given by the contribution of thousands unresolved extragalactic point-like sources. Moreover, part of the extragalactic component may be related with the decay of exotic particles in the Primordial Universe.

In the following, a review of the celestial γ-ray sources known is given. AGN, the main topic of this work, are covered in the next chapter.

1.3.1 Diffuse gamma-ray emission

In Figure is shown the map of the γ-ray sky (E > 100 MeV) based on data taken by the FERMI-LAT instrument. It is evident that the diffuse emission dominates the entire γ-ray sky with the highest intensity coming from the plane of our Galaxy. The diffuse γ-ray emission can be divided in two components, the Galactic diffuse emission, placed along the Galactic plane and coming from our Galaxy, and the extragalactic diffuse emission, characterized by an isotropic distribution in the sky.

The Galactic diffuse emission

In 1968 was detected for the first time an emission of high-energy photons coming from our Galaxy and not attributable to point-like sources. A detailed map of the Galactic diffuse γ-ray emission was accomplished after the SAS-2 and COS-B observations between 1972 and 1982. About 90% of γ rays with energies above 100 MeV detected by FERMI LAT comes from the Milky Way galaxy. The Galactic diffuse γ-ray emission can be explained through the energetic interactions between cosmic rays and the interstellar medium. Cosmic Rays (CRs) are very high-energy particles, composed primarily of protons, atomic nuclei and leptons, and their origin is still a mystery. Once they are accelerated up to relativistic velocities through not well known mechanisms,

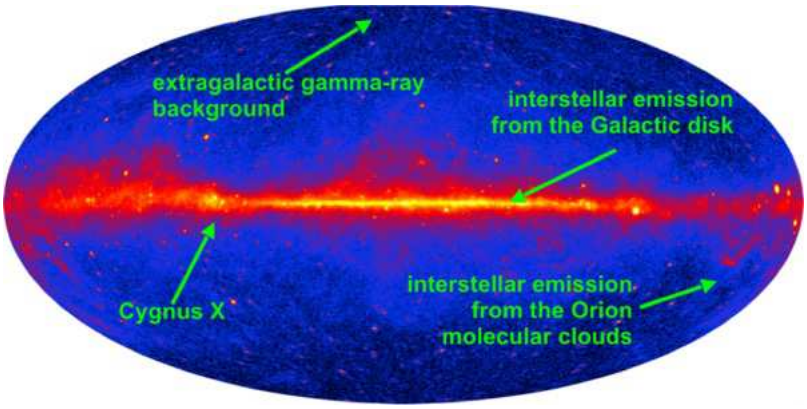

Figure 1.14: γ-ray sky (E > 100MeV) by Fermi Lat. Credit: NASA

they move through the interstellar medium where are trapped by the Galactic magnetic field. The Galactic diffuse γ-ray emission is then produced via *Bremsstrahlung*, if a high-energy electron is deflected by nuclei of the ISM, Inverse Compton (IC), if a high-energy electron transfers part of its energy to a soft photon coming from the stellar radiation, and π^0 decay, if a high-energy proton or atomic nucleus collides an interstellar proton creating a neutral pion [61]. All these three type of interactions product γ rays and their spectra are very different.

Detection of this diffuse γ-ray emission should give information about the production and propagation of cosmic rays in the Milky Way galaxy. After removal of identified galactic point-like sources, the Galactic diffuse emission shows a structure that reflects the main features of the mass distribution in the Galaxy known in other wavelengths. The study of the diffuse emission gives information about spectra and intensities of CR species at distant locations and allows to study CR acceleration in Supernova Remnants (SNRs) and other sources and their propagation in the ISM. On the other hand, the Galactic diffuse emission is a structured background source for point-like sources and its accurate determination is essential in order to understand if an excess of photon emission in a specific region of the sky is related to the existence of a γ-ray source or to statistical fluctuation of the background and it is also important for accurate localization of such source and its spectrum [39].

The Extragalactic diffuse emission

An apparently isotropic, presumably extragalactic, component of the diffuse γ-ray flux above 30 MeV was discovered by the SAS-2 satellite and confirmed by the subsequent space telescopes .

The hypothesis on the origin of the extragalactic γ-ray background emission were various, from the most conservative, such as the summed contribution of thousands of unresolved AGNs, to more exotic, such as the contribution of the annihilation from exciting particles which came from some unknown processes that took place in the primordial Universe. Other explanations involve particles deriving from extension of the Standard Model to supersymmetric particles (SUSY), which can contribute substantially to the Dark Matter content of the Universe and that can be found in the Galactic halos.

The extragalactic diffuse γ-ray emission is well described by a power law over FERMI energies and it is consistent with the average index for blazars detected by FERMI, which lends some support to the hypothesis that the isotropic flux is from unresolved AGN sources [75].

Diffuse emission has also been observed from the Large Magellanic Cloud (LMC), characterized by a flux consistent with production by cosmic rays. Other sources of diffuse emission are the Small Magellanic Cloud (SMC) , an irregular dwarf galaxy which appears as a huge and diffuse cloud in the souther sky , and M31 galaxy too. Since 1999 , with EGRET, gamma rays emission was detected from starbust galaxies.

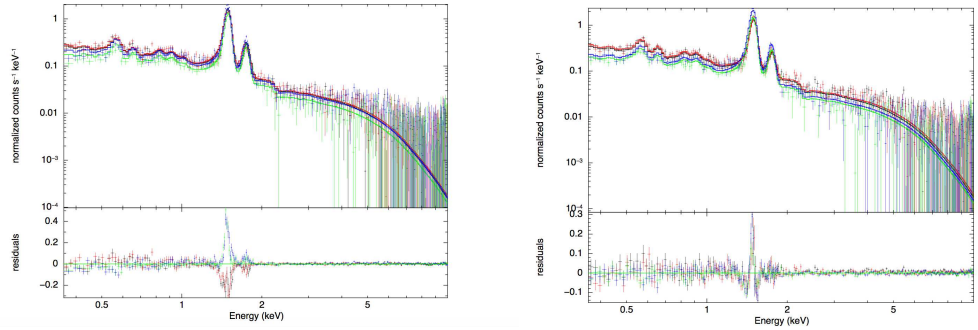

Figure 1.15: diffuse γ-ray emission in M31. (right) Nothern part of the disk , (left) Southern part.

1.3.2 Gamma-ray Pulsars and Pulsar Wind Nebulae

A pulsar (*PULSating StAR*) is a rapidly-rotating neutron star, i.e. the stellar remnant of a massive star ($M > 8M_{\odot}$) after its gravitational collapse, with a very intense dipole magnetic field, which emits a beam of detectable electromagnetic radiation with observed periods ranging from about 1 ms to 10 s. The period is observed increase in time. The radiation can only be observed when the beam of emission is pointing toward the Earth. From timing mea-

surements, it is possible to estimate the strength of the magnetic field on the surface of the star, the age of the pulsar and other physical parameters [80].

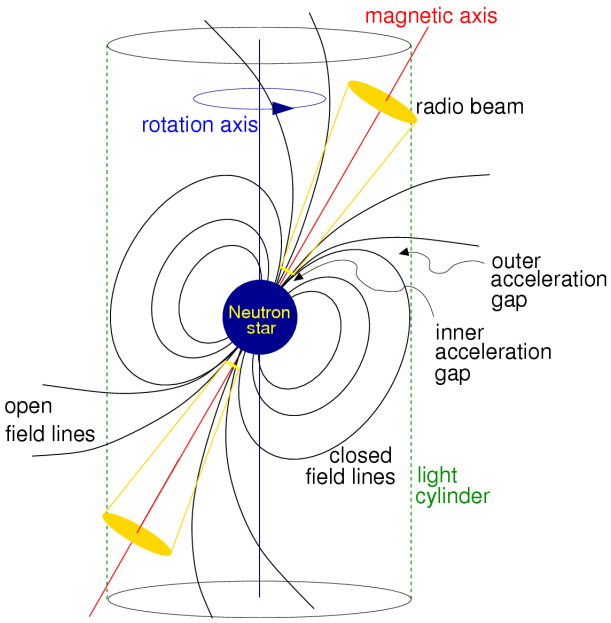

Figure 1.16: schematic view of a pulsar with the *polar cap* and *outer gap*

Pulsars are generally discovered in radio wavelengths, but they can emit in all wavelengths of the electromagnetic spectrum, in particular the first two γ-ray emissions from point-like sources were observed from the *Crab* and *Vela* pulsars by SAS-2 [26]. The first radio pulsar was discovered in August 1967 by A. Hewish and J. Bell during a radio astronomy project [37]. With its discoveries the Fermi LAT has established pulsars as the dominant GeV gamma-ray source class in the Milky Way. Among those gamma ray pulsars are dozens of young radio-quiet pulsars discovered by their pulsed gamma-ray signal in LAT, dozens of radio-loud young and millisecond pulsars (MSPs) previously known from their radio pulsations, and dozens of MSPs newly detected in the radio following their discovery as unassociated LAT sources. If at the end of 2004 EGRET observed only seven pulsars emitting in γ-ray energy band, the Fermi Second Catalog of Gamma-ray Pulsar presents 117 gamma-ray pulsars unveiled in three years (2008 - 2012) of on-orbit observations.

The γ-ray spectrum of pulsars are extremely flat showing a peak of emission in the GeV (*cut-off* energy), above this energy the spectrum decreases very quickly. Light curves of γ-ray pulsars are extremely regular showing one or

two peaks not always in phase among energy bands.

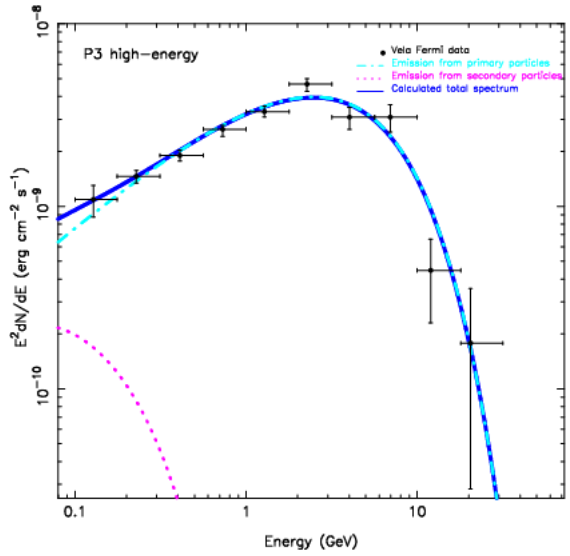

Figure 1.17: the γ-ray phase-resolved spectra for the Vela pulsar.

A neutron star has a radius of about 15 km, a mass of about 1.4 $M_\odot$ (this means an average density of about 10^{15} g/cm^3) and a very intense magnetic field with a strength at poles of order of 10^{12} – 10^{13} Gauss. There are other classes of isolated neutron stars characterized by the lack of a steady radio band emission and a very different strength of the magnetic field, with a value of about 10^{10} Gauss for the CCO (*Central Compact Object*) [23] up to 10^{15} Gauss for the Magnetars [55].

The emission mechanism is not clear but it may be related to the strong magnetic field that neutron stars must have. Current models assume the magnetic axis of the star is probably not aligned with the rotation axis. If the beam of radiation is somehow collimated along the magnetic axis, we only see it when the beam points in our direction. We may even see two pulsed as opposite magnetic poles pass by.[39].

Different kinds of pulsar are known, one of them is the *Millisecond Pulsars* (MSPs).They are found near from us, because they are fainter than normal pulsars A MSP is a pulsar with a rotational period in the range of about 1 and 10 milliseconds (this is the origin of their name), a weaker magnetic field (less than 10^{10} Gauss) and their frequency decreases much slower in time. The origin of millisecond pulsars is still unknown. The leading theory is that they begin life as longer period pulsars but are spun up through accretion. For this reason, millisecond pulsars are sometimes called "recycled" pulsars. MSPs are very old pulsars (about 10^9 years) and are thought to be related to low-mass

X-ray binary systems. In these systems, X-rays are emitted by the accretion disk of a neutron star produced by the outer layers of a companion star that has overflowed its Roche lobe. The transfer of angular momentum from this accretion event can increase the rotation rate of the pulsar to hundreds of times a second, as is observed in MSPs.

Pulsed radio emission represents only a little fraction of the total energy emitted by a pulsar. The rapidly rotating, superstrong magnetic field of the spinning pulsars accelerates charged particles of the magnetosphere to ultra-relativistic speed, creating the pulsar wind. The pulsar wind streams into the interstellar medium, creating a standing shock wave, where it is decelerated to sub-relativistic speed. In this region, ultrarelativistic charged particles interact and are confined by the ram pressure of the ambient medium and by the magnetic field of the pulsar, setting up the *Pulsar Wind Nebula* (PWN). Beyond this radius Synchrotron emission increases in the magnetized flow.

1.3.3 Supernova Remnants

Supernova remnants (SNRs) represent the relics of a supernova explosion, that cause a burst of radiation that often briefly outshines an entire galaxy. They are important because connected to the study of the late stages of stellar evolution of high-mass stars ($M > 8\ M_{\odot}$), of the properties of the explosive nucleosynthesis and because of their interaction with the surrounding space, that is contaminated and energized by the products of the supernova explosion.

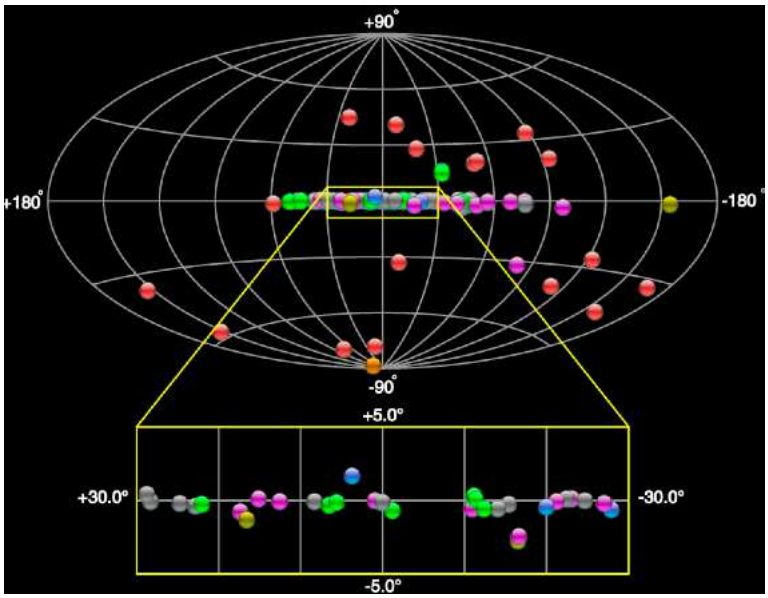

Figure 1.18: the FERMI γ - sky for Supernova Remnants .

The importance of SNRs in astroparticles physics is related to the origin of the Cosmic Rays (CRs). Cosmic Rays, relativistic cosmic particle from the space, have been studied since early in the twentieth century. To date, the question about the origin of cosmic rays nuclei remains only partially answered, with widely accepted theoretical expectations but incomplete observational confirmation. Theoretical models and indirect observational evidence support the idea that CRs with energy below $\sim 10^{15}$ eV are produced and accelerated in the Galaxy by SNRs. The main mechanism which is believed to be responsible for the CR production is the shock acceleration, happening when the Supernovae shell shocks interact with the interstellar medium. The shock mechanism is an efficient particle accelerator up to very high energy (TeV energies) and in the case of SNe on time scales of $10^3 - 10^4$ years. The accelerated CR escape from the SNR remaining trapped in the Galactic magnetic field. It has been calculated that roughly 10% of kinetic energy of a SNR must be transferred to CRs [38]. Observing charged particles, there is no possibility to directly observe the sites of their production, due to chaotic magnetic deviation. Cosmic rays interact with the interstellar gas and dust and photons, producing γ rays. Photons are not deviated by the Galactic magnetic field and a direct observation of the accelerator sites is then possible. During their explosion supernovae can accelerate protons and heavy ions to high energies. The protons can interact in the interstellar medium, producing cascades of secondary particles, such as neutral pions (π^0) that decay quickly into γ rays. The heavy ions are radioactive and they decay, emitting γ rays. Moreover, the electrons accelerated by the shock wave during the supernova explosion can interact with the photons of the Galactic background radiation and the radiation fields of the SNR (this process is responsible also for the X-ray emission from the SNR) by the *Bremsstrahlung* and the Inverse Compton. To date, it is not completly clear the leptonic and hadronic contribution by the various spectral components observed for the γ-ray SNRs. In the First Fermi LAT Supernova Remnant Catalog, edit in 2015, 102 candidates SNR with a final source TS >25 are classified.

1.3.4 Gamma-Ray Bursts

Gamma-Ray Bursts (GRBs) are the most powerful and most distant known sources of γ rays. The brightest GRB at GeV energy is about 10^4 times brighter than the brightest AGN. GRBs are intense flashes of γ rays, lasting from some milliseconds up to hundreds of seconds and they are detected with a frequency of about one GRB per day.

GRBs were discovered serendipitously in the late 1960s by VELA satellites, a series of U.S. military satellites designed to detect covert nuclear weapons tests, but their discovery was first reported in 1973. An advance in understand-

ing these mysterious objects occurred in 1991 with the launch of the *Compton Gamma-Ray Observatory* (CGRO). The all-sky survey from BATSE onboard CGRO, which measured about 3000 bursts, showed that they are isotropically distributed, as shown in Figure 1.8, suggesting a cosmological origin for these objects [57]. Analysis of the distribution of the observed duration for a large number of GRBs showed a clear bimodality, suggesting the existence of two separate populations: a "short" population with an average duration of about 0.3 seconds and a "long" population with an average duration of about 30 seconds [63]. Both distributions are very broad with a significant overlap region in which the identity of a given event is not clear from duration alone. Their spectra are very hard, with a peak of emission at some hundreds of keV, they follow a power law characterized by a spectral index that vary during the explosion.

The prompt γ-ray emission from a GRB is sometimes followed by a second transient event called *afterglow* at energies with longer lasting emission in the X rays, optical and radio. The first X-ray GRB afterglow was measured by the *BeppoSax* mission (1996 - 2002). *BeppoSax* was a program of the Italian Space Agency (ASI) with participation of the Netherlands Agency for Aerospace programs (NIVR). On 28 February 1997 *BeppoSax* detected the X-ray afterglow from GRB 970228 [85]. This was the first accurate determination of the distance to a GRB and, together with the discovery of the host galaxy of 970228, it proved that GRBs occur in extremely distant galaxies.

The questions about which type of celestial object can emit GRBs is still unsolved. GRBs show an extraordinary degree of diversity. The near complete lack of observational constraint led to a profusion of theories, including evaporating black holes, magnetic flares on white dwarfs, accretion of matter onto neutron stars, hypernovae, rapid extraction of rotational energy from supermassive black holes and fusion of two neutron stars or one neutron star and one black hole of a binary system. There are at least two different types of progenitors of GRBs: one responsible for the long-duration, soft-spectrum bursts and one responsible for short duration, hard-spectrum bursts. The progenitors of long GRBs are believed to be massive, low-metallicity stars exploding due to the collapse of their cores (*collapsar model*) [54]. The progenitors of short GRBs are still unknown but mergers of neutron stars is probably the most plausible model (*merger model*). Both models suggest the final creation of a black hole, surrounded by an accretion torus which realizes gravitational energy that feeds the explosion.

Several models have been developed in order to explain the γ-ray emission from GRBs. Probably the *Fireball model* (FBM), introduced by Piran in 1999 [65], is the most plausible one. The term "fireball" refers to an opaque radiation-plasma ball (composed by electrons, positrons and γ rays) which would expand

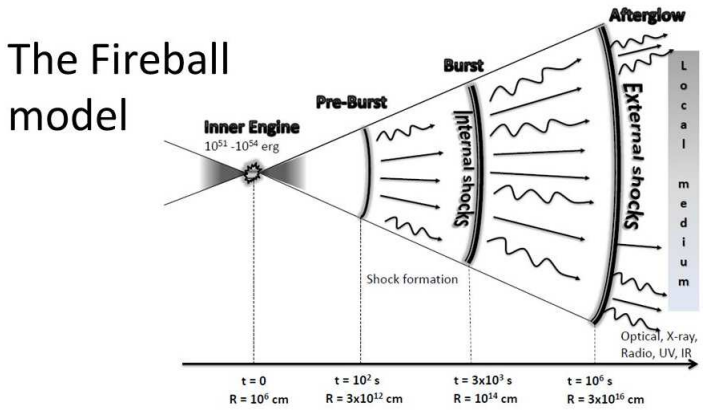

Figure 1.19: Schematic view of the fireball model for GRBs.

relativistically. Two different types of shocks may arise in this scenario. In the first case, the expanding fireball runs into external medium, the ISM or a pre-ejected stellar wind. The second possibility is that even before external shocks occur, internal shocks develop in the relativistic wind itself. The model hypothesis is that γ-ray burst is due to internal shocks, while afterglow is due to the relativistic expanding wind, which decelerates producing radiation of lower energy, going from X rays to optical and radio, as time goes on [56]. A schematic view of the fireball model for GRBs is shown in Figure 1.20.

1.3.5 Solar flares

The Sun, the star of our planetary system, has been known to produce γ rays during its flaring period with energies greater than several MeV. This emission was detected for the first time by the American satellite OSO-VII between August 4 and 7, 1972. Subsequently, other missions were dedicated to the study of the γ-ray emission by the solar flares and the first important results came from EGRET and COMPTEL telescopes onboard of the CGRO observatory, which discovered that the Sun is a source of GeV γ rays. During a powerful solar blast on 2012 March 7, FERMI detected the highest-energy light ever associated with an eruption on the sun. The discovery heralds FERMI's new role as a solar observatory, a powerful new tool for understanding solar outbursts during the sun's maximum period of activity.

Accelerated charged particles interact with the ambient solar atmosphere, radiating high-energy γ rays via *Bremsstrahlung* (see. e.g., [67], [62]). Secondary $\pi^{\pm}$ are produced by nuclear interaction and yield to γ rays with a spectrum that extends to the energies of the primary particles. Protons and

heavy ions interactions also produce γ rays through π^0 decay, resulting in a spectrum that has a maximum at 68 MeV and is distinctly different from the *Bremsstrahlung* spectrum. The processes that accelerate the primary particles are not well known, but stochastic acceleration through MagnetoHydroDynamics (MHD) turbulence or shocks ([28], [70]) are though to be the most creditable mechanisms. Particles are accelerated in large magnetic loops that are energized by flares, and they get trapped due to magnetic field, generating γ rays ([49], [50]). However, it is not clear where the acceleration takes place and whether protons are accelerated along with the electrons.

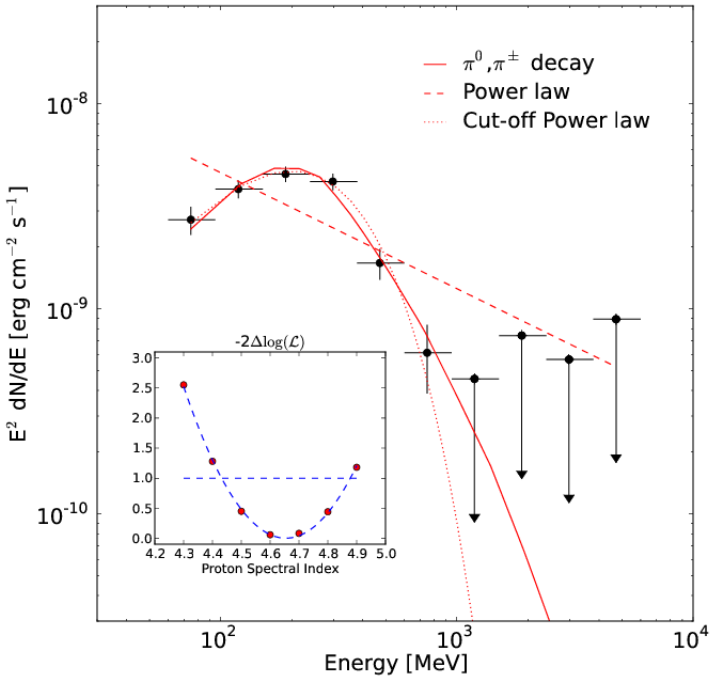

Figure 1.20: Reconstructed Fermi-LAT spectral energy distributions of a solar flare.

Some models are proposed for production of γ rays from the Sun also in quiescent state, e.g. from nuclear gamma decay of nuclei like ^{58}Co, or from *microflares*, already observed in UV and X rays but never seen in γ rays.

1.3.6 Dark Matter

To date, it is not known if dark matter can be a source of γ rays. FERMI detections confim that probably an important fraction of the extragalactic dif-

fuse γ-ray emission is related to the emission of unresolved AGNs. However, any remaining extragalactic diffuse emission would be of great interest. It is thought that a fraction of the extragalactic γ-ray diffuse emission could originate from the decay of exotic particles in the primordial Universe. The energy spectrum of this component should be different from the AGNs contribution. The difficulty in detecting γ rays from dark matter is distinguishing which are produced by dark matter annihilations from those generated by numerous other sources in the Universe.

This contribution could be related to the possible decay of supersymmetric particles. Current models assumes the existence of the Dark Matter (DM) in the halo of our Galaxy, this hypothesis is also sustained by the comparison between the rotational curves of the spiral galaxies and the baryonic visible matter, which tell us that the visible mass is not sufficient to explain the rotational velocities of the stars in the spiral galaxies. Current theory suggests that DM is composed by WIMPs (*Weakly Interacting Massive Particles*) which are massive particles that do not emit or absorb light. Such particles are predicted by supersymmetry, a theory that extends the Standard Model of particle physics. According to supersymmetry, WIMPs act as their own antimatter particles. When two WIMPs interact, they annihilate each other and release secondary particles such as γ rays. Dark matter interacts much more weakly than ordinary matter, but it is not spread out evenly through space and should form clumps in and around galaxies.

The lightest supersymmetric particle is the *Neutralino* (χ) and it is perhaps the most promising candidate for the WIMPs ([86], [31]). Although the highest energy accelerators have begun to probe regions of supersymmetric parameter space, the limits set at this time are not very restrictive. The mass of the Neutralino particle can be constrained, in order to make up the overall dark matter in the Universe. The required mass is in the range 30 GeV $<$ M_χ $<$ 10 TeV, depending on the model chosen. If Neutralinos make up the dark matter of the Milky Way, they can annihilate into the $\gamma\gamma$ final state giving rise to photons with unique energies, which are γ-ray lines depending on the preferred channel. The signature would be spatially diffuse, narrow line emission peaked toward the Galactic center. Figure 1.21 shows the predicted signal from Neutralino annihilation into $\gamma\gamma$, with an assumed mass of about 47 GeV. While the signal would be the most spectacular of all possible indirect signals, its rates are suppressed with respect to other Neutralino annihilation channels. On the other hand, photons may also be produced in the cascade decays of other primary annihilation products. In contrast to the line signal, cascade decays produce a large flux of photons with a continuum of energies detectable as an excess in the γ-ray flux.

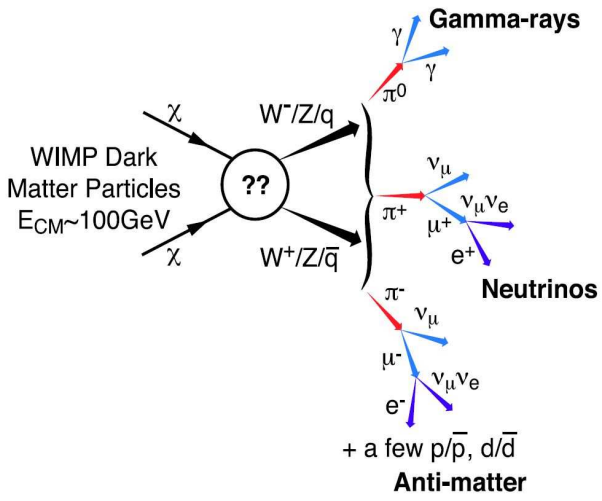

Figure 1.21: Dark matter particles probably don't produce photons on their own. However, if they interact via the weak nuclear force, they could create a particle-antiparticle pair when they collide. These byproducts can produce gamma-rays, neutrinos, etc., resulting in observable traces of dark matter..

1.3.7 Unidentified Sources

Only four of the 25 sources in the second COS-B catalog had identifications [78], and over half the 271 sources in the third EGRET catalog had no associations with known objects in other wavelengths [34]. The 3FGL FERMI catalog unassociated 1010 sources
Since association is primarily based on positional coincidence of possible counterparts known at other wavelengths with a γ-ray source, a principal reason for the difficulty of finding counterparts to high-energy γ-ray sources has been the large positional errors in their measured locations, which are related to the limited photon statistics, associated with a relatively small effective area, and poor angular resolution of the γ-ray observations. Also the bright diffuse γ-ray emission from the Milky Way is a limit in the procedure of association of γ-ray sources, only a very detail knowledge of the model of the γ-ray emission of our Galaxy can help in distinguishing if an excess of γ-ray photons in a specific region in the Galactic plane is related to a statistical fluctuation of the background or to the presence of a γ-ray source.

Gamma-ray sources are tracers of the most energetic processes in the Universe, they are very exotic objects, characterized by very intense magnetic fields and the presence of very high energy particles. For this reason, understanding the nature of the γ-ray unidentified sources is one of the most important open questions in high energy astrophysics. Gamma-ray unidentified sources

represent discovery space for new members of existing γ-ray source classes, or new source classes. These sources should have an high value of the ratio L_γ/L_λ, where L_γ is the γ-ray luminosity of the source and L_λ is the luminosity of the source at lower energy. This makes them possible powerful accelerator of particles.

Since pulsars and blazars represent the two most numerous γ-ray source classes, the first suggested hypothesis was to associate the FERMI unidentified sources with these two classes [52]. In particular, less than one third of these are far from the Galactic plane, probably associated with blazars because extra-galactic, with the remaining most likely within the Milky Way. Further works suggest that many of these unidentified sources are associated with nearby Gould Belt of star-forming regions that surrounds the solar neighborhood [29], while apparently-steady sources are likely to be *radio-quiet* pulsars [33].

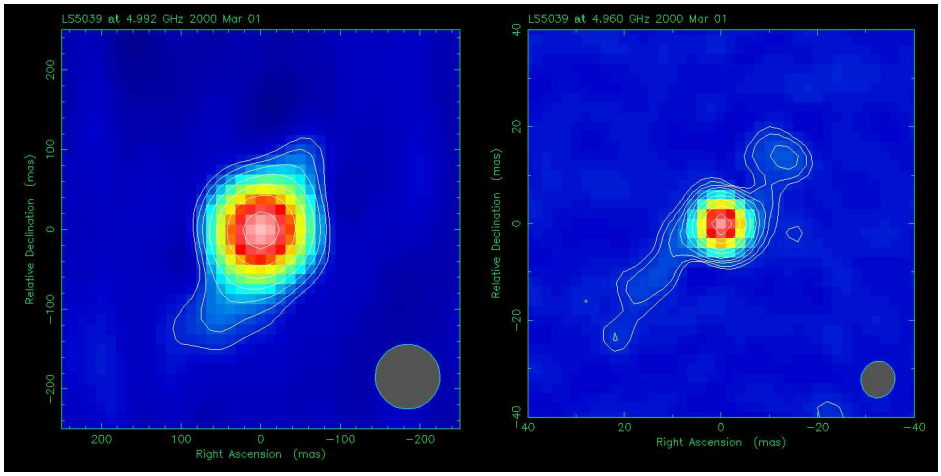

Figure 1.22: Persistent relativistic radiojets in the microquasar LS 5039

Among new γ-ray source classes, some of the unidentified FERMI sources might be associated with Galactic *microquasars*. Microquasars are a subclass of X-ray Binaries (XRBs) that show a jet of mild relativistic accelerated particles. They are believed to be a binary system made up of a compact object, perhaps a neutron star or a black hole, orbiting around a massive star.

To identify γ-ray sources, the study of the emission at other wavelengths is crucial. One of the most significant example was the *Geminga* pulsar. In that case, a search for pulsed emission using X-ray data led to find the characteristic spin period of a neutron star. Gamma-ray observations confirmed this pulsation and so *Geminga* was found to be a γ-ray pulsar.

The progress in finding the identity of all γ-ray sources are correlated to the ability of the γ-ray experiments to localize γ-ray objects with higher precision

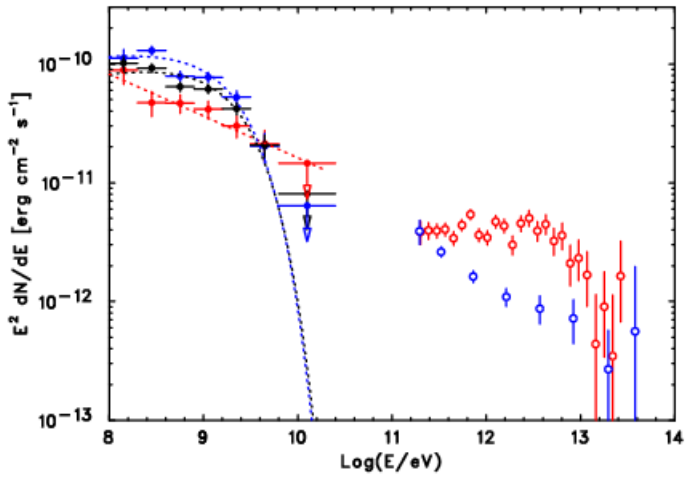

Figure 1.23: Fermi LAT observation of the microquasar LS 5039

in order to find exactly the other wavelength counterparts.

In the end, the spatial, spectral and variability properties may provide a framework that could allow to predict the expected source classes for the sources that remain unassociated. Because of the limits of the space telescopes detector, these information were not enough accurate to compare intrinsic properties of the sources for both associated and unassociated populations, potentially providing insight into the likely classes of the unidentified sources. The increased FERMI performance allowed to do it by using the properties of the associated sources to define a model that describes the distributions and correlations between measured properties of the γ-ray behavior of each source class. This model will be able to be then compared to the γ-ray properties of each unidentified source in order to classify some of them as likely members of one of these source types on the basic of their γ-ray properties.

In this Chapter the main issues regarding γ-ray astrophysics have been reviewed. The development of γ-ray astronomy have been carried mainly from space and the last important mission is the FERMI - LAT observatory.

Although the FERMI - LAT mission has allowed to improve our knowledge of the γ-ray sky, many questions are still open. This space observatory is a member of the new generation of γ-ray telescopes together with *AGILE* and it is contributing in a decisive way in several topics of modern understanding of the γ-ray Universe, from the study of Galactic and extragalactic cosmic accelerators to the detailed investigation of the diffuse emission and the nature of the unidentified sources.

Chapter 2

The Active Galactic Nuclei

2.1 The Active Galactic Nuclei and Blazars

In the Universe there are billions of galaxies, which differ basically from their morphology in the Hubble diagram.

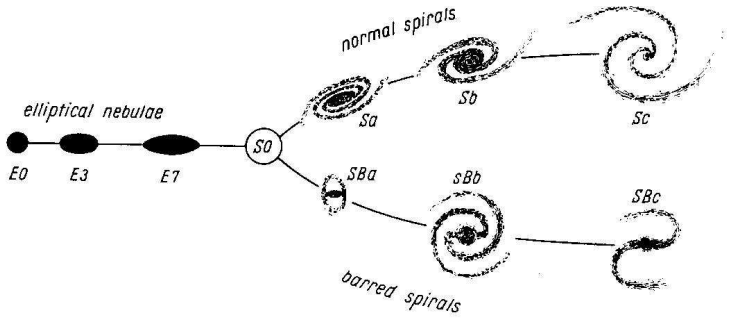

Figure 2.1: Hubble galaxies sequence

Galaxies are composed of stars and ISM (gas and dust), which contribute in the total luminosity of the galaxy (for Milky Way L $\sim 10^{11}$ $L_\odot$). Every galaxy contains a black hole at its centre. While the centres of some galaxies are quiet and non-violent, such as the Milky Way galaxy with its black hole Sagittarius A^* , the centres of others have been obeserved to be emitting electromagnetic radiation very energetically. In the Forties, the American astronomer C. Seyfert discovered a new class of galaxies, with intense emission from a star-like nuclei and with broad emission lines, that are more than 10^3 km/s wide. This kind of objects are now called *Seyfert galaxies* and later, together with other extragalactic sources such as *Quasars* and *BL Lac objects*, they were referred to as active galactic nuclei, or AGN. Observations of AGN

have revealed emissions over an extremely wide range of wavelenghts, from radio though to VHE γ- ray.

2.1.1 Current Model

The currently accepted model for AGN was first proposed by Urry and Padovani [83], and is shown in Figure 4.2

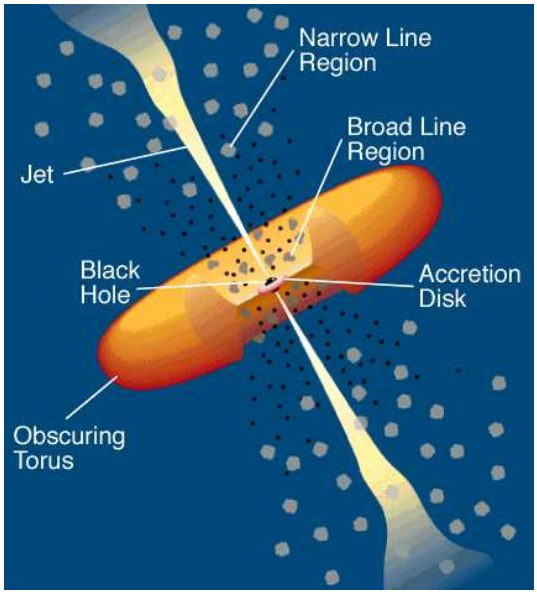

Figure 2.2: The Urry and Padovani Model for Radio-Loud AGN.shown are the supermassive black hole, accretion disk, dust torus, broad line region and narrow line region

At the heart of the AGN, there is a supermassive black hole (SMBH), with a mass between approximately 10^6 and 10^{10} $M_\odot$ [88] Some nearby matter under the influence of the SMBH falls to a low orbit, forming a disc of matter known as the accretion disc within around 1 pc of the black hole. The accretion disc has a width in the plane of motion, and so matter in the disc has different orbital speeds depending on the distance from the SMBH. Friction therefore causes matter in the disc to become heated, and so the accretion disc emits blackbody radiation which manifests itself in the form of various wavelengths, typically from infra-red through to x-rays. As the rate of accretion of matter into the disc changes, so the x-ray output of the disc changes. This relationship is thought to be strongly linked to the total activity of an AGN. Further out from the SMBH, but not on the same plane as the accretion disc, there are regions of relativistic particles with various velocities. These particles reprocess

the radiation emitted by the accretion disc into other wavelengths. The region closest to the SMBH (within 0.1 pc), which necessarily contains particles with higher velocities than those further out, has its emission lines significantly widened by Doppler effects and is thus known as the broad line region (BLR). Similarly, the region further out (within 1 kpc) is known as the narrow line region (NLR). On the same plane as the accretion disc, at a distance of around 1pc from the SMBH, is a torus-shaped region of dust. This dusty torus blocks emissions from the accretion disc, BLR and NLR, meaning that AGN viewed from an angle close to the plane of the torus will appear to have reduced flux. The torus also reprocesses absorbed photons into infra-red energies, adding to the total observed spectrum of AGN. The final, and perhaps most enigmatic components of the AGN model are the relativistic jets. The jets are elongated regions, sitting approximately along the axis of rotation of the accretion disc, in which charged particles, accelerated to relativistic speeds, emit γ radiation [27] With accelerated charged particles involved, the most natural explanation of the jets structure and behaviour involves some sort of magnetic effect; it has not been determined exactly how such a field precisely acts or comes to exist, however. The jets are thought to be linked to the accretion disc, although the exact mechanism for this effect is also currently unknown. Models for the emission exist, however, that each posit something about the inner workings of the jet.

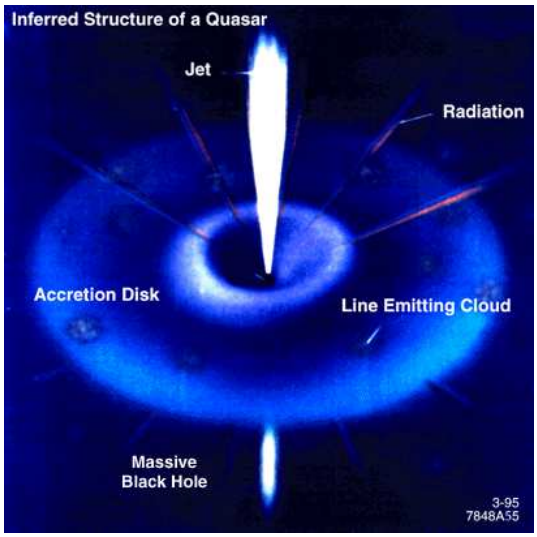

Figure 2.3: Inferred structure of a quasar

2.1.2 Classification

The model described above indicates a consistent structure in all AGN. Observations of AGN, however, show differences in the relative fluxes corresponding to certain components. Classes of AGN have been developed to categorise these differences. The differing observations can be explained by the model when one considers the angle of the AGN relative to the viewer: the angles and relative positions of the various components will affect the observed radiation, meaning that the emissions of AGN are not the same over all angles. For example, an AGN viewed from an angle near the plane of the accretion disc, as described above, will display reduced flux from central components due to the dusty torus blocking radiation. Conversely, an AGN viewed from an angle close to the axis of the jet will receive a much larger share of the emissions from the jet; a marked increase in γ-ray flux. This is precisely what is thought to mark blazar-type AGN apart from others. In addition to the viewing angle, however, the accretion rate can also strongly affect the observed characteristics. Blazars have been noted as being among the brightest of AGN types, as well as displaying the most variability. Within the blazar class, AGN can be further divided into flat spectrum radio quasars (FSRQs) and BL Lac objects. The distinguishing difference between these two classes is the width of emission lines, with FSRQs exhibiting broad lines where BL Lac objects do not. Observationally, FSRQs are frequently brighter than BL Lac objects at certain wavelengths.

AGN		**Type 2** (Narrow Line)	**Type 1** (Broad Line)	**Type 0** (unusual spectra)
Black Hole Spin? ⇓	Radio quiet	Seyfert 2	Seyfert 1 QSO	
	Radio loud	NLRG { FR I, FR II }	BLRG { SSRQ, FSRQ }	Blazars { BL Lacs, (FSRQ) }
		decreasing angle to the line of sight ⇒		

Figure 2.4: AGNs Unified Model. Focusing on UV/optical properties (emission line widths) and on radio properties (quiet/loud) it is possible to classify AGN population as illustrated. The observation angle and the black hole spin are probably the causes of this partition.

2.1.3 Spectra

As previously mentioned, AGN emit over a very wide portion of the electromagnetic spectrum. The overall spectrum of an AGN, known as the spectral energy distribution or SED, can be described by a *double-hump* structure, with each hump corresponding to a specific set of physical phenomena . The lower energy hump generally spans from radio energies ($\simeq$ 1eV) through to x-rays ($\simeq$1 keV), with a peak at around 100 eV. The higher energy hump can span from soft x-rays ($\simeq$100 eV) all the way to TeV γ-rays. The range of the LAT detector, which will be described later in Appendix C, 30 MeV - 300 Gev, falls on the high-energy side of the peak of this hump in most cases. In this subset, the spectrum is often well described by a power law of the form

$$\frac{dN}{dE} = \mathrm{N}_0 \;) \; \frac{E}{E_0} \;)^{-\Gamma}$$

where N_0 is a prefactor, $\mathrm{E}^{-\Gamma}$ is a defined energy scale and Γ is known as the photon index or spectral index. For those AGN with spectra that this equation describes well, the photon index is useful as an indicator of the state of the spectrum at a given time. For spectra where the flux is decreasing with higher energies, the photon index is negative, and for Fermi data usually has a value around -2. A spectrum with increased flux at higher energies, i.e. a more positive photon index, is referred to as being 'harder'; similarly, a 'softer' spectrum is one with a more negative photon index.

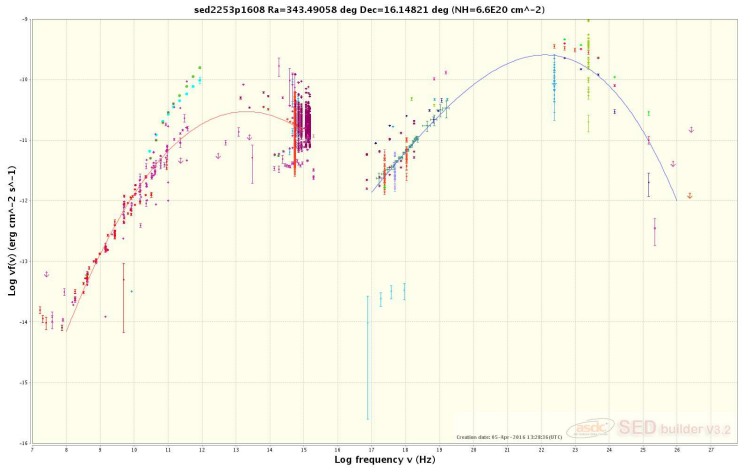

Figure 2.5: SED of 3c 454.3 FSRQ Credit : ASI Science Data Center

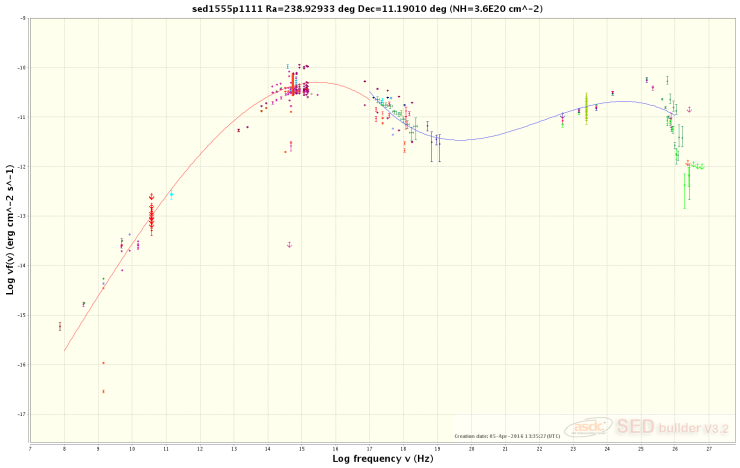

Figure 2.6: SED of PG 1553+113 BL Lac Credit : ASI Science Data Center

2.1.4 Synchrotron Self-Compton Emission Model

The synchrotron self-Compton (SSC) model proposes a single region of relativistic electrons, which by a combination of processes are responsible for the γ-ray emission of AGN.

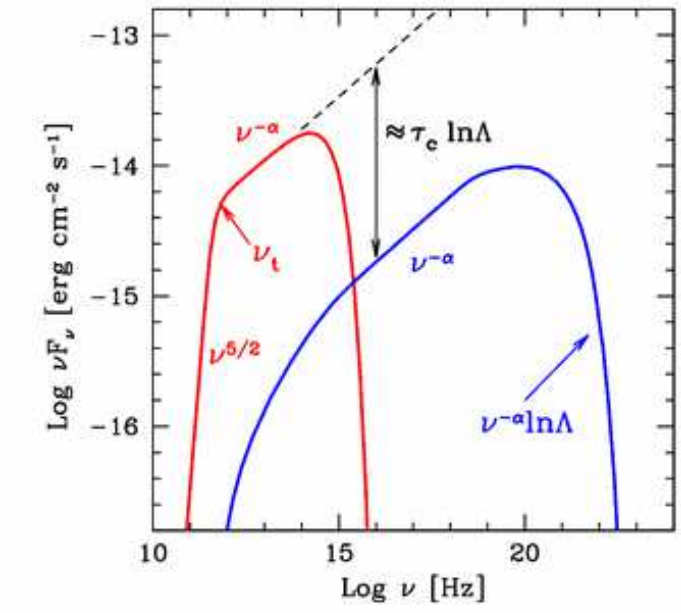

Figure 2.7: Example of SSC spectrum shown in νFν versus ν rappresentation

The region first produces x-rays via synchrotron processes, and then up-scatters them via inverse-Compton (IC) scattering to much higher energies. In this way, the single region is responsible for the entire double-hump structure of the SED. As a result, a change in the output of the seed photon region will result in a corresponding change in the IC emission, meaning that quasi-simultaneous variation should be seen between the two photon populations. By observing the output of an AGN at a point on the low-energy as well as the high-energy hump in the SED, the applicability of the SSC model can therefore be tested. If the model holds, a correlation between the two observations should be found. Due to the energy ranges of the peaks in the SED, observations in soft x-rays as well as γ-rays should thus be sufficient to show a correlation. Since the positions of the seed photon region and the emission are constant, one would expect to see a constant characteristic time lag in the correlation. In addition to this fact, the emission regions of AGN are thought to be moving at relativistic speeds, and so a doppler correction needs to be applied to correctly model this effect.

2.1.5 External Compton Emission Model

The external Compton (EC) model differs from the SSC model in several respects.

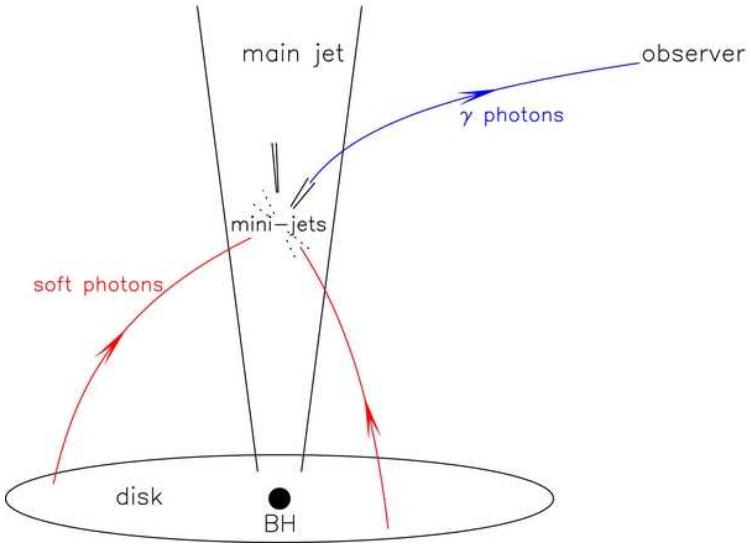

Figure 2.8: Schematic picture for the disk-dominating external Compton-scattering model. A mini-jet is beaming toward the infinity observer, and the soft photons are from the disk

In this model, a population of relativistic electrons still exists, and still

upscatters photons via the IC process, but this region is no longer the primary source of seed photons. A number of external sources also provide seed photons to the IC emission, for example radiation from the accretion disc or dusty torus, or reprocessed radiation from the broad and narrow line regions. The correlation characteristic to the SSC model is thus greatly complicated, since no single source is likely responsible for the majority of seed photons, and the region of particles posited in the SSC model may not even be present. If there remains an SSC component to a given source's emission, a correlation between soft x-rays and γ-rays still exists, although correlations between other wavelengths such as infrared and γ-rays likely also exist in this model, and provide significant numbers of seed photons. The characteristic time lag of the correlation depends on the source of the seed photons, and so different characteristic time lags arise corresponding to each source.

2.1.6 Variability

In contrast to non-active galaxies which have a constant luminosity, AGN emission is frequently observed to be variable. This variability can be used to quantify some of the physical differences between AGN, as well as to place limits on the size of emission regions via causality. When analysing the variability of an object, it is useful to have a numeric indicator of the variability itself. The logical way to analyse the variability of time-dependent values is to

fit some function between the values, taking into account both the dfferences in the observed variable and the time elapsed between the data. While a simple answer would be to

fit a line between data, and take the gradient, this does not take into account that any changes in the emission of AGN are unlikely to be linear in nature. To this end, it is better to model an exponential increase or decrease to the variability, as exponents take into account the state of a system having an effect on its variability. One commonly used indicator of AGN variability is therefore the characteristic e-folding timescale *e*-folding time), defined by

$$\mathrm{F(t)} = \mathrm{F}(t_0)\ e^{\frac{(t-t_0)}{\tau}}$$

where F(t) is the final value of the variable, $\mathrm{F}(t_0)$ is the initial value and τ is the e-folding time. The e-folding time τ can be found between any two data points, although in practice it is most useful to find it for the smallest time period possible, i.e. between adjacent data points. Using the smallest change in time means that the shortest timescales may be found, which can be used to place limits on the time needed for emission regions to change. This in turn means that, via causality, a limit on the size of the emitting region can be found. In order to accurately do this, however, the redshift of the source must

be taken into account and the calculated e-folding time adjusted accordingly. The redshift-corrected e-folding times are given by

$$\tau_{actual} = \frac{\tau_{actual}}{1+z}$$

where z is the redshift.

When calculating limits on the size of an emission region, the movement of the region must be taken into account in the form of the Doppler factor, δ , such as in Brown [11]. The inequality representing the limit on the size of the region is then

$$\mathrm{R} \sim c\,\delta$$

where R is the size of the emission region and δ is the Doppler factor. Another common indicator of variability is the doubling timescale which, rather than an increase or decrease by a factor of e, corresponds to an increase or decrease by a factor of two. Conversion between the two is a simple matter of changing from base e to base 2.

2.1.7 High Synchrotron Peak Blazars

In the literature Blazars can also be classified into different subclasses [..ref Abdo arXiv:0912.2040]based on the position of the peak of the synchrotron bump in their spectral energy distribution (SED), namely :

- **LSP** or low synchrotron peaked blazars. These sources have the synchrotron power peak al low energies ($\nu^S_{peak} < 10^{14}$ Hz), a flat X-ray emission
- **ISP** or intermediate synchrotron peaked blazars. Sources where the synchrotron emission peaks at itermediate energies (10^{14} Hz $< \nu^S_{peak} < 10^{15}$ Hz) and , in these sources, the X-rayband includes both the tail of the synchrotron emission and the rise of the inverse Compton component.
- **HSP** or high synchrotron peaked blazars where the emission is accelerated at higher energies than in LSP. These sources have a peak of the synchrotron power that reaches UV or higher energies ($\nu^S_{peak} > 10^{15}$ Hz). Under these condi- tions the synchrotron emission dominates the observed flux in the X-ray band [ref. Padovani, P., Giommi, P. 1996, MNRAS,279, 526]

Fig.4.9 shows the SED of the three subclasses.This subclassification improves the possibility that the γ-ray properties of the sources may lead to constraints on the type of objects responsible for the radiation especially in view of the increasing number of detections obtained by the *Fermi* Large Area Telescope (LAT) that still have to be properly classified.

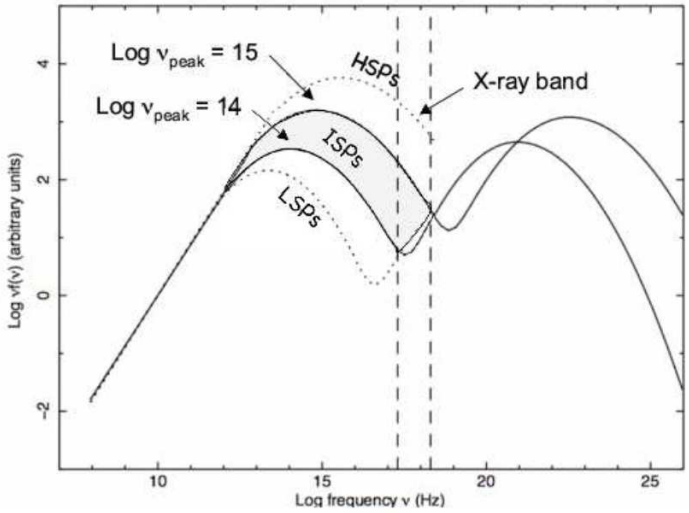

Figure 2.9: The definition of different blazar types based on the peak of the synchrotron component in their SED

Chapter 3

The Fermi-LAT Source Catalogs

The FERMI Gamma-ray Space Telescope (a detailed description of the telescope is reported in Appendix C)[13] has been routinely surveying the sky with the Large Area Telescope (LAT) since the mission began in 2008 August. The excellent performances of the LAT in terms of deep and fairly uniform exposure, good per-photon angular resolution and stable response, provide the best resolved survey of the sky in the 100 MeV to 100 GeV energy range. For this reason the LAT survey data provide a detailed characterizations for each γ-ray source detected as for as localization, time variability and spectral shape are concerned. Since the subject of this study is based on the γ-ray point-like sources presented in the FERMI-LAT Source Catalogs, an overview of the procedure to construct a FERMI catalogs is necessary to describe how it is established if an excess of γ-ray photons in a region of the sky is related to a point-like source emission and how this γ-ray source can be associated with an object known in other wavelengths. In this study are treated γ-ray sources with a threshold likelihood *Test Statistic* (TS) greater than 25, corresponding to a significance of just over 4σ, in the energy range between 100 MeV and 100 GeV. This means that the Bright Source List (BLS) characterized by a TS $>$ 100[5], nor γ-ray objects with an energy greater than 10 GeV detected by the LAT [11] are not here discussed.

3.1 Onboard the Fermi - LAT

FERMI LAT data were collected during the flight of the satellite in an almost circular orbit at an altitude of 565 km, an inclination of 25.6° and an orbital period of 96 minutes. After an initial period of engineering data taking and on-orbit calibration,[4] FERMI was put into sky-scanning survey mode in which the normal to the front of the instrument (z-axis) is $\pm 50°$ [after september

2009, it was 35° for about 80% of the time before that.] above and below the rocking orbital plane on alternate orbits. In this way, after 2 orbits, corresponding about 3 hours, the sky exposure is almost uniform.
During the survey, observations are nearly continuous, although a few data gaps are present due to operational issues, special calibration runs, or in rare cases, data loss in transmission. This results in a total live time of satellite during this period of about 1109 days, which corresponds to an absolute efficiency of 76%. Most of the inefficiency is due to readout dead time (9.2%) and to time lost during passages through the South Atlantic Anomaly (∼13%), which is responsible for the nonuniformity of the exposure (about 30% difference between minimum and maximum). In order to limit the contamination from albedo γ rays from interactions of cosmic rays with the upper atmosphere of the Earth, [82] which is a very bright γ-ray source, a cut on zenith angle (angle between the foresight of the LAT and the local zenith) at 105° was applied for data analysis.
Onboard the satellite there is a first analysis of the data. Immediately the data are filtered and analyzed reconstructioning and classifying each detected event [13]. In reconstructing the events from the hits in the LAT, various cuts are made classifying the events on the basis of probability that they result from photons and the quality of the reconstruction. The events are then separated into various event classes, each class is characterized by its own set of instrument response functions[1]. For the construction of the catalog, the class with the least residual contamination from charged particle background events is chosen.
The instrument response functions (IRFs) – effective area, energy redistribution, and point-spread function (PSF) – use the analyses derived from Monte Carlo simulations of the LAT, which were calibrated before and after the launch of the observatory using the event-selection criteria corresponding to the chosen event classes [13], [68]. After these analyses, only the events with energy above 100 MeV were selected for the construction of the catalog because below 100 MeV the effective area is relatively small and strongly dependent on energy and because at low energy the width of the PSF increases (scaling approximately as $0.8°(\mathrm{E}/1\mathrm{GeV})^{-0.8}$). The Figure 3.1 summarizes the data set used for the construction of the catalog, it shows the γ-ray intensity map for energies above 300 MeV. The map is dominated by a dramatic increase of the brightness of the γ-ray sky at low Galactic latitudes.

[1] see `http://fermi.gsfc.nasa.gov/ssc/data/analysis/documentation/Cicerone/Cicerone_Data/LAT_DP.html`

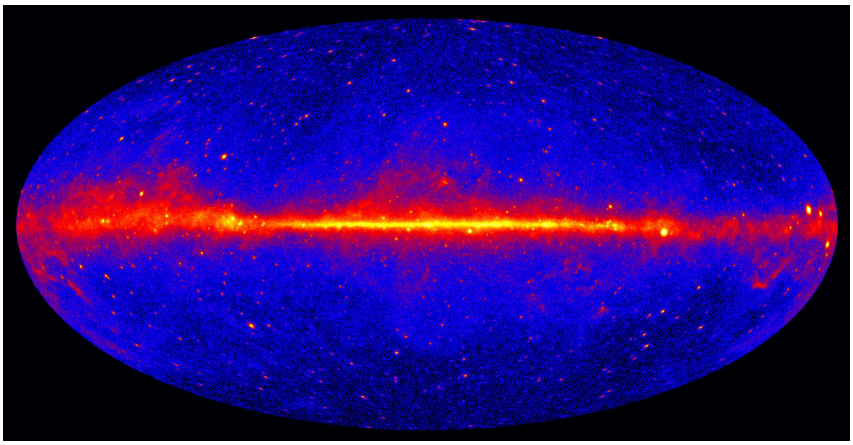

Figure 3.1: Aitoff projection in Galactic coordinates of the sky map of the LAT data detected during the 48 months of mission. The image shows γ-ray intensity for energies above 300 MeV, in units of photons m^{-2} s^{-1} sr^{-1} [2].

3.1.1 Construction of a Fermi- LAT catalog

A fundamental input to the construction of a FERMI catalog is a detailed model for the diffuse γ-ray emission. The diffuse emission as explained in Section 1.3.1. can be divided in two components: the Galactic diffuse emission, related to the interaction between cosmic rays and interstellar gas and photons, and the extragalactic diffuse emission, related to the isotropic unresolved emission of extragalactic sources. In addition, also residual charged particle background, i.e. cosmic rays, misclassified as γ rays from the LAT, provides another approximately isotropic background. The models for the Galactic diffuse emission and isotropic backgrounds were developed by the LAT team and are available, along with descriptions of their derivation, from the FERMI Science Support Center[2]. A detailed model of the γ-ray emission is essential for assessing if an excess of photons is related to the presence of a γ-ray source and for characterizing it. Unfortunately it is extremely difficult to develop a very accurate model, especially for the Galactic diffuse emission, because of a lot of parameters, such as the distribution of interstellar gas in Galactocentric rings and the propagation of the cosmic rays in our Galaxy [77], are not completely known. This could change significantly all the results. A γ-ray source can be included in the catalog only if it was detected on the basis of its average flux. In this way, bright flaring sources detected only on shorter timescales, as GRBs, are not included in the catalog. The procedure used to build a FERMI catalog follows three important steps applied in sequence: the

[2] `http://fermi.gsfc.nasa.gov/ssc/data/access/lat/BackgroundModels.html`

detection, the localization and the significance estimation. In this scheme the threshold for inclusion in a FERMI catalog is defined at the last step, but the completeness is controlled by the first one. After the list is defined, the source characteristics are determined (flux in 5 energy bands, spectral shape and time variability). Hereafter flux F means photon flux and spectral index Γ is for power law photon spectra (i.e. $F \propto E^{-\Gamma}$)

3.1.2 The procedure

Detection

The detection is based on three energy bands, combining *Front* and *Back* events to preserve spatial resolution [2]. The detection does not use events below 200 MeV, which have poor angular resolution, and it uses events up to 100 GeV. The soft band starts at 200 MeV for *Front* and 400 MeV for *Back* events. The medium band starts at 1 GeV for *Front* and 2 GeV for *Back* events. The hard band starts at 5 GeV for *Front* and 10 GeV for *Back* events. The sky is then partitioned into 24 planar projections and the methods used to look for sources on top of the diffuse emission model are *Point find* [32] , the *Minimum Spanning Tree* algorithm and wavelet-based algorithms [18] , as *mr_filter* [76] and *PGWave* [22]. The "seed" positions from those four methods were then combined in order to minimize the number of missed sources.

Localization

The position of each source was determined by maximizing the likelihood with respect to its position only and the image-based detection algorithms provide estimates of the source positions, but the positions are not optimal because no information about the energy is taken into account. These methods also do not provide error estimates on the positions. At this point an advanced statistical method is introduced to localize each detected source. The method used to localize the sources is an iterative binned likelihood technique [2]. Each source is treated independently in descending order such that brighter sources are included in the background model for fainter sources. The photons are assigned to 12 energy bands (four per decade from 100 MeV to 100 GeV) and HEALpix-based spatial bins for which the size is selected to be small compared with the scale set by the PSF. For each band, the likelihood is defined as a function of the position and flux of the assumed point source, while the background is the sum of Galactic diffuse, isotropic diffuse and any nearby, i.e. within 5°, other point sources in the catalog. The function of the position ($\mathbf{p}$) is defined as 2(log(L_{max})-log(L($\mathbf{p}$)), where L is the product of the band likelihoods. According to Wilks' theorem, [87] this is the probability

distribution for the coordinates of the point source consistent with the observed data. The width of this distribution is a measure of the uncertainty, and it scales directly with the width of the PSF. The distribution is fitted by a two-dimensional quadratic form with five parameters describing the expected elliptical shape: the coordinates (R.A. and dec.) of the center of the ellipse, semimajor and semiminor axis extents (α and β), and the position angle ϕ of the ellipse.

Significance and Thresholding

Although the detection and localization steps provide estimates of source significances, these estimates are not sufficiently accurate since the detection step does not use the energy information and the localization step fits only one source at a time. To better estimate the source significances the LAT team used at higher energies a 3-dimensional maximum likelihood algorithm in unbinned mode (i.e., the position and energy of each event is considered individually) where keeping track of the exact direction of each event helps. At low energy binned likelihood is used in order to cap the memory and CPU resources This is part of the standard *Science Tools* software package. The tool does not vary the source position, but does adjust the source spectrum. The tool provides the best-fit parameters for each source and the *Test Statistic* TS = 2Δlog(likelihood) between models with and without the source. The TS associated to each source is a measure of the source significance. For this stage the sources are modelled with simple power-law spectra.The detection and initial localization process resulted in 4029 candidate point sources with T S $\geq$10. The TS of each source can be related to the probability that such an excess can be obtained from background fluctuations alone. The probability distribution in such a situation (source over background) is not known precisely [66]. However, since only positive fluctuations are considered, and each fit involves four degrees of freedom (two for position, plus fluxand spectral index), the probability to get at least TS at a given position in the sky is close to half of the χ^2 distribution with four degrees of freedom [51], so that TS = 25 corresponds to a false detection probability of about 4σ.

Flux determination, spectral shape and time variability

Since the spectra of most sources do not follow a single power law over the considered energy range, the maximum likelihood method does not provide very accurate estimates of the fluxes of the sources detected with TS $>$ 25. Within the two most populous categories of γ sources, the AGNs often have broken power-law spectra and the pulsars have power-law spectra with an exponential cutoff. In both cases fitting a single power law over the entire

range overpredicts the flux in the low-energy region of the spectrum, which contains the majority of the photons from the source, biasing the fluxes to higher values. To provide better estimates of the source fluxes, the LAT team split the range into five energy bands from 100 to 300 MeV, 300 MeV to 1 GeV, 1 to 3 GeV, 3 to 10 GeV, and 10 to 100 GeV [2]. Since it is generally not possible to fit the spectral index in each of those energy bands (and the flux estimate does not depend very much on the index), the spectral index of each source was frozen to the best fit over the full interval. The five fluxes provide a rough spectrum, allowing departures from a power law to be quantified. In order to quantify departures from a power-law shape, it was introduced a *Curvature Index*:

$$C = \sum_i \frac{\left(F_i - F_i^{PL}\right)^2}{\sigma_i^2 + \left(f_i^{rel} F_i\right)^2} \tag{3.1}$$

where i runs over all bands and F_i^{PL} is the flux predicted in that band from the global power-law fit. f_i^{rel} reflects the relative systematic uncertainty on effective area and its values are 0.1, 0.05, 0.1, 0.15 and 0.2 in each energy band. C follows a χ^2 distribution with 5- - 2 = 3 degrees of freedom if the power-law hypothesis is true because the fit involves two parameters, the normalization and the spectral index. At the 99% confidence level, the spectral shape is significantly different from a power law if $C > 11.34$. The curvature index is not an estimate of curvature itself, just a statistical indicator. A faint source with a strongly curved spectrum can have the same curvature index as a bright source with a slightly curved spectrum. Moreover, any kind of deviation from the best-fit power law can trigger that index, thus the curvature index is not exclusively an indicator of curvature. Moreover, in order to estimate the time variability for each source it was also introduced a *Variability Index* computed by splitting the full mission month interval into N_{int} = mission intervals of about 1 month each freezing the spectral index of each source to the best fit over the full interval. In this way, it is possible to detect if a source varies above a specific threshold, but not to characterize such variation. The variability index is defined as a χ^2 criterion:

$$w_i = \frac{1}{\sigma_i^2 + \left(f_{rel} F_i\right)^2} \tag{3.2}$$

$$F_{wt} = \frac{\sum_i w_i F_i}{\sum_i w_i} \tag{3.3}$$

$$V = \sum_i w_i \left(F_i - F_{wt}\right)^2 \tag{3.4}$$

where i runs over the montly mission intervals and σ_i is the statistical uncertainty in F_i. f_{rel} = 3% of the flux for each interval F_i, related to the time

scale where the instrument and the event classification are stable. Since the weighted average flux F_{wt} is not known a priori, V is expected, in the absence of variability, to follow a χ^2 distribution

Variability is considered probable when Variability Index exceeds the threshold of 72.44 corresponding to 99% confidence in a χ^2 distribution with 47 degrees of freedom Examples of light curves are given in Figure 5.2 for a bright constant source (the *Vela* pulsar) and a bright variable source (the blazar *3C 454.3*). With a 3% systematic uncertainty no pulsar is found to be variable.

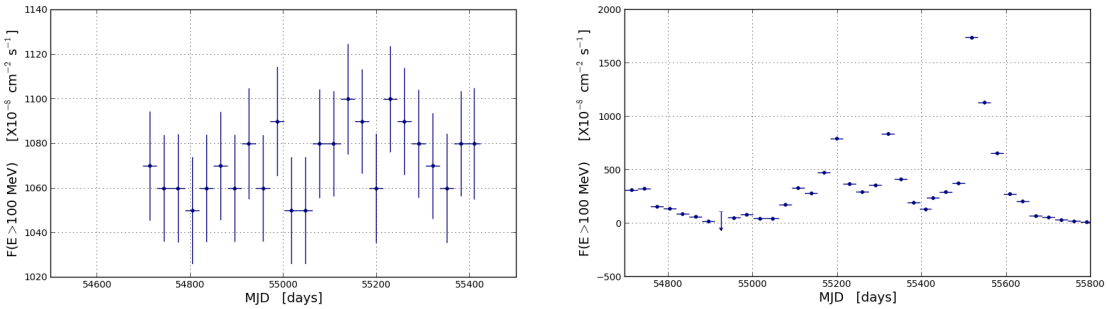

Figure 3.2: On the left is shown the light curve of the *Vela* pulsar while on the right the light curve of the bright blazar *3C 454.3*. .

3.1.3 Source identification and association

Even with the good angular resolution of LAT, source location accuracy is typically not precise enough to make a firm identification based on positional coincidence alone. A typical LAT error region contains numerous stars, galaxies, X-ray sources, infrared sources and radio sources. Determining the nature of a given LAT source must therefore rely on more information than simply location, including time variability, spectral information and availability of sufficient energy at the source and a plausible physical process to produce γ rays. The LAT team introduced a distinction between a source *identification* and an *association* with an object known at other wavelengths. A firm identification of a source is based on a periodicity for a pulsar or a binary system or on a variability correlated with observations at another wavelength, in the case of a blazar, or on measurement of finite angular extent, which is the case for some Galactic sources, e.g., SNRs. Otherwise, an association is defined as a positional coincidence that is statistically unlikely to have occurred by chance between a plausible γ-ray-producing object and a LAT source. In order to associate the LAT sources with a plausible γ-ray emitter an automated

source association algorithm is used. The approach to automated source association of the LAT team is based on a list of 32 catalogs containing potential counterparts of LAT sources on the basis either of a priori knowledge about classes of high-energy γ-ray emitters or on theoretical expectations. The selected catalogs contain AGNs, nearby and starburst galaxies, pulsars and their nebulae, massive stars and star clusters, X-ray binaries and MSPs. This approach follows the ideas developed by Mattox in 1997 [53] for the identification of EGRET sources with flat-spectrum radio sources. For each catalog in the list, the a posteriori probabilities P_{ik} that an object i from the catalog is the correct association of the LAT source k can be computed using the Bayes' theorem:

$$P_{ik} = \left(1 + \frac{1 - P_{prior}}{P_{prior}} 2\pi\rho_k a_k b_k e^{\Delta_k}\right)^{-1} \tag{3.5}$$

where P_{prior} is the prior probability that a counterpart i is detectable by the LAT and it is determined through Monte Carlo simulations, a_k and b_k are the axes of the ellipse at 1σ, ρ_k is the local counterpart density around source k and

$$\Delta_k = \frac{r^2}{2}\left(\frac{\cos^2(\phi - \phi_k)}{a_k^2} + \frac{\sin^2(\phi - \phi_k)}{b_k^2}\right) \tag{3.6}$$

for a given position angle ϕ between LAT source k and the counterpart i, ϕ_k being the position angle of the error ellipse, and r being the angular separation between LAT source k and counterpart i. For the automated association of the FERMI catalog a LAT source is associated with an objects in the selected catalogs if the a posteriori probability is greater than a threshold set as $P_{thr} = 0.8$, which means that each individual association has $\leq 20\%$ chance of being spurious.

3.2 The Third FERMI/LAT Source Catalog

The third Fermi Large Area Telescope source catalog (3FGL) is the most recent high-energy γ-ray (energy range 100 MeV - 100 GeV) catalog. [8] It is the successor to the 1FGL and 2FGL catalogs and it is based on data collected in four years of operation from 2008 August 4 (MJD 54682) to 2012 July 31 (MJD 56139). Relative to the 2FGL catalog, the 3FGL catalog incorporates twice as much data as well as a number of analysis improvements, including proved calibrations at the event reconstruction level, an updated model for Galactic diffuse gamma-ray emission, a refined procedure for source detection, and improved methods for associating LAT sources with potential counterparts at other wavelengths. The 3FGL catalog includes 3033 sources above 4 σ significance, with source location regions, spectral properties, and monthly

light curves for each. Of these, 78 are flagged as potentially being due to imperfections in the model for Galactic diffuse emission. Twenty-five sources are modeled explicitly as spatially extended, and overall 232 sources are considered as identified based on angular extent or correlated variability (periodic or otherwise) observed at other wavelengths. For 1009 sources plausible counterparts at other wavelengths are not found. 1726 sources are identified or associated Active Galaxy Nuclei (AGN) objects. 1144 of them are galaxies of blazar class , 660 BL Lacertae (BLL) and 484 Flat Spectrum Radio Quasar (FSRQ) . 3FGL includes also 573 blazar of undetermined type (BCUs) which are the main target of this study. Fig. 3.3 and 3.4 show the Aitoff projection in Galactic coordinates of the sky map of the LAT data detected in 1FGL , 2 FGL and 3FGL catalogues . It is very evident the increase in the number of sources in the three different catalogs. Fig. 3.5 shows the Aitoff projection of 3LAC sources. The third catalog of active galactic nuclei (3LAC) is based on the third Fermi-LAT catalog (3FGL) of sources detected between 100 MeV and 300 GeV with a Test Statistic (TS) greater than 25, between 2008 August 4 and 2012 July 31. The 3LAC includes 1591 AGNs located at high Galactic latitudes (|b|>10 ∘), a 71% increase over the second catalog based on 2 years of data. In this study we use both the catalogs.

Sources without firm identifications that are in regions of enhanced diffuse γ-ray emission along the Galactic plane or are near local interstellar cloud complexes (like Orion), sources that lie along the Galactic ridge ($300^\circ < l < 60^\circ$, $|b| < 1^\circ$), and sources that are in regions with source densities great enough that their position error estimates overlap in the γ-ray data are called c-sources to indicate “caution” or “confused region”.

3.2.1

3.2.1 Instrument response functions. Improvement respect to the 2FGL catalog

The systematic uncertainties on effective area have improved since 2FGL, going from P7SOURCE V6 to P7REP SOURCE V15. They are now estimated to be 5% between 316 MeV and 10 GeV, increasing to 10% at 100 MeV and 15% at 1 TeV. As in previous LAT catalogs those uncertainties have not been included in any of the error columns, because they apply uniformly to all sources. The systematic uncertainties on effective area have been included in the curvature significance and a systematic uncertainty of 2% on the stability of monthly flux measurements, measured directly on the bright pulsars, has been included in the variability index.

These improvements mean the 3FGL catalog is not simply derived from an extension of the 2FGL data set but from a new data set .

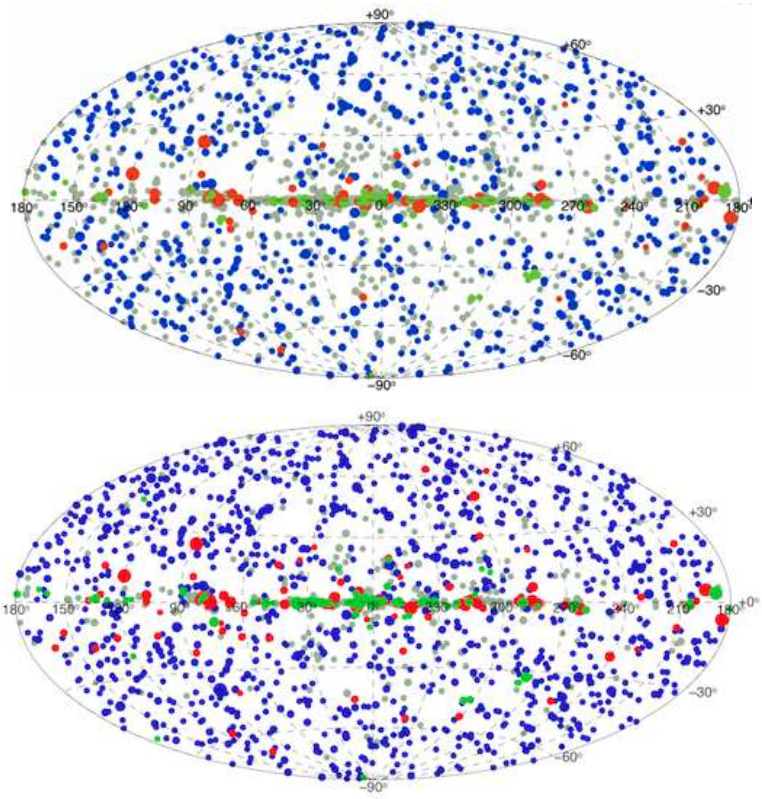

Figure 3.3: Aitoff projection in Galactic coordinates of the sky map of the 1FGL (top) and 2 FGL LAT (bottom) catalogues. The image shows γ-ray intensity for energies above 300 MeV, in units of photons m^{-2} s^{-1} sr^{-1} [2].

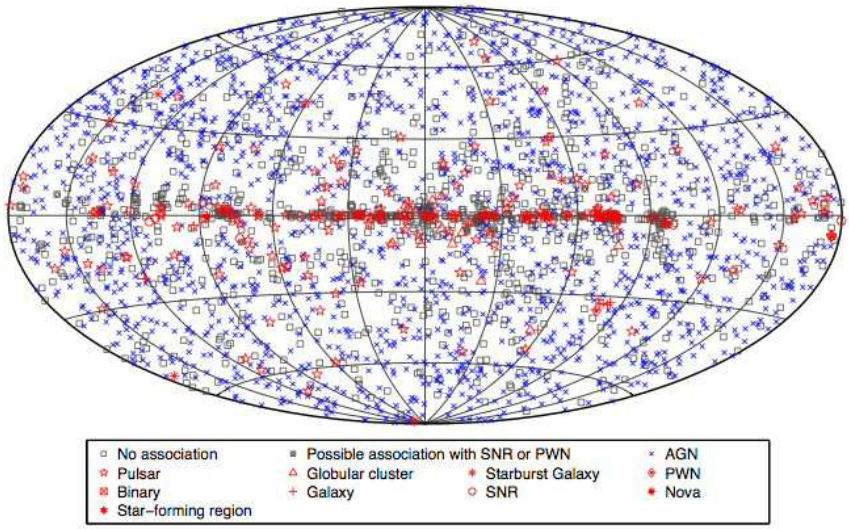

Figure 3.4: Aitoff projection in Galactic coordinates of the sky map of the LAT data detected during the 48 months of mission (3FGL). The image shows γ-ray intensity for energies above 300 MeV, in units of photons m^{-2} s^{-1} sr^{-1} [2].

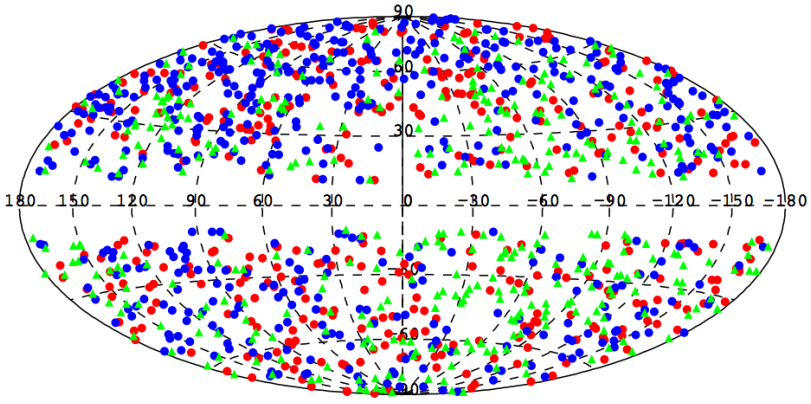

Figure 3.5: Aitoff projection in Galactic coordinates of the 3rd Catalog of AGN Detected by the Fermi LAT (3LAC). In blue BL Lacs, in red FSRQs , in green BCUs. The image shows γ-ray intensity for energies above 300 MeV, in units of photons m^{-2} s^{-1} sr^{-1}

Chapter 4

Classifying blazar of uncertain type

The aim of this work is to find a simple estimator of the likelihood in order to classify BCUs and when it is possible, to identify very high confidence HSP candidates.The percentage of *blazar unclassified sources*(BCU), due to the increased sensitivity of FERMI in detection, progressively increased over the first Fermi catalog. (1FGL).[3] Third FERMI/LAT Source Catalog (3FGL), [10] which represent the *field of work* of this study, listed 3033 γ-ray sources collected in four years of operation from 2008 August 4 (MJD 54682) to 2012 July 31 (MJD 56139). The catalog, which covers all the sky, includes all the sources in the 100 MeV – 300 GeV energy range with a Test Statistic (TS) greater than 25. 1726 sources are identified or associated Active Galaxy Nuclei (AGN) objects. 1144 of them are galaxies of blazar class , 660 BL Lacertae (BLL) and 484 Flat Spectrum Radio Quasar (FSRQ) . 3FGL includes also 573 Blazar of undetermined type (BCUs). Then in 3FGL BCUs represent about the 50% of the classified blazars. Because of the related increased difficulty to have extensive optical observation campaigns for a full classification of blazars, if we compare the 3FGL with previous catalogs released by the LAT collaboration we can see the significant increase of the unclassified sources. BCUs full classification requires much time in spectra and analysis and this fact shifts and limits the contribution of BCUs in BL Lac or FSRQ population. In Table 1 we show the growth of the number of sources detected in Fermi LAT published catalogs. The percentage weight of BCUs , see Table 4.1, increased from 13.8% of 1FGl up to 33.4% of 3FGL. Pending further multiwavelenght analysis , a first classifying screening of BCUs , as our method proposes , might be very useful for the blazar scientific community.

It would therefore very useful to have a method which : ***First***: facilitates the classification of blazars by a fast recognition of BCUs when accurate mul-

Table 4.1: Blazar class sources distribution as in released Fermi LAT catalogs

Class	**1FGL**	**2FGL**	**3FGL**
BLL	295 (44.4%)	436 (41%)	660 (38.4%)
FSRQ	278 (41.8%)	370 (34.8%)	484 (28.2%)
BCU	92 (13.8%)	257 (24.2%)	573 (33.4%)
Total	665	1063	1717

tiwaveleght counterpart informations are not available.
Second : facilitates a quick and preliminary selection of HSP blazars as new targets for the atmospheric Cherenkov telescopes observations. The present generation of atmospheric Cherenkov telescopes (VERITAS, H.E.S.S., MAGIC) has opened the realm of ground-based γ-ray astronomy in the energy range above $\sim$100 GeV. The Cherenkov Telescope Array (CTA) will explore our Universe in depth in Very High Energy (E >100 GeV) γ rays. For a recent review of present and future Cherenkov telescopes, see [24]. Blazars and the HSP subclass are the most numerous class of TeV sources; The TeV catalog [1] reports 176 TeV sources. 46 of them are HSP BL Lacs and only 5 FSRQs therefore the ability to correctly identify these objects will be very important for the determination of CTA targets, in order to increase the rate of detections, since IACTs have a small field of view. The method would be interesting if it will be free from constraints related to other multiwavelenght thresholds. One solution might be to use an estimator which relies exclusively on one parameter of data collected at γ-ray energies where FERMI/LAT is sensitive. This parameter might be the γ flux. This was the first assumption of this research.At the first steps of the works, in order to decide if the γ -ray flux might be the *main road to walk* we checked the γ flux distribution against the time. Tab. 4.2 shows, for BL Lacs and FSRQs classes in 3FGL , the % of the time spent within three flux ranges that we selected according with the flux histories of the classified blazars. The result was interesting because the γ flux appeared to be a significant parameter for the BCU classification.

4.1 Blazar Flaring Patterns (B-FlaP)

Because we considered the γ -ray flux variability of blazars as a consistent estimator on which to develop the method, we called it B-FlaP as an acronym for Blazar Flaring Patterns.

[1] `http://tevcat.uchicago.edu/`

Table 4.2: BL Lacs and FSRQs γ - flux percentage distribution in 3FGL. 0.1 – 100 GeV flux in units of 10^{-8} ph cm^{-2} s^{-1}

Flux	BL Lac	FSRQ
> E-07	33.36%	74.40%
E-08<F<E-07	61.71%	24.36%
<E-08	4.93%	1.24%

4.2 The method

The original idea was to compare the γ-ray light curve of the unclassified source under investigation with a *template* of a classified blazar light curve, then measure the difference in a proper metric.

4.2.1 Empirical Cumulative Distribution Function

An Empirical Cumulative Distribution Function (ECDF) is a non parametric estimator of the underlying cumulative distribution function (CDF) of a set of variable data [44]. It assigns a probability of 1/n to each datum, orders the data from smallest to largest in value, and calculates the sum of the assigned probabilities up to and including each datum. The result is a step function that increases by 1/n at each datum. The ECDF is usually denoted by $\hat{F}_n(x)$ or $\hat{P}_0(X \leq x)$, and is defined as

$$\hat{F}_n(x) = \hat{P}_0(X \leq x) = n^{-1} \sum_{i=1}^{n} I(X_i \leq x)$$

where $I()$ is the indicator function. It has 2 possible values: 1 if the event inside the brackets occurs, and 0 if not

$$I(X_i \leq x) = \begin{cases} 1. \; when \; x_i \leq x \\ 0. \; when \; x_i > x \end{cases}$$

Essentially, to calculate the value of $\hat{F}_n(x)$ at x , a) count the number of data less than or equal to x b) divide the number found in Step a) by the total number of data in the sample

Why is the Empirical Cumulative Distribution Useful in Exploratory Data Analysis? The ECDF is useful because

• it approximates the true CDF well if the sample size (the number of data) is large, and knowing the distribution is helpful for statistical inference

• a plot of the empirical CDF can be visually compared to known CDFs of

frequently used distributions to check if the data came from one of those common distributions
• it can visually display "how fast" the CDF increases to 1; plotting key quantiles like the quartiles can be useful to "get a feel" for the data

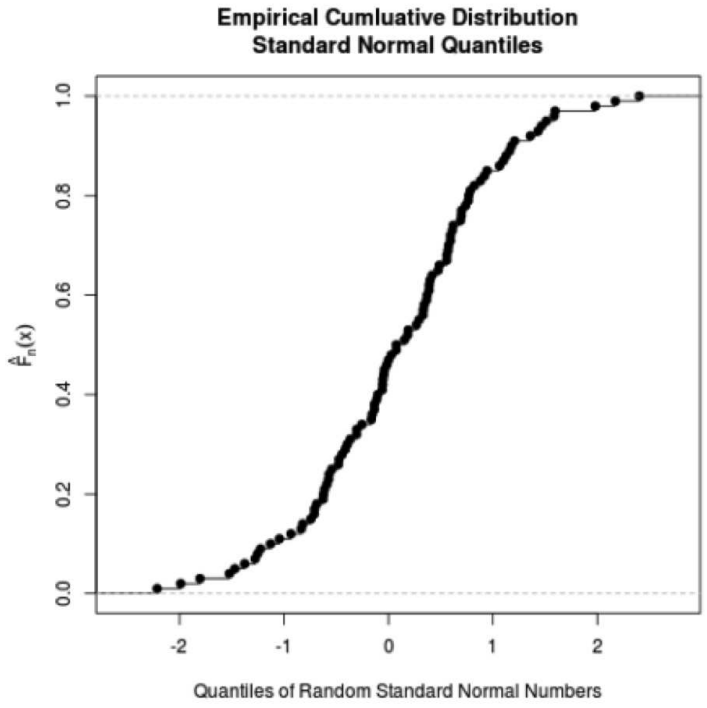

Figure 4.1: Empirical Cumulative Distribution Function (ECDF)

In this work the variable data were the gamma rays light curves from Fermi LAT data . CDF assigns a probability of 1/n to each datum, orders the data from smallest to largest in value, and calculates the sum of the assigned probabilities up to and including each datum. The result is a step function that increases by 1/n at each datum.

4.2.2 ECDF for BCUs

Variability is one of the defining characteristics of blazars [64], Typically γ-ray AGN are characterized by fast transients that could alter significantly the light curve and could make the comparison difficult. In addition, different flux levels could hide the actual similarity of light curves. As first step of this thesis we computed the Empirical Cumulative Distribution Function (ECDF) of the3

FGl blazars light curves evaluated with a monthly binning (48) within FERMI LAT four years mission from August 2008 up to July 2012. and with these data we designed the basic structure of the B-FlaP method. We constructed the percentage of time when a source was below a given flux by sorting the data in ascending order of flux and then compared the ECDFs of BCUs with the ECDFs of blazars whose class is already established, This is our variation of the Empirical Cumulative Distribution Function (ECDF) method. Then we plotted this cumulative percentage as a function of the γ-ray flux in the bins for a given source to produce the B-FlaP plot.

In principle, differences due to the flaring patterns of BL Lacs and FSRQ appear in two ways: (1) The flux where the percentage reaches 100 represents the brightest flare seen for the source; and (2) the shape of the cumulative distribution curve reveals information about the flaring pattern, whether the source had one large flare, multiple flares, or few flares.The BL Lacs have fewer large flares than the FSRQs, and the FSRQ curves are more jagged, suggesting multiple flares compared to the smoother BL Lac curves. The reasons for such differences are very likely connected with the processes occurring at the base of the jet, where the largest concentration of relativistic particles and energetic seed photons are expected. While in FSRQs accretion onto the central black hole produces a prominent and variable spectrum, characterized by continuum and emission-line photons, usually accompanied by the ejection of relativistic blobs of plasma in the jet, BL Lacs do not show such kind of activity and most of the observed radiation originates within the jet itself. As a consequence, the production of γ-ray emission through inverse Compton (IC) scattering can change much more dramatically in FSRQs than in BL Lac-type sources, where the contribution of the central engine to the seed radiation field is weaker [69]. Then the main difference between the ECDFs of BL Lac and FSRQ is just a consequence of the different spectrum between the two classes. Because the BL Lac are harder, they are detected at lower photon flux in the 0.1 - 100 GeV band (but comparable energy flux). So their ECDFs are shifted to the left with respect to FSRQ, as well as the maximum flux values. This is interesting because this is the result in which we based this classification method that should be applied when clean information about the spectrum are not available. The difference between the classes is observed where we plotted the two blazar classes together. At the bottom left of Fig.4.2 is shown the significant overlap between the types where it is hard to distinguish individual objects, and there are outliers that extend beyond the range of the plots, but it is possible to recognize on the top left of the diagram a specific area (blue color) where the BL Lac / FSRQ overlap is minimal. This area, at values of the flux less than $\sim 2.5 \times 10^{-8}$ ph cm^{-2} s^{-1}, could lead to a first *qualitative* recognition of BCUs

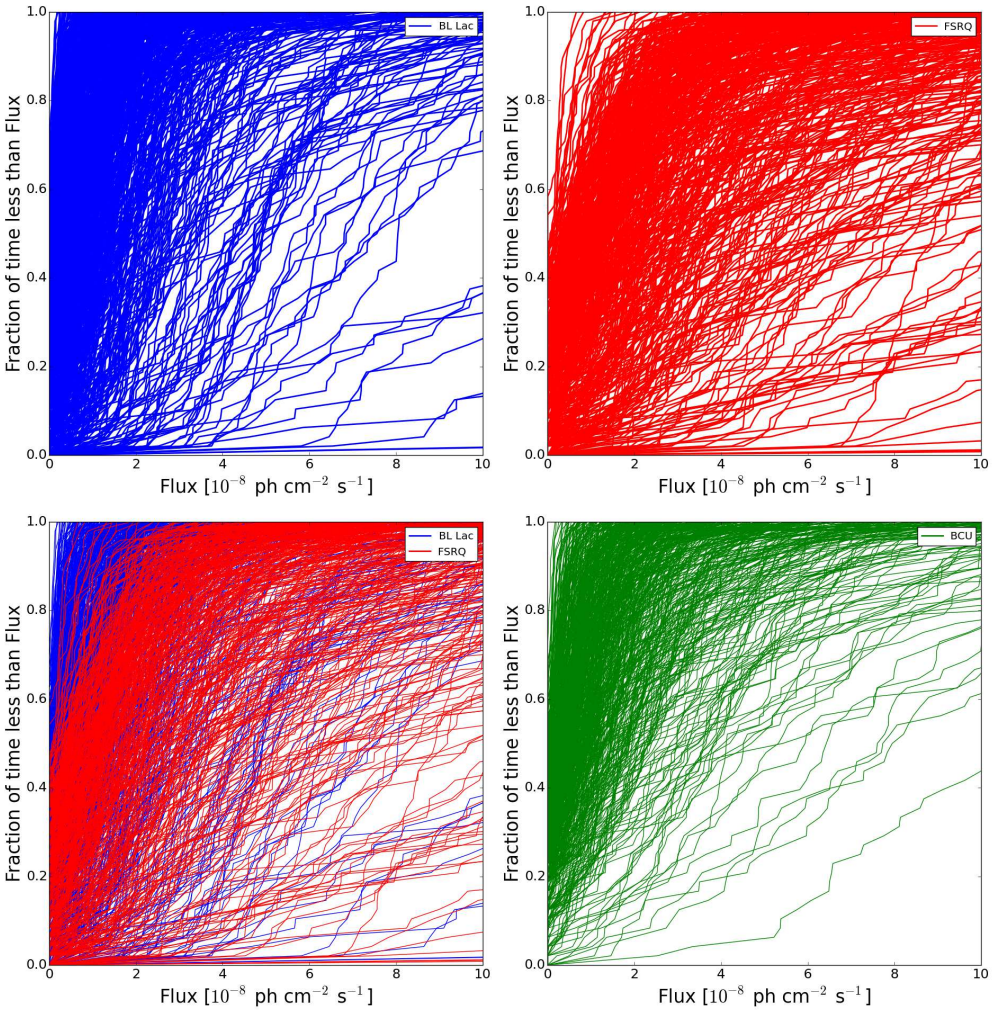

Figure 4.2: ECDF plots of FERMI Blazars: BL Lacs (top left) , FSRQ (top right) , BL Lacs and FSRQ overlap (bottom left) , BCUs (bottom right). The cumulative percentage of bins with flux below a given level is shown as a function of the 0.1 – 100 GeV flux in a bin, in units of 10^{-8} ph cm^{-2} s^{-1}

as BL Lac object.
In B-FlaP, special attention is needed for upper limits, which arise whenever light curves are constructed with fixed binning, as is the case here. They can be naturally incorporated into the current method, as the points plotted in the diagrams are the percentage of time that the source is below a given flux value. Nevertheless, upper limits can introduce biases, skewing the cumulative distribution toward higher percentages. Upper limits could be avoided entirely

by producing light curves with adaptive binning [6] a technique that could be implemented into a possible follow-up study.

4.2.3 ECDF for HSP blazars

With reference to the aim of this thesis and in accordance with the ECDF result for blazars we applied the same technique to blazar subclasses. Because not all the blazars have a subclass classification and we considered the objects only clearly classifyied as HSP, LSP and ISP in the FERMI catalog. Blazars are divided into high/intermediate/low-synchrotron peaked, according to the frequency of the synchrotron in peak ν. We used this classification, proposed by [7] as high synchrotron peaked (HSPs), low synchrotron peaked (LSPs) and intermediate synchrotron-peaked (ISPs) blazars. While ISP and LSP blazars show the most variable patterns and can belong to the BL Lac or FSRQ families, HSP objects are characterized by nearly constant emission. This difference can be expected if we assume that important flaring activity originates from large instabilities at the base of the jet, where the most energetic particles lose their energy in the production of γ rays and are therefore no longer available for synchrotron emission. If the jet, on the contrary, is not subject to such kind of instabilities, the relativistic particles in the plasma are able to produce high-frequency synchrotron radiation before the occurrence of IC processes leads to γ-ray emission [12].

Another catalog is available from Fermi -LAT Collaboration it is the Catalog of Active Galactic Nuclei Detected by the Fermi Large Area Telescope (3LAC). We used the 3 LAC catalog [21] to collect information about classification and SED distribution of the blazars The third release of the catalog considers only 1591 AGN detected at $|b| > 10^{\circ}$ where $|b|$ is the Galactic latitude, 289 clean classified sources as HSP, where 286 of them are represented by BL Lac objects and 3 by FSRQ. 160 of the 573 BCUs are HSP suspects. For all the other data in this study we referred to 3FGL . In Fig.4.3 we plotted the ECDF for 3LAC blazar subclasses (right) and HSPs against FSRQs (left) . As we expected, because of the fact that HSP are almost exclusively represented by BL Lac objects (98.96%), the HSPs went through the BLL clean area at the upper left corner of the plot on the left. Even if the FSRQ (which are mainly ISP and LSP) contamination is not neglegible, the result observed in Fig.4.3, suggests *the potential ability* of B-FlaP to identify a flow range (less than $\sim 2.0 \times 10^{-8}$ ph cm^{-2} s^{-1}) where it is possible to assume not only the Blazar class but also *to suspect* the HSP subclass for a BCU source.

However, even here, visual inspection of the curves in all the ECDF figures shows that the shape of the curve does not show major differences between the observed blazar classes.Instead, a distinguishing factor is the *maximum gamma*

flux found for any of the 48 monthly bin of the 3FGL flux history (max-flux) . We therefore focus our work on the possible use of this simple empirical parameter to help γ-ray BCU classification.

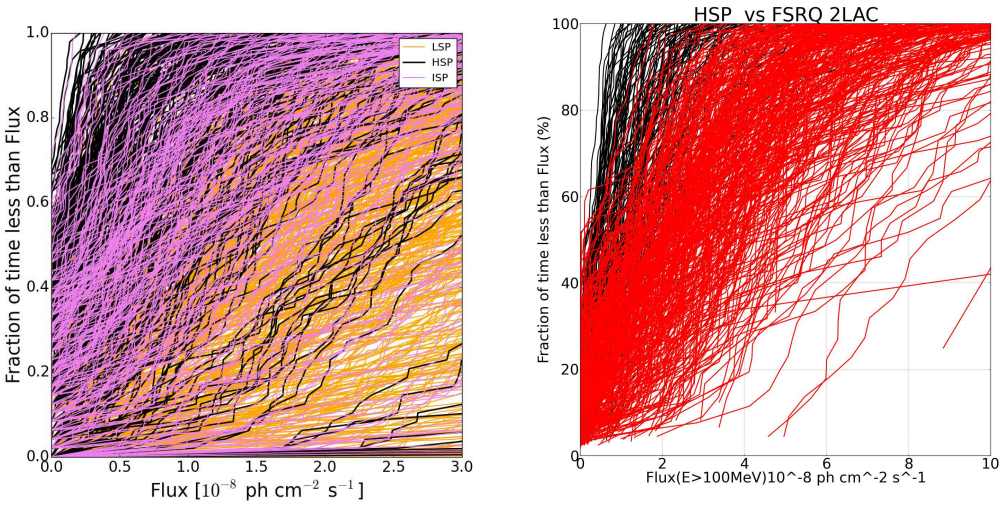

Figure 4.3: ECDF plots for blazars subclasses : (on left) LSP(orange) - ISP(purple) - HSP (black) , (on right) HPS vs FSRQ . The cumulative percentage of bins with flux below a given level is shown as a function of the 0.1 – 100 GeV flux in a bin, in units of 10^{-8} ph cm^{-2} s^{-1}

4.2.4 Usefulness of the max-flux parameter

The ECDF results show that the average γ-ray flux over the 4-year span of the 3FGL catalog can help distinguish BL Lacs from FSRQs, with BL Lacs having a smaller average flux. Small values of the max-flux parameter indicate a low average flux, but they also incorporate the information that these sources have little flaring activity. Such sources would be expected to have small values of the variability parameter that appears in the FERMI catalogues. We therefore investigate whether the max-flux parameter carries any information beyond what is already found in the variability parameter. Although many FSRQs and some BL Lacs have high values of max-flux and show variability indices above the value of 72.44 used in FERMI 3FGL catalog to indicate significant variability, we focus on the lower values of both parameters. Fig. 4.4 and Table 4.3 show the numbers of sources with max-flux values in the lowest ranges of this parameter. As an illustrative value, In the range 0.0 – 4.0, there are 162 BL Lacs compared to 12 FSRQs, giving a purity of $\sim 93\%$. The corresponding

efficiency for recognizing BL Lacs is 162/436, or about 37%. Fig. 4.5 and Table 4.4 show similar numbers for the variability index, again concentrating only on the lowest part of the range. It is clear from the table that no choice of variability index can produce as high a purity as the max-flux parameter. In the range 0.0 – 30.0, the efficiency for finding BL Lacs of $\sim 45\%$ is higher than that of the max-flux parameter, but in the same interval the purity is only about 76%. Fig. 4.6 and 4.7, and Tables 4.5 and 4.6, show a similar analysis for the HSPs compared to the ISPs/LSPs. Using the same ranges, for 0.0 – 4.0 max-flux, HSPs are found with purity 99/117, or about 85%, while for 0.0 – 30 variability index, HSPs are found with purity 102/133, or about 77%. For these choices of the ranges, the efficiency is equivalent within uncertainties.

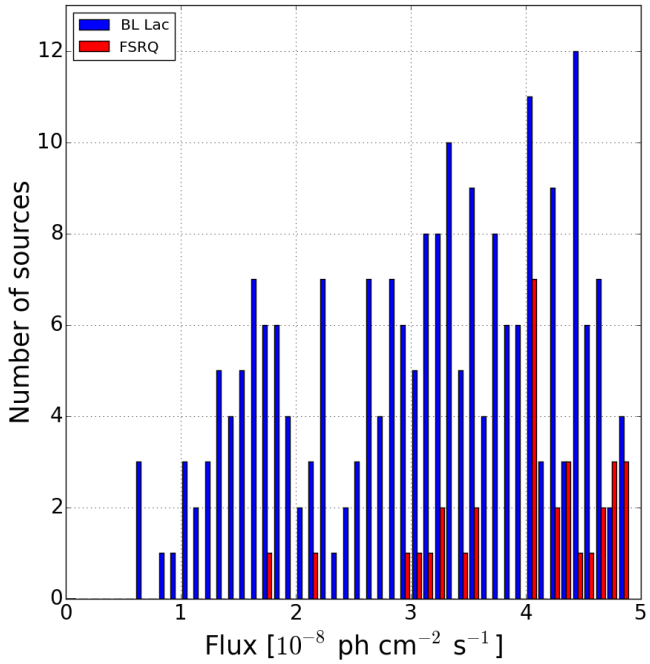

Figure 4.4: 3FGL blazar γ-ray max-flux histogram in units of 10^{-8} ph cm^{-2} s^{-1} (E>0.1 GeV). Not shown are the many AGN with max-flux values greater than 5 in these units.

Our conclusion is that the max-flux parameter does contain different information than the variability index. For classification applications, the high purity that can be achieved with the simple *max-flux* parameter offers an additional promising resource for the development of B-FlaP method.

Table 4.3: BL Lacs and FSRQs in the max-flux intervals illustrated in Fig. 4.4

max-flux	BL Lac	FSRQ	Total sources	BL Lac purity
0.0 –1.0	5	0	5	100%
1-0 – 2.0	44	1	45	98%
2.0 – 3.0	42	3	45	93%
3.0 – 4.0	71	8	79	90%
4.0 – 5.0	51	22	73	70%

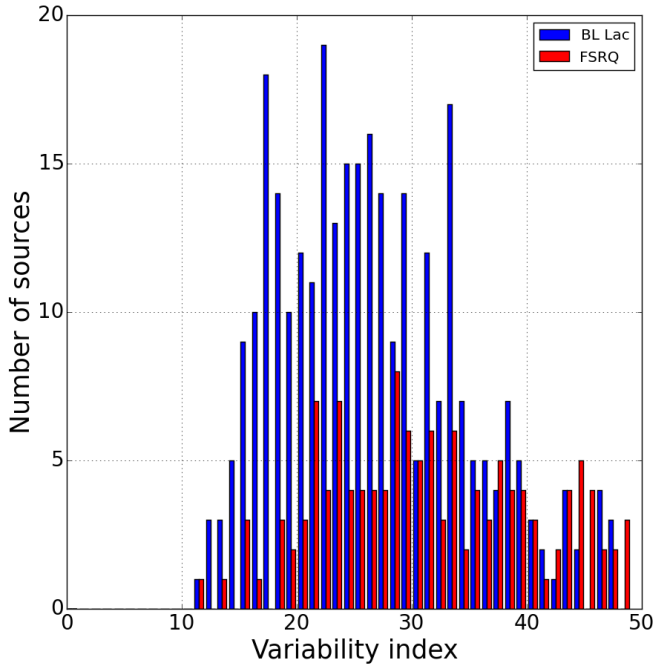

Figure 4.5: Blazar variability index histogram for non-variable or weakly variable 3FGL sources. Not shown are the many strongly variable AGN with higher variability index values (which can exceed 1000).

Table 4.4: BL Lacs and FSRQ in the variability index intervals illustrated in Fig. 4.5

var-index	BL Lac	FSRQ	Total sources	BL Lac purity
0 –10	0	0		undefinied
10 – 20	57	9	66	86%
20 – 30	138	52	190	73%
30 – 40	70	56	126	56%
40 – 50	20	31	51	39%

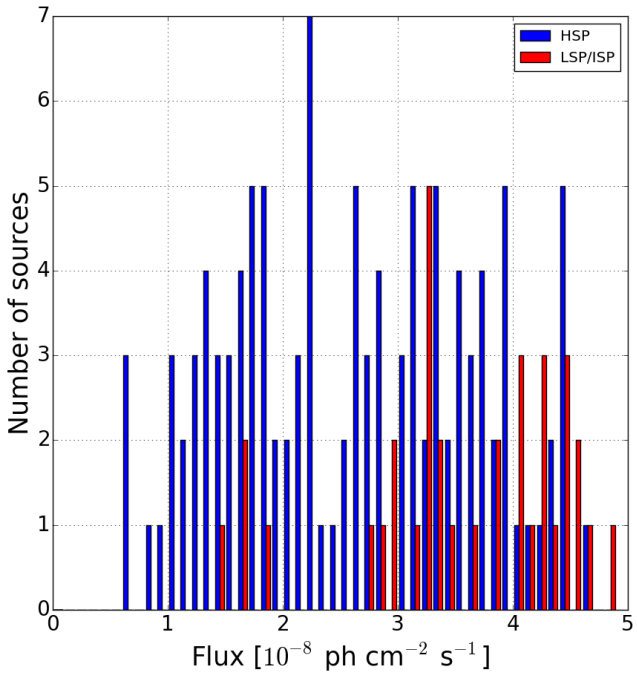

Figure 4.6: Blazar subclass max-flux histogram using the same construction as Fig. 4.4

Table 4.5: 3FGL HSP, ISP, LSP sources in the max-flux intervals illustrated in Fig. 4.6

max-flux	HSP	LSP+ ISP	Total sources	HSP purity
0.0 – 1.0	4	0	4	100%
1.0 – 2.0	34	4	38	89%
2.0 – 3.0	28	4	32	88%
3.0 – 4.0	33	10	43	77%
4.0 – 5.0	11	13	23	48%

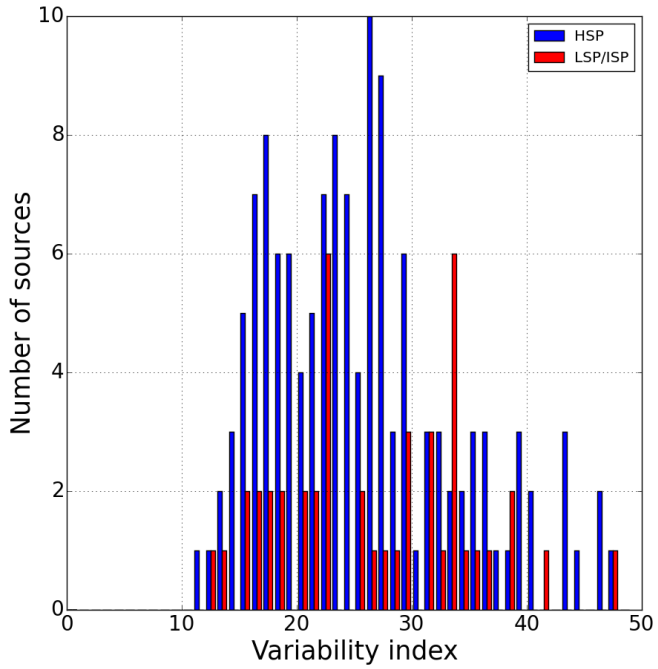

Figure 4.7: 3FGL Blazar subclass variability index histogram using the same construction as Fig. 4.4

Table 4.6: 3FGL HSP, ISP, LSP sources in the variability index intervals illustrated in Fig. 4.7

var-index	HSP	LSP+ ISP	Total sources	HSP purity
0.0 – 10	0	0	0	undefinied
10 – 20	39	10	49	80%
20 – 30	63	21	84	75%
30 – 40	22	15	37	59%
40 – 50	8	2	10	80%

Chapter 5

Classification using Artificial Neural Networks (ANN)

In this section we describe the use of Artificial Neural Networks (ANNs) as a promising method to classify blazar of uncertain types on the basis of their EDCF extracted from their γ-ray light curves.Neural networks were originally conceived as simple models for the behavior of the brain, but have since found many real world applications in fields as diverse as medicine, linguistics, or high-energy physics. The simplest definition of a neural network, more properly referred to as an 'artificial' neural network (ANN), is provided by the inventor of one of the first neurocomputers, Dr. Robert Hecht-Nielsen. He defines a neural network as: *a computing system made up of a number of simple, highly interconnected processing elements, which process information by their dynamic state response to external inputs.*
ANNs are processing devices (algorithms or hardware) that are loosely modeled after the neuronal structure of the mamalian cerebral cortex but on much smaller scales. A large ANN might have hundreds or thousands of processor units, whereas a mamalian brain has billions of neurons with a corresponding increase in magnitude of their overall interaction and emergent behavior. To better understand artificial neural computing it is important to know first how a conventional 'serial' computer and it's software process information. A serial computer has a central processor that can address an array of memory locations where data and instructions are stored. Computations are made by the processor reading an instruction as well as any data the instruction requires from memory addresses, the instruction is then executed and the results are saved in a specified memory location as required. In a serial system (and a standard parallel one as well) the computational steps are deterministic, sequential and logical, and the state of a given variable can be tracked from one

operation to another. In comparison, ANNs are not sequential or necessarily deterministic. There are no complex central processors, rather there are many simple ones which generally do nothing more than take the weighted sum of their inputs from other processors. ANNs do not execute programed instructions; they respond in parallel (either simulated or actual) to the pattern of inputs presented to it. There are also no separate memory addresses for storing data. Instead, information is contained in the overall activation 'state' of the network. 'Knowledge' is thus represented by the network itself, which is quite literally more than the sum of its individual components. Artificial neural networks can be considered as an extension of generalized linear models (e.g. logistic regression), and are applied to approximate complicated functional relationships. At variance with generalized linear models, it is not necessary to specify a priori the type of relationship between the input and output variables. This often leads to superior results, compared to simple logistic regression analyses [84]

5.1 Architecture of the ANN

The basic building block of an ANN is the *neuron*. Information is passed as inputs to the neuron, which processes them and produces an output. The output of an ANN can be interpreted as a Bayesian *a posteriori* probability that models the likelihood of membership class on the basis of input parameters [30].

In γ-ray astronomy, ANNs are often used for such applications as background rejection, though other techniques (e.g. classification trees) are also used for such purposes. In recent years ANNs were also used for classifying *Fermi*-LAT unassociated sources [25]. This technique uses identified objects as a training sample, learning to distinguish each source class on the basis of parameters that describe its γ-ray properties. By applying the algorithm to unknown objects, such as the unclassified sources, it is possible to quantify their probability of belonging to a specific source class. There are different packages available to perform an ANN analysis (e.g. *MATLAB Neural Network Toolbox*[1] or *PyBrain*[2]), but we decided to develop our own 2LP algorithms to address our specific problem. We wrote our algorithms in *Python* programming language[3]. Our choice gives us a number of advantages. First of all our ANN does not work as a "*black box*", which is a typical problem of any available ANN package for which the learning process is always unknown. Since we have implemented our algorithms, we can examine step by step how our

[1] `http://www.mathworks.com/products/neural-network/`
[2] `http://pybrain.org`
[3] `http://www.python.org`

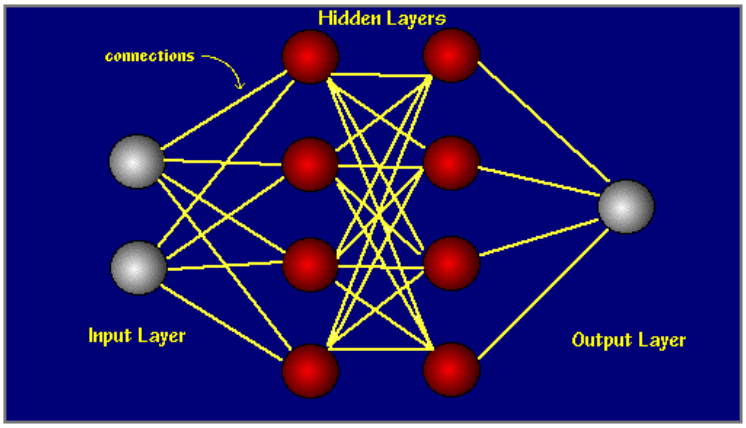

Figure 5.1: Schematic view of a Two Layer Perceptron (2LP), the Artificial Neural Network architecture we used for our analysis. Data enter the 2LP through the nodes in the input layer. The information travels from left to right across the links and is processed in the nodes through an activation function. Each node in the output layer returns the likelihood of a source to be a specific class.

network is learning to distinguish 3FGL source classes.

To date,[9, 47, 58, 35] have explored the application of machine learning algorithms to source classification, based on some γ-ray observables, showing that there is much to be gained in developing an automated system of sorting (and ranking) sources according to their probability of being a specific source class. The present work differs from these in applying the technique to different types of blazars rather than trying to separate AGN in general from other source classes.

5.2 Training session

For a given network architecture the first step is the "training" of the ANN. In this step the weights $\mathbf{w}$ (the "free parameters") are determined by a specific learning algorithm. The basic learning algorithm for 2LP is the so-called back-propagation which is based on the error-correction learning rule. In essence, back-propagation consists of two passes through the different layers of the network: a forward pass and a backward pass. In the forward pass an input vector is applied to the input nodes of the network, and its effect propagates through the network layer by layer. Finally, a set of outputs is produced as the actual response of the network. During the backward pass, on the other hand, the weights are all adjusted in accordance with the error correction rule.

Specifically, the actual response of the network is subtracted from a desired (target) response which we denote as a vector $\mathbf{t} = (t_1, t_2, ..., t_c)$ to produce an error signal. This error signal is then propagated backward through the network. There are several choices for the form of the error signal and this choice still depends on the nature of the problem, we choose the sum-squared error (E) defined in the Equation 15.1. Moreover, we define the mean square error (mse) as the sum of the errors given by each object in the training sample:

$$mse = \frac{1}{N} \sum_{n} E^{(n)} \tag{5.1}$$

where $E^{(n)}$ is the error related to the nth source in the training sample and N is the number of sources in the training sample. The weights are adjusted to make the actual response of the network move closer to the desired response in a statistical sense. The set of weights that minimizes the error function are found using the method of gradient descendent. Starting from a random set of weights $\mathbf{w}$ the weights are updated by moving a small distance in w-space into the direction $-\nabla_{\mathbf{w}} E$ where E decreases most rapidly:

$$\mathbf{w}_{new} = \mathbf{w}_{old} - \eta \frac{\partial E}{\partial \mathbf{w}} \tag{5.2}$$

where the positive number η is the learning rate and we set it to 0.2. The algorithm is stopped when the value of the error function has become sufficiently small. We analyzed also the possibility to use the "heavy ball method" defined in the Equation 15.4 adding a momentum $\alpha = 0.9$ in the Equation 5.2 but without a significant improvement in the performance of the network thus we decided to not use this learning algorithm. We tuned a number of ANN parameters to improve the performance of the algorithm. We renormalized all input parameters between 0 and 1 to minimize the influence of the different ranges. We used a hyperbolic tangent function as activation function connected to each hidden and output nodes. The outputs were renormalized between 0 and 1 to handle it as a probability of membership class. We randomly initialized the weights in the range between -1 and 1, not including any bias. The optimal number of hidden nodes was chosen through the *pruning* method [**?**]. We used the standard back-propagation algorithm as learning method setting the learning rate parameter to 0.2. We did not add the momentum factor in the learning algorithm because does not improve the performance of the network. We used the learning algorithm in the *on-line* version, in which weights associated to each link are updated after each example is processed by the network. Backpropagation is an abbreviation for the backwards propagation of error. With the delta rule, as with other types of backpropagation, 'learning' is a supervised process that occurs with each cycle or 'epoch' (i.e. each time the

network is presented with a new input pattern) through a forward activation flow of outputs, and the backwards error propagation of weight adjustments. More simply, when a neural network is initially presented with a pattern it makes a random 'guess' as to what it might be. It then sees how far its answer was from the actual one and makes an appropriate adjustment to its connection weights. More graphically, the process looks something like Figure 5.2.

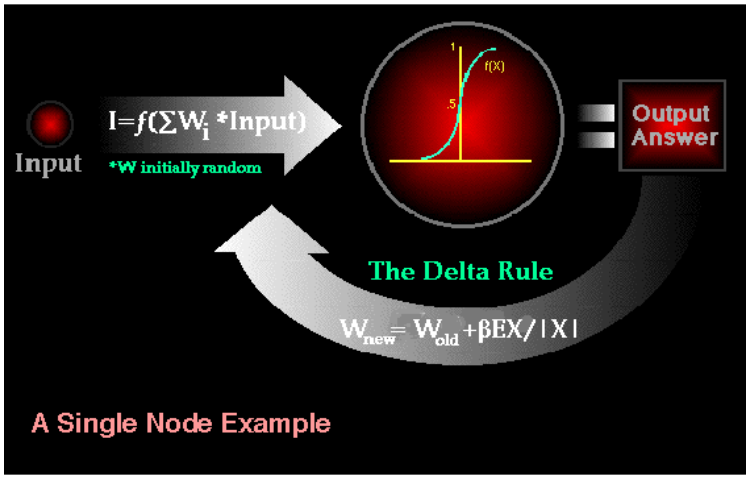

Figure 5.2: A single node in a standard back-propagation algorithm

Backpropagation performs a gradient descent within the solution's vector space towards a 'global minimum' along the steepest vector of the error surface. The global minimum is that theoretical solution with the lowest possible error. The error surface itself is a hyperparaboloid but is seldom 'smooth' as is depicted in Figure 5.3. Indeed, in most problems, the solution space is quite irregular with numerous 'pits' and 'hills' which may cause the network to settle down in a 'local minum' which is not the best overall solution. See Figure **??**

Since the nature of the error space can not be known a prioi, neural network analysis often requires a large number of individual runs to determine the best solution. Most learning rules have built-in mathematical terms to assist in this process which control the 'speed' (Beta-coefficient) and the 'momentum' of the learning. The speed of learning is actually the rate of convergence between the current solution and the global minimum. Momentum helps the network to overcome obstacles (local minima) in the error surface and settle down at or near the global minimum.

Once a neural network is 'trained' to a satisfactory level it may be used as an analytical tool on other data. To do this, the user no longer specifies any training runs and instead allows the network to work in forward propagation mode only. New inputs are presented to the input pattern where they filter

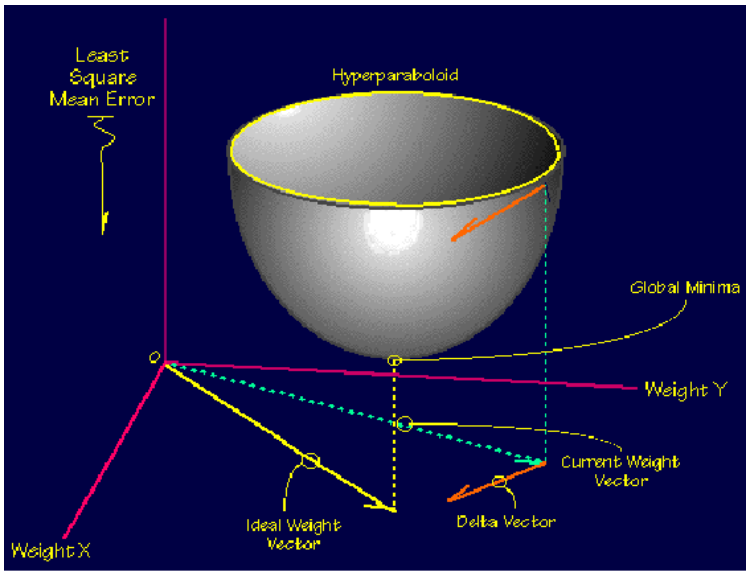

Figure 5.3: Hyperparaboloid error surface in a backpropagation

into and are processed by the middle layers as though training were taking place, however, at this point the output is retained and no backpropagation occurs. The output of a forward propagation run is the predicted model for the data which can then be used for further analysis and interpretation.

It is also possible to over-train a neural network, which means that the network has been trained exactly to respond to only one type of input; which is much like rote memorization. If this should happen then learning can no longer occur and the network is refered to as having been "grandmothered" in neural network jargon. In real-world applications this situation is not very useful since one would need a separate grandmothered network for each new kind of input.

5.3 Source sample and predictor parameters

Since the aim of this work is to quantify the likelihood of each 3FGL BCU to be more similar to a BLL or a FSRQ source class, we chose all the 660 BL Lac, 484 FSRQ as source sample.

This is a two-class approach where the output $L_{\rm BLL}$ expresses the likelihood of a BCU source to belong to the BLL source class and $L_{\rm FSRQ}$= 1−$L_{\rm BLL}$ to the FSRQ one. We encoded the output of the associated blazars so that $L_{\rm BLL}$ is 1 if the known object is a BL Lac, and $L_{\rm BLL}$ is 0 if it is a FSRQ.

Following the standard approach, we randomly split the 3FGL blazars sam-

ple into 3 subsamples, the training, the validation and the testing one. Training sample is used to optimize the network and classify correctly the encoded sources. Validation sample is used to avoid over-fitting during the training, this is not used for optimizing the network but during the training session it monitors the generalization error. The learning algorithm is stopped at the lowest validation error. Testing sample is independent both of the training and validation ones and was used to monitor the accuracy of the network, once all optimizations were made the network is applied to the testing sample and the related error provides an unbiased estimate of the generalization error. We chose a training sample as large as possible ($\sim$ 70% of the full sample) while keeping the other independent samples homogeneous ($\sim$ 15% each one). Since we used an *on-line* version of the learning algorithm, we decided to shuffle the training sample after all of the training sample was used once to optimize the network, this choice allowed us to maintain a good generalization of our network.

Because we want to distinguish BLL from FSRQ only on the basis of their γ-ray ECDF, we selected flux values related to such a distribution as predictor parameters. We included in our ANN algorithm γ-ray fluxes below such values a blazar emitted for 10, 20, 30, 40, 50, 60, 70, 80, 90 and 100 per cent of the entire observation. Our choice originates from a compromise between a good representation of each ECDF and a limited number of input parameters to avoid problems related to upper limits associated to some bin time.

Because our interest is only for blazars, we do not expect any contribution to the BCU sample given by other extragalactic source class. However we analyzed AGN in classified as radio galaxy, starbust galaxy, art galaxy and seyfer galaxy in order to estimate any possibility of their contamination in our analysis.

Figs. 5.4 , 5.5 and 5.6 show that no significant contamination on the BCU candidates Bl Lac comes from other AGN classes . However, we noted a small contamination from Seyfert and Radio Galaxies in the classification of BCUs as FSRQ candidates . That's why the ANN analysis was implemented by optical and radio observations data in order to confirm ANN uncertain data.

We even tested the performance of the netwok adding the Variability Index defined in 3FGL catalog [**?**] as an additional time parameter. Variability Index is a statistical parameter that tests if a γ-ray source is variable above a certain confidence level, in particular if its value is greater than 72.5 the object is statistically variable at 99% confidence level. The information given by Variability Index is more limited with respect to ECDF, that also provides a characterization of the variability pattern, which is probably related to a spectral variability during the flare state. Including the Variability Index in the algorithm the performance of the network do not significantly increase

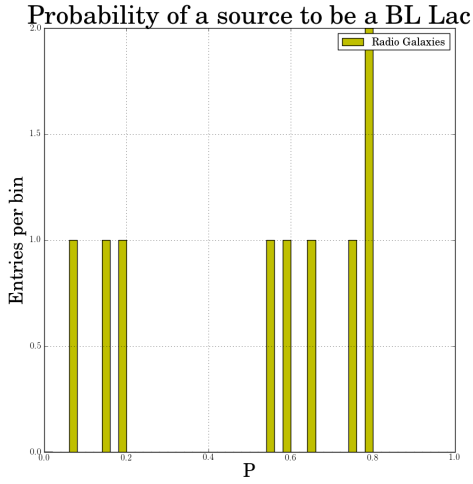

Figure 5.4: B-FlaP ANN likelihood for 3FGL Radio Galaxies

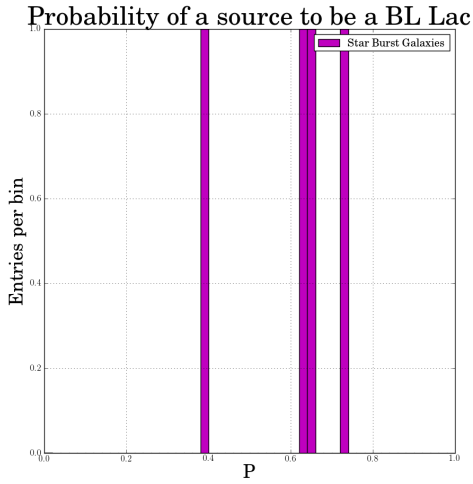

Figure 5.5: B-FlaP ANN likelihood for 3FGL Star Burst Galaxies

showing that this parameter is not important at distinguishing the two blazar subclasses. Defining the importance of each input parameter as the product of the mean-squared of the input variables with the sum of the weights-squared of the connection between the variable's nodes in the input layer and the hidden layer, Variability Index was observed to be the less important parameter. Fig. 5.7 confirms that the distribution of Variability Index is very similar for 3FGL BLL and FSRQ making this parameter unimportant for our purpose.

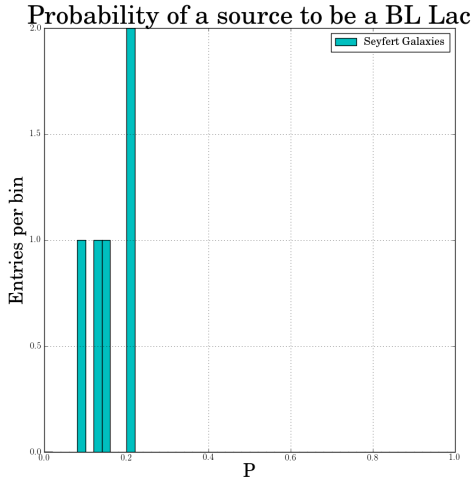

Figure 5.6: B-FlaP ANN likelihood for 3FGL Seyfert Galaxies

We excluded by our analysis both γ-ray and multiwavelength spectral parameters because the aim of this work is to develop a classification algorithm that can be efficiently applied to γ-ray sources when rigorous γ-ray spectra or multiwavelength information are missing. Since, to date, the best way to single out BLL from FSRQ is to analyse their spectral energy distribution [**?**], we used multiwavelength spectral information to validate our algorithm comparing the distribution of BL Lac and FSRQ candidates with known ones as discussed in Section 5.6, 8.2.

As a result, our feed-forward 2LP is built up of 10 input nodes, 6 hidden nodes and 2 output nodes.

5.4 Optimization of the algorithm and classification thresholds

At the end of the learning session, the ability of the algorithm to distinguish BLL from FSRQ is optimized and for each blazar produces a likelihood of membership class. Fig. 5.8 shows the likelihood distribution applied to the testing sample. The distribution clearly shows two distinct and opposite peaks for BL Lac (blue) and FSRQ (red), the former at $L_{\rm BLL}\sim 1$ while the latter at $L_{\rm BLL} \sim 0$. Since the testing sample was not used to train the network, the distribution shows the excellent performance of our algorithm in classifying new BL Lacs and FSRQs.

We defined two classification thresholds to label BCU as BL Lac or FSRQ

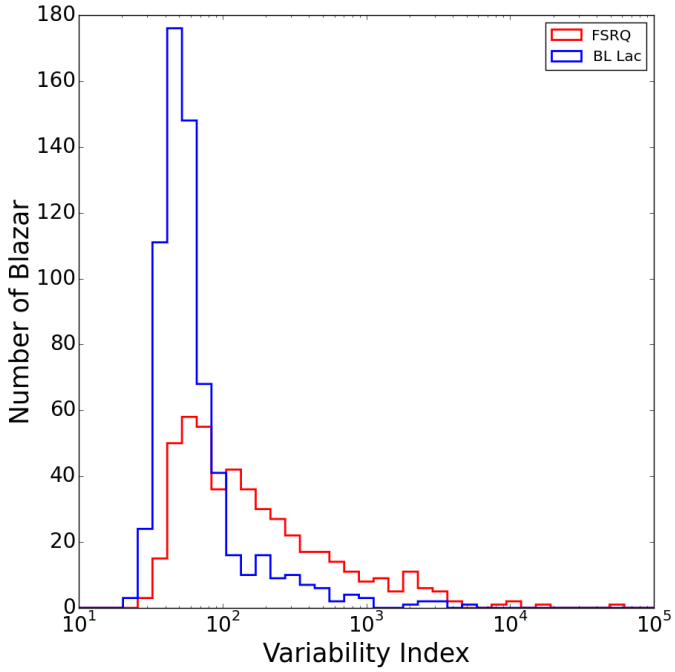

Figure 5.7: Variability Index distribution for 3FGL BL Lac (blue) and FSRQ (red).

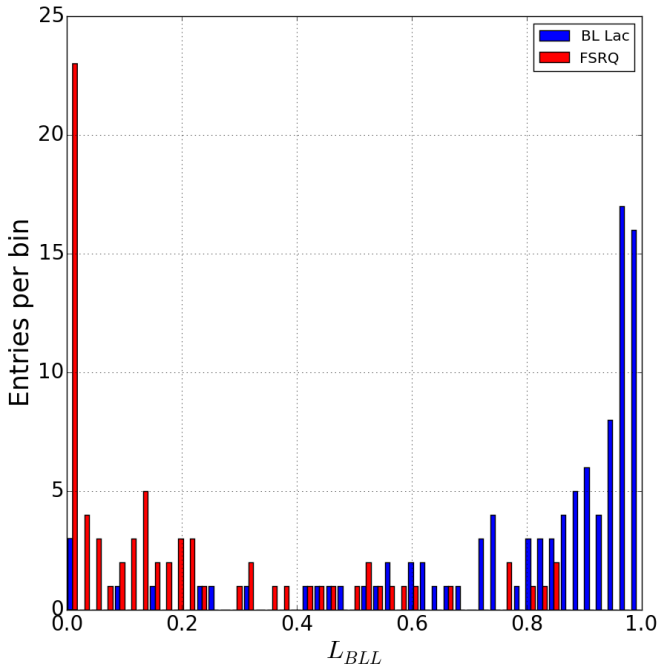

Figure 5.8: Distribution of the ANN likelihood to be a BL Lac candidate for 3FGL BL Lac (blue) and FSRQ (red) in the testing sample. The distribution of the likelihood to be an FSRQ candidate ($L_{\rm FSRQ}$) is $1-L_{\rm BLL}$.

candidates. Our thresholds are based on the optimization of the positive association rate (*precision*), that is defined as the fraction of true positive with respect to the objects classified as positive, of $\sim 90\%$. The classification threshold of $L_{\rm BLL}> 0.566$ identifies BLL candidates, while threshold $L_{\rm FSRQ}> 0.770$ identify FSRQ candidates. Another parameter useful to characterize the performance of our classification algorithm is the *sensitivity*, defined as the fraction of objects of a specific class correctly classified as such. According to this definition, the threshold for BLL classification is characterized by a sensitivity of $\sim 84\%$, while of $\sim 69\%$ for FSRQ thresholds. Precision and sensitivity of our classification algorithm help us to predict the completeness and the fraction of spurious sources in the list of BL Lac and FSRQ candidates. Thresholds defined on the basis of high *precision* are useful to select the best targets to observe with ground telescopes, optical or Cherenkov, to unveil their nature, while on high *sensitivity* give us an idea of how many BLL and FSRQ remain to be identified in the 3FGL BCU sample. In the end, according to our classification thresholds the expected false negative rate (*misclassification*) is $\sim 5\%$ for

BL Lac and $\sim 12\%$ for FSRQ. *Sensitivity*, *misclassification* and classification thresholds reveal FSRQ γ-ray ECDF is broader and more contaminated than BL Lac ones as we expected by Fig. 5.9 The combination of high precision rate and low misclassification rate indicates a very high performance of our optimized network.

5.5 Selecting the most promising HSP candidates

Although the ECDF of HSP is not clearly separated from ISP and LSP ones, we decided to develop a new ANN algorithm to select the best HSP candidates among BCU for VHE observations increasing the pointing accuracy and save time during observations. Following the procedure described in the previous sections we chose as source sample all the 289 HSP and the 824 non-HSP identified by their spectral energy distribution. We used as predictor variables the same ECDF parameters used to classify BLL and FSRQ. The new feed-forward 2LP is built up of 10 input nodes, 5 hidden nodes and 2 output nodes.

Fig. 5.9 shows the optimized networks applied to testing sample that represents 15% of the full sample. The distribution reveals only a peak at low L_{HSP} for non-HSP and a nearly flat distribution for HSP sources showing the optimized netwok was not able to clearly classify HSP on the basis of ECDF as we expected. Defining a classification threshold of $L_{HSP} > 0.891$ so that the *precision* rate is $\sim 90\%$, we are able to discover the best HSP candidates. According to this definition, the *sensitivity* of our algorithm is 4.5%. This result shows that only a very small fraction of HSP can be separated from non-HSP to be identified. We name all the BCU in this region as *Very High Confidence* (VHC) HSP candidates. All the blazars in this area are BL Lac. The FSRQ characterized by the highest L_{HSP} value, ~ 0.85, is 3FGL J1145.8+4425. This means that all the VHC HSP candidates will also be VHC BLL candidates. In addition, we decided to define a less conservative classification threshold ($L_{HSP} > 0.8$) in order to increase the number of targets to observe with VHE telescopes at the expense of a less precision rate ($\sim 75\%$). We label BCU characterized by a L_{HSP} greater than such a classification threshold as High Confidence (HC) HSP candidates.

5.6 ANN Results and validation

In this section we will first discuss the results of our optimized ANN algorithm at classifying BL Lac and FSRQ candidates among 3FGL BCU sources. Then we will validate our statistical method comparing the PowerLaw Index distri-

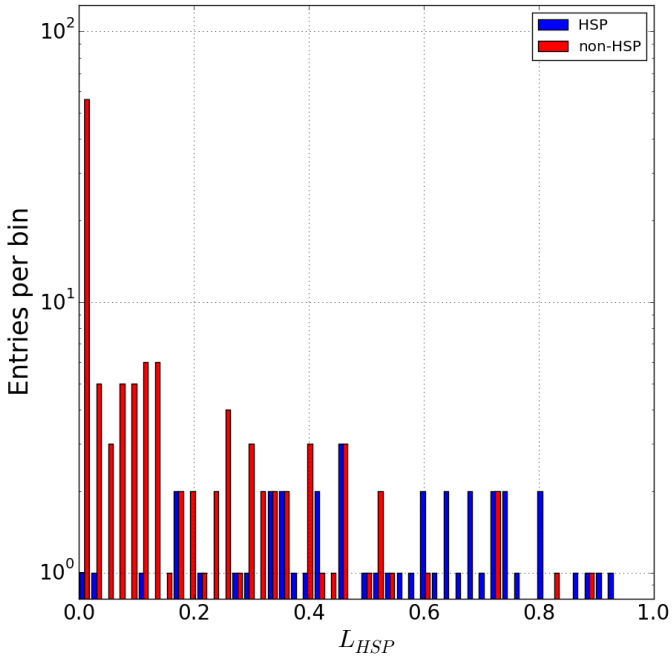

Figure 5.9: Distribution of the ANN likelihood to be a HSP candidate for HSP (blue) and non-HSP (red) in the testing sample.

bution of known BLL and FSRQ with that of our best candidates. Then we will analyze the performance of our algorithm based on ECDF with respect to the other γ-ray parameters usually used to classify blazars, such as PowerLaw Index and Variability Index. In the end we will discuss the results on the identification of the most promising HSP candidates.

Applying our optimized algorithm to 573 3FGL BCU we find that 342 are classified as BLL candidates ($L_{BLL} > 0.566$), 154 as FSRQ candidates ($L_{FSRQ} > 0.770$) and 77 remain unclassified. Hereafter we will define as $\mathrm{BLL_{3FGL}}$ and $\mathrm{FSRQ_{3FGL}}$ blazars classified in the 3FGL catalog, while as $\mathrm{BLL_{ANN}}$ and $\mathrm{FSRQ_{ANN}}$ BCUs classified by ANN and $\mathrm{BCU_{ANN}}$ BCUs that remain uncertain. The likelihood distribution of BCUs membership class is shown in Fig. 5.10 and such a distribution reflects very well those of $\mathrm{BLL_{3FGL}}$ and $\mathrm{FSRQ_{3FGL}}$ in the testing sample (see Fig. 5.8) as we expect for a well-built classification algorithm. Taking into account *precision* and *sensitivity* rates, our optimized algorithm predicts that there are about 365 BL Lac and about 200 FSRQ to be still identified. This prediction is rather interesting because at present the fraction of $\mathrm{BLL_{3FGL}}$ is ~ 1.4 times that of $\mathrm{FSRQ_{3FGL}}$ while a larger

fraction ($\sim$ 1.8) of BL Lac to be identified is expected by our analysis. This disagreement may be explained by their γ-ray features. FSRQ are typically more variable than BL Lac and they are very bright for a large fraction of time allowing both to characterise in detail their spectral energy distribution and to identify their position on the sky with more accuracy, which are essential requisites to associate it with a FSRQ known at other wavelengths. On the other hand, BL Lac are usually fainter and worse characterized in γ-ray and their association is more difficult, leaving much more BL Lac objects to be identified in the 3FGL catalog than FSRQ. The different brightness between BL Lac and FSRQ does not seem to be intrinsic but related to the strong bias observed toward hard sources in the photon-flux limit as described in [1].

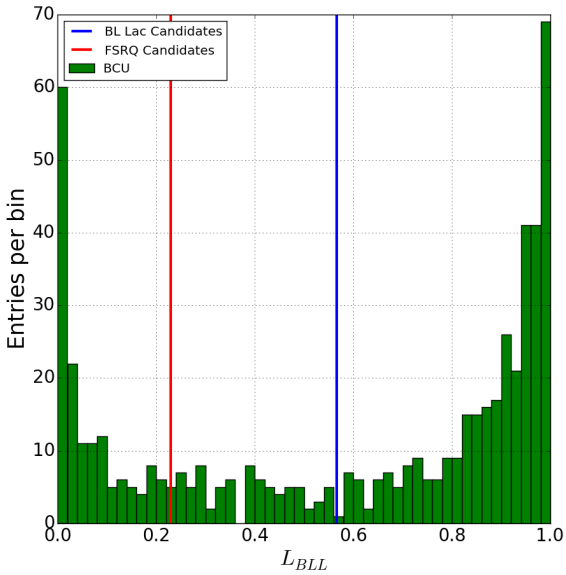

Figure 5.10: Distribution of the ANN likelihood of 573 3FGL BCU to be BL Lac candidates. Vertical blue and red lines indicate the classification thresholds of our ANN algorithm to label a source as BL Lac or FSRQ respectively as described in the text.

After the launch of the *Fermi* Space Telescope it was discovered that BLL and FSRQ are characterized by different γ-ray spectral properties, in fact the former usually show harder spectra than the latter. [1]. Fitting 3FGL blazars assuming a power-law spectral model we observe that the best-fit photon spectral index (in 3FGL named *PowerLaw Index*) distribution is rather dissimilar for the two subclasses as shown in Fig. 5.11. The PowerLaw Index distribution means and standard deviations are 2.02 ± 0.25 and 2.45 ± 0.20 for BL Lac and

FSRQ respectively, making this observable one of the most powerful γ-ray parameter to distinguish the two blazar subclasses. Since we did not include this parameter in our algorithm, we compared the PowerLaw Index distribution for $\mathrm{BLL_{ANN}}$ and $\mathrm{FSRQ_{ANN}}$ with what we know from already classified objects to test the performance of our algorithm and to validate it. Fig. 5 shows in the right panel the PowerLaw Index distributions for BL Lacs while in the left one for the FSRQ. Such distributions are in good agreement confirming the accuracy of our classification algorithm. The PowerLaw Index distribution means and standard deviations are 2.02 ± 0.27 and 2.48 ± 0.18 for $\mathrm{BLL_{ANN}}$ and $\mathrm{FSRQ_{ANN}}$ respectively as expected. Moreover almost all sources classified through the BFLaP-ANN method are within the PowerLaw Index distribution range associated to their blazar subclass.

An effective way to evaluate the powerful of our method is to compare ANN predictions at distinguishing blazar subclasses based on B-FlaP information with those found by a simple analysis of γ-ray spectral or timing properties. Analyzing the PowerLaw Index distribution shown in Fig. 5.11 we can define two classification thresholds to separate BLL from FSRQ with a degree of purity equal to what we used for ANN thresholds, 90%. According to this hypothesis all blazars characterized by a PowerLaw Index < 2.25 or > 2.64 will be classify as BLL and FSRQ candidates respectively with a precision rate of 90%. All blazar with an intermediate value will remain unclassified owing to high contamination. Fig.5.13 shows the PowerLaw Index distribution against the ANN likelihood to be a BL Lac of all 3FGL BCU. Vertical and horizontal dashed lines indicate classification thresholds defined for the two distributions to single out BL Lac from FSRQ. Comparing the two different predictions we observe they agree for $\sim 63\%$ of BCU (diagonal blocks from top left to bottom right), while disagree only for $\sim 3.5\%$ (top right and bottom left blocks). As a key result we observe that ANN method based on B-FlaP is able to provide a classification for $\sim 30\%$ of BCU remaining uncertain on the basis of their spectra (top and bottom central blocks) while the opposite occurs only for $\sim 3.5\%$ of BCU. This comparing highlights the powerful of our analysis with respect to the standard one based on spectral information.

To be thorough we followed the same approach to compare ANN predictions based on B-FlaP with those obtained by Variability Index. As discuss in the previous Section, we expect this parameter is not efficient at distinguishing blazar subclasses so that we did not include it in our analysis. We defined two classification thresholds as before from the Variability Index distribution (see Fig. 5.7) so that blazar with a value smaller than 31 are classified as BL Lac candidates while with a value larger than 5710 are FSRQ candidates in according with the 90% of precision. These areas are very small because the overlap in the Variability Index distribution is very large. As shown in

Table 5.1: BLL_{3FGL}, $FSRQ_{3FGL}$, BCU_{3FGL}, and the new classification of blazars after B-FlaP ANN analysis.

$\mathbf{BLL_{3FGL}}$	$\mathbf{FSRQ_{3FGL}}$	$\mathbf{BCU_{3FGL}}$
660(38.4%)	484(28.2%)	573(33.4%)
$\mathbf{BLL_{3FGL+ANN}}$	$\mathbf{FSRQ_{3FGL+ANN}}$	$\mathbf{BCU_{3FGL+ANN}}$
1002(58.3%)	638(37.2%)	77(4.5%)

Fig. 5.14, the two methods agree only for $\sim$ 17% of BCU and disagree for $\sim$ 0.2%. No BCU is classified by the Variability Index remaining uncertain by ANN, while for a very large fraction, $\sim$ 83%, ANN is able to provide a classification remaining unclassified by Variability Index. This analysis clearly shows Variability Index is rather unimportant at classifying blazar subclasses as we expect and it must be replaced by the more robust B-FLaP for this purpose.

In the end, applying our algorithm optimized to select the most promising HSP among 573 3FGL BCU, we can single out 14 VHC HSP candidates ($L_{HSP} > 0.891$) and 38 HC ones ($L_{HSP} > 0.8$) for a total of 52 very interesting targets to be observed through Very High Energy telescopes. Fig. 5.15 plots the likelihood distribution of BCUs and such a distribution reflects very well those of the entire testing sample (see Fig. 5.9) showing a nearly flat distribution at high L_{HSP} values related to a large overlap between HSP and non-HSP in the B-FlaP parameter space. We compared our predictions with those found by the 3LAC catalog on the basis of the study of broadband Spectral Energy Distributions (SED) collected all data available in the literature. SED classification provided by is based on the estimation of the synchrotron peak frequency ν^S_{peak} value extracted from a 3rd-degree polynomial fitt of the low-energy hump of the SED. Out of 14 VHC HSP, 10 ($\sim$ 73%) are classified as HSP on the basis of their broadband SED and 4 ($\sim$ 28%) remain unclassified. Out of 38 HC HSP, 22 ($\sim$ 58%) are classified as HSP, 8 ($\sim$ 21%) are classified as non-HSP and 8 ($\sim$ 21%) remain unclassified by their broadband SED. To conclude, classifications agree for $\sim$ 63% of most promising HSP selected by ANN, validating the efficiency of our algorithm; disagree for $\sim$ 15%, in agreement with the expected contamination rate; and for the remaining $\sim$ 22% ANN provides a classification as most promising HSP while the SED is not enough rigorous or available.

~~NON CONSIDERARE~~ ~~VEDI PAPER 2 HSP~~

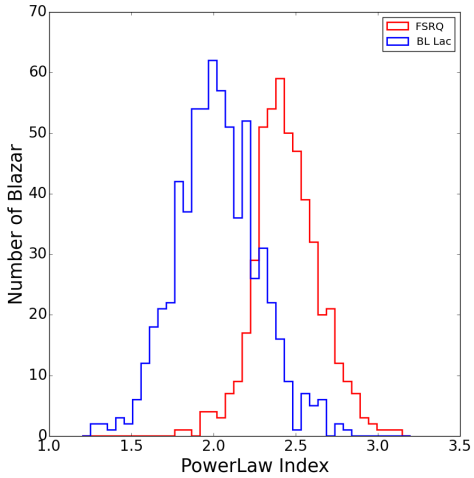

Figure 5.11: PowerLaw Index distribution for 3FGL BL Lac (blue) and FSRQ (red).

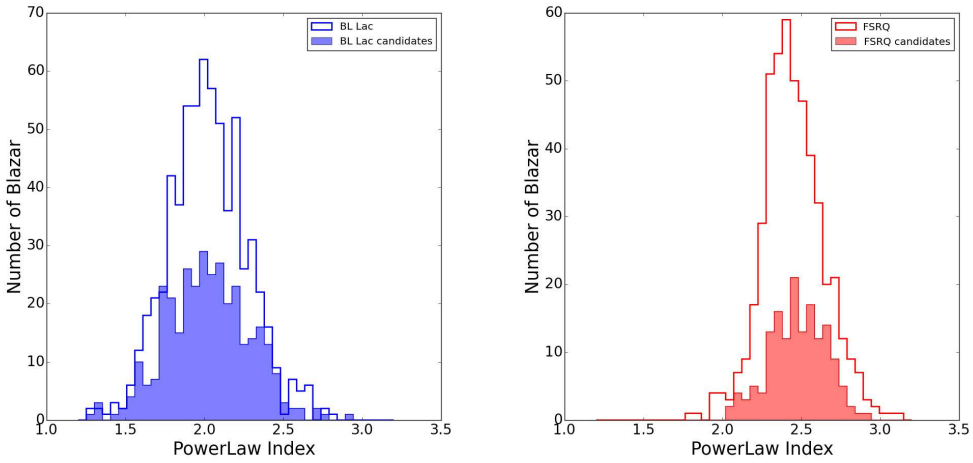

Figure 5.12: PowerLaw Index distribution for the blazars classified through the ANN method (filled histograms) in comparison to the previously classified blazars. Left: BL Lacs; right: FSRQs.

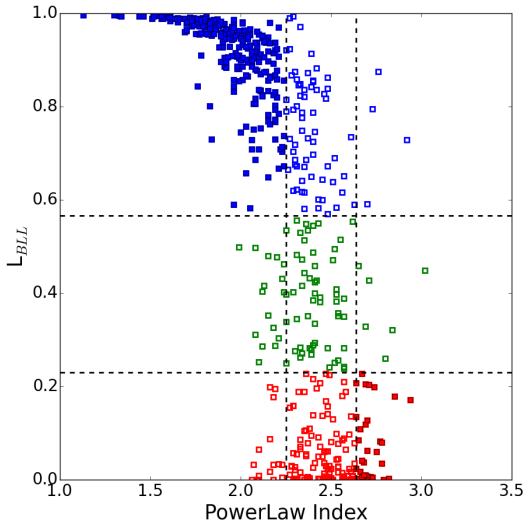

Figure 5.13: ANN likelihood against PowerLaw Index distributions. Colors indicate the classification proposed by the ANN method: blue for BL Lacs, red for FSRQs, and green for still uncertain objects. Filled symbols indicate the sources for which the PowerLaw Index indicates a matching classification.

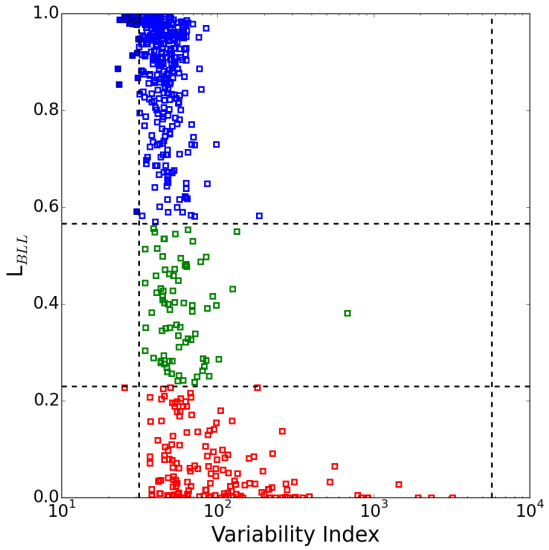

Figure 5.14: ANN likelihood against Variability Index distributions. Colors and symbols as in Fig. 5.13

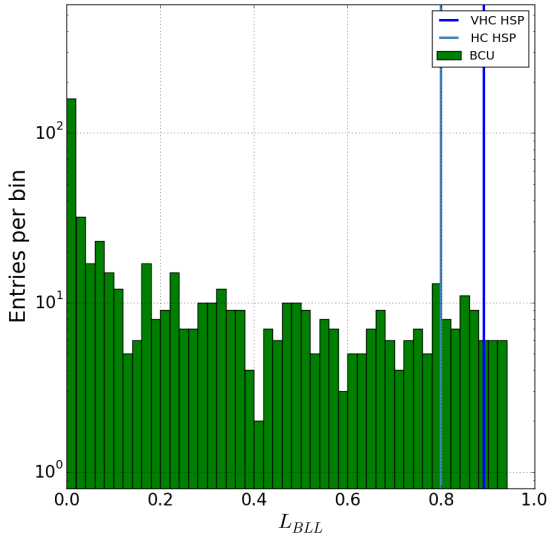

Figure 5.15: Distribution of the ANN likelihood of 573 3FGL BCU to be HSP candidates. Vertical blue and steel blue lines indicate the classification thresholds of our ANN algorithm to identify a source as Very High Confidence or High Confidence HSP respectively as described in the text.

Chapter 6

B-FlaP Classification List

6.1 The List

The Classification List represents the main result of this study and contains two of the main goals of the examination : to classify 3FGL BCUs as BL Lac or FSRQ candidates and to identify the most promising BCUs to target in VHE observations.We used an innovative method to extract useful information. We investigated for the first time the distribution of blazars in the ECDF of γ-ray flux parameter space, and we applied an advanced machine learning algorithm as ANN to learn to distinguish BL Lacs from FSRQs and to recognize the most likely HSP candidates. The power of our approach was tested in the previous Chapter, and here we present a summary of our results in Table 6.2.

The full table of individual results contains the classification of BCUs listed in the 3FGL *Fermi*-LAT as the key parameter. We provide for each 3FGL BCU the ANN likelihood (L) to be a BL Lac or a FSRQ, and the predicted

Table 6.1: BLL_{3FGL}, $FSRQ_{3FGL}$, BCU_{3FGL}, and the new classification of blazars after B-FlaP ANN analysis.

$\mathbf{BLL_{3FGL}}$	$\mathbf{FSRQ_{3FGL}}$	$\mathbf{BCU_{3FGL}}$
660(38.4%)	484(28.2%)	573(33.4%)
$\mathbf{BLL_{3FGL+ANN}}$	$\mathbf{FSRQ_{3FGL+ANN}}$	$\mathbf{BCU_{3FGL+ANN}}$
1002(58.3%)	638(37.2%)	77(4.5%)

Table 6.2: Classification List of 3FGL BCUs – sample. The table is published in its entirety in Appendix A of this thesis. The columns are: 3FGL Name, Galactic Latitude and Longitude (b and l), the ANN likelihood to be classified as a BL Lac (L_{BLL}) and a FSRQ (L_{FSRQ}), the predicted classification and the most promising HSP candidates labeled as Very High C. or High C., where C. is for *Confidence*

3FGL Name	b (°)	l (°)	L_{BLL}	L_{FSRQ}	Classification	HSP Candidates
J0002.2–4152	–72.040	334.320	0.877	0.123	BL Lac	
J0003.2–5246	–62.820	318.940	0.976	0.024	BL Lac	
J0003.8–1151	–71.080	84.660	0.952	0.048	BL Lac	
J0009.6–3211	–79.570	0.880	0.859	0.141	BL Lac	
J0012.4+7040	8.140	119.620	0.022	0.978	FSRQ	
J0014.6+6119	–1.270	118.540	0.896	0.104	BL Lac	
J0015.7+5552	–6.660	117.890	0.835	0.165	BL Lac	
J0017.2–0643	–68.150	99.510	0.953	0.047	BL Lac	
J0019.1–5645	–59.890	311.690	0.650	0.350	BL Lac	
J0021.6-6835	–48.580	306.730	0.459	0.541	Uncertain	
J0028.6+7507	12.300	121.400	0.749	0.251	BL Lac	
J0028.8+1951	–42.540	115.610	0.602	0.398	BL Lac	
J0030.2–1646	–78.570	96.580	0.981	0.019	BL Lac	High C.
J0030.7–0209	–64.580	110.690	2.35e–04	1.000	FSRQ	
J0031.3+0724	–55.120	114.190	0.984	0.016	BL Lac	

classification according to the defined classification thresholds. We label the most promising HSP candidates, splitting these objects into High Confidence HSPs and Very High Confidence HSPs in agreement with their likelihood to be an HSP-like source. Table 6.2 shows a portion of these results, the full table being available in Appendix A of this thesis.

6.2 HSP candidates for Cherenkov telescopes

B-FlaP Classification List shows 52 BCUs classified as BL Lac HSP. In order to obtain a *narrow selection* of candidates for direct observation by the present generation of Imaging Atmospheric Cherenkov Telescopes (IACTs), such as VERITAS, H.E.S.S. and MAGIC we refined our first HSP selection through additional parameters which might characterize the AGN as TeV sources, as following:

- γ-ray spectral photon index < 1.6
- Average significance over the 100 MeV to 300GeV energy band larger than 4.0

For each source we calculate the expected energy flux in the 50 GeV - 5 TeV energy range assuming that the spectral shape does not change to much compared to what the *Fermi*-LAT obtainted in the range between 300 MeV and 100 GeV. We compute the expected energy flux using the following relation:

$$EFlux_{[50\,\mathrm{GeV}-5\,\mathrm{TeV}]} = \int_{50\,\mathrm{GeV}}^{5\,\mathrm{TeV}} \frac{dN}{dE} E\, dE \tag{6.1}$$

where $dN/\,dE$ is the photon flux per unit energy, in units of $\mathrm{cm}^{-2}\ \mathrm{s}^{-1}\ \mathrm{MeV}^{-1}$, derived from the spectral model that fits the data.

We use the best-fit model parameters included in the public *XML Model File* for LAT 4-year Point Source Catalog The file can be retrieved from the *Fermi* Science Support Center.
In Fig.5 we report the pyhton script used to compute the expected energy.

As **final result** of the analysis we report in Tab.6.3 the full HSP list selected by Artificial Neural Network from 3FGL BCUs and in Tab.6.4 the *clean* list of HSP object identified as Very High Candidates for IACTs. Listed sources in Tab.6.4 have favorable coordinates to grant their visibility from all three observatories.

3FGLname	Assoc	Signif Avg	Spectral Ind.	B-FlaP Likelihood
3FGL J0030.2-1646	1RXS J003019.6-164723	9.160	1.647	0.981
3FGL J0039.0-2218	PMN J0039-2220	4.411	1.715	0.984
3FGL J0040.3+4049	B3 0037+405	6.379	1.132	0.996
3FGL J0043.5-0444	1RXS J004333.7-044257	5.840	1.735	0.984
3FGL J0043.7-1117	1RXS J004349.3-111612	5.896	1.594	0.993
3FGL J0047.9+5447	1RXS J004754.5+544758	5.042	1.334	0.995
3FGL J0132.5-0802	PKS 0130-083	4.525	1.753	0.986
3FGL J0153.4+7114	TXS 0149+710	7.056	1.567	0.992
3FGL J0204.2+2420	B2 0201+24	5.146	1.792	0.983
3FGL J0305.2-1607	PKS 0302-16	5.635	1.688	0.989
3FGL J0342.6-3006	PKS 0340-302	4.729	1.846	0.986
3FGL J0439.6-3159	1RXS J043931.4-320045	6.437	1.771	0.988
3FGL J0506.9-5435	1ES 0505-546	14.856	1.603	0.991
3FGL J0515.5-0123	NVSS J051536-012427	4.623	1.755	0.987
3FGL J0528.3+1815	1RXS J052829.6+181657	4.869	1.646	0.990
3FGL J0620.4+2644	RX J0620.6+2644	5.032	1.65	0.987

3FGL J0640.0-1252	TXS 0637-128	7.961	1.513	0.989
3FGL J0646.4-5452	PMN J0646-5451	7.056	2.189	0.993
3FGL J0648.1+1606	1RXS J064814.1+160708	5.270	1.775	0.985
3FGL J0650.5+2055	1RXS J065033.9+205603	10.030	1.558	0.989
3FGL J0733.5+5153	NVSS J073326+515355	6.251	1.741	0.989
3FGL J0742.4-8133	SUMSS J074220-813139	4.518	1.464	0.995
3FGL J0746.9+8511	NVSS J074715+851208	9.662	1.787	0.990
3FGL J0921.0-2258	NVSS J092057-225721	4.101	1.553	0.994
3FGL J1040.8+1342	1RXS J104057.7+134216	4.887	1.76	0.989
3FGL J1141.2+6805	1RXS J114118.3+680433	7.089	1.611	0.993
3FGL J1155.4-3417	NVSS J115520-341718	6.193	1.335	0.995
3FGL J1158.9+0818	RX J1158.8+0819	5.428	1.869	0.981
3FGL J1203.5-3925	PMN J1203-3926	7.312	1.639	0.989
3FGL J1319.6+7759	NVSS J131921+775823	9.097	1.785	0.987
3FGL J1434.6+6640	1RXS J143442.0+664031	6.913	1.517	0.995
3FGL J1446.8-1831	NVSS J144644-182922	4.179	1.723	0.987
3FGL J1547.1-2801	1RXS J154711.8-280222	4.285	1.708	0.982
3FGL J1612.4-3100	NVSS J161219-305937	9.014	1.88	0.986
3FGL J1711.6+8846	1RXS J171643.8+884414	6.668	1.57	0.993
3FGL J1714.1-2029	1RXS J171405.2-202747	6.795	1.344	0.994
3FGL J1824.4+4310	1RXS J182418.7+430954	4.952	1.725	0.992
3FGL J1841.2+2910	MG3 J184126+2910	8.353	1.567	0.989
3FGL J1855.1-6008	PMN J1854-6009	4.206	1.813	0.987
3FGL J1908.8-0130	NVSS J190836-012642	9.026	2.148	0.990
3FGL J1910.8+2855	1RXS J191053.2+285622	6.536	1.464	0.993
3FGL J1939.6-4925	SUMSS J193946-492539	5.986	1.624	0.989
3FGL J1944.1-4523	1RXS J194422.6-452326	5.397	1.56	0.993
3FGL J1959.8-4725	SUMSS J195945-472519	1.924	1.524	0.992
3FGL J2036.6-3325	1RXS J203650.9-332817	4.208	1.305	0.996
3FGL J2046.7-1011	PMN J2046-1010	4.814	1.609	0.991
3FGL J2104.2-0211	NVSS J210421-021239	4.060	1.524	0.993
3FGL J2108.6-8619	1RXS J210959.5-861853	4.729	1.74	0.990
3FGL J2312.9-6923	SUMSS J231347-692332	4.931	1.804	0.989
3FGL J2316.8-5209	SUMSS J231701-521003	5.606	1.735	0.988
3FGL J2347.9+5436	NVSS J234753+543627	4.694	1.733	0.984

Table 6.4: Very High Candidates for IACTs telescopes

3FGLname	Assoc	RA	Dec	Signif Avg	Spectral Ind.	TeV E -11
3FGL J0040.3+4049	B3 0037+405	00 43 44.4	-11 17 17.08	6.379	1.132	7.432
3FGL J1714.1-2029	1RXS J171405.2-202747	17 14 07.9	-20 29 46.6	6.795	1.344	7.098
3FGL J2036.6-3325	1RXS J203650.9-332817	20 36 41.8	-33 25 36.8	4.208	1.305	4.036
3FGL J1155.4-3417	NVSS J115520-341718	11 55 26.8	-34 17 57.4	6.193	1.335	3.863
3FGL J0506.9-5435	1ES 0505-546	05 06 58.3	-54 35 01.28	14.856	1.603	3.828
3FGL J0047.9+5447	1RXS J004754.5+544758	00 47 56.2	+54 47 49.19	5.042	1.334	3.814
3FGL J0640.0-1252	TXS 0637-128	06 40 04.99	-12 52 33.2	7.961	1.513	3.526
3FGL J0650.5+2055	1RXS J065033.9+205603	06 50 34.6	20 55 47.6	10.030	1.558	3.502
3FGL J1910.8+2855	1RXS J191053.2+285622	19 10 53.89	28 55 44.68	6.536	1.464	3.131
3FGL J1841.2+2910	MG3 J184126+2910	18 41 12.29	+29 10 58.4	8.353	1.567	2.945
3FGL J0153.4+7114	TXS 0149+710	01 53 26.2	71 14 30.08	7.056	1.567	1.916
3FGL J0742.4-8133	SUMSS J074220-813139	07 42 28.9	-81 33 31.28	4.518	1.464	1.818
3FGL J0030.2-1646	1RXS J003019.6-164723	00 30 15.7	-16 46 29.6	9.160	1.647	1.668
3FGL J0043.7-1117	1RXS J004349.3-111612	00 43 44.4	11 17 17.08	5.896	1.594	1.652
3FGL J1711.6+8846	1RXS J171643.8+884414	17 11 37.9	88 46 26.0	6.668	1.57	1.609
3FGL J1939.6-4925	SUMSS J193946-492539	19 39 40.9	-49 25 46.88	5.986	1.624	1.604
3FGL J1434.6+6640	1RXS J143442.0+664031	14 34 37.19	+66 40 55.48	6.913	1.517	1.544
3FGL J2104.2-0211	NVSS J210421-021239	21 04 12.29	-02 11 27.2	4.060	1.524	1.541
3FGL J1203.5-3925	PMN J1203-3926	12 03 31.6	-39 25 31.4	7.312	1.639	1.525
3FGL J2046.7-1011	PMN J2046-1010	20 46 44.09	-10 11 14.6	4.814	1.609	1.392
3FGL J0620.4+2644	RX J0620.6+2644	06 20 28.99	+26 44 22.19	5.032	1.65	1.340
3FGL J1944.1-4523	1RXS J194422.6-452326	19 44 10.8	-45 23 54.2	5.397	1.56	1.297
3FGL J0921.0-2258	NVSS J092057-225721	09 21 00.4	-22 58 00.4	4.101	1.553	1.202
3FGL J1141.2+6805	1RXS J114118.3+680433	11 41 17.7	+68 05 56.4	7.089	1.611	1.196
3FGL J0528.3+1815	1RXS J052829.6+181657	05 28 18.7	+18 15 38.8	4.869	1.646	1.145

```
#! /usr/bin/env python

# these modules come with the standard Python
import argparse, sys, os, shutil
# reopen stdout to turn off the buffered output
sys.stdout = os.fdopen(sys.stdout.fileno(), 'w', 0)

# these modules are essential
import numpy as np

def main():
  # Energy range on where perform the integer
  emin = 5.e4 # MeV  ->  50 GeV
  emax = 5.e6 # MeV  ->   5 TeV
  delta = 10.

  #j0650
  n0 = 0.7261442133e-14
  pi = -1.558256791
  e0 = 0.9887826601e4

  flux = 0

  for e in np.arange(emin, emax, delta):
    flux += n0 * ((e / e0)**pi) * e * delta * 1.6022e-6

  print "Energia = %e erg/cm2/s" % flux

if __name__ == '__main__':
  main()
```

Figure 6.1: Python script used for TeV flux extrapolation

Chapter 7

Radio Analysis

7.1 Radio flux density distribution

Besides the different γ-ray properties and optical spectra, BL Lacs and FSRQs are also dissimilar in their radio properties, BL Lacs are generally less luminous than FSRQs, so a classification based on radio luminosity could be a useful diagnostic for BCUs. However, radio luminosity is a quantity that can only be calculated if a redshift is known – and very often, nearly by definition, BCUs do not have an available optical spectrum suitable for the determination of z (this is actually the case for $\sim 91\%$ of our BCUs). In any case, as we are going to show the separation between BL Lacs and FSRQs remains rather clear also according to the flux density parameter. For this reason, we study here the radio flux density distribution of the 3FGL BL Lacs, FSRQs, and BCUs, in order to show that (1) the classification proposed by our *B-FlaP*$_{ANN}$ method is in agreement with the typical radio properties of known BL Lacs and FSRQs (i.e. the radio flux density distribution of the BCUs classified by us matches with that of the already classified BL Lacs and FSRQs) and (2) our method is more powerful than a simple analysis of the radio properties (i.e. there are many BCUs that can be classified as BL Lacs or FSRQs based on the ANN method, but would remain uncertain if we only looked at their radio flux density).

Since blazars are, nearly by definition, radio-loud sources, radio flux densities for all of them can be readily obtained from large sky surveys. In particular, the 3LAC reports the radio flux density at 1.4 GHz from the NRAO VLA Sky Survey [NVSS, 20] or at 0.8 GHz from the Sydney University Molonglo Sky Survey [SUMSS, 16] for blazars located at Dec. $> -40^\circ$ or $< -40^\circ$, respectively. In very few cases (only 20 in the entire clean 3LAC), radio flux densities are obtained at 20 GHz from the Australia Telescope Compact Array. In any

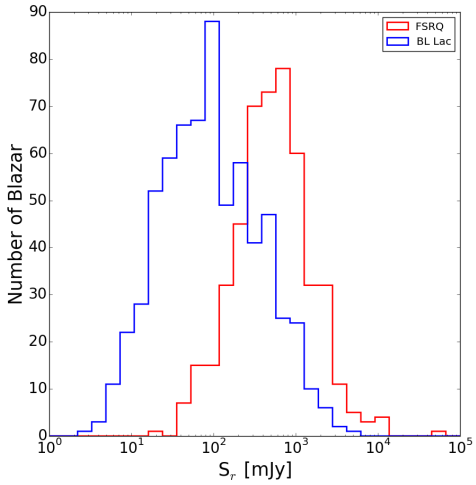

Figure 7.1: S_r distribution for the 3FGL sources classified as BL Lacs (blue histogram) and FSRQ (red histogram).

case, blazars are flat-spectrum sources, and the error associated to assuming that $\alpha = 0$ (i.e. treating all data as if they were taken at the same frequency) is negligible. Hereafter, we indicate with S_r the radio flux density, regardless of the source catalog.

In Fig. 7.1, we show the distribution of S_r over the entire range of BCU flux densities, dividing between BL Lacs (blue histogram) and FSRQs (red histogram). The overall distribution is clearly bimodal, with BL Lacs peaking at lower flux density than FSRQs. Based on these distributions, we define two *clean areas* where the density of sources of one class is predominant with respect to the other and where it is possible to separate BL Lacs and FSRQs with a 90% degree of purity. These areas are defined by the thresholds $S < 140$ mJy (90% probability of being a BL Lac) and $S > 2300$ mJy (90% probability of being a FSRQ). We further note that there is only one FSRQs with $S < 35$ mJy (while there are 170 BL Lacs in the same interval), corresponding to a *superclean area* with 99.5% probability of being a BL Lac. On the other hand, the overlap in the high flux density region is much larger and the radio flux density is not as reliable a predictor when it comes to identifying FSRQs.

7.2 Radio S_r distribution versus BFlaP

In Figs. 7.2, we compare the S_r distribution for the sources classified through the *B-FlaP*$_{ANN}$ method (BLL$_{\rm ANN}$ and FSRQ$_{\rm ANN}$, shown by shaded histograms)

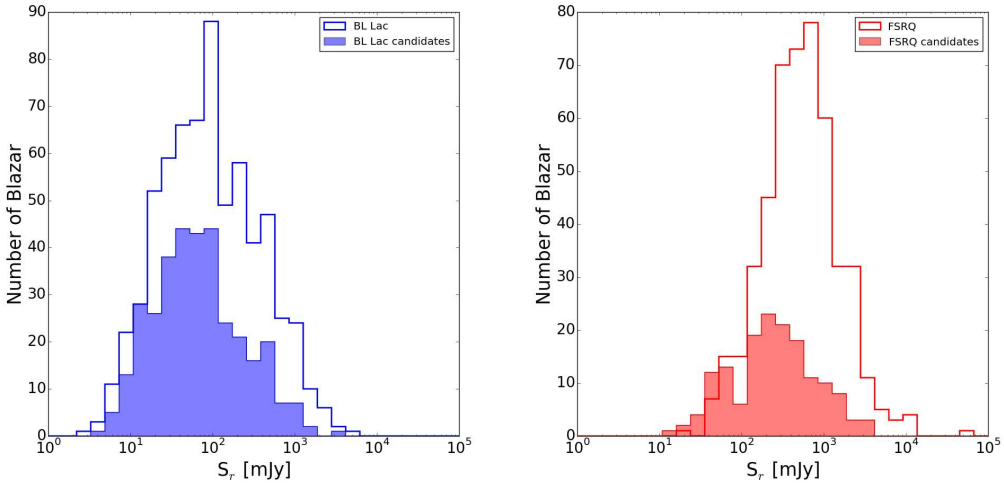

Figure 7.2: S_r distribution for the blazars classified through the *B-FlaP*$_{ANN}$ method (shaded histograms) in comparison to the previously classified blazars. Left: BL Lacs; right: FSRQs.

with that of the sources already classified in the 3FGL ($\mathrm{BLL_{3FGL}}$ and $\mathrm{FSRQ_{3FGL}}$, shown by the empty histograms). In the left panel, we show the BL Lacs, in the right panel the FSRQs. It is readily seen that the radio flux density distributions are in good agreement, which confirms the validity of our classification. In general, the *B-FlaP*$_{ANN}$ classified sources tend to lie on the fainter end of the distribution; that is not a surprise, since the brightest sources are more likely to have been selected for optical spectroscopy in past projects and therefore were not part of the starting BCU list.

In Fig. 7.3, we plot the ANN likelihood of a BCU being a BL Lac against S_r, divided in blocks according to the classification as a BL Lac or a FSRQ based on the ANN method and on the radio flux density. The diagonal blocks are those where the two methods agree, and they contain over 50% of the total population of BCUs (295/573). Then, there is a large fraction (190/573, i.e. $\sim$ 33%) of BCUs for which the ANN method provides a classification, while the S_r remains uncertain; these are the top and bottom blocks of the central column. This highlights the power of the ANN method in comparison to the simple flux density: only $\sim$ 6% of the BCUs can be classified through S_r while they would remain uncertain for ANN. Finally, there is a $\sim$ 8% of sources for which the two methods disagree (top right and bottom left squares). These are probably quite peculiar objects or spurious associations that deserve a dedicated analysis beyond the scope of this thesis.We further note that the analysis based on radio flux density could be subject to outliers, and in particular sources in the bottom left corner could be dim FSRQs that are located at very large redshift.

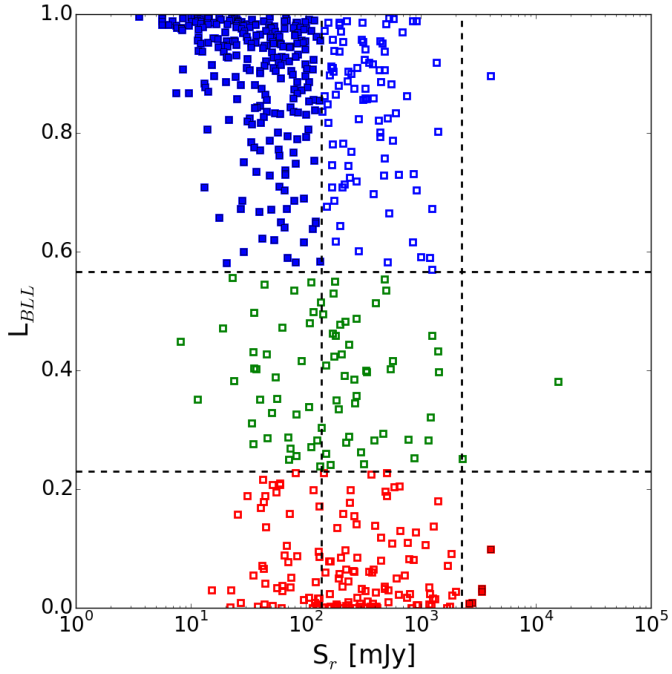

Figure 7.3: ANN likelihood against S_r in units of mJy. Colors indicate the classification proposed by the *B-FlaP*$_{ANN}$ method: blue for BL Lacs, red for FSRQs, and green for still uncertain objects. Filled symbols indicate the sources for which the radio flux density indicates a matching classification.

Chapter 8

Optical analysis

8.1 Quasar and Blazar in the optical

Quasar, after their detection at radio wavelenghts, show in the optical part of the spectrum something peculiar that caracterize these objects. The first key feature that was noticed was the emission line spectrum.The lines are very strong in emission featuring elements of Hydrogen (the Blamer and Lyman series are prominent), Helium, Carbon and Mgnesium, amongst others. The emission lines are also very broad. It was realised early that this implied very large velocity widths for the emitting gas as several thousand km sec^{-1}.Together with the broad lines are narrow, forbidden lines. The strongest are [O III] , [O II] nad [N II]. These type of emission line features are seen also in the active nuclei of some local galaxies - the Seyfert galaxies. Quasars occur in spiral or elliptical host galaxies but Seyferts in spiral galaxies only. *Blazars* as a subset of the radio-loud quasars, have extreme properties that set them apart fromn the rest of the galaxy population. These properties include rapid variability at alla frequencies and on all timescales, then high polarisation at both optical and radio frequencies, and in BL Lacs, a lack of any strong optical emission lines. The cause of the lack of emission lines in BL Lacs is explained that these objects are viewed close the axis of a relativistic jet. The synchrotron emission from this jet is Doppler boosted, increasing its intensity so that it swamps the continuum line and line emission that would otherwise be visible. As well as BL Lacs, the blazar class contains FSRQ (Flat-Spectrum Radio Quasar). These are quasars that share many of the same properties of BL Lacs, such as high polarisation and rapid variability, but with quasar-like emission lines.

8.1.1 Optical emission in blazars

The optical emission in blazars tends to be highly polarized, with level of at least a few percent, and often much higher. This gives the first important clue as to the nature of this optical emisison. A form of radiation that is naturally quite higly polarised is synchrotron radiation. This is radiation that is emitted when relativic particles, such as electrons, move through a magnetic field. The particles spiral around the field lines and as they to do so they emitt photons. In blazars, the synchrotron emission is most likely to come from a relativic jet that extends out from the centre of the source, (*although this is not always where synchrotron emission comes from , i.e. supernova remnants emit most of their radio emission in the form of synchrotron*) . From examining the multi wavelenght SEDs of blazars it is found that a continuous, perphaps slightly curved, spectrum connects the radio, IR, and optical data points. (and in some cases the X -ray points as well). This, and the observed polarization of the IR ad optical, has led to models that invoke a single synchrotron component to explain the emission over this entire range. A further argument for synchrotron emission at optical wavelenghts is the featureless continuum seen in Bl Lacs. A continuum with no emission lines is precisely what you would expect when the emisison is dominated by synchrotron.

The spectral differences from Bl Lacs , continuous line spectra, and FSRQ with quasar-like emission line were the features that we wanted for the BCUs during our observations with optical telescopes at Asiago observatory .In Fig. 8.1 we show the comparison of optical spectra of various kind od AGN.

8.2 Optical spectroscopy

In order to assess the reliability of the B-FlaP method in the identification of the various blazar classes, we carried out optical spectroscopic analysis of a sample of BCUs listed 3FGL, for which we had a classification likelihood by our ANN algoritm. Spectral data were obtained combining both the public products of the 12^{th} data release of the Sloan Digital Sky Survey data release of the 6dF Galaxy Redshift Survey as well as by direct observations performed with the 1.22m and the 1.82m telescopes of the Asiago Astrophysical Observatory.The selection of targets for the spectroscopic analysis is affected by the possibility to associate the low energy counterpart within the positional uncertainty of the γ-ray source. Since the energies of the charged particles, which emit γ-ray photons through inverse Compton scattering, are such that we expect strong synchrotron emission in the radio and the x-ray domain from the same source, we chose the targets for spectroscopic observations by looking for coincident emission at these frequencies. The typical positional uncertainties

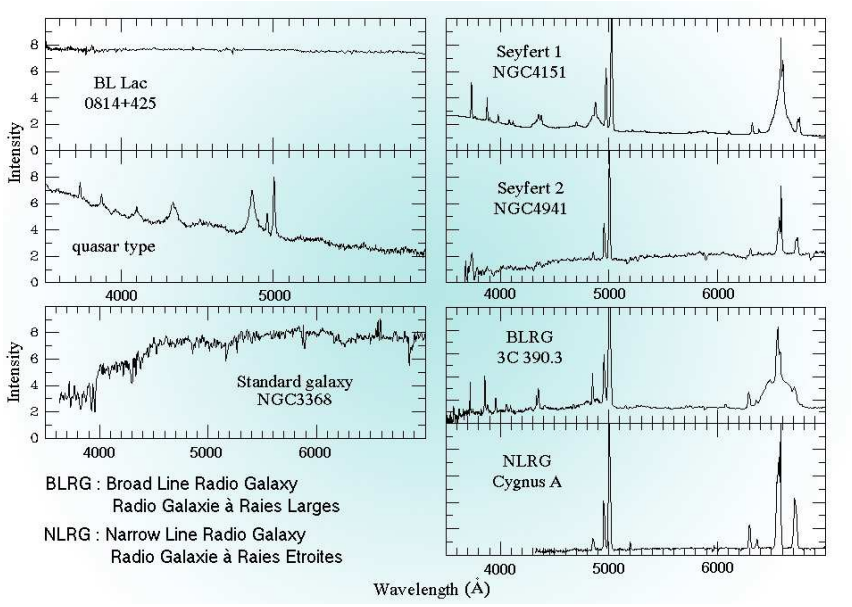

Figure 8.1: Comparison of the visible-light spectra of various kind of AGN, all shifted to zero redshift

of few arc seconds, achieved by radio and x-ray instruments, can constrain the source position on the sky better than the γ-ray detection and, therefore, greatly reduce the number of potential counterparts. When the candidate counterpart turned out to be covered by a spectroscopic survey, we analyzed the corresponding spectrum. If, on the contrary, it was not covered by a public survey, but it was still bright enough to be observed with the Asiago instruments (typically operating below the visual magnitude limit of $V \leq 18$ in spectroscopy), we carried out specific observations. The observational procedure involved exposures of each target and standard star, immediately followed by comparison lamps. The spectroscopic data reduction followed detector bias and flat field correction, wavelength calibration, flux calibration, cosmic rays and sky emission subtraction. All the tasks were performed through standard IRAF tools, customized into a proper reduction pipeline for the analysis of long slit spectra obtained with the specific instrumental configuration of the telescopes. At least one standard star spectrum per night was used for flux calibration, while the extraction of mono-dimensional spectra was performed by tracking the centroid of the target along the dispersion direction and choosing the aperture on the basis of the seeing conditions. The sky background was estimated in windows lying close to the target, in order to minimize the effects of non uniform sky emission along the spatial direction, while cosmic rays were identified and masked out through the combination of multiple exposures of

Table 8.1: The sample of objects selected from the 3FGL Source Catalogue for optical observation. The table columns report, respectively, the 3FGL source name, the associated counterpart, the coordinates (right ascension and declination) of the γ-ray signal centroid, and the source of optical spectroscopic data.

3FGL name	Counterpart	R.A. (J2000)	Dec. (J2000)	Data source
J0040.3 + 4049	B3 0037+405	00 : 40 : 19.9	+40 : 49 : 05	Asiago T182
J0043.7 − 1117	1RXS J004349.3-111612	00 : 43 : 44.4	−11 : 17 : 17	Asiago T122
J0103.7 + 1323	NVSS J010345+132346	01 : 03 : 45.8	+13 : 23 : 31	Asiago T122
J0134.5 + 2638	1RXS J013427.2+263846	01 : 34 : 31.2	+26 : 38 : 17	Asiago T122
J0156.3 + 3913	MG4 J015630+3913	01 : 56 : 22.3	+39 : 13 : 52	Asiago T122
J0204.2 + 2420	B2 0201+24	02 : 04 : 14.9	+24 : 20 : 38	Asiago T122
J0256.3 + 0335	PKS B0253+033	02 : 56 : 19.9	+03 : 35 : 46	Asiago T122
J0339.2 − 1738	PKS 0336-177	03 : 39 : 12.5	−17 : 38 : 42	6dFGRS
J0602.2 + 5314	GB6 J0601+5315	06 : 02 : 14.9	+53 : 14 : 06	Asiago T122
J0708.9 + 2239	GB6 J0708+2241	07 : 08 : 56.9	+22 : 39 : 58	Asiago T122
J0730.5 − 6606	PMN J0730-6602	07 : 30 : 35.0	−66 : 06 : 22	6dFGRS-DR2
J0904.3 + 4240	S4 0900+42	09 : 04 : 21.1	+42 : 40 : 55	SDSS-DR12
J1031.0 + 7440	S5 1027+74	10 : 31 : 02.9	+74 : 40 : 55	Asiago T182
J1256.3 − 1146	PMN J1256-1146	12 : 56 : 20.9	−11 : 46 : 52	6dFGRS-DR2
J1315.4 + 1130	1RXS J131531.9+113327	13 : 15 : 28.6	+11 : 30 : 54	Asiago T182
J1412.0 + 5249	SBS 1410+530	14 : 12 : 04.8	+52 : 49 : 01	SDSS-DR12
J1418.9 + 7731	1RXS J141901.8+773229	14 : 18 : 59.3	+77 : 31 : 01	Asiago T122
J1647.4 + 4950	SBS 1646+499	16 : 47 : 29.5	+49 : 50 : 13	Asiago T122
J1736.0 + 2033	NVSS J173605+203301	17 : 36 : 04.8	+20 : 33 : 43	Asiago T122
J2014.5 + 0648	NVSS J201431+064849	20 : 14 : 33.8	+06 : 48 : 36	Asiago T122

the same target. The targets for which we obtained spectral data are listed in Table 8.1.

8.3 Optical results

The spectra obtained with our optical campaign are illustrated in Appendix B. Although the various targets were probably observed at different levels of activity, most of the objects located at high redshift (with $z \geq 0.1$) turned out to belong to the typical BL Lac and FSRQ blazar families. In four cases we detect clear indications of emission lines, which are not expected in BL Lac objects. These are:

- 3FGL J0156.3+3913, a prototypical FSRQ with $z = 0.456$ and $L_{\rm BLL}$= 0.024

- 3FGL J0904.3+4240, a high redshift FSRQ with $z = 1.342$ and $L_{\rm BLL}$= 0.673
- 3FGL J1031.0+7440, a Seyfert 1 / FSRQ at $z = 0.122$ and $L_{\rm BLL}$= 0.783
- 3FGL J1647.4+4950, a Seyfert 1.9 with $z = 0.0475$ and $L_{\rm BLL}$= 0.550.

With the adopted thresholds of $L_{\rm BLL} \geq 0.566$ to predict a BL Lac classification and $L_{\rm BLL} \leq 0.230$ to give a FSRQ classification, ***these data are fully consistent with the expected 90% precision of the B-FlaP method***, because only 3FGL J0904.3+4240 and 3FGL J1031.0+7440 turn out to be misclassified (exactly 2 sources out of 20). We note, however, that the choice of more severe likelihood thresholds could easily give even more accurate results, at the obvious cost of classifying a smaller fraction of the BCU population. In Fig. 8.2 we show the spectra of the sources listed above.

8.3.1 Optical spectra and ECDF comparison for HSP classification

In order to further validation of the B-FlaP method we compared the optical spectra ECDF and plots of some of BCUs when their likelihood ANN showed significant values for BL Lac or FSRQ classification In Figure 8.3 we report the comparison results for the first four BCUs as listed in Tab 8.2.

Table 8.2: Optical spectra comparison with ECDF plots The table columns report, respectively, the 3FGL source name, the RA and Dec coordinates , the BL Lac and FSRQ ANN Likelihood for the source.

Id.	b (°)	l (°)	bll	fsrq	*HSP*
3FGL J0040.3 + 4049	-21.990	120.640	0.996	0.004	BLL Very High C.
3FGL J0043.7 − 1117	-74.040	116.110	0.993	0.007	BLL High C.
3FGL J0156.3 + 3913	-21.920	136.130	0.024	0.976	FSRQ no HSP
3FGL J0904.3 + 4240	41.860	156.920	0.673	0.327	FSRQ no HSP

With reference with the data in Tab. 8.2 we compared the optical spectra with the ECDF plots and the results are fully compatible The yellow line of the single source is plotted in the area where we really expect to see it, according with its classfication by the optical spectra. This to validate once more the *screening* power of the B-FlaP method to select blazar candidates just from the initial ECDF plots.

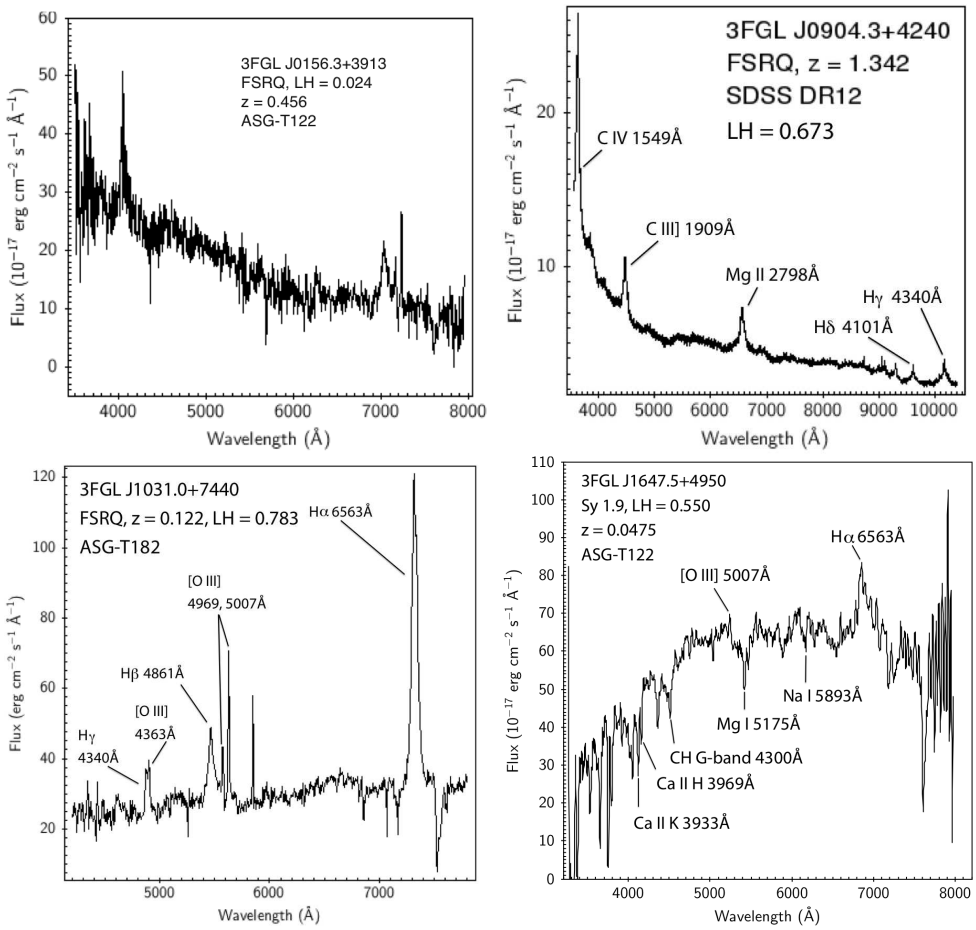

Figure 8.2

8.3.2 Notes on bright sources

In Fig.8.4 we show the spectra of some bright sources obtained by direct obeservations by Asiago telescopes or by Sloan Digital Sky Survey (SDSS). In Table 8.3 we report the Synchrotron self-Compton model (SSC) parameters. The associated SEDs are shown in Fig.8.5.

3FGL J0134.5+2638, observed with the Asiago 1.22m telescope, reveals a power law continuum spectrum with faint absorption lines. Absence of emission lines having equivalent width EW ≥ 5 Å leads to a BLL classification. Its SED shows the characteristic two-hump behavior of blazars and it is appreciably well interpolated by a SSC model.

3FGL J0339.2–1738 is associated with an elliptical galaxy, with spectrum available from 6dFGRS. Flux calibration of the spectrum was obtained deriving an average sensitivity curve for the 6dF instrument, based on the flux

calibrated spectra of IC 5135 and UGC 842. The resulting spectrum shows the characteristic continuum and absorption lines of an old stellar population, typical of ellipticals. The associated SED is a two-hump distribution with a prominent radiation excess in the optical window.

3FGL J0904.3+4240, detected by the SDSS, shows the highest redshift in this sample, which brings the strong UV emission lines of C IV λ1549, C III] λ1909 and Mg II λ2798 of quasar spectra into the optical domain. The SED is characteristic of blazars, but with a dominant IC component over the Synchrotron part.

3FGL J1031.0+7440 was observed in Asiago, with the 1.82m telescope. It shows the prominent emission lines of a Seyfert 1 galaxy, with a full width at half the maximum FWHM(Hβ)= $2286 \pm 350\,\mathrm{km\,s^{-1}}$. In a standard ΛCDM cosmology with $H_0 = 70\,\mathrm{km\,s^{-1}\,Mpc^{-1}}$, $\Omega_\Lambda = 0.7$ and $\Omega_M = 0.3$, its redshift corresponds to a distance of 569.8 Mpc. From an apparent magnitude $V = 17.2$ we infer an absolute magnitude $M_V = -21.6$, placing this object on the border between faint quasar and bright Seyfert 1 activity. The blazar SED is accompanied by a small radiation excess in the optical domain, suggesting that the jet power and the thermal contribution from the central engine are comparable in this object.

3FGL J1315.4+1130, also detected by the SDSS, is characterized by the BLL power law continuum and by faint absorption lines. Identification of the strongest features as a Ca II doublet is consistent with the presence of an absorption feature at the predicted wavelength of Mg I. Fewer data points are available to reconstruct the SED of this source and we do not appreciate any deviation from a two component blazar SED.

3FGL J1412.0+5249 is detected by the SDSS and it shows the characteristics of an elliptical galaxy. Its counterpart is actually a giant elliptical located in a galaxy cluster. The associated SED is the most complex of this sample, featuring a strong optical excess, emitted by the bright host galaxy, and a high energy IC component that is hardly reproduced by SSC models.

Table 8.3: SSC model parameters. The table columns report, respectively, the 3FGL source name, the electron energy distribution power-law index before break $\alpha_{el}^{(1)}$, the electron distribution index after break $\alpha_{el}^{(2)}$, the logarithm of the break energy (in units of $m_e c^2$), the magnetic field B (expressed in Gauss), the Doppler factor δ, the jet radius expressed in parsec, and the reduced residuals.

Id.	$\alpha_{el}^{(1)}$	$\alpha_{el}^{(2)}$	$\log E_{break}$	B	δ	R_{jet}	χ^2_{red} [a]
3FGL J0134.5 + 2638	1.5	4.7	4.0	1.00	10	0.001	1.180
3FGL J0339.2 − 1738	1.5	5.0	4.0	0.75	15	0.001	1.097
3FGL J0904.3 + 4240	2.3	3.6	3.5	0.05	30	0.003	1.455
3FGL J1031.0 + 7440	1.8	5.0	4.1	1.00	15	0.001	1.339
3FGL J1315.4 + 1130	1.6	4.8	4.8	0.60	20	0.002	1.732
3FGL J1412.0 + 5249	1.5	4.7	4.0	1.00	10	0.001	1.889

[a] Residuals of SSC models are computed without taking into account the thermal excess data points.

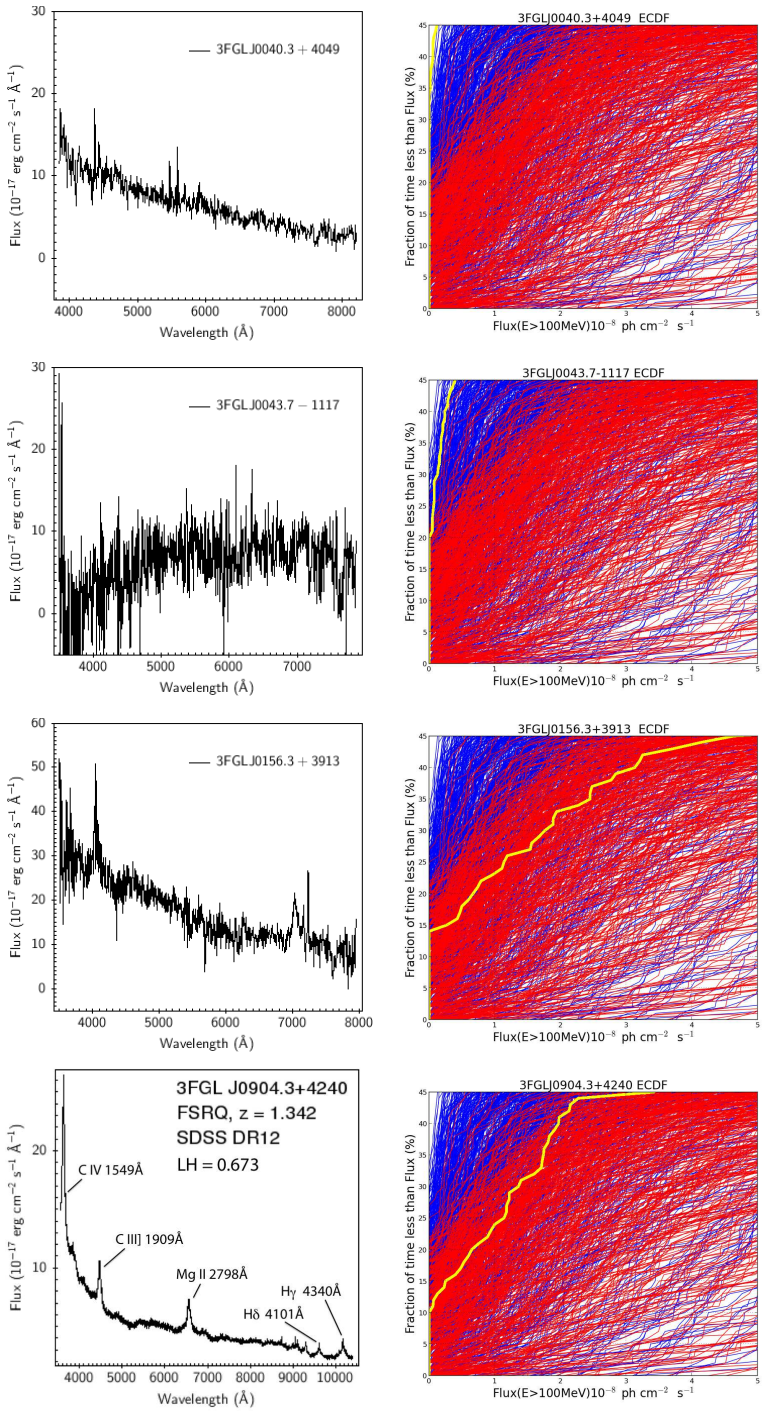

Figure 8.3: The yellow line on the left of the ECDF plot selects the class BL Lac or FSRQ of the source. 3FGLJ0040.3+4049 and 3FGLJ0043.7-1117 show a BL Lac plot . 3FGLJ0156.3+3913 and 3FGLJ0904.3+4240 an FSRQ one. This in agreement with the related optical spectra (on the right).

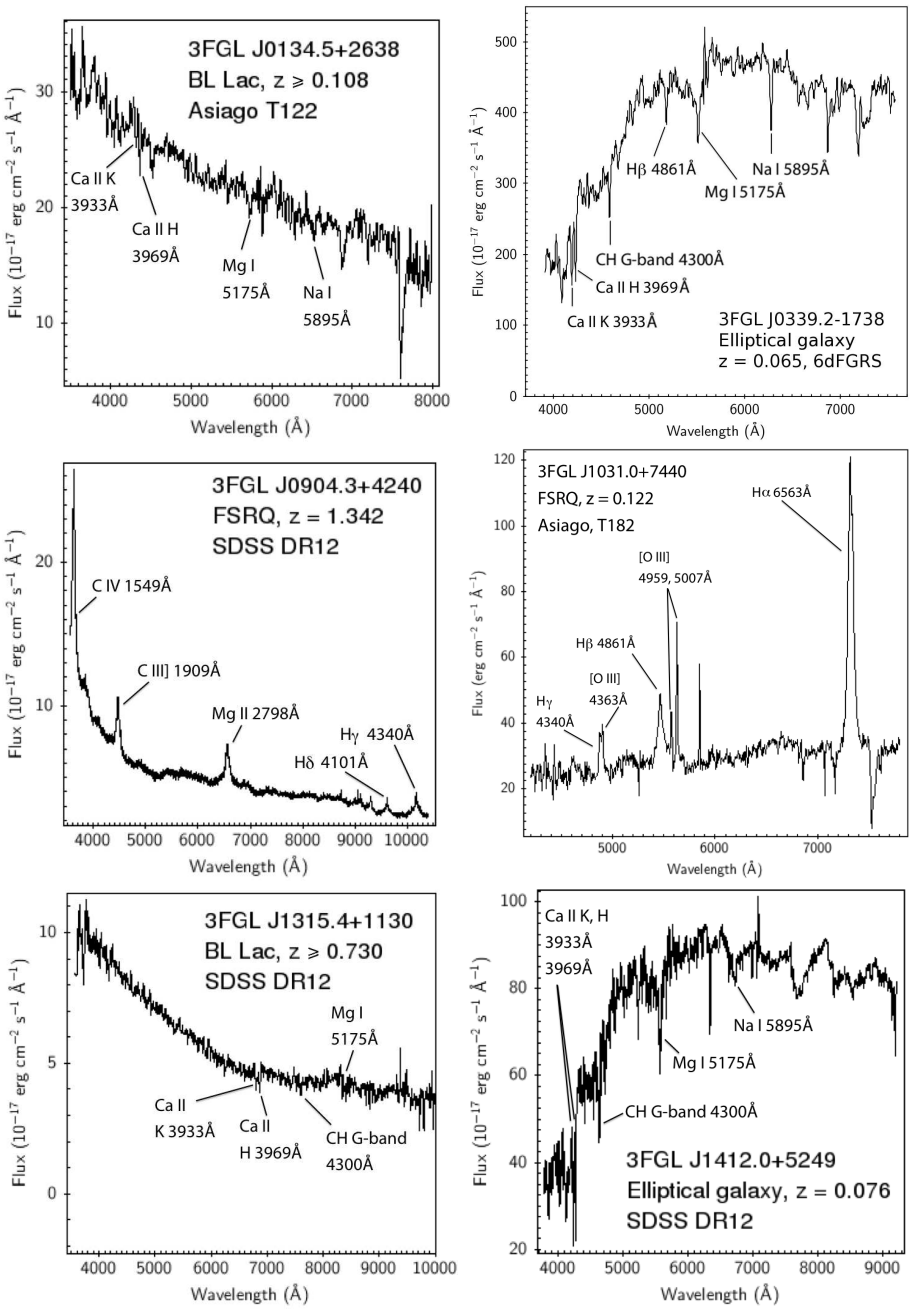

Figure 8.4: Optical spectra obtained from 6 BCUs in Tab. 8.3 . For each object we report the associated γ-ray source, the classification, the redshift, the origin of spectroscopic data and markers for the detected spectral features. Broad emission lines are detected where the central engine power is at least comparable to the jet power and they allow for firm redshift determinations. Absorption lines can both arise in the host galaxy , so that they only place lower limits to the actual source redshift.

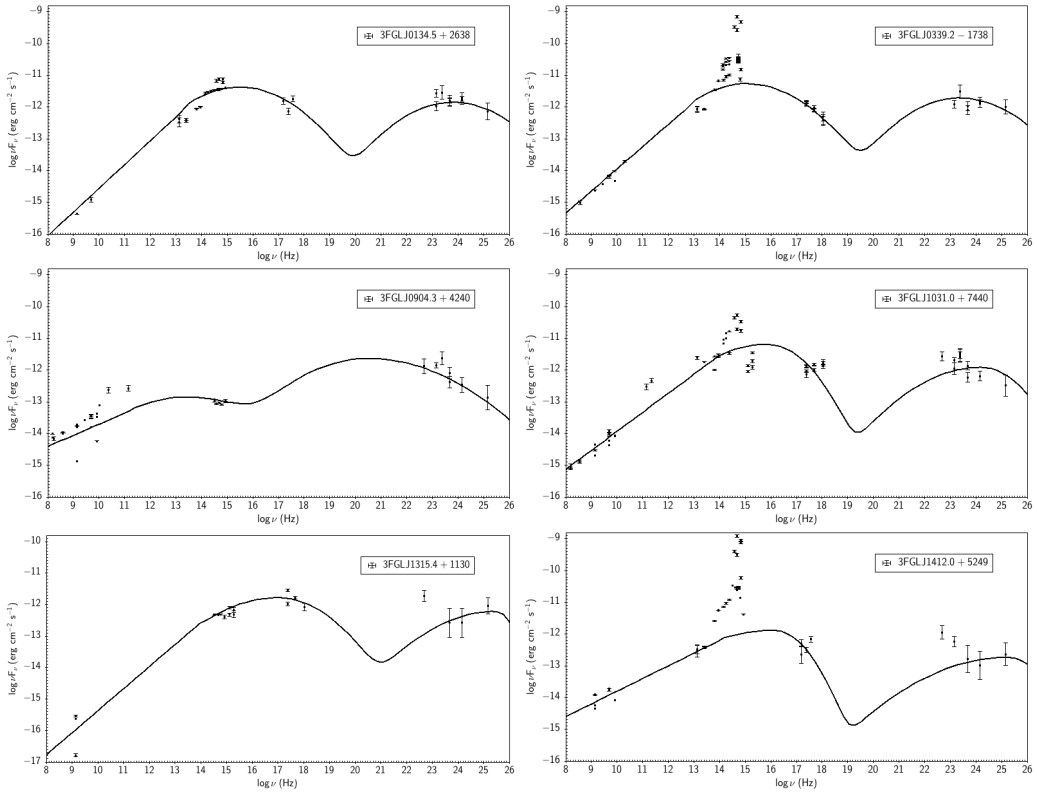

Figure 8.5: The spectral energy distributions of the sources presented in Table 8.3 . Every panel illustrates the multiple-frequency SED associated to the γ-ray source identified by the top label. The two-hump blazar SED is reproduced by means of SSC models, here represented with the continuous lines. It can be appreciated that thermal excesses above the SSC models are relevant in elliptical galaxies, faint in low luminosity FSRQ / Sey 1, while they are not detected elsewhere.

Chapter 9

Conclusion

9.1 In this study

In this study I developed **B-FlaP** a method based on ECDF and Artificial Neural Network as techniques intended to assess the likelihood that a γ-ray source can belong to the BL Lac or FSRQ family, or more interestingly to the HSP blazar subclass, using only γ-ray data.
I tested the method on sources that are classified as BL Lacs or FSRQs in 3FGL, and focusing my attention on the HSP blazars, I found, and here I confirm, that the method is very effective in the identification of blazars and offers an opportunity to suspect an HSP classification. By B-Flap I complete a full classification of the 3FGL BCUs classified according to their likelihood. The List in Appendix A describes the BCUs as BL Lacs or FSRQs and high expected HSP. Only 77 of 573 3FGL BCUs remained unclassified, but, thanks the List, a preliminary selection of high suspect candidates for Cherenkov ground telescope observations is possible. In order to validate the method I compared B-FlaP with the Variability Index and the Power Law Index. In both the comparisons B-FlaP showed a full consistency and It seems that, in some cases, the sensitivity of the B-FlaP is greater than what is obtainable by the two index.
To further assess the reliability of the method I performed direct optical observations for a sample of BCUs with Galactic latitude $|b| > 10^{o}$ and maximum γ-ray flux less than $6 \cdot 10^{-8}\,\mathrm{ph\,cm^{-2}\,s^{-1}}$. In those cases where I was able to perform spectroscopic observations, I found that the optical spectra were fully consistent with the expectations of the B-FlaP results. Even the results of benchmarking between the radio data and B -FlaP showed a consistency of assessment with the two approaches . As well as in the comparative analysis of the method with the Variability Index and the Power Law Index , even in the

radio flux comparison, B-FlaP was consistent with radio data and its ability to effectively discriminate the different classes of blazars is fully confirmed. I conclude that, although B-FlaP cannot replace confirmed and rigorous techniques for blazar classification, but it may be configured as an additional powerful approach for the preliminary and reliable identification of BCUs and HSP blazar subclass, when detailed observational data are not yet available.

9.2 Collaboration

I developed some specific parts of the analysis included in this thesis in collaboration with a team of colleagues in order to discuss and confirm methods and results. In detail :

- I fully and indendently developed the ECDF method as described in § 4.
- with David Salvetti, Istituto di Astrofisica Spaziale e Fisica Cosmica IASF/ INAF Milano I developed the B-FlaPann algorithm and analysis for the costruction of the BCU Classification List as described in § 5, § 6 and Appendix A
- with Marcello Giroletti , Instituto di Radioastronomia CNR Bologna I discuss the radio data as described in § 7
- with Giovanni La Mura , Dip Fisica ed Astronomia Univ Padova, I made all the optical observation and related spectra included in this thesis by the telescopes in Osservatorio Astronomico Asiago. The results are described in § 8 and Appendix D

This thesis is original and completely written by me.

Graziano Chiaro

12

Chapter 10

Follow On Results

This chapter contains the last follow on for this thesis. I want to show here several other potential analysis by B-Flap beyond the classification of blazar illustrated in this thesis. Because of this is a follow on, everything written here is very preliminary and the work is going on. Two are the analysis under my hunting attention :

- Misaligned agn (MAGN)
- Hidden Seyfert galaxies among $\mathrm{FSRQ_{ANN}}$

The *flame in the fireplace* that ignited my interest was a different way of reading Fig.5.4 and Fig.5.6 in Chapter 5 of this thesis which here I report as Fig. 10.1 and Fig. 10.10

10.1 MAGN hunting by B-FlaP

Fig.10.1 shows that the only contamination we have in $\mathrm{BLL_{ANN}}$analysis cames from radio galaxies (RDG). It creates *a suspect* that some RDG might be hidden in that Likelihood range. Follow on this suspect, and because it is well known the correlation, already explained in this thesis, between gamma and radio flux , I investigated 3LAC objects as in Fig. 10.2 , 10.3 where in X axis I considered Sr/γ flux ratio and in Y axis the Power Law Index.

Could it possible to hunt radio galaxies by B-FlaP data? Fig. 10.2 shows a significant separation from Blazars and RDG and using Fig.10.3, where BCUs are overlapped to the blazars. Observing the plot ,in range between 1.01E+09 and 1.73E+12 of Sr/γ-Flux which includes all the 3LAC radio galaxies , it seems to be possible to select in this range , today *looking by eye* only because

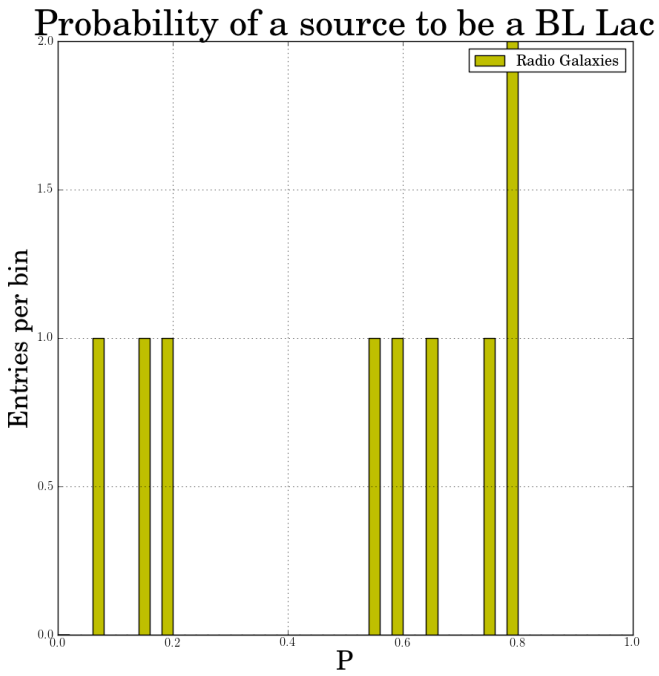

Figure 10.1: B-FlaP ANN likelihood for 3FGL Radio Galaxies

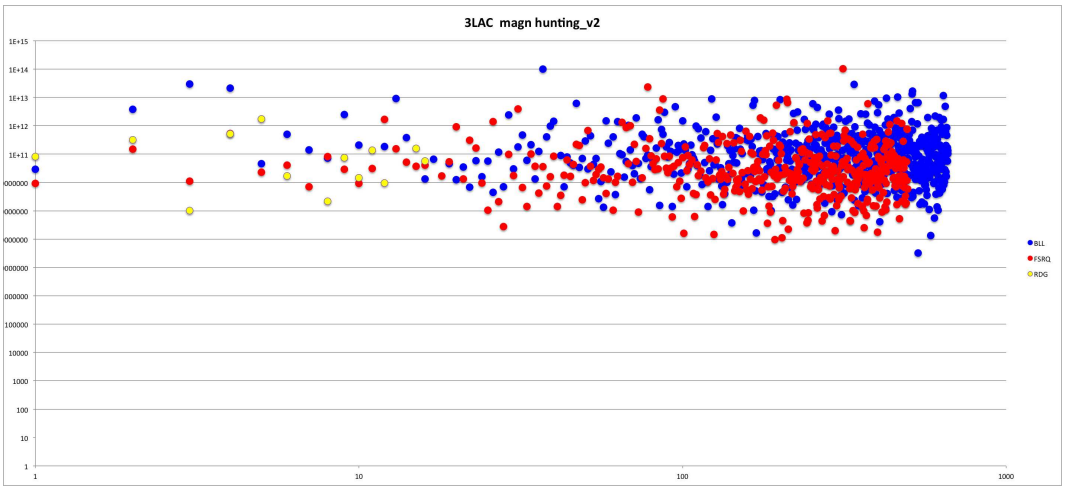

Figure 10.2: The plot shoes the distribution of BL Lacs (blue) , FSRQ(red) and radio galaxies (yellow) with the x and Y axies as discussed above

preliminary, a BCU_{ANN}group of objects classified as *uncertain* in B-FlaP where

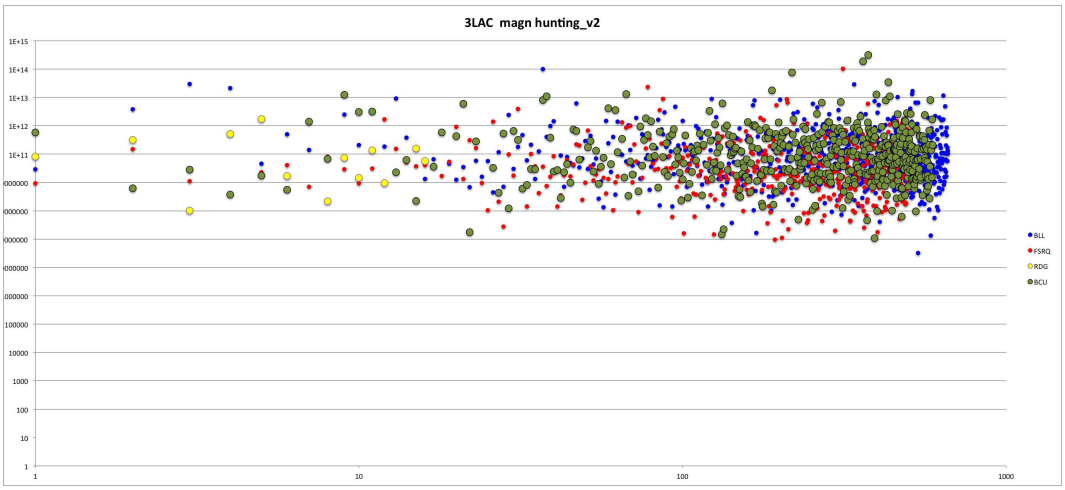

Figure 10.3: The plot shows the overlap of B-FlaP BCUs in plot Fig. 10.2

to hunt RDGs.

Concerning to the selection listed in Tab. 10.1 , because no optical spectra are available (bcu I in 3LAC) the NVSS image is an interesting first information about the class of objects. In NVSS analysis most of them, as expected, show a tipical BL Lac image. It is the classical big dot that BLL objects show in radio plots. By NVSS images I selected 5 five BCUs which NVSS show a significative broad design.

- 3FGL J0009.6 -3211 or IC 1531
- 3FGL J0039.0-2218 or PMN J0039-2220
- 3FGL J0059.1-5701 or PKS 0056-572
- 3FGL J0132.5-0802 or PKS 0130-083
- 3FGL J0153.4+7114 or TXS 0149+710

The first literature check shows that:

- PKS0056-572 is already known as an high redshift quasar [see https://arxiv.org/pdf/1501.02022] and in some other papers as a Seyfert2
- TXS 0149+710, although its broad radio spectrum, seems to be an eliptical galaxy Seyfert 2 [see optical spectrum in Fig....]
- PKS0130-083 remains a suspect because it's *double image* in VLBI

Table 10.1: The sample of 3LAC bcu I objects and uncertain in B-FlaP selected from Fig 10.3. The table columns report, respectively, the 3FGL source name, the associated counterpart, the radio flux (mJk) at 1.4 GHz, the γ-ray flux, the Power Law Index.

3FGL name	Counterpart	radio flux	γ flux	PowerLaw Ind
J0040.3 + 4049	B3 0037+405	48.152	1.553 E-10	1.132
J0003.8 − 1151	PKS 0001-121	352.478	2.489 E-9	2.023
J0009.6 − 3211	IC 1531	388.846	5.658 E-9	2.309
J0039.0 − 2218	PMN J0039-2220	117.152	9.288 E-10	1.715
J0040.5 − 2339	PMN J0040-2340	53.675	1.684 E-9	1.946
J0059.1 − 5701	PKS 0056-572	479.399	2.049 E-8	2.616
J0131.3 + 5548	TXS 0128+554	174.953	2.829 E-9	1.903
J132.5 − 0802	PKS 0130-083	307.577	1.355 E-9	1.752
J0134.5 + 2638	1RXS J013427.2+263846	30.572	8.339 E-9	1.991
J0147.0 − 5204	PKS 0144-522	329.299	5.579 E-9	2.199
J0152.2 + 3707	B2 0149+37	333.948	7.687 E-9	2.406
J0153.4 + 7114	TXS 0149+710	578.321	9.570 E-10	1.567

- PMN J0039-2220 seems to be a BL Lac with Swift data and suspected HSP subclass. For this object BLL_{ANN}= 0.990 and HSP likelihood = 0.9. For B-FlaP it really seems a BL Lac, but I'm not convinced of this classification.More data are necessary and I'll continue the investigation.

- IC 1531 is an already know and interesting radiogalaxy. [https://hea-www.harvard.edu/XJET/]. Its BCU classification in 3LAC is because of its Flag1 reserved for sources with TS $\geq$ 35 went to TS $\leq$ 25 when changing the diffuse model in Fermi analysis.

If IC 1531 confirm the B-FlaP *eye*, PKS0130-083 and PMNJ0039-2220 might be new radiogalaxies if their optical spectra will confirm this hypotesis. The follow on with optical spectra improved with the jet angle calculation will confirm or not my initial suspects for these two objetcs and if it will be possible to classify them as MAGN.

Figures 10.4, 10.5 and 10.6 show the avalilable NVSS of the sources where the broad image suggests a RDG. Fig 10.7 shows the double VLBI image for PKS0130-083 . FIg 10.8 shows the TXS 0149+710 optical spectrum and Fig 10.9 shows the objects posistion in the sky towards 3LAC radiogalaxies.

A second step might be the calculation of the angles of the object. Of course jet orientation and inclination angle are difficult quantities to observationally

establish. One of the methods is based on different observational quantities: the jet sidedness(J), the VLBI apparent velocity $\beta_a = \upsilon_a$c of the jet knots, and the core dominance. Because of the assumption of an intrinsic simmetry J can be expressed in terms of orientation(θ) as : $J = [(1+\beta\cos\theta)/(1-\beta\cos\theta)]^{(2+\alpha)}$ where α is the radio spectral index. With this method it will be possible to have a final plot $\beta - \theta$ where to estimate the permitted value of θ.

This study wil continue with the collaboration of some colleagues at NASA Goddard Space Flight Center MD USA, at NTG (Telescopio Nazionale Galileo) and NOT (Nordic Optical Telescope) observatories in Canary Islands, at SALT observatory in South Africa and the Radiostronomy Institute of Bologna Italy.

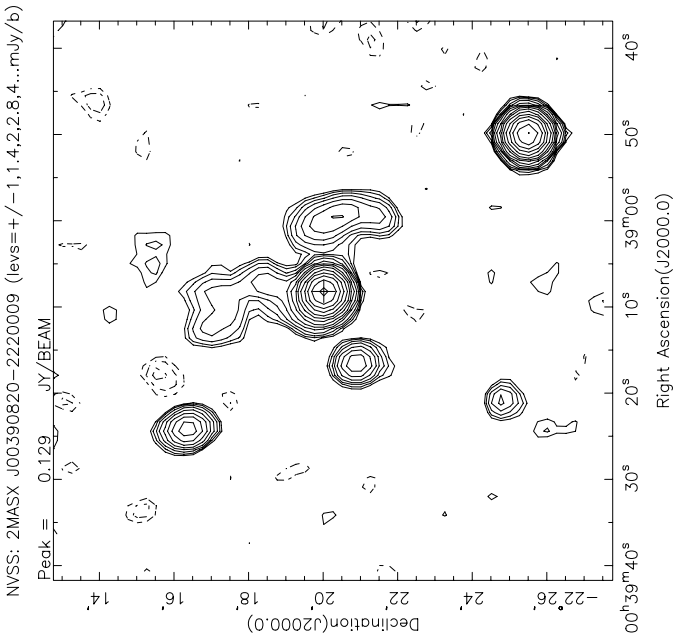

Figure 10.4: NVSS image for PMNJ0039

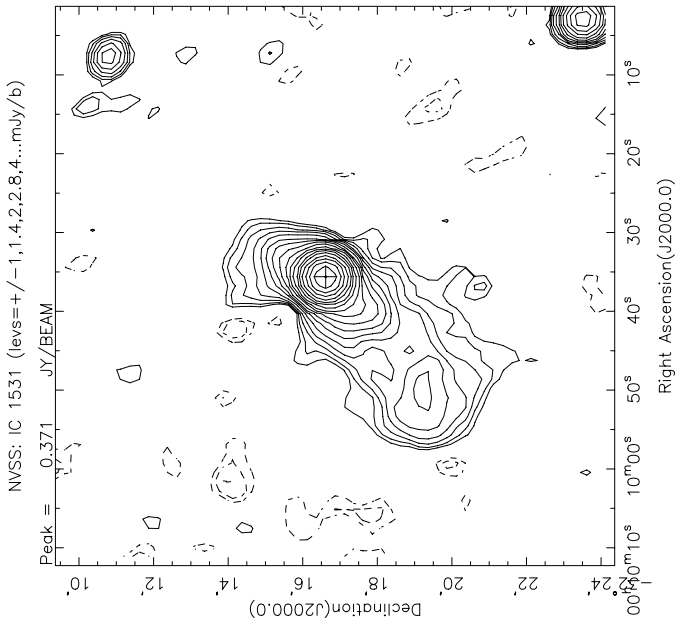

Figure 10.5: NVSS image for IC1531

10.2 Hidden Seyfert galaxies and B-FlaP

With reference to Fig.10.8, another study as improvement for this thesis might be to verify the B-FlaP ability to regognize hidden Seyfert galaxies into the contamined FSRQ area.Three are the main features that differentiate a quasar from a Seyfert galaxy:

- **The brightness**: the quasar is defined by an absolute magnitude Mv brighter than -22.1 (virtually the absolute magnitude of an entire galaxy like the Milky Way: if the nucleus is more brilliant, we call them quasars, if it is not, Seyfert galaxy.)

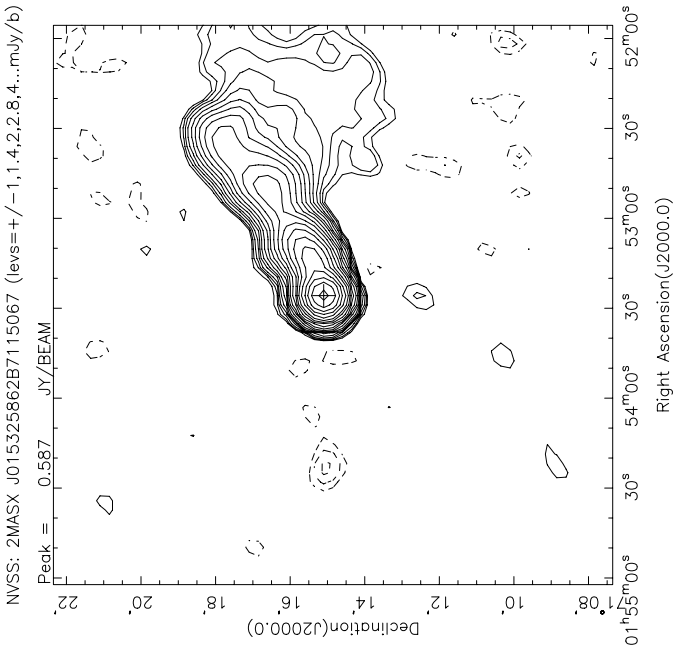

Figure 10.6: NVSS image for TXS0149

- **The width of the lines in optical spectrum** : quasars have larger lines than the Seyfert galaxies. Because of they are distant and bright objects they are also naturally fed from more massive black holes, whose gravitational fields induce motions with the higher orbital velocity of the gas and therefore the Doppler enlargements.

The optical observations demonstrate that between the two classes there is a certain continuity. This is not only because quasars are in turn placed in galaxies, but also because there are Seyfert galaxies at redshift comparable to quasars, but they are more difficult to observe because of their lower brightness.

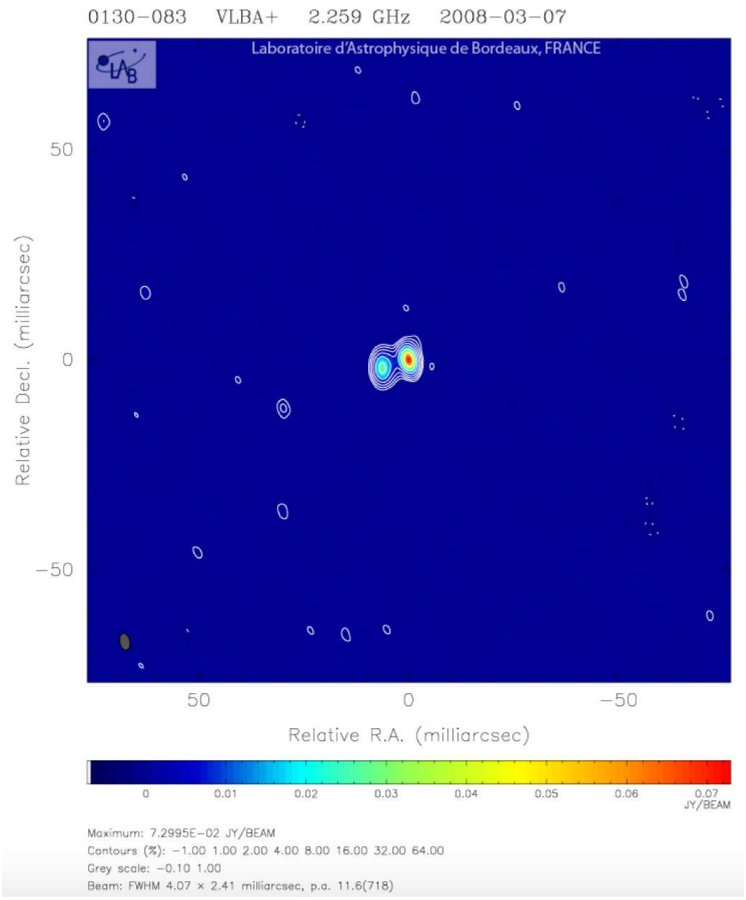

Figure 10.7: VLBI image for PKS0130 where is shown the double design of the object

The first attempt to use once more B-FlaP, as I made for radio galaxies, does not give a favorable outcome (see Fig 10.9) but I'm not surprised by this result because of, as discussed above,the similar nature of the two classes FSRQ and Seyfert galaxy.

Because of Sr/γ-Flux ratio shows no result, a further potential investigation, could be to consider the X-ray spectrum in Seyfert galaxy which is harder than in FSRQ. However I'm convinced that the final answer in Seyfert hunt remains an *Optical Spettroscopy affair*.

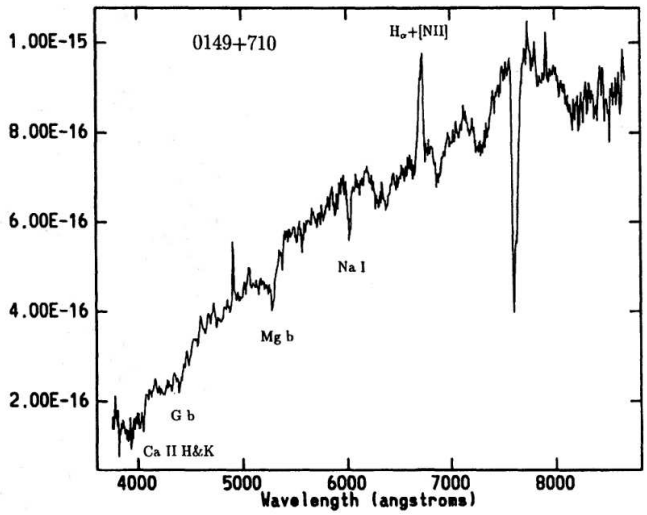

Figure 10.8: TXS 0149 optical spectrum as elliptical galaxy with a suspected faint Seyfert nucleus

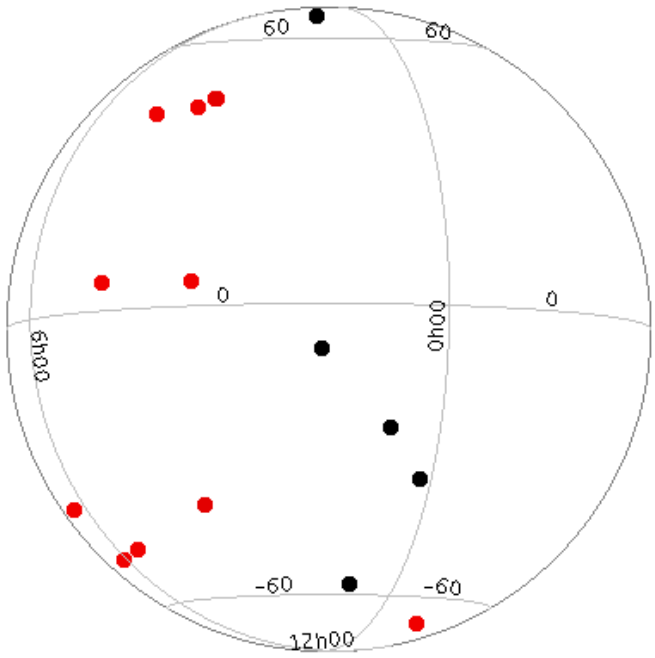

Figure 10.9: Sky postion of RDG (red) and suspected sources (black)

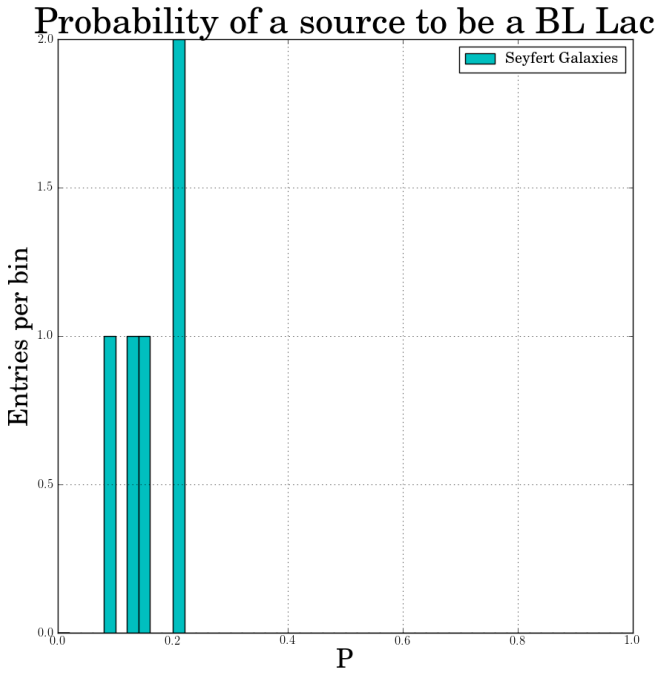

Figure 10.10: B-FlaP ANN likelihood for 3FGL Seyfert Galaxies

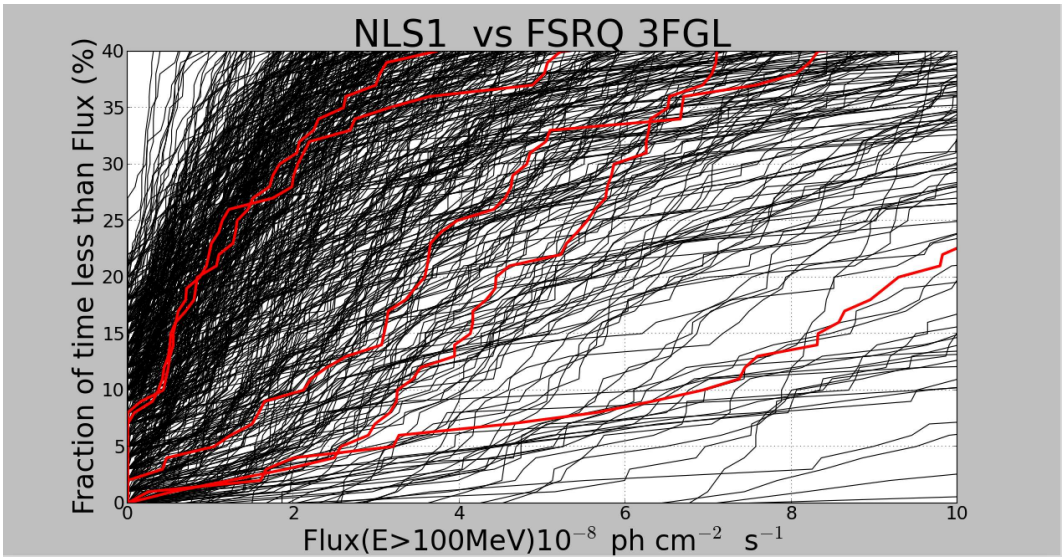

Figure 10.11: NLS1 vs FSRQ in ECDF plot.

13

Chapter 11

Appendix A

11.1 3FGL BCU Classification List

The List contains the classification of BCUs (Blazar of Unknown Type) listed in the 3FGL Fermi–LAT catalogue and relies on the artificial neural networks likelihood which used the Empirical Cumulative Distribution Function of the γ-ray flux as key parameter.
The second and the third columns show the galactic coordinates.
ANN likelihood (L) to be a BL Lac or an FSRQ is in unit $0 \leq L \leq 1$are in columns 4 and 5. The closer to 1 is the value of L , the greater the likelihood that the source is in that specific source class.
The column HSP Candidates lists only BCUs characterized by a large confidence level to be a HSP candidate, we splitted these objects in High Confidence HSP and Very High Confidence HSP in according to their likelihood to be an HSP-like source. Applying our algorithm optimized to select the most promising HSP among 573 3FGL BCU, we can single out 15 VHC HSP candidates ($L_{HSP} > 0.891$) and 38 HC ones ($L_{HSP} > 0.8$) for a total of 53 very interesting targets to be observed through Very High Energy telescopes. All the details of HSP classification are in section *ANN Results and validation* of this thesis

BCU are classified as a BL Lac candidates if $L_{\rm BLL}$is greater than 0.566, or FSRQ candidates if $L_{\rm FSRQ}$is greater than 0.770.

3FGL Name	b (°)	l (°)	$L_{\rm BLL}$	$L_{\rm FSRQ}$	Classification	HSP Candidates
J0002.2–4152	–72.040	334.320	0.877	0.123	BL Lac	
J0003.2–5246	–62.820	318.940	0.976	0.024	BL Lac	

3FGL Name	b (°)	l (°)	L_{BLL}	L_{FSRQ}	Classification	HSP Candidates
J0003.8–1151	–71.080	84.660	0.952	0.048	BL Lac	
J0009.6–3211	–79.570	0.880	0.859	0.141	BL Lac	
J0012.4+7040	8.140	119.620	0.022	0.978	FSRQ	
J0014.6+6119	–1.270	118.540	0.896	0.104	BL Lac	
J0015.7+5552	–6.660	117.890	0.835	0.165	BL Lac	
J0017.2–0643	–68.150	99.510	0.953	0.047	BL Lac	
J0019.1–5645	–59.890	311.690	0.650	0.350	BL Lac	
J0021.6–6835	–48.580	306.730	0.459	0.541	Uncertain	
J0028.6+7507	12.300	121.400	0.749	0.251	BL Lac	
J0028.8+1951	–42.540	115.610	0.602	0.398	BL Lac	
J0030.2–1646	–78.570	96.580	0.981	0.019	BL Lac	High C.
J0030.7–0209	–64.580	110.690	2.35e–04	1.000	FSRQ	
J0031.3+0724	–55.120	114.190	0.984	0.016	BL Lac	
J0039.0–2218	–84.460	92.050	0.990	0.010	BL Lac	High C.
J0039.1+4330	–19.310	120.560	0.976	0.024	BL Lac	
J0040.3+4049	–21.990	120.640	0.996	0.004	BL Lac	Very High C.
J0040.5–2339	–85.740	86.620	0.971	0.029	BL Lac	
J0043.5–0444	–67.510	117.800	0.984	0.016	BL Lac	High C.
J0043.7–1117	–74.040	116.110	0.993	0.007	BL Lac	High C.
J0045.2–3704	–79.950	310.070	0.029	0.971	FSRQ	
J0047.9+5447	–8.080	122.410	0.995	0.005	BL Lac	Very High C.
J0049.4–4149	–75.270	304.240	0.949	0.051	BL Lac	
J0049.4–5401	–63.090	303.460	0.938	0.062	BL Lac	
J0050.0–4458	–72.180	304.180	0.397	0.603	Uncertain	
J0051.2–6241	–54.430	302.960	0.989	0.011	BL Lac	
J0055.2–1213	–75.150	126.510	0.385	0.615	Uncertain	
J0059.1–5701	–60.120	300.920	0.554	0.446	Uncertain	
J0103.7+1323	–49.370	127.530	0.910	0.090	BL Lac	
J0107.0–1208	–74.610	137.580	0.915	0.085	BL Lac	
J0116.2–2744	–84.540	220.760	0.945	0.055	BL Lac	
J0121.7+5154	–10.670	127.640	0.908	0.092	BL Lac	
J0127.2+0325	–58.290	140.110	0.960	0.040	BL Lac	
J0131.3+5548	–6.690	128.540	0.939	0.061	BL Lac	
J0132.5–0802	–68.590	151.960	0.986	0.014	BL Lac	High C.
J0133.2–5159	–63.930	288.260	0.589	0.411	BL Lac	
J0133.3+4324	–18.810	130.830	0.676	0.324	BL Lac	
J0134.5+2638	–35.240	134.710	0.910	0.090	BL Lac	
J0135.0+6927	6.860	126.730	0.085	0.915	FSRQ	
J0137.8+5813	–4.090	129.020	0.910	0.090	BL Lac	
J0139.9+8735	24.810	123.470	0.975	0.025	BL Lac	

3FGL Name	b (°)	l (°)	$L_{\rm BLL}$	$L_{\rm FSRQ}$	Classification	HSP Candidates
J0145.6+8600	23.270	124.010	0.690	0.310	BL Lac	
J0146.4–6746	–48.530	295.200	0.843	0.157	BL Lac	
J0147.0–5204	–63.010	284.010	0.859	0.141	BL Lac	
J0148.3+5200	–9.860	131.750	0.973	0.027	BL Lac	
J0150.5–5447	–60.270	285.640	0.947	0.053	BL Lac	
J0151.0+0537	–54.170	148.840	0.687	0.313	BL Lac	
J0151.0–3609	–74.420	251.790	0.827	0.173	BL Lac	
J0152.2+3707	–24.040	136.130	0.400	0.600	Uncertain	
J0153.4+7114	8.980	127.920	0.992	0.008	BL Lac	Very High C.
J0156.3+3913	–21.920	136.450	0.024	0.976	FSRQ	
J0156.9–4742	–65.770	275.500	0.981	0.019	BL Lac	
J0200.9–6635	–49.060	292.490	0.530	0.470	Uncertain	
J0203.1–0227	–59.930	160.620	0.673	0.327	BL Lac	
J0204.2+2420	–35.650	143.470	0.983	0.017	BL Lac	High C.
J0205.0+1510	–44.050	147.920	0.099	0.901	FSRQ	
J0207.9–3846	–70.270	254.500	0.357	0.643	Uncertain	
J0210.7–5101	–61.780	276.100	0.028	0.972	FSRQ	
J0211.2–0649	–62.160	169.470	0.955	0.045	BL Lac	
J0211.7+5402	–6.990	134.520	0.118	0.882	FSRQ	
J0213.1–2720	–71.910	218.170	0.962	0.038	BL Lac	
J0214.7–5823	–55.590	283.800	0.651	0.349	BL Lac	
J0216.1–7016	–45.230	293.000	0.389	0.611	Uncertain	
J0216.6–1019	–63.800	176.990	0.263	0.737	Uncertain	
J0217.3+6209	0.960	132.730	0.818	0.182	BL Lac	
J0218.9+3642	–22.970	141.840	2.92e–04	1.000	FSRQ	
J0219.0+2440	–33.990	147.030	0.978	0.022	BL Lac	
J0223.3+6820	6.980	131.240	0.887	0.113	BL Lac	
J0223.5+6313	2.080	133.110	0.282	0.718	Uncertain	
J0224.1–7941	–36.550	297.910	0.710	0.290	BL Lac	
J0225.2–2602	–69.050	215.340	9.29e–05	1.000	FSRQ	
J0226.5–4442	–64.110	261.860	0.961	0.039	BL Lac	
J0228.0+2248	–34.910	150.220	0.286	0.714	Uncertain	
J0228.5+6703	6.030	132.260	0.008	0.992	FSRQ	
J0228.7–3106	–68.550	229.210	0.941	0.059	BL Lac	
J0232.9+2606	–31.380	149.700	0.916	0.084	BL Lac	
J0241.3+6542	5.220	133.910	0.880	0.120	BL Lac	
J0244.4–8224	–33.610	298.410	0.037	0.963	FSRQ	
J0249.1+8438	22.400	125.810	0.898	0.102	BL Lac	
J0250.6+5630	–2.640	138.890	0.881	0.119	BL Lac	
J0253.5+3216	–23.860	150.930	0.582	0.418	BL Lac	

3FGL Name	b (°)	l (°)	L_{BLL}	L_{FSRQ}	Classification	HSP Candidates
J0255.8+0532	–45.590	170.190	0.806	0.194	BL Lac	
J0256.3+0335	–46.980	172.300	0.954	0.046	BL Lac	
J0301.4–1652	–58.320	200.860	0.781	0.219	BL Lac	
J0301.8–2721	–61.090	221.220	0.980	0.020	BL Lac	
J0301.8–7157	–41.770	290.010	0.083	0.917	FSRQ	
J0302.0+5335	–4.490	141.740	0.004	0.996	FSRQ	
J0303.0+3150	–23.220	153.060	0.802	0.198	BL Lac	
J0304.9+6817	8.580	134.720	0.322	0.678	Uncertain	
J0305.2–1607	–57.150	200.350	0.989	0.011	BL Lac	High C.
J0310.4–5015	–54.880	263.610	0.978	0.022	BL Lac	
J0318.7+2134	–29.660	162.830	0.730	0.270	BL Lac	
J0326.0–1842	–53.610	207.940	0.907	0.093	BL Lac	
J0331.3–6155	–46.340	276.960	0.917	0.083	BL Lac	
J0332.0+6308	5.690	139.940	0.066	0.934	FSRQ	
J0333.4+4003	–12.900	153.620	0.737	0.263	BL Lac	
J0333.4+7853	18.450	130.550	0.878	0.122	BL Lac	
J0338.5+1303	–32.950	173.570	0.960	0.040	BL Lac	
J0339.2–1738	–50.250	208.070	0.957	0.043	BL Lac	
J0342.6–3006	–52.530	227.920	0.986	0.014	BL Lac	High C.
J0343.3+3622	–14.690	157.530	0.583	0.417	BL Lac	
J0343.3–6443	–43.670	279.190	0.649	0.351	BL Lac	
J0352.9+5655	2.350	145.840	0.962	0.038	BL Lac	
J0354.1+4643	–5.380	152.490	0.110	0.890	FSRQ	
J0356.3–6948	–39.750	283.920	0.409	0.591	Uncertain	
J0357.1+2325	–22.470	169.020	0.424	0.576	Uncertain	
J0358.7+0633	–33.670	183.340	0.002	0.998	FSRQ	
J0409.4+3158	–14.360	164.640	0.351	0.649	Uncertain	
J0418.0–0251	–35.060	195.980	0.014	0.986	FSRQ	
J0425.2+6319	9.780	144.400	0.858	0.142	BL Lac	
J0426.3+6827	13.360	140.690	0.283	0.717	Uncertain	
J0426.6+0459	–29.100	189.750	0.015	0.985	FSRQ	
J0427.3–3900	–43.930	242.180	0.227	0.773	FSRQ	
J0429.8+2843	–13.480	170.240	0.589	0.411	BL Lac	
J0430.5+1655	–21.040	179.740	0.216	0.784	FSRQ	
J0431.6+7403	17.360	136.580	0.962	0.038	BL Lac	
J0433.1+3228	–10.450	167.860	0.915	0.085	BL Lac	
J0433.7–6028	–40.160	270.840	4.05e–04	1.000	FSRQ	
J0434.0–5726	–40.930	266.940	0.952	0.048	BL Lac	
J0434.4–2341	–39.930	222.140	0.671	0.329	BL Lac	
J0434.6+0921	–24.770	186.920	0.754	0.246	BL Lac	

3FGL Name	b (°)	l (°)	$L_{\rm BLL}$	$L_{\rm FSRQ}$	Classification	HSP Candidates
J0439.6–3159	–40.730	233.100	0.988	0.012	BL Lac	High C.
J0439.9–1859	–37.280	216.950	0.950	0.050	BL Lac	
J0440.3+1444	–20.550	183.250	0.279	0.721	Uncertain	
J0444.5+3425	–7.360	167.960	0.178	0.822	FSRQ	
J0453.2+6321	12.160	146.450	0.582	0.418	BL Lac	
J0456.3+2702	–10.050	175.370	0.060	0.940	FSRQ	
J0501.8+3046	–6.820	173.080	0.404	0.596	Uncertain	
J0502.7+3438	–4.380	170.140	2.07e–04	1.000	FSRQ	
J0503.4+4522	2.300	161.810	0.055	0.945	FSRQ	
J0505.5–1558	–30.430	216.240	0.907	0.093	BL Lac	
J0506.9–5435	–36.780	262.410	0.991	0.009	BL Lac	High C.
J0508.2–1936	–31.180	220.430	0.733	0.267	BL Lac	
J0509.7–6418	–35.200	274.270	0.949	0.051	BL Lac	
J0512.2+2918	–5.710	175.600	6.07e–04	0.999	FSRQ	
J0512.9+4038	0.910	166.500	0.252	0.748	Uncertain	
J0515.5–0123	–21.870	202.800	0.987	0.013	BL Lac	High C.
J0519.3+2746	–5.470	177.880	0.072	0.928	FSRQ	
J0519.5+0852	–15.950	193.930	0.428	0.572	Uncertain	
J0521.7+0103	–19.350	201.290	0.978	0.022	BL Lac	
J0521.9–3847	–33.390	243.350	0.079	0.921	FSRQ	
J0522.9–3628	–32.720	240.600	0.381	0.619	Uncertain	
J0525.6–6013	–33.880	269.100	0.984	0.016	BL Lac	
J0525.8–2014	–27.610	222.690	0.888	0.112	BL Lac	
J0526.0+4253	4.090	166.000	0.071	0.929	FSRQ	
J0526.6+6321	15.170	148.640	0.257	0.743	Uncertain	
J0528.3+1815	–8.990	186.960	0.990	0.010	BL Lac	High C.
J0529.1+0933	–13.470	194.570	0.189	0.811	FSRQ	
J0529.8–7242	–31.860	283.850	0.141	0.859	FSRQ	
J0532.0–4827	–32.820	255.020	5.37e–05	1.000	FSRQ	
J0533.0–3939	–31.420	244.790	0.242	0.758	Uncertain	
J0535.6–2749	–27.900	231.770	0.459	0.541	Uncertain	
J0538.4–3909	–30.320	244.400	0.896	0.104	BL Lac	
J0542.2–8737	–27.730	300.390	0.926	0.074	BL Lac	
J0542.5–0907	–19.380	213.540	0.008	0.992	FSRQ	
J0553.5–2036	–21.630	225.730	0.904	0.096	BL Lac	
J0602.2+5314	14.560	160.060	0.902	0.098	BL Lac	
J0602.8–4016	–25.970	246.920	0.905	0.095	BL Lac	
J0603.8+2155	0.030	188.060	0.009	0.991	FSRQ	
J0604.7–4849	–27.540	256.300	0.725	0.275	BL Lac	
J0606.4–4729	–26.950	254.900	0.824	0.176	BL Lac	

3FGL Name	b (°)	l (°)	L_{BLL}	L_{FSRQ}	Classification	HSP Candidates
J0611.2+4323	11.540	169.820	0.865	0.135	BL Lac	
J0611.7+2759	4.540	183.610	0.030	0.970	FSRQ	
J0618.2–2429	–17.770	231.840	0.883	0.117	BL Lac	
J0618.9–1138	–12.420	219.830	0.228	0.772	FSRQ	
J0620.4+2644	5.660	185.730	0.987	0.013	BL Lac	High C.
J0622.9+3326	9.140	179.930	2.19e–07	1.000	FSRQ	
J0623.3+3043	8.010	182.390	0.928	0.072	BL Lac	
J0626.6–4259	–22.410	251.030	0.984	0.016	BL Lac	
J0627.9–1517	–12.050	224.140	0.006	0.994	FSRQ	
J0630.3+6906	23.270	145.770	0.914	0.086	BL Lac	
J0631.2+2019	4.830	192.510	4.85e–04	1.000	FSRQ	
J0640.0–1252	–8.320	223.210	0.989	0.011	BL Lac	High C.
J0641.8–0319	–3.660	214.820	5.75e–07	1.000	FSRQ	
J0643.4–5358	–22.790	263.320	0.208	0.792	FSRQ	
J0644.3–6713	–25.530	277.530	0.065	0.935	FSRQ	
J0644.6–2853	–14.060	238.440	0.834	0.166	BL Lac	
J0646.4–5452	–22.580	264.370	0.993	0.007	BL Lac	High C.
J0647.0–5134	–21.580	261.020	0.921	0.079	BL Lac	
J0647.1–4415	–19.360	253.630	0.788	0.212	BL Lac	
J0647.6–6058	–23.950	270.860	0.271	0.729	Uncertain	
J0648.1+1606	6.580	198.160	0.985	0.015	BL Lac	High C.
J0649.6–3138	–14.220	241.520	0.978	0.022	BL Lac	
J0650.4–1636	–7.720	227.700	0.003	0.997	FSRQ	
J0650.5+2055	9.190	194.040	0.989	0.011	BL Lac	High C.
J0651.3+4014	17.060	175.930	0.824	0.176	BL Lac	
J0652.0–4808	–19.770	257.780	0.945	0.055	BL Lac	
J0653.6+2817	12.930	187.570	0.815	0.185	BL Lac	
J0654.5+0926	4.940	204.860	0.042	0.958	FSRQ	
J0658.3–5832	–22.020	268.550	0.697	0.303	BL Lac	
J0658.6+0636	4.630	207.850	0.157	0.843	FSRQ	
J0700.0+1709	9.570	198.470	0.205	0.795	FSRQ	
J0700.2+1304	7.840	202.210	0.977	0.023	BL Lac	
J0700.3–6310	–23.090	273.610	0.927	0.073	BL Lac	
J0703.4–3914	–14.660	249.840	0.402	0.598	Uncertain	
J0706.1–4849	–17.820	259.250	0.334	0.666	Uncertain	
J0708.9+2239	13.800	194.240	0.818	0.182	BL Lac	
J0712.2–6436	–22.060	275.370	0.432	0.568	Uncertain	
J0720.0–4010	–12.180	252.080	0.704	0.296	BL Lac	
J0723.2–0728	3.510	223.240	0.970	0.030	BL Lac	
J0723.7+2050	16.220	197.410	0.545	0.455	Uncertain	

3FGL Name	b (°)	l (°)	$L_{\rm BLL}$	$L_{\rm FSRQ}$	Classification	HSP Candidates
J0725.8–0054	7.220	217.690	0.803	0.197	BL Lac	
J0728.0+4828	25.780	169.580	0.872	0.128	BL Lac	
J0729.5–3127	–6.520	245.120	0.002	0.998	FSRQ	
J0730.5–0537	6.060	222.400	0.709	0.291	BL Lac	
J0730.5–6606	–20.790	277.590	0.981	0.019	BL Lac	
J0732.2–4638	–12.850	259.110	0.181	0.819	FSRQ	
J0733.5+5153	27.350	165.990	0.989	0.011	BL Lac	High C.
J0734.3–7709	–24.060	289.130	0.159	0.841	FSRQ	
J0742.4–8133	–24.970	293.800	0.995	0.005	BL Lac	Very High C.
J0744.1–3804	–7.050	252.330	0.004	0.996	FSRQ	
J0744.8–4028	–8.100	254.590	0.642	0.358	BL Lac	
J0746.6–0706	8.800	225.700	0.195	0.805	FSRQ	
J0746.6–4756	–11.310	261.340	0.339	0.661	Uncertain	
J0746.9+8511	28.180	128.210	0.990	0.010	BL Lac	High C.
J0747.2–3311	–4.000	248.420	0.055	0.945	FSRQ	
J0748.0–1639	4.450	234.220	0.024	0.976	FSRQ	
J0748.5+7910	29.380	134.980	0.618	0.382	BL Lac	
J0748.8+4929	29.300	169.110	0.776	0.224	BL Lac	
J0749.4+1059	17.780	209.490	0.478	0.522	Uncertain	
J0756.3–6433	–17.730	277.220	0.708	0.292	BL Lac	
J0803.3–0339	14.170	224.590	0.745	0.255	BL Lac	
J0804.0–3629	–2.760	253.040	0.802	0.198	BL Lac	
J0804.4+0418	18.090	217.390	0.243	0.757	Uncertain	
J0805.0–0622	13.170	227.330	0.928	0.072	BL Lac	
J0807.1+7744	30.420	136.380	0.392	0.608	Uncertain	
J0813.3+6509	32.920	150.930	0.819	0.181	BL Lac	
J0816.7–2421	6.110	244.320	0.050	0.950	FSRQ	
J0825.4–0213	19.720	226.050	0.854	0.146	BL Lac	
J0825.8–3217	3.290	252.050	2.41e–04	1.000	FSRQ	
J0827.2–0711	17.530	230.890	0.904	0.096	BL Lac	
J0828.8–2420	8.400	245.840	0.900	0.100	BL Lac	
J0829.6–1137	15.650	235.250	0.955	0.045	BL Lac	
J0830.3–5855	–11.540	274.300	0.137	0.863	FSRQ	
J0836.3+2143	32.240	203.320	0.238	0.762	Uncertain	
J0841.3–3554	3.730	256.870	0.844	0.156	BL Lac	
J0842.0–6055	–11.360	276.890	0.284	0.716	Uncertain	
J0845.1–5458	–7.500	272.310	0.704	0.296	BL Lac	
J0849.5–2912	9.200	252.590	0.822	0.178	BL Lac	
J0849.9–3540	5.210	257.750	1.78e–04	1.000	FSRQ	
J0852.6–5756	–8.510	275.310	0.026	0.974	FSRQ	

3FGL Name	b (°)	l (°)	L_{BLL}	L_{FSRQ}	Classification	HSP Candidates
J0853.0–3654	4.920	259.190	0.709	0.291	BL Lac	
J0855.2–0718	23.340	234.990	0.282	0.718	Uncertain	
J0858.1–1951	16.530	246.290	0.004	0.996	FSRQ	
J0858.1–3130	9.190	255.610	0.982	0.018	BL Lac	High C.
J0904.3+4240	41.860	178.680	0.673	0.327	BL Lac	
J0904.8–3516	7.820	259.380	0.085	0.915	FSRQ	
J0904.8–5734	–7.050	276.110	0.398	0.602	Uncertain	
J0912.6–2757	13.950	254.880	0.063	0.937	FSRQ	
J0915.0+5844	41.480	156.920	0.862	0.138	BL Lac	
J0917.3–0344	29.870	235.160	0.979	0.021	BL Lac	
J0921.0–2258	18.640	252.370	0.994	0.006	BL Lac	Very High C.
J0922.8–3959	7.180	265.350	0.007	0.993	FSRQ	
J0923.1+3853	45.420	184.000	0.060	0.940	FSRQ	
J0928.7+7300	36.980	139.400	0.728	0.272	BL Lac	
J0928.9–3530	11.220	263.000	0.383	0.617	Uncertain	
J0939.2–1732	25.480	251.170	0.155	0.845	FSRQ	
J0939.9–2831	17.900	259.720	0.008	0.992	FSRQ	
J0940.7–6102	–6.310	281.880	0.196	0.804	FSRQ	
J0947.1–2542	21.020	258.870	0.943	0.057	BL Lac	
J0953.1–7657	–17.540	293.370	0.955	0.045	BL Lac	
J0956.7–6441	–7.890	285.520	0.077	0.923	FSRQ	
J0958.4–6752	–10.290	287.710	0.667	0.333	BL Lac	
J0958.6–2447	23.430	260.190	0.463	0.537	Uncertain	
J1003.6+2608	52.660	204.710	0.794	0.206	BL Lac	
J1005.0–4959	4.360	277.920	0.034	0.966	FSRQ	
J1007.8+0026	42.650	240.230	0.937	0.063	BL Lac	
J1008.9–2910	21.500	265.240	0.269	0.731	Uncertain	
J1009.0–3137	19.600	266.870	0.443	0.557	Uncertain	
J1014.2+4115	54.950	178.980	0.836	0.164	BL Lac	
J1015.2–4512	9.410	276.090	0.403	0.597	Uncertain	
J1016.0–0635	39.570	249.170	0.351	0.649	Uncertain	
J1016.1+5555	50.000	156.210	0.583	0.417	BL Lac	
J1021.8+8023	34.580	129.990	0.972	0.028	BL Lac	
J1022.3–4234	12.320	275.740	0.417	0.583	Uncertain	
J1024.8+0105	46.120	243.360	0.516	0.484	Uncertain	
J1026.5+7423	39.200	134.640	0.350	0.650	Uncertain	
J1028.0+1829	55.920	219.830	0.856	0.144	BL Lac	
J1030.4–2030	31.420	263.690	0.957	0.043	BL Lac	
J1031.0+7440	39.210	134.200	0.783	0.217	BL Lac	
J1035.2+5545	52.440	153.970	0.172	0.828	FSRQ	

3FGL Name	b (°)	l (°)	$L_{\rm BLL}$	$L_{\rm FSRQ}$	Classification	HSP Candidates
J1038.9–5311	4.650	283.720	3.03e–04	1.000	FSRQ	
J1040.4+0615	52.570	240.770	0.432	0.568	Uncertain	
J1040.8+1342	56.750	230.160	0.989	0.011	BL Lac	High C.
J1040.9–1205	39.650	259.780	0.871	0.129	BL Lac	
J1042.0–0557	44.450	254.730	0.951	0.049	BL Lac	
J1042.1–4126	15.130	278.400	0.955	0.045	BL Lac	
J1047.8–6216	–2.800	289.080	0.252	0.748	Uncertain	
J1049.8+1425	59.000	230.790	0.086	0.914	FSRQ	
J1051.5–6517	–5.300	290.810	0.097	0.903	FSRQ	
J1052.8–3741	19.440	278.430	0.946	0.054	BL Lac	
J1106.4–3643	21.470	280.540	0.620	0.380	BL Lac	
J1109.4–4815	11.210	285.920	0.225	0.775	FSRQ	
J1123.2–6415	–3.040	293.550	0.017	0.983	FSRQ	
J1125.0–2101	37.510	277.290	0.983	0.017	BL Lac	
J1126.7–3834	21.460	285.240	0.665	0.335	BL Lac	
J1129.4–4215	18.130	287.220	0.062	0.938	FSRQ	
J1131.9–0503	52.500	268.920	0.109	0.891	FSRQ	
J1136.1–7411	–12.150	297.790	0.570	0.430	BL Lac	
J1136.6–6826	–6.600	296.070	0.203	0.797	FSRQ	
J1138.2+4905	63.950	151.000	0.179	0.821	FSRQ	
J1141.2+6805	47.720	132.550	0.993	0.007	BL Lac	Very High C.
J1141.6–1406	45.400	278.480	0.893	0.107	BL Lac	
J1153.7–2555	35.160	286.940	0.932	0.068	BL Lac	
J1154.0–3243	28.620	289.200	0.953	0.047	BL Lac	
J1155.4–3417	27.160	289.920	0.995	0.005	BL Lac	Very High C.
J1156.7–2250	38.300	286.750	0.959	0.041	BL Lac	
J1158.9+0818	67.460	267.010	0.981	0.019	BL Lac	High C.
J1159.3–2226	38.810	287.380	0.006	0.994	FSRQ	
J1159.6–0723	53.250	281.070	0.836	0.164	BL Lac	
J1200.8+1228	71.150	261.300	0.922	0.078	BL Lac	
J1200.9+2010	76.500	241.400	0.496	0.504	Uncertain	
J1203.5–3925	22.490	292.890	0.989	0.011	BL Lac	High C.
J1207.6–2232	39.200	289.840	0.210	0.790	FSRQ	
J1207.6–4537	16.680	294.950	0.913	0.087	BL Lac	
J1208.2–7810	–15.490	300.640	0.768	0.232	BL Lac	
J1218.5+6912	47.790	127.000	0.449	0.551	Uncertain	
J1218.8–4827	14.080	297.400	0.472	0.528	Uncertain	
J1223.3–3028	31.940	295.870	0.976	0.024	BL Lac	
J1224.6–8312	–20.400	302.090	0.010	0.990	FSRQ	
J1225.7–7314	–10.460	301.030	0.345	0.655	Uncertain	

3FGL Name	b (°)	l (°)	L_{BLL}	L_{FSRQ}	Classification	HSP Candidates
J1229.8–5305	9.670	299.610	0.353	0.647	Uncertain	
J1233.9–5736	5.190	300.600	0.763	0.237	BL Lac	
J1238.2–1958	42.770	298.750	0.617	0.383	BL Lac	
J1238.3–4543	17.110	300.490	0.480	0.520	Uncertain	
J1239.4+0727	70.160	294.110	0.787	0.213	BL Lac	
J1243.9–0217	60.500	299.090	0.768	0.232	BL Lac	
J1244.3–4955	12.940	301.760	0.794	0.206	BL Lac	
J1251.0–0203	60.830	302.860	0.095	0.905	FSRQ	
J1254.1–2203	40.790	303.830	0.686	0.314	BL Lac	
J1256.1–5919	3.530	303.520	0.159	0.841	FSRQ	
J1256.3–1146	51.070	304.810	0.905	0.095	BL Lac	
J1256.7+5328	63.530	121.190	0.135	0.865	FSRQ	
J1258.7+5137	65.380	120.330	0.937	0.063	BL Lac	
J1259.0–2310	39.650	305.230	0.758	0.242	BL Lac	
J1259.8–3749	25.020	304.760	0.673	0.327	BL Lac	
J1302.6+5748	59.250	119.950	0.923	0.077	BL Lac	
J1304.2–2411	38.570	306.670	0.832	0.168	BL Lac	
J1304.3–5535	7.150	304.690	0.128	0.872	FSRQ	
J1304.9–2109	41.640	307.160	0.834	0.166	BL Lac	
J1306.8–2146	40.920	307.610	0.856	0.144	BL Lac	
J1307.6–4300	19.770	306.070	0.953	0.047	BL Lac	
J1308.1–6707	–4.310	304.570	0.050	0.950	FSRQ	
J1310.6+2446	85.090	5.690	0.923	0.077	BL Lac	
J1312.7–2349	38.760	309.200	0.972	0.028	BL Lac	
J1314.7–4237	20.040	307.550	0.806	0.194	BL Lac	
J1315.1–5329	9.130	306.480	0.081	0.919	FSRQ	
J1315.4+1130	73.430	324.070	0.946	0.054	BL Lac	
J1318.7–1232	49.730	313.260	0.189	0.811	FSRQ	
J1319.6+7759	39.050	121.060	0.987	0.013	BL Lac	High C.
J1322.3+0839	70.190	325.880	0.250	0.750	Uncertain	
J1322.6–1619	45.920	313.750	0.549	0.451	Uncertain	
J1323.0+2942	82.600	55.060	0.919	0.081	BL Lac	
J1328.5–4728	14.930	309.430	0.963	0.037	BL Lac	
J1328.9–5607	6.350	308.180	0.004	0.996	FSRQ	
J1330.1–7002	–7.440	306.250	1.84e–04	1.000	FSRQ	
J1330.9+5201	64.020	109.070	0.790	0.210	BL Lac	
J1331.1–1328	48.290	317.600	0.004	0.996	FSRQ	
J1338.6–2403	37.570	316.670	0.189	0.811	FSRQ	
J1340.6–0408	56.510	325.610	0.881	0.119	BL Lac	
J1342.7+0945	68.870	340.230	0.987	0.013	BL Lac	

3FGL Name	b (°)	l (°)	$L_{\rm BLL}$	$L_{\rm FSRQ}$	Classification	HSP Candidates
J1344.5–3655	24.730	314.550	0.825	0.175	BL Lac	
J1345.9–3357	27.580	315.610	0.169	0.831	FSRQ	
J1346.9–2958	31.350	317.050	0.976	0.024	BL Lac	
J1351.7–2913	31.840	318.440	0.139	0.861	FSRQ	
J1356.3–4029	20.730	316.080	0.899	0.101	BL Lac	
J1400.7–5605	5.490	312.530	0.004	0.996	FSRQ	
J1406.0–2508	34.710	323.580	0.956	0.044	BL Lac	
J1407.7–4256	17.670	317.430	0.875	0.125	BL Lac	
J1412.0+5249	60.270	98.170	0.616	0.384	BL Lac	
J1416.0+1325	65.910	2.200	0.107	0.893	FSRQ	
J1418.5+3543	69.600	63.190	8.36e–06	1.000	FSRQ	
J1418.9+7731	38.560	117.020	0.977	0.023	BL Lac	
J1419.1–5156	8.620	316.460	0.018	0.982	FSRQ	
J1419.5–0836	48.360	336.780	0.011	0.989	FSRQ	
J1421.0–1122	45.840	335.360	0.729	0.271	BL Lac	
J1424.6–6807	–6.830	311.480	0.028	0.972	FSRQ	
J1427.8–3215	26.330	325.590	0.951	0.049	BL Lac	
J1434.6+6640	47.380	108.170	0.995	0.005	BL Lac	Very High C.
J1440.0–3955	18.350	324.530	0.970	0.030	BL Lac	
J1446.8–1831	36.490	337.600	0.987	0.013	BL Lac	High C.
J1503.7–6426	–5.140	316.620	0.016	0.984	FSRQ	
J1504.5–8242	–20.990	307.230	0.276	0.724	Uncertain	
J1507.6–3710	18.230	330.900	0.874	0.126	BL Lac	
J1508.7–4956	7.170	324.400	0.005	0.995	FSRQ	
J1509.9–2951	24.050	335.640	0.080	0.920	FSRQ	
J1511.8–0513	43.120	354.590	0.658	0.342	BL Lac	
J1512.2–2255	29.490	340.510	0.948	0.052	BL Lac	
J1512.3+8005	35.170	115.970	0.639	0.361	BL Lac	
J1514.8–3623	18.170	332.690	0.294	0.706	Uncertain	
J1518.0–2732	24.980	338.670	0.416	0.584	Uncertain	
J1525.2–5905	–1.860	321.540	2.51e–04	1.000	FSRQ	
J1532.7–1319	33.720	352.140	2.23e–10	1.000	FSRQ	
J1536.6+8331	31.980	117.840	0.839	0.161	BL Lac	
J1537.8–8000	–19.460	309.970	0.287	0.713	Uncertain	
J1539.8–1128	33.830	355.150	0.687	0.313	BL Lac	
J1543.5+0451	43.380	12.260	0.910	0.090	BL Lac	
J1547.1–2801	20.560	343.780	0.982	0.018	BL Lac	High C.
J1549.0+6309	43.850	96.840	0.795	0.205	BL Lac	
J1549.5+1709	47.800	28.790	0.966	0.034	BL Lac	
J1549.7–0658	34.980	1.230	0.884	0.116	BL Lac	

3FGL Name	b (°)	l (°)	L_{BLL}	L_{FSRQ}	Classification	HSP Candidates
J1550.3+7409	37.730	108.930	0.328	0.672	Uncertain	
J1557.4–7040	–13.170	317.210	0.719	0.281	BL Lac	
J1559.7+8512	30.350	118.810	0.837	0.163	BL Lac	
J1559.8–2525	20.540	347.940	0.947	0.053	BL Lac	
J1600.3–5810	–3.940	325.740	0.886	0.114	BL Lac	
J1604.4–4442	5.760	335.150	0.138	0.862	FSRQ	
J1607.9–2040	22.580	352.950	0.858	0.142	BL Lac	
J1612.4–3100	14.670	345.850	0.986	0.014	BL Lac	High C.
J1617.3–2519	17.610	350.670	0.009	0.991	FSRQ	
J1626.4–7640	–18.810	314.280	0.855	0.145	BL Lac	
J1628.2+7703	34.080	110.300	0.643	0.357	BL Lac	
J1630.8+1047	35.990	26.590	0.260	0.740	Uncertain	
J1636.7+2624	40.130	45.790	0.949	0.051	BL Lac	
J1637.6–3449	8.150	346.750	0.972	0.028	BL Lac	
J1640.9+1142	34.220	28.790	0.875	0.125	BL Lac	
J1643.6–0642	24.480	10.660	0.752	0.248	BL Lac	
J1645.2–5747	–7.960	330.170	0.007	0.993	FSRQ	
J1647.1–6438	–12.480	325.030	0.730	0.270	BL Lac	
J1647.4+4950	40.070	76.640	0.550	0.450	Uncertain	
J1648.5–4829	–2.300	337.760	0.003	0.997	FSRQ	
J1650.2–5044	–3.970	336.130	0.021	0.979	FSRQ	
J1656.0+2044	34.330	40.530	0.030	0.970	FSRQ	
J1656.8–2010	14.050	1.060	0.844	0.156	BL Lac	
J1659.7–3132	6.700	352.270	0.289	0.711	Uncertain	
J1704.0+7646	32.400	108.930	0.089	0.911	FSRQ	
J1711.5–5029	–6.490	338.440	7.79e–04	0.999	FSRQ	
J1711.6+8846	27.630	121.620	0.993	0.007	BL Lac	Very High C.
J1714.1–2029	10.610	3.210	0.994	0.006	BL Lac	Very High C.
J1716.7–8112	–23.370	311.660	0.887	0.113	BL Lac	
J1718.1–3056	3.890	355.050	0.079	0.921	FSRQ	
J1719.3+1206	25.850	33.730	0.919	0.081	BL Lac	
J1723.5–5609	–11.220	334.630	0.003	0.997	FSRQ	
J1723.7–7713	–21.810	315.690	0.030	0.970	FSRQ	
J1735.4–1118	11.230	13.900	0.088	0.912	FSRQ	
J1736.0+2033	25.410	44.070	0.981	0.019	BL Lac	
J1739.0+8716	27.950	120.020	0.029	0.971	FSRQ	
J1740.4+5347	31.850	81.410	0.964	0.036	BL Lac	
J1741.9–2539	2.430	2.380	0.033	0.967	FSRQ	
J1744.9–1725	6.080	9.760	0.311	0.689	Uncertain	
J1747.1+0139	15.110	26.960	0.208	0.792	FSRQ	

3FGL Name	b (°)	l (°)	$L_{\rm BLL}$	$L_{\rm FSRQ}$	Classification	HSP Candidates
J1753.5–5010	–12.050	342.210	9.44e–07	1.000	FSRQ	
J1757.1+1533	18.940	41.170	0.865	0.135	BL Lac	
J1757.4+6536	30.070	95.270	0.846	0.154	BL Lac	
J1759.1–4822	–11.930	344.340	4.36e–04	1.000	FSRQ	
J1807.8+6427	28.980	94.030	0.928	0.072	BL Lac	
J1816.9–4944	–15.170	344.390	0.970	0.030	BL Lac	
J1819.1+2134	16.490	49.100	0.535	0.465	Uncertain	
J1819.1+4259	23.660	70.630	0.471	0.529	Uncertain	
J1820.3+3625	21.550	63.890	0.986	0.014	BL Lac	
J1822.1–7051	–23.310	323.600	0.592	0.408	BL Lac	
J1823.6–3453	–9.950	358.670	0.956	0.044	BL Lac	
J1824.4+4310	22.860	71.110	0.992	0.008	BL Lac	High C.
J1825.2–5230	–17.470	342.260	0.032	0.968	FSRQ	
J1828.9–2417	–6.210	8.760	0.499	0.501	Uncertain	
J1830.0–4439	–15.170	350.100	0.002	0.998	FSRQ	
J1831.0–2714	–7.950	6.330	0.304	0.696	Uncertain	
J1835.4+1349	9.700	43.560	0.036	0.964	FSRQ	
J1838.5–6006	–21.670	335.400	0.964	0.036	BL Lac	
J1841.2+2910	14.850	58.430	0.989	0.011	BL Lac	High C.
J1842.3–5841	–21.820	336.930	0.981	0.019	BL Lac	
J1844.3+1547	8.630	46.300	0.867	0.133	BL Lac	
J1848.1–4230	–17.380	353.490	0.909	0.091	BL Lac	
J1849.3–1645	–7.120	17.670	0.984	0.016	BL Lac	
J1855.1–6008	–23.720	335.850	0.987	0.013	BL Lac	High C.
J1858.4–2509	–12.610	10.880	0.058	0.942	FSRQ	
J1904.5+3627	13.360	67.290	0.897	0.103	BL Lac	
J1908.8–0130	–4.490	33.600	0.990	0.010	BL Lac	High C.
J1910.8+2855	8.890	60.970	0.993	0.007	BL Lac	Very High C.
J1911.4–1908	–12.890	17.810	0.955	0.045	BL Lac	
J1912.0–0804	–8.250	28.040	0.002	0.998	FSRQ	
J1912.6–1223	–10.230	24.160	0.016	0.984	FSRQ	
J1913.5–3631	–19.860	1.210	0.017	0.983	FSRQ	
J1913.9+4441	14.950	75.800	0.987	0.013	BL Lac	
J1918.0+3750	11.430	69.820	0.868	0.132	BL Lac	
J1924.9+2817	5.820	61.780	0.928	0.072	BL Lac	
J1925.7+1228	–1.780	47.900	0.001	0.999	FSRQ	
J1933.4+0727	–5.820	44.370	0.975	0.025	BL Lac	
J1935.5+8355	25.760	116.330	0.821	0.179	BL Lac	
J1939.6–4925	–27.880	348.940	0.989	0.011	BL Lac	High C.
J1941.2–6210	–29.550	334.500	0.091	0.909	FSRQ	

3FGL Name	b (°)	l (°)	L_{BLL}	L_{FSRQ}	Classification	HSP Candidates
J1941.8+7218	22.090	104.310	0.045	0.955	FSRQ	
J1942.7+1033	–6.370	48.250	0.955	0.045	BL Lac	
J1944.1–4523	–27.890	353.590	0.993	0.007	BL Lac	Very High C.
J1949.0+1312	–6.350	51.350	0.198	0.802	FSRQ	
J1949.4–6140	–30.490	335.190	0.482	0.518	Uncertain	
J1954.9–5640	–31.000	340.980	0.974	0.026	BL Lac	
J1955.0–1605	–21.130	25.150	0.932	0.068	BL Lac	
J1955.9+0212	–13.220	42.460	0.906	0.094	BL Lac	
J1959.8–4725	–30.850	351.800	0.992	0.008	BL Lac	High C.
J2000.1+4212	6.440	77.520	0.061	0.939	FSRQ	
J2002.7+6303	16.430	96.190	0.939	0.061	BL Lac	
J2007.7–7728	–30.510	316.660	0.010	0.990	FSRQ	
J2014.5+0648	–15.030	48.920	0.897	0.103	BL Lac	
J2014.9+1623	–10.150	57.350	0.036	0.964	FSRQ	
J2017.6–4110	–33.100	359.530	0.863	0.137	BL Lac	
J2018.5+3851	1.660	76.580	0.004	0.996	FSRQ	
J2023.2+3154	–3.100	71.400	0.033	0.967	FSRQ	
J2024.4–0848	–24.660	35.560	0.965	0.035	BL Lac	
J2025.2+3340	–2.370	73.120	0.016	0.984	FSRQ	
J2026.3+7644	21.200	109.920	0.983	0.017	BL Lac	
J2031.0+1937	–11.530	62.210	0.966	0.034	BL Lac	
J2033.6+6309	13.490	98.150	0.977	0.023	BL Lac	
J2036.6–3325	–35.530	9.620	0.996	0.004	BL Lac	Very High C.
J2040.0–5734	–37.060	339.630	0.731	0.269	BL Lac	
J2040.2–7115	–34.230	323.160	0.984	0.016	BL Lac	
J2041.9–7318	–33.740	320.730	0.785	0.215	BL Lac	
J2046.7–1011	–30.240	36.870	0.991	0.009	BL Lac	High C.
J2049.0–6801	–35.830	326.610	0.919	0.081	BL Lac	
J2049.7+1002	–20.680	56.690	0.488	0.512	Uncertain	
J2051.8–5535	–39.000	341.910	0.065	0.935	FSRQ	
J2056.7+4938	2.760	89.320	0.910	0.090	BL Lac	
J2103.9–3546	–41.380	7.840	0.051	0.949	FSRQ	
J2103.9–6233	–38.940	332.720	0.887	0.113	BL Lac	
J2104.2–0211	–30.330	47.380	0.993	0.007	BL Lac	Very High C.
J2106.1+2505	–14.830	71.770	0.044	0.956	FSRQ	
J2107.7–4822	–42.230	350.790	0.427	0.573	Uncertain	
J2108.0+3654	–7.220	81.110	0.946	0.054	BL Lac	
J2108.6–8619	–29.190	306.400	0.990	0.010	BL Lac	High C.
J2109.1–6638	–38.170	327.550	0.942	0.058	BL Lac	
J2110.3+3540	–8.360	80.280	0.023	0.977	FSRQ	

3FGL Name	b (°)	l (°)	$L_{\rm BLL}$	$L_{\rm FSRQ}$	Classification	HSP Candidates
J2112.7+0819	–26.310	58.680	0.957	0.043	BL Lac	
J2114.7+3130	–11.900	78.000	0.514	0.486	Uncertain	
J2118.0–3241	–43.880	12.440	0.556	0.444	Uncertain	
J2119.2–3313	–44.160	11.710	0.105	0.895	FSRQ	
J2126.5–3926	–46.050	3.250	0.859	0.141	BL Lac	
J2132.4–5420	–44.850	341.840	0.036	0.964	FSRQ	
J2133.3+2533	–18.970	76.340	0.904	0.096	BL Lac	
J2133.8+6648	10.990	105.170	0.497	0.503	Uncertain	
J2141.6–6412	–42.280	328.600	0.001	0.999	FSRQ	
J2142.2–2546	–47.910	23.500	0.713	0.287	BL Lac	
J2144.2+3132	–16.290	82.610	0.227	0.773	FSRQ	
J2149.6+1915	–26.010	74.540	0.001	0.999	FSRQ	
J2156.0+1818	–27.780	74.910	0.945	0.055	BL Lac	
J2159.2–2841	–52.120	20.230	0.928	0.072	BL Lac	
J2200.9–2412	–51.590	27.400	0.600	0.400	BL Lac	
J2212.3–7039	–41.040	319.280	0.875	0.125	BL Lac	
J2212.6+2801	–23.000	85.140	0.972	0.028	BL Lac	
J2213.6–4755	–53.020	348.040	0.983	0.017	BL Lac	
J2220.3+2812	–23.860	86.800	0.978	0.022	BL Lac	
J2230.5–7817	–36.470	311.320	0.130	0.870	FSRQ	
J2232.9–2021	–57.680	37.410	0.937	0.063	BL Lac	
J2233.5–1235	–54.680	50.500	0.534	0.466	Uncertain	
J2234.1–2655	–59.530	25.270	0.831	0.169	BL Lac	
J2235.6–2319	–59.290	32.770	0.003	0.997	FSRQ	
J2236.2–5049	–55.090	340.750	0.735	0.265	BL Lac	
J2243.2–3933	–60.730	359.590	0.951	0.049	BL Lac	
J2246.2+1547	–37.440	83.840	0.326	0.674	Uncertain	
J2246.7–5205	–55.840	337.420	0.994	0.006	BL Lac	Very High C.
J2250.3–4206	–61.170	353.770	0.929	0.071	BL Lac	
J2250.7–2806	–63.320	23.750	0.032	0.968	FSRQ	
J2251.5–4928	–57.940	340.630	0.951	0.049	BL Lac	
J2258.1–8248	–33.430	307.030	0.773	0.227	BL Lac	
J2305.3–4219	–63.600	350.940	0.967	0.033	BL Lac	
J2309.6–3633	–66.530	2.950	0.957	0.043	BL Lac	
J2312.9–6923	–45.410	314.880	0.989	0.011	BL Lac	High C.
J2316.8–5209	–59.360	331.730	0.988	0.012	BL Lac	High C.
J2317.3–4534	–63.780	342.070	0.771	0.229	BL Lac	
J2318.6+1912	–38.440	94.500	0.199	0.801	FSRQ	
J2321.2–6439	–49.860	317.620	0.857	0.143	BL Lac	
J2322.9–4917	–62.070	334.570	0.968	0.032	BL Lac	

3FGL Name	b (°)	l (°)	L_{BLL}	L_{FSRQ}	Classification	HSP Candidates
J2328.4–4034	–68.220	349.480	0.003	0.997	FSRQ	
J2336.5+2356	–35.860	101.750	0.906	0.094	BL Lac	
J2336.5–7620	–39.950	308.610	0.848	0.152	BL Lac	
J2338.7–7401	–42.130	309.500	0.952	0.048	BL Lac	
J2344.4+0549	–53.260	94.060	0.937	0.063	BL Lac	
J2346.7+0705	–52.370	95.980	0.958	0.042	BL Lac	
J2347.9+5436	–7.130	113.730	0.984	0.016	BL Lac	High C.
J2348.4–5100	–63.310	325.080	0.623	0.377	BL Lac	
J2353.3–4805	–66.160	327.480	0.978	0.022	BL Lac	
J2353.7–3911	–72.940	344.050	0.867	0.133	BL Lac	
J2358.3–2853	–78.150	21.290	0.746	0.254	BL Lac	

14

Chapter 12

Appendix B

12.1 Optical spectra

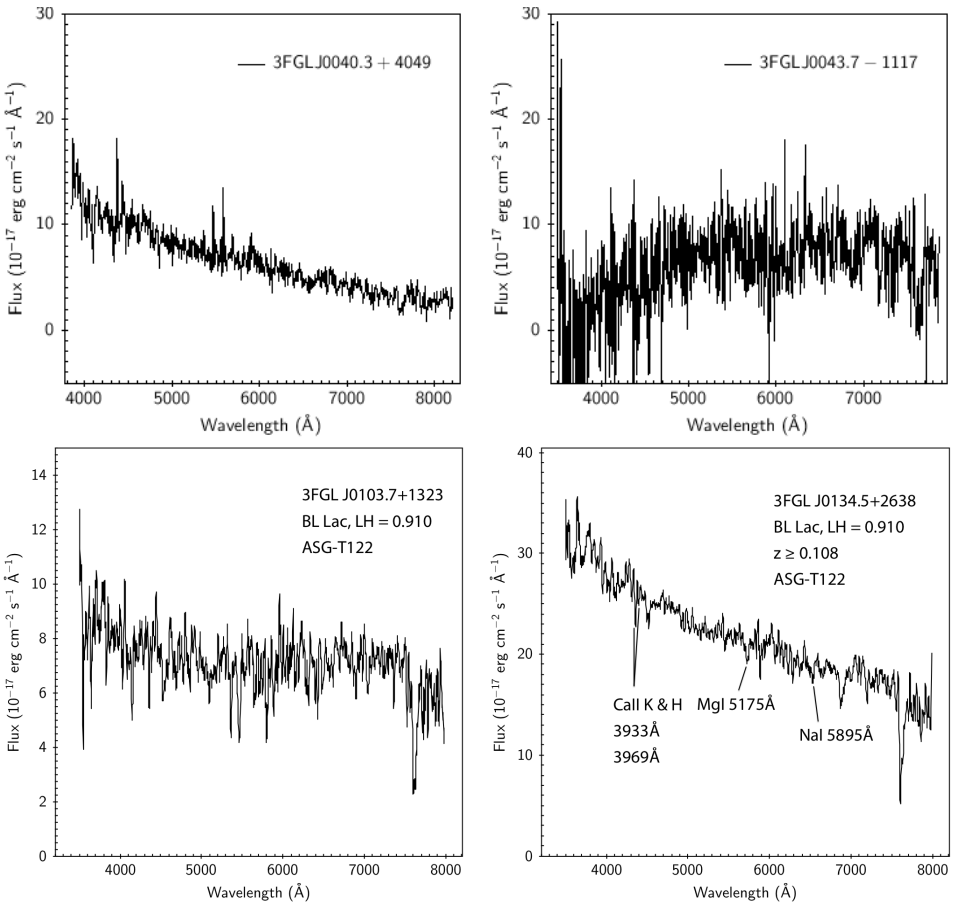

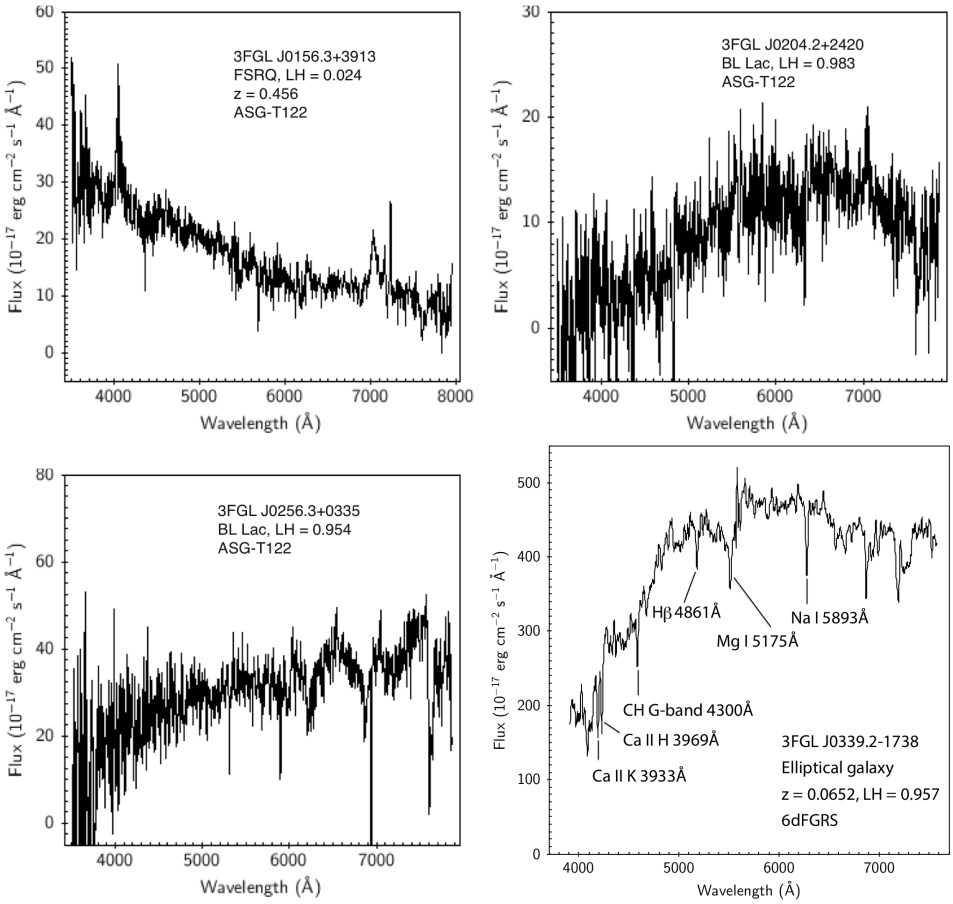
3FGL J0156.3+3913
FSRQ, LH = 0.024
z = 0.456
ASG-T122
3FGL J0204.2+2420
BL Lac, LH = 0.983
ASG-T122
3FGL J0256.3+0335
BL Lac, LH = 0.954
ASG-T122
Hβ 4861Å
Na I 5893Å
Mg I 5175Å
CH G-band 4300Å
Ca II H 3969Å
Ca II K 3933Å
3FGL J0339.2-1738
Elliptical galaxy
z = 0.0652, LH = 0.957
6dFGRS
Wavelength (Å)
Flux (10⁻¹⁷ erg cm⁻² s⁻¹ Å⁻¹)

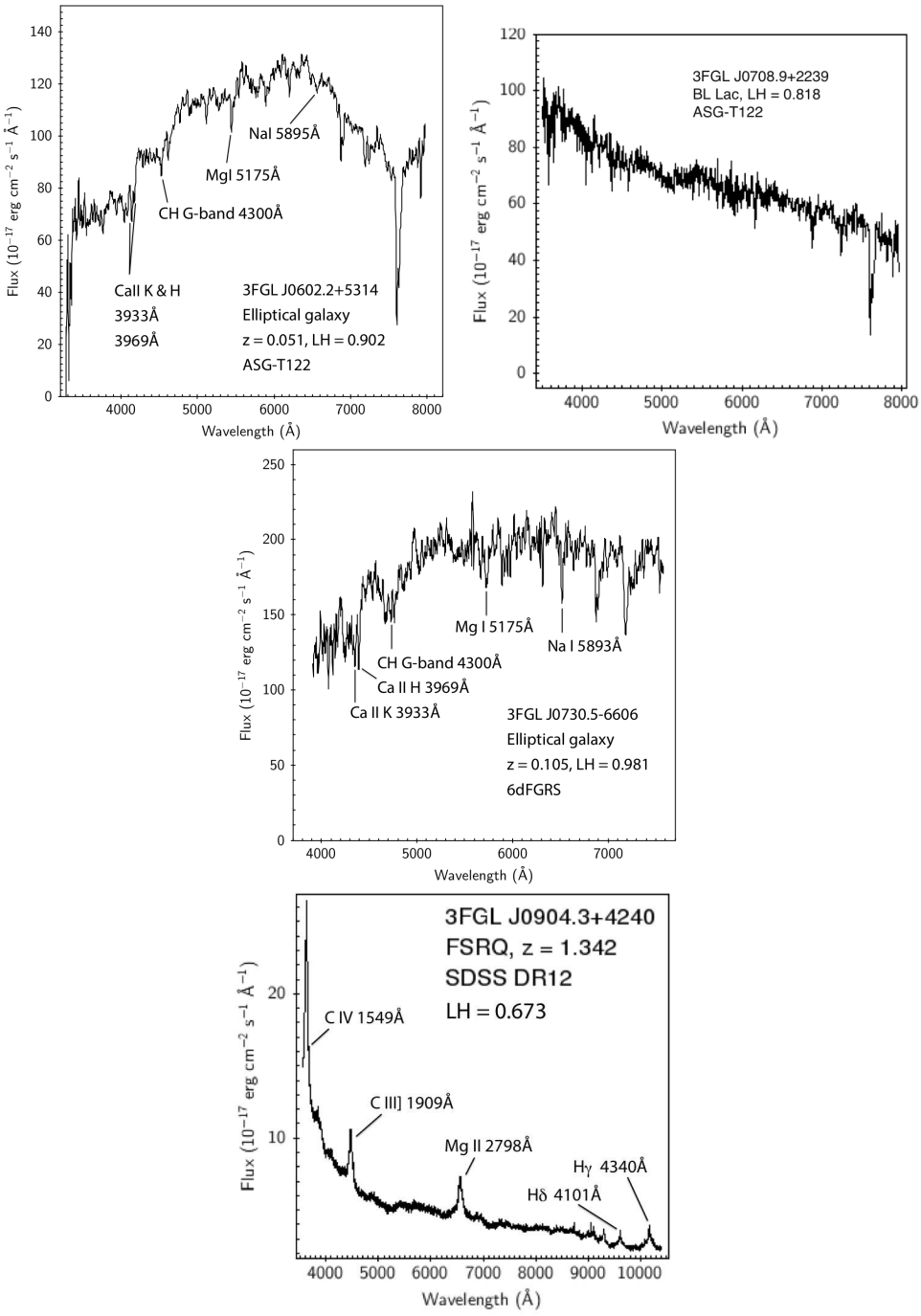
Flux (10^{-17} erg cm^{-2} s^{-1} Å^{-1})
Wavelength (Å)
NaI 5895Å
MgI 5175Å
CH G-band 4300Å
CaII K & H
3933Å
3969Å
3FGL J0602.2+5314
Elliptical galaxy
z = 0.051, LH = 0.902
ASG-T122
3FGL J0708.9+2239
BL Lac, LH = 0.818
ASG-T122
Mg I 5175Å
Na I 5893Å
CH G-band 4300Å
Ca II H 3969Å
Ca II K 3933Å
3FGL J0730.5-6606
Elliptical galaxy
z = 0.105, LH = 0.981
6dFGRS
3FGL J0904.3+4240
FSRQ, z = 1.342
SDSS DR12
LH = 0.673
C IV 1549Å
C III] 1909Å
Mg II 2798Å
Hγ 4340Å
Hδ 4101Å

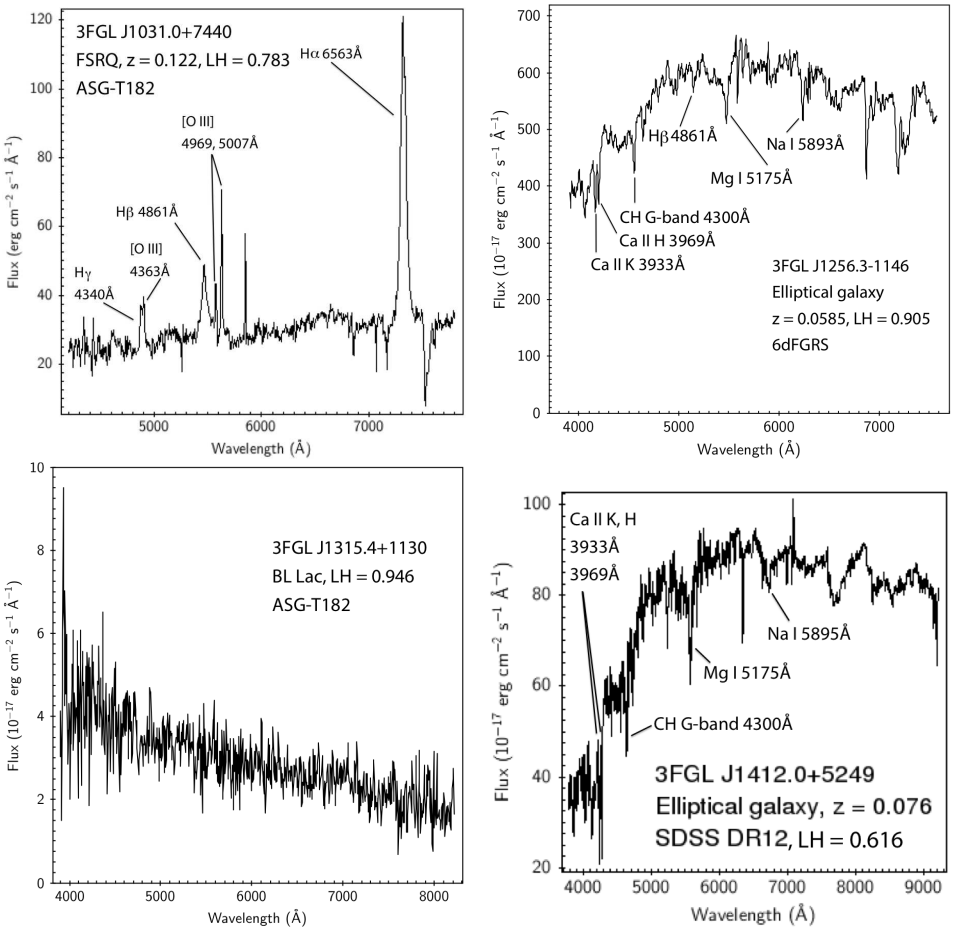
3FGL J1031.0+7440
FSRQ, z = 0.122, LH = 0.783
ASG-T182
Hα 6563Å
[O III]
4969, 5007Å
Hβ 4861Å
[O III]
4363Å
Hγ
4340Å
Flux (erg cm⁻² s⁻¹ Å⁻¹)
Wavelength (Å)
Hβ 4861Å
Na I 5893Å
Mg I 5175Å
CH G-band 4300Å
Ca II H 3969Å
Ca II K 3933Å
3FGL J1256.3-1146
Elliptical galaxy
z = 0.0585, LH = 0.905
6dFGRS
Flux (10⁻¹⁷ erg cm⁻² s⁻¹ Å⁻¹)
Wavelength (Å)
3FGL J1315.4+1130
BL Lac, LH = 0.946
ASG-T182
Flux (10⁻¹⁷ erg cm⁻² s⁻¹ Å⁻¹)
Wavelength (Å)
Ca II K, H
3933Å
3969Å
Na I 5895Å
Mg I 5175Å
CH G-band 4300Å
3FGL J1412.0+5249
Elliptical galaxy, z = 0.076
SDSS DR12, LH = 0.616
Flux (10⁻¹⁷ erg cm⁻² s⁻¹ Å⁻¹)
Wavelength (Å)

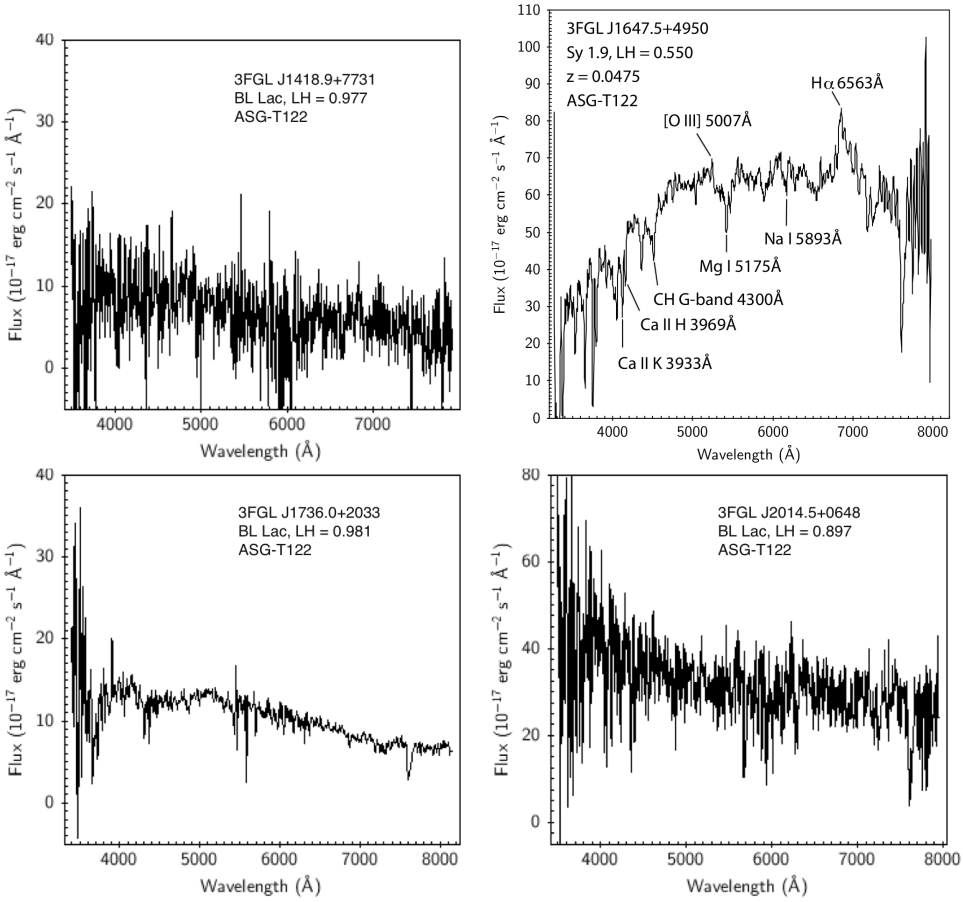
3FGL J1418.9+7731
BL Lac, LH = 0.977
ASG-T122
3FGL J1647.5+4950
Sy 1.9, LH = 0.550
z = 0.0475
ASG-T122
[O III] 5007Å
Hα 6563Å
Na I 5893Å
Mg I 5175Å
CH G-band 4300Å
Ca II H 3969Å
Ca II K 3933Å
3FGL J1736.0+2033
BL Lac, LH = 0.981
ASG-T122
3FGL J2014.5+0648
BL Lac, LH = 0.897
ASG-T122
Flux (10^−17 erg cm^−2 s^−1 Å^−1)
Wavelength (Å)

15

Chapter 13

Appendix C

13.1 The FERMI LAT Telescope

The Large Area Telescope (LAT) is the principal scientific instrument on the Fermi Gamma Ray Space Telescope spacecraft. Originally called the Gamma-Ray Large Area Space Telescope (GLAST), the mission was renamed for the physicist Enrico Fermi. The Fermi spacecraft was launched into a near-earth orbit on 2008 June 11.[13]

13.2 The Tracker

The TKR subsystem is the central detector of the LAT and serves to convert γ rays into electron-positron pairs and to track the pair in order to measure the direction of the incoming γ ray. The TKR consists of 16 modules, each one composed by planes of high Z material (Tungsten) in which γ rays incident on the LAT can convert into an electron-positron pair, interleaved with position-

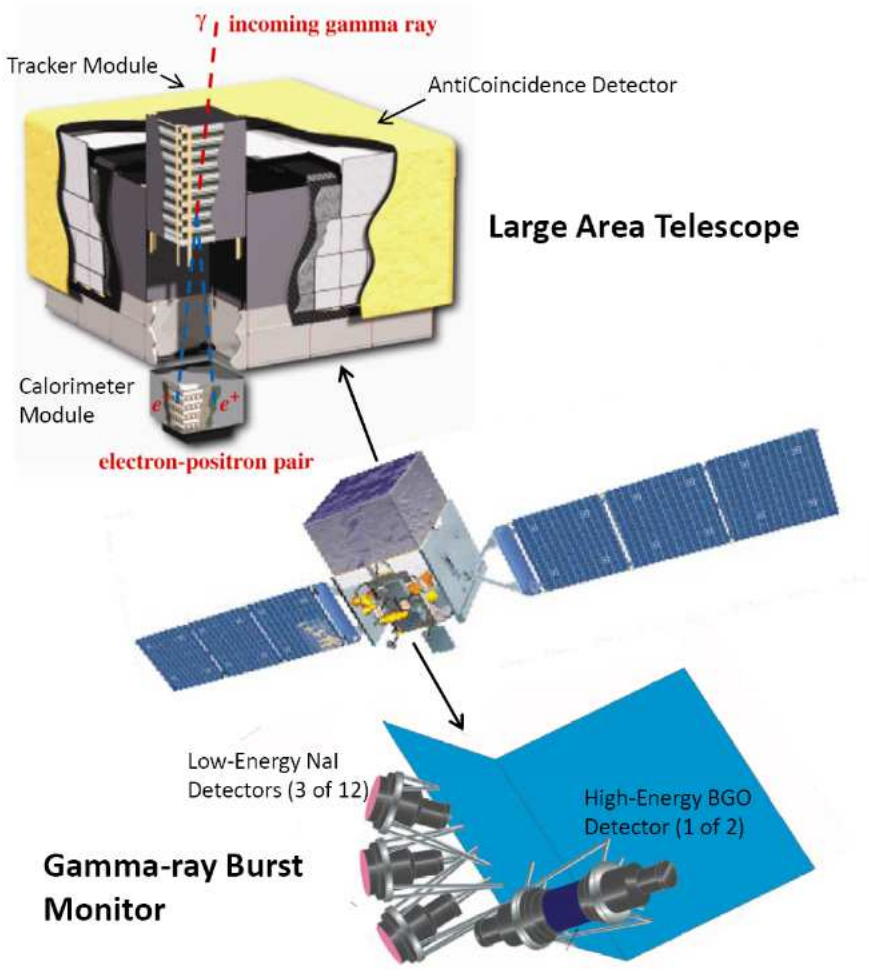

Figure 13.1: The Fermi Gamma ray Space Telescope and its two instruments. The Large Area Telescope (LAT) images the sky in the energy band from 20 MeV to more than 300 GeV while the Gamma-ray Burst Monitor (GBM) complements the LAT for the study of GRBs and transients, providing spectral coverage from 8 keV to about 40 MeV.

sensitive detectors (silicon strip detectors) that record the passage of charged particles measuring the tracks of the particles resulting from pair conversion.

The LAT tracker uses conversion foils of Tungsten (Z=74) because the pair production cross section is proportional to Z^2, then using an high Z conversion foils the conversion probability is maximized. The technology employed in past years in High Energy Physics has been fundamental to choose the tracking detectors, since the alternatives were gas-filled trackers and scintillating fibers

detectors. The silicon-based detectors were chosen for the LAT because of their higher sensitivity and angular resolution. The total silicon surface of the LAT tracker is of about 82 m^2. A scheme of the LAT TKR is displayed in Figure 13.2. As for the other part of the LAT, carefully studies have produced the parameters for the Tracker in order to satisfy all the requirements and maintain the basic constraints as low consumed power, low detector noise and low computation power required.

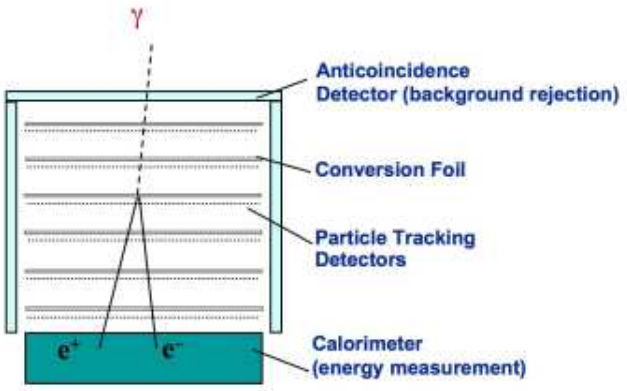

Figure 13.2: The Fermi Gamma ray Space Telescope and its two instruments. The Large Area Telescope (LAT) images the sky in the energy band from 20 MeV to more than 300 GeV while the Gamma-ray Burst Monitor (GBM) complements the LAT for the study of GRBs and transients, providing spectral coverage from 8 keV to about 40 MeV.

The basic unit of the TKR is a square *Silicon Strip Detector* (SSD) with the size of 8.95 cm $\times$ 8.95 cm, where are implanted 384 parallel microstrips spaced by 228 μm. Four SSDs, each of them is 400 μm thick, are assembled in a *ladder*. In a ladder the end of each microstrip of a SSD can be connected to the end of the correspondent microstrip on the adjacent SSD in order to form a single longer microstrip. At this point 4 ladders are assembled to form a sensitive silicon microstrip layer, which is then inserted in a *tray*. A tray is a composite structure with a mechanical structure in carbon fiber that bring at both faces a sensitive silicon plane. The main components of a tray are a detecting silicon layer on the top face, an aluminum core, a Tungsten foil for the conversion of γ rays and another silicon layer on the bottom face of the tray. The two silicon layers are mounted in a tray with parallel orientation of the microstrips. Each tray is then connected to the reading electronics. Trays are then piled up with a separation of 2 mm and each tray is rotated of 90° with respect to the adjacent tray. In this way the resulting system is made

by a conversion foil followed by a couple of silicon layers with perpendicular microstrips in order to have XY detection capability. The resulting module form *tower* and it is made by 19 trays with 18 XY detection layers.

The layout of the converters (in terms of thickness) is organized into two different sections: a *Front* section, composed of 12 layers of 0.03 radiation length converter, and a *Back* section with 4 layers of 0.18 radiation length converters. The last two XY planes have no converter at all since the main *Fermi* trigger primitive requires three silicon layers in a row hit, so that a photon converted right above the last two planes would never trigger and the Tungsten would only introduce further useless multiple scattering. The two section provide measurements in a complementary manner: while the front has an excellent *Point Spread Function* (PSF), the back section greatly enhances the photon statistics, in such a way that a large effective area and a good angular resolution can be achieved, on average, at the same time.

13.3 The Calorimeter

The Calorimeter [13] measures the energy of the electron-positron pair and gives information about the high-energy photons that have not converted in the Tracker. From the measure of the electron-positron energy it is possible to determine the energy of the primary photon using the conservations of the energy and momentum. A schematic view of the LAT Calorimeter is in Figure 13.3.

The LAT calorimeter is composed of a set of CsI(Tl) crystals read by photodiodes. As the energy resolution strongly depends on depth, sampling and longitudinal segmentation, each CAL module is finely segmented both in depth and lateral directions. Each CAL tower will contain eight layers, each constituted by 12 crystals ($27 \times 20 \times 326$ mm^3), wrapped in reflective foils, for a total of 8.6 radiation lengths. As with the silicon detection planes in the tracker, each layer will be rotated by 90° with respect to the previous one (hodoscopic configuration), in order to achieve XY imaging capabilities. The lateral segmentation provides the necessary imaging capability to correlate the events in the tracker with the energy depositions in the calorimeter and derive loose (at the level of few degrees) directional information for those photons not converting in the tracker. On the other side the longitudinal segmentation allows to derive an estimate of the initial energy of the pair from the longitudinal shower profile by fitting the measurements to an analytical description of the energy-dependent mean longitudinal the showers and the subsequent leakage correction which highly enhance the response at high energy (up to several hundreds GeV) with respect to EGRET.

At both ends of each bar is placed a PIN photo diode used for reading, and

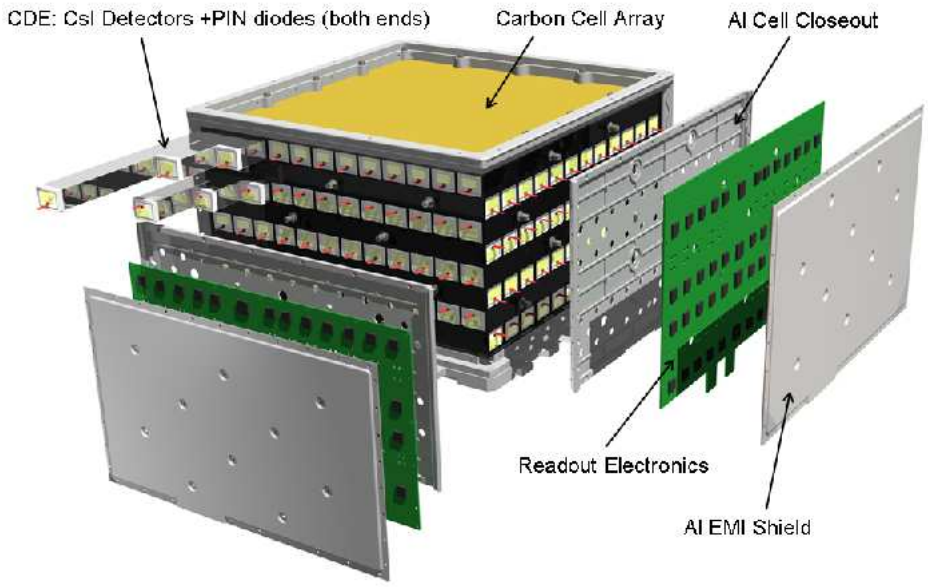

Figure 13.3: LAT calorimeter module. The 96 CsI(Tl) scintillator crystal detector elements are arranged in 8 layers, with the orientation of the crystals in adjacent layers rotated by 90°. The total calorimeter depth (at normal incidence) is 8.6 radiation lengths [13].

the measurement of the relative intensity at both ends helps to determine the position where the energy deposition has taken place. The precision that can be obtained varies from some mm at low energies (about 10 MeV), up to less than a mm for energies above 1 GeV.

13.3.1 The AntiCoincidence Detector

The purpose of the ACD is to detect incident charged cosmic ray particles that outnumber cosmic γ rays by more than 5 orders of magnitude. When a γ-ray photon enter the LAT, it does not produce any signal in the ACD, but gives a signal in the TKR and in the CAL due to the produced pair. A charged particle behaves differently, since during the passage a signal also in the ACD is produced, then it is possible to recognize a γ ray from a charged particle thanks to the different signature in the subsystems and in particular in the ACD. The events that give a signal in the TKR and in the CAL but not in the ACD can start the trigger, the other are refused as background events.

The LAT *AntiCoincidence Detector* (ACD) is made by a set of plastic scintillators coupled to Photo-Multipliers Tubes (PMTs) that use Wavelength-Shifting Fibers (WSFs) in order to increase the reading efficiency. With respect

to the EGRET anticoincidence system, that was made by a single module, the LAT ACD is fine segmented. A scheme of the ACD assembly is displayed in Figure 13.4.

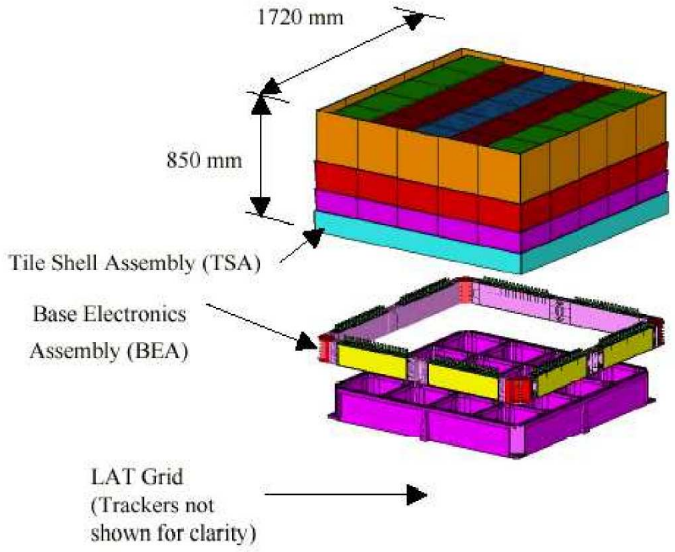

Figure A.6: Schematic view of the LAT ACD assembly [22].

Figure 13.4: Schematic view of the LAT ACD assembly [13].

The efficiency of background rejection, in particular for high-energy γ rays, is increased thanks to the ACD segmentation. In EGRET it was necessary to reduce the triggers frequency in order to avoid gas consuming in the spark chambers. The EGRET ACD was implemented in the Level 1 trigger (see Section 13.4). This reduced the working efficiency, mainly at GeV energies, where the *self-veto* becomes important. The self-veto happens when a member of the electromagnetic shower produced by the electron-positron pair is deflected and give a signal in the ACD (*backsplash*). The event has a signature of a cosmic ray and then it is rejected since it is confused with a background event. The segmentation helps to know exactly which scintillator has been hit, and it is then possible to compare the track direction with the position of the hit scintillator. In case of backsplash the position of the hit scintillator panel does not correspond exactly with the intersection of the track and the ACD, then a self-veto is recognized and avoided.

Thanks to the lower dead time and to the absence of consumables in the TKR, the LAT can undergo a much higher Level 1 trigger frequency, then the

ACD can be inserted in the Level 2 trigger. In this way each event can be analyzed with more care (as explained in the Section 13.4) and the self-veto can be avoided in a very efficient way.

A total of 89 panels constitute the ACD, some of them are disposed in a 5 $\times$ 5 array on top of the TKR and the others are at the sides of the LAT. The assembling scheme of these panels has been designed with overlap in one dimension and scintillating fibers covering the gaps in the other dimension. Each scintillator is read out by an interleaved set of Wavelength Shifting (WS) fibers, with bundles connected to two phototubes, in order to guarantee redundancy.

The ACD is the first step in the background rejection scheme. The estimated Monte Carlo efficiency, confirmed by the beam tests, is greater then 0.9997.

13.4 The Data Acquisition System and Trigger

The LAT Data Acquisition System (DAQ) has three main functions. It controls the trigger, it guides the event reading sequence and stores it in a temporary memory. The DAQ also manages the data elaboration and transfers to the ground. This system is also responsible for other functions, among others the control, monitoring and housekeeping of the instrument and the power management of the whole LAT.

The DAQ is made by 16 *Tower Electronic Modules* (TEM) located below each tower and two TEM specific for the ACD. Also two *Spacecraft Interface Unit* TEM are in this system and are located in the spacecraft below the LAT.

13.4.1 Trigger and background rejection

The LAT trigger must be very efficient on γ rays and at the same time provide a high rejection power for the charged particles background. Because of the large uncertainties in cosmic ray fluxes the system flexibility is a particularly important feature.

The LAT trigger has a multi-level structure, in a similar way of the triggers employed in High Energy Physics experiments. The hardware trigger is based on special signals, called *primitives*, that originate from LAT subsystems. Primitives from Tracker, Calorimeter and Anticoincidence Detector are combined to decide if an event is recorded or not. The trigger of the LAT is very flexible in order to allow change of configuration to optimize trigger efficiency and versatile in order to accommodate various signatures of events.

The LAT trigger is organized in two levels. The first level, *Level 1 Trigger* (L1T), is a hardware trigger, based on special combinations of signals at the

level of a single tower. The workhorse γ-ray trigger is the so called *three in a row*, consisting into 3 XY consecutive tracker planes sending a trigger request. There are also two different calorimeter based trigger primitives with different adjustable thresholds (nominally set at 100 MeV and 1 GeV of energy deposition in a crystal log). The ACD adds two other trigger signals: a veto signal and CNO signal. The latter has a threshold of several MIPs and is used to identify cosmic ions with $Z > 2$ for CAL on orbit calibration. In addition there are three other trigger sources: the *Periodic* trigger to sample detector noise and pedestals at regular interval, the *Solicited* trigger for special software trigger request and the External trigger for ground testing. An electronic module (the TEM) combines these signal in a 600 ns coincidence window and then "decides" if the event must be recorded and how to read out the detector: using or not the zero suppression, read all the four calorimeter ranges or just the "best" one, pre-scale this kind of events. The correspondence between trigger primitives coincidence and readout mode is configurable with a look-up table that allows up to 16 combinations (*engines*).

With exception of specific calibration event the typical read out time is about 26 μs allowing to trigger on almost all the particles that cross the LAT (whose rate is estimated of the order of few kHz). The fact that cosmic rays can be included in the trigger actually constitutes a sort of revolution with respect to the trigger scheme implemented in EGRET, in which that would not have been possible due to the high instrumental dead time in the spark chambers. In fact the only reason why further levels of data reduction are required onboard is the limited bandwidth of the telemetry.

The second trigger level, *Level 2 Trigger* (L2T), is software, two *Event Processing Unit* (EPUs) work in parallel to process LAT events. Multiple filters in succession are applied to each event, each filter optimized to select a different class of event (i.e. γ rays or heavy ions for calibration). Within each filter events are accepted or rejected based on a sequence of test each one with tunable parameters. Together with the *Gamma Filter*, designed to accept γ rays with high efficiency during normal operation, other filters are implemented to identify MIPs and heavy ions for instrument calibration.

13.5 Overview of the Gamma-ray Burst Monitor

The *Gamma-ray Burst Monitor* (GBM), the successor of BATSE onboard the CGRO, is designed to detect transient objects, such as GRBs. The development of the GBM and the analysis of its observational data is a collaborative effort between the National Space Science and Technology Center in the U.S.

and the Max Planck Institute for Extraterrestrial Physics (MPE) in Germany. The GBM consists of 12 detectors made of Sodium Iodide (NaI) for catching X rays and low energy γ rays, and other two detectors made of Bismuth Germanate (BGO) for high-energy γ rays placed as shown in Figure 13.5. The two detectors together detect X rays and γ rays in the energy range between 8 keV to 30MeV, overlapping with the lower energy limit of the LAT. Together the NaI and BGO detectors have similar characteristics to the combination of the BATSE large area and spectroscopy detectors but cover a wider energy range and have a smaller collection area.

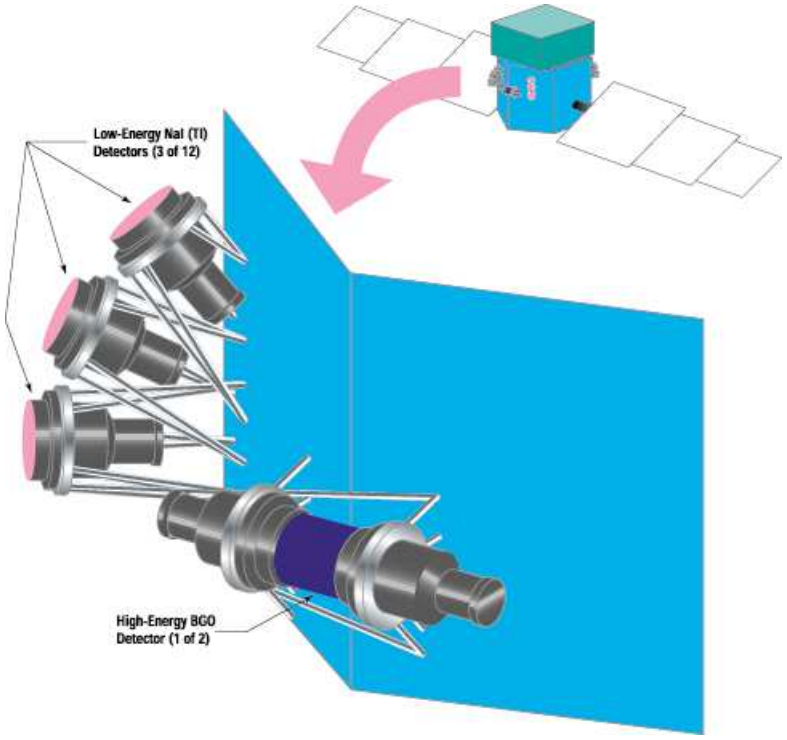

Figure 13.5: Schematic view of the GBM in the *Fermi* spacecraft. Credit: *Fermi*-GBM Team

The detectors do not block any part of the *Large Area Telescope* (LAT) Field-of-View nor interfere with the solar panels. They easily fit between the LAT and the shroud envelope on two sides of the spacecraft. The mounting arrangement is flexible with the two BGO detectors mounted on opposite sides of the spacecraft, and the NaI detectors mounted in 4 banks of 3 detectors in such a way that they sample a wide range of azimuth and elevation angles[1].

[1]A more specific description of the Gamma-ray Burst Monitor can be found in the following link: `http://fermi.gsfc.nasa.gov/science/instruments/gbm.html`

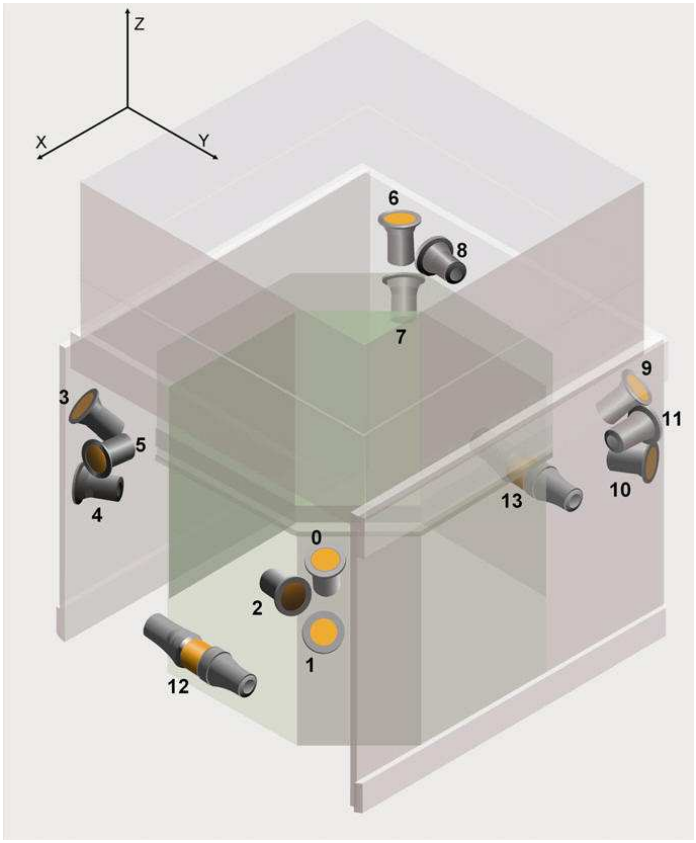

Figure 13.6: GBM detector location in the Fermi spacecraft

Chapter 14

Appendix D

14.1 The Asiago Observatory

The observatory, founded in 1942, is located in Asiago, Italy. (coordinates 45.8664° N 11.5264° E). It hosts the largest optical telescope on Italian soil. The telescopes and instrumentation are operated by Padova Observatory, member of the National Institute for Astrophysics (INAF)

14.1.1 The telescopes

The 182 cm telescope. The telescope is located at Cima Ekar (Asiago). East Longitude +00h 46m 17.13s (+/- 0.03s) Latitude +45d 50' 36.2" (+/- 0.03"). The telescope, inaugurated in 1973 and dedicated to N. Copernicus, is a classic Cassegrain reflector with a primary mirror of 182cm. It is the main observing facility at the observing site of Cima Ekar (1350m). It is also the largest astronomical telescope in Italy. The telescope is equipped with both an imager/spectrograph camera (AFOSC) and an high dispersion echelle spectrograph (Echelle)

The 122 cm telescope. It is a reflector constructed in 1940/42 by the firm Officine Galileo in Florence. It is of a conventional design, having a parabolic primary mirror, and two secondary mirrors providing Newtonian and Cassegrain foci. The primary mirror has a clear aperture of 120 cm, a focal length of 600 cm and is paraboidal with a central hole of 19.5 cm diameter. All mirrors are made of pyrex glass. The mounting is of the English type with north and south piers supporting a polar axis with the tube offset and short declination axis. The north pier does not permit full sky coverage about the pole. The telescope has a completely enclosed tube; the entire upper end of the tube can be rotated about the optical axis for ease of observation at the

Newtonian focus. The rear end of the tube contains the adjustment system for the primary mirror cell. The latter is supported axially by 18 pads and radially by a system of 24 lever counter balance units equally spaced around the cell. The mirror cell is created using a variable iris diaphragm.

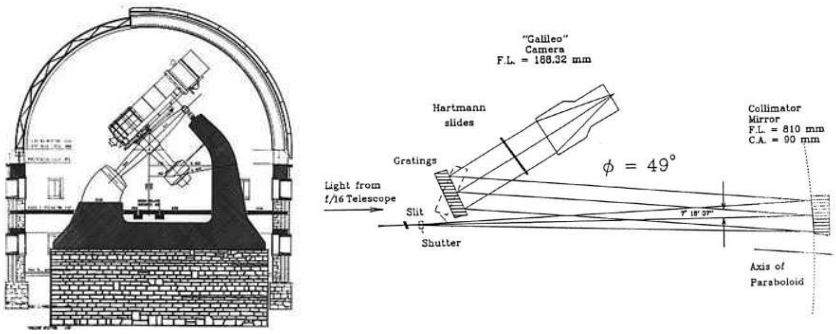

Figure 14.1: Schematic view of the Galileo telescope in Asiago Observatory

Chapter 15

Appendix E

15.1 Artificial Neural Networks

An artificial neural network is a system composed of many simple processing elements operating in parallel whose function is determined by the network structure, connection strengths, and the processing performed at the computing elements or nodes.

An artificial neural network has a natural proclivity for storing experimental knowledge and making it available for use. The knowledge is acquired by the network through a learning process and the interneuron connection strengths – known as synaptic weights – are used to store the knowledge.

There are numerous types of artificial neural networks (ANNs) for addressing many different types of problems, such as modelling memory, performing pattern recognition, and predicting the evolution of dynamical systems. Most networks therefore perform some kind of data modelling.

The two main kinds of learning algorithms are: *supervised* and *unsupervised*. In the former the correct results (target values) are known and given to the ANN during the training so that the ANN can adjust its weights to try to match its outputs to the target values. In the latter, the ANN is not provided with the correct results during training. Unsupervised ANNs usually perform some kind of data compression, such as dimensionality reduction or clustering.

The two main kinds of network topology are *feed-forward* and *feed-back*. In feed-forward ANN, the connections between units do not form cycles and usually produce a relatively quick response to an input. Most feed-forward ANNs can be trained using a wide variety of efficient conventional numerical methods (e.g. conjugate gradients, Levenberg-Marquardt, etc.) in addition to algorithms invented by ANN researchers. In a feed-back or recurrent ANN, there are cycles in the connections. In some feed-back ANNs, each time an

input is presented, the ANN must iterate for a potentially long time before producing a response.

15.1.1 The multilayer perceptron

In the present work we have used one of the most important types of supervised neural networks, the *feed-forward multilayer perceptron* (MLP), in order to understand the nature of *Fermi*-LAT unassociated sources. The term *perceptron* is historical, and refers to the function performed by the nodes. An introduction on Artificial Neural Networks is provided by Sarle (1994) [72], and on multilayer Perceptron by Bailer-Jones et al. (2001) [14] and Sarle (1994) [71]. A comprehensive treatment of feed-forward neural networks is provided by Bishop (1995) [48].

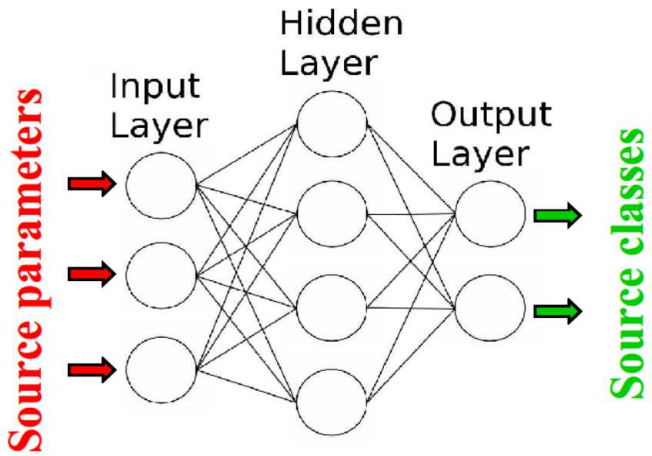

Figure 15.1: Schematic view of a Two Layer Perceptron (2LP), the type of Artificial Neural Network we use. The data enter the 2LP through the Nodes in the Input Layer. The information travels from left to right across the Links and is processed in the Nodes. Each Node in the Output Layer returns the probability that a source belongs to a specific class.

In Figure 15.1 the general architecture of a network is shown. The network is made up of nodes (analogous to human neurons) arranged in a series of layers. The nodes in a given layer are fully connected to the nodes in the next layer by links. The input layer consists of the input parameters, and the output layer consists of the classes. Any layer between the input and the output layers is called a "hidden layer". The complexity (and non-linearity) of the ANN depends on the number of inputs, hidden nodes, layers, outputs and connections.

For each input pattern, the network produces an output pattern through the propagation rule, compares the actual output with the desired one and computes an error. The learning algorithm adjusts the weights of the connections by an appropriate quantity to reduce the error (sliding down the slope). This process continues until the error produced by the network is low, according to a given criterion.

15.1.2 The propagation rule

The network operates as follows. Except for the nodes in the input layer, an input of a node at layer s ($I_j^{(s)}$) is the combination of the output of the previous nodes ($o_i^{(s-1)}$) and the weights of the corresponding links ($w_{ij}^{(s)}$), the combination is linear: $I_j^{(s)} = \sum_i w_{ij}^{(s)} o_i^{(s-1)}$. Each node has a transform function (or activation function), which provides the output of the node as a function of the $I_j^{(s)}$. Nonlinear activation functions are needed to introduce nonlinearity into the network. We have used the *logistic* (or sigmoid) function: $out = 1/[1 + \exp(-I)]$ (in the interval [0, 1]) and the tanh function $out = tanh(I)$ (in the interval $[-1, 1]$), for all nodes. For the input nodes we decide to use a linear activation function. The propagation rule, from the input layer to the output layer, is a combination of activation functions.

No significant difference has been found in the training process between using the logistic and tanh functions, only that the training process is faster if we use the tanh function.

15.1.3 Back-propagation of the error

The weights, w, are randomly initialized, they are the free parameters of the network and the goal is to minimize the total error function with respect to w (maintaining a good generalization power, see below).

The error function in the weight space defines the multidimensional error surface and the objective is to find the global (or acceptable local) minima on this surface. The solution implemented in the present work is the *gradient descent*, within which the weights are adjusted (from small initial random values) in order to follow the steepest downhill slope. The error surface is not known in advance, so it is necessary to explore it in a suitable way.

The error function typically used is the sum-of-squares error, which for a single input vector, n, is:

$$E^{(n)} = \frac{1}{2} \sum_i \left(y_i^{(n)} - t_i^{(n)} \right)^2 \tag{15.1}$$

where y_i is the output of the ANN and t_i is the target output value for the ith output node and n runs form 1 to the total number of examples in the training set. In the present work $i = 2$, two output nodes are used to understand the nature of 2FGL unassociated sources. In the gradient descent process the weight vector is adjusted in the negative direction of the gradient vector *backwards* from the output layer to one ore more hidden layers by a small change in each time-step:

$$\Delta \mathbf{w} = -\eta \frac{\partial E}{\partial \mathbf{w}} \tag{15.2}$$

and the new generic weight is:

$$w_{new} = w_{old} + \Delta w \tag{15.3}$$

The amplitude of the step on the error surface is set by the η-learning parameter: large values of η mean large steps. Typically η belongs to the interval [0, 1] (where the opening bracket means that the lower value is excluded). In our application a small value has been used (0.2). If η is too small the training time becomes very long, while a large value can produce oscillations around a minimum or even lead to miss the optimal minimum in the error surface. The algorithm is stopped when the value of the error function has become sufficiently small.

The learning algorithm used in the present work is the standard *back-propagation*. It refers to the method for computing the gradient of the case-wise error function with respect to the weights for a feed-forward network. "*Standard backprop*" is a definition of the *generalized delta rule*, the training algorithm that remains one of the most widely used supervised training methods for neural network.

This learning algorithm implies that the error function is continuous and derivable, so that it is possible to calculate the gradient. For this reason the activation functions (and their final combination through the propagation rule) must be continuous and derivable. From the computational point of view, the derivative of the activation functions adopted in the present work is easily related to the value of the function out = F(net) itself (see Section 15.1.2: F' $\propto$ out(1-out) in the case F = sigmoid or F' $\propto$ (1-out^2) if F = tanh).

When the network weights approach a minimum solution, the gradient becomes small and the step size diminishes too, giving origin to a very slow convergence. Adding a momentum (a residual of the previous weight variation) to the equations of the weight update, the minimization improves [48]:

$$w_{new} = w_{old} + \Delta w + \alpha \Delta w_{old} \tag{15.4}$$

where α is the momentum factor (set to 0.9 in our applications). This can reduce the decay in learning updates and cause the learning to proceed through

the weight space in a fairly constant direction. Besides a faster convergence to the minimum, this method makes it possible to escape from a local minimum if there is enough momentum to travel through it and over the following hill The generalized delta rule including the *momentum* is called the "*heavy ball method*" in the numerical analysis literature [15].

The learning algorithm has been used in the so called online (or *incremental*) version, in which the weights of the connections are updated after each example is processed by the network. One epoch corresponds to the processing of all examples one time. The other possibility is to compute the training in the so called *batch learning* (or epoch learning), in which the weights are updated only at the end of each epoch (not used in the present application).

15.1.4 The training technique

During the learning process, the output of a supervised neural network comes to approximate the target values given the inputs in the training set. This ability may be useful in itself, but more often the purpose of using a neural network is to generalize, i.e. to get some output from inputs that are *not* in the training set (*generalization*). ANNs, like other flexible nonlinear estimation methods such as kernel regression and smoothing splines, can suffer from either under fitting or over fitting. A network that is not sufficiently complex[1] can fail to fully detect the signal in a complicated data set, leading to under fitting: an *inflexible* model will have a large *bias*. On the other hand a network that is too complex may fit the noise, not just the signal, leading to over-fitting: a model that is too flexible in relation to the particular data set will produce a large *variance* [73]. The best generalization is obtained when the best compromise between these two conflicting quantities (bias and variance) is reached. There are several approaches to avoid under- and overfitting, and obtain a good generalization. Part of them aim to *regularize* the complexity of the network during the training phase, such as the *Early Stopping* and *weight-decay* methods (the size of the weights are tuned in order to produce a mapping function with small curvature, the large weights are penalized. Reducing the size of the weights reduces also the "effective" number of weights [59]).

[1]The complexity of a network is related to both the number of weights and the amplitude of the weights (the mapping produced by a ANN is an interpolation of the training data, a high order fit to data is characterized by large curvature of the mapping function, which in turn corresponds to large weights).

Generalize error

The most commonly used method for estimating the generalization error in neural networks is to reserve part of the data as a *testing set*, which must not be used in *any* way during the training. After the training, the network is applied to the testing set, and the error on the testing set provides an unbiased estimate of the generalization error, provided that the testing set was chosen in a random way.

In order to avoid (possible) over-fitting during the training, another part of the data can be reserved as a *validation set* (independent both of the training and testing sets, not used for updating the weights), and used during the training to monitor the generalization error. The best epoch corresponds to the lowest validation error, and the training is stopped when the validation error rate "starts to go up" (*early stopping* method). The disadvantage of this technique is that it reduces the amount of data available for both training and validation, which is particularly undesirable if the available data set is small. Moreover, neither the training nor the validation make use of the entire sample.

Bibliography

[1] A. A. Abdo, M. Ackermann, I. Agudo, M. Ajello, H. D. Aller, M. F. Aller, E. Angelakis, A. A. Arkharov, M. Axelsson, U. Bach, and et al. The Spectral Energy Distribution of Fermi Bright Blazars. *ApJ*, 716:30–70, June 2010.

[2] A. A. Abdo, M. Ackermann, M. Ajello, A. Allafort, E. Antolini, W. B. Atwood, M. Axelsson, L. Baldini, J. Ballet, G. Barbiellini, and et al. Fermi Large Area Telescope First Source Catalog. *ApJS*, 188:405–436, June 2010.

[3] A. A. Abdo, M. Ackermann, M. Ajello, A. Allafort, E. Antolini, W. B. Atwood, M. Axelsson, L. Baldini, J. Ballet, G. Barbiellini, and et al. Fermi Large Area Telescope First Source Catalog. *ApJS*, 188:405–436, June 2010.

[4] A. A. Abdo, M. Ackermann, M. Ajello, J. Ampe, B. Anderson, W. B. Atwood, M. Axelsson, R. Bagagli, L. Baldini, J. Ballet, and et al. The on-orbit calibration of the Fermi Large Area Telescope. *Astroparticle Physics*, 32:193–219, October 2009.

[5] A. A. Abdo, M. Ackermann, M. Ajello, W. B. Atwood, M. Axelsson, L. Baldini, J. Ballet, D. L. Band, G. Barbiellini, D. Bastieri, and et al. Fermi/Large Area Telescope Bright Gamma-Ray Source List. *ApJS*, 183:46–66, July 2009.

[6] A. A. Abdo, M. Ackermann, M. Ajello, W. B. Atwood, M. Axelsson, L. Baldini, J. Ballet, G. Barbiellini, D. Bastieri, K. Bechtol, R. Bellazzini, B. Berenji, R. D. Blandford, E. D. Bloom, E. Bonamente, A. W. Borgland, A. Bouvier, J. Bregeon, A. Brez, M. Brigida, P. Bruel, T. H. Burnett, S. Buson, G. A. Caliandro, R. A. Cameron, P. A. Caraveo, S. Carrigan, J. M. Casandjian, E. Cavazzuti, C. Cecchi, Ö. Çelik, E. Charles,

A. Chekhtman, C. C. Cheung, J. Chiang, S. Ciprini, R. Claus, J. Cohen-Tanugi, J. Conrad, S. Cutini, C. D. Dermer, A. de Angelis, F. de Palma, S. W. Digel, E. d. C. e. Silva, P. S. Drell, R. Dubois, D. Dumora, C. Farnier, C. Favuzzi, S. J. Fegan, W. B. Focke, P. Fortin, M. Frailis, Y. Fukazawa, S. Funk, P. Fusco, F. Gargano, D. Gasparrini, N. Gehrels, S. Germani, B. Giebels, N. Giglietto, P. Giommi, F. Giordano, T. Glanzman, G. Godfrey, I. A. Grenier, M.-H. Grondin, J. E. Grove, L. Guillemot, S. Guiriec, A. K. Harding, R. C. Hartman, M. Hayashida, E. Hays, S. E. Healey, D. Horan, R. E. Hughes, M. S. Jackson, G. Jóhannesson, A. S. Johnson, W. N. Johnson, T. Kamae, H. Katagiri, J. Kataoka, N. Kawai, M. Kerr, J. Knödlseder, M. Kuss, J. Lande, L. Latronico, M. Lemoine-Goumard, F. Longo, F. Loparco, B. Lott, M. N. Lovellette, P. Lubrano, G. M. Madejski, A. Makeev, M. N. Mazziotta, W. McConville, J. E. McEnery, C. Meurer, P. F. Michelson, W. Mitthumsiri, T. Mizuno, A. A. Moiseev, C. Monte, M. E. Monzani, A. Morselli, I. V. Moskalenko, S. Murgia, P. L. Nolan, J. P. Norris, E. Nuss, T. Ohsugi, N. Omodei, E. Orlando, J. F. Ormes, D. Paneque, J. H. Panetta, D. Parent, V. Pelassa, M. Pepe, M. Persic, M. Pesce-Rollins, F. Piron, T. A. Porter, S. Rainò, R. Rando, M. Razzano, A. Reimer, O. Reimer, T. Reposeur, S. Ritz, L. S. Rochester, A. Y. Rodriguez, R. W. Romani, M. Roth, F. Ryde, H. F.-W. Sadrozinski, D. Sanchez, A. Sander, P. M. Saz Parkinson, J. D. Scargle, C. Sgrò, E. J. Siskind, D. A. Smith, P. D. Smith, G. Spandre, P. Spinelli, M. S. Strickman, D. J. Suson, H. Tajima, H. Takahashi, T. Takahashi, T. Tanaka, J. B. Thayer, J. G. Thayer, D. J. Thompson, L. Tibaldo, D. F. Torres, G. Tosti, A. Tramacere, Y. Uchiyama, T. L. Usher, V. Vasileiou, N. Vilchez, M. Villata, V. Vitale, A. P. Waite, P. Wang, B. L. Winer, K. S. Wood, T. Ylinen, and M. Ziegler. Spectral Properties of Bright Fermi-Detected Blazars in the Gamma-Ray Band. *ApJ*, 710:1271–1285, February 2010.

[7] A. A. Abdo, M. Ackermann, M. Ajello, W. B. Atwood, M. Axelsson, L. Baldini, J. Ballet, G. Barbiellini, D. Bastieri, K. Bechtol, R. Bellazzini, B. Berenji, R. D. Blandford, E. D. Bloom, E. Bonamente, A. W. Borgland, A. Bouvier, J. Bregeon, A. Brez, M. Brigida, P. Bruel, T. H. Burnett, S. Buson, G. A. Caliandro, R. A. Cameron, P. A. Caraveo, S. Carrigan, J. M. Casandjian, E. Cavazzuti, C. Cecchi, Ö. Çelik, E. Charles, A. Chekhtman, C. C. Cheung, J. Chiang, S. Ciprini, R. Claus, J. Cohen-Tanugi, J. Conrad, S. Cutini, C. D. Dermer, A. de Angelis, F. de Palma, S. W. Digel, E. d. C. e. Silva, P. S. Drell, R. Dubois, D. Dumora, C. Farnier, C. Favuzzi, S. J. Fegan, W. B. Focke, P. Fortin, M. Frailis, Y. Fukazawa, S. Funk, P. Fusco, F. Gargano, D. Gasparrini, N. Gehrels, S. Germani, B. Giebels, N. Giglietto, P. Giommi, F. Giordano, T. Glanz-

man, G. Godfrey, I. A. Grenier, M.-H. Grondin, J. E. Grove, L. Guillemot, S. Guiriec, A. K. Harding, R. C. Hartman, M. Hayashida, E. Hays, S. E. Healey, D. Horan, R. E. Hughes, M. S. Jackson, G. Jóhannesson, A. S. Johnson, W. N. Johnson, T. Kamae, H. Katagiri, J. Kataoka, N. Kawai, M. Kerr, J. Knödlseder, M. Kuss, J. Lande, L. Latronico, M. Lemoine-Goumard, F. Longo, F. Loparco, B. Lott, M. N. Lovellette, P. Lubrano, G. M. Madejski, A. Makeev, M. N. Mazziotta, W. McConville, J. E. McEnery, C. Meurer, P. F. Michelson, W. Mitthumsiri, T. Mizuno, A. A. Moiseev, C. Monte, M. E. Monzani, A. Morselli, I. V. Moskalenko, S. Murgia, P. L. Nolan, J. P. Norris, E. Nuss, T. Ohsugi, N. Omodei, E. Orlando, J. F. Ormes, D. Paneque, J. H. Panetta, D. Parent, V. Pelassa, M. Pepe, M. Persic, M. Pesce-Rollins, F. Piron, T. A. Porter, S. Rainò, R. Rando, M. Razzano, A. Reimer, O. Reimer, T. Reposeur, S. Ritz, L. S. Rochester, A. Y. Rodriguez, R. W. Romani, M. Roth, F. Ryde, H. F.-W. Sadrozinski, D. Sanchez, A. Sander, P. M. Saz Parkinson, J. D. Scargle, C. Sgrò, E. J. Siskind, D. A. Smith, P. D. Smith, G. Spandre, P. Spinelli, M. S. Strickman, D. J. Suson, H. Tajima, H. Takahashi, T. Takahashi, T. Tanaka, J. B. Thayer, J. G. Thayer, D. J. Thompson, L. Tibaldo, D. F. Torres, G. Tosti, A. Tramacere, Y. Uchiyama, T. L. Usher, V. Vasileiou, N. Vilchez, M. Villata, V. Vitale, A. P. Waite, P. Wang, B. L. Winer, K. S. Wood, T. Ylinen, and M. Ziegler. Spectral Properties of Bright Fermi-Detected Blazars in the Gamma-Ray Band. *ApJ*, 710:1271–1285, February 2010.

[8] F. Acero, M. Ackermann, M. Ajello, A. Albert, W. B. Atwood, M. Axelsson, L. Baldini, J. Ballet, G. Barbiellini, D. Bastieri, A. Belfiore, R. Bellazzini, E. Bissaldi, R. D. Blandford, E. D. Bloom, J. R. Bogart, R. Bonino, E. Bottacini, J. Bregeon, R. J. Britto, P. Bruel, R. Buehler, T. H. Burnett, S. Buson, G. A. Caliandro, R. A. Cameron, R. Caputo, M. Caragiulo, P. A. Caraveo, J. M. Casandjian, E. Cavazzuti, E. Charles, R. C. G. Chaves, A. Chekhtman, C. C. Cheung, J. Chiang, G. Chiaro, S. Ciprini, R. Claus, J. Cohen-Tanugi, L. R. Cominsky, J. Conrad, S. Cutini, F. D'Ammando, A. de Angelis, M. DeKlotz, F. de Palma, R. Desiante, S. W. Digel, L. Di Venere, P. S. Drell, R. Dubois, D. Dumora, C. Favuzzi, S. J. Fegan, E. C. Ferrara, J. Finke, A. Franckowiak, Y. Fukazawa, S. Funk, P. Fusco, F. Gargano, D. Gasparrini, B. Giebels, N. Giglietto, P. Giommi, F. Giordano, M. Giroletti, T. Glanzman, G. Godfrey, I. A. Grenier, M.-H. Grondin, J. E. Grove, L. Guillemot, S. Guiriec, D. Hadasch, A. K. Harding, E. Hays, J. W. Hewitt, A. B. Hill, D. Horan, G. Iafrate, T. Jogler, G. Jóhannesson, R. P. Johnson, A. S. Johnson, T. J. Johnson, W. N. Johnson, T. Kamae, J. Kataoka, J. Katsuta, M. Kuss, G. La Mura, D. Landriu, S. Larsson, L. Latronico,

M. Lemoine-Goumard, J. Li, L. Li, F. Longo, F. Loparco, B. Lott, M. N. Lovellette, P. Lubrano, G. M. Madejski, F. Massaro, M. Mayer, M. N. Mazziotta, J. E. McEnery, P. F. Michelson, N. Mirabal, T. Mizuno, A. A. Moiseev, M. Mongelli, M. E. Monzani, A. Morselli, I. V. Moskalenko, S. Murgia, E. Nuss, M. Ohno, T. Ohsugi, N. Omodei, M. Orienti, E. Orlando, J. F. Ormes, D. Paneque, J. H. Panetta, J. S. Perkins, M. Pesce-Rollins, F. Piron, G. Pivato, T. A. Porter, J. L. Racusin, R. Rando, M. Razzano, S. Razzaque, A. Reimer, O. Reimer, T. Reposeur, L. S. Rochester, R. W. Romani, D. Salvetti, M. Sánchez-Conde, P. M. Saz Parkinson, A. Schulz, E. J. Siskind, D. A. Smith, F. Spada, G. Spandre, P. Spinelli, T. E. Stephens, A. W. Strong, D. J. Suson, H. Takahashi, T. Takahashi, Y. Tanaka, J. G. Thayer, J. B. Thayer, D. J. Thompson, L. Tibaldo, O. Tibolla, D. F. Torres, E. Torresi, G. Tosti, E. Troja, B. Van Klaveren, G. Vianello, B. L. Winer, K. S. Wood, M. Wood, S. Zimmer, and Fermi-LAT Collaboration. Fermi Large Area Telescope Third Source Catalog. *ApJS*, 218:23, June 2015.

[9] M. Ackermann, M. Ajello, A. Allafort, E. Antolini, L. Baldini, J. Ballet, G. Barbiellini, D. Bastieri, R. Bellazzini, B. Berenji, R. D. Blandford, E. D. Bloom, E. Bonamente, A. W. Borgland, A. Bouvier, T. J. Brandt, J. Bregeon, M. Brigida, P. Bruel, R. Buehler, T. H. Burnett, S. Buson, G. A. Caliandro, R. A. Cameron, P. A. Caraveo, J. M. Casandjian, E. Cavazzuti, C. Cecchi, Ö. Çelik, E. Charles, A. Chekhtman, A. W. Chen, C. C. Cheung, J. Chiang, S. Ciprini, R. Claus, J. Cohen-Tanugi, J. Conrad, S. Cutini, A. de Angelis, M. E. DeCesar, A. De Luca, F. de Palma, C. D. Dermer, E. d. C. e. Silva, P. S. Drell, A. Drlica-Wagner, R. Dubois, T. Enoto, C. Favuzzi, S. J. Fegan, E. C. Ferrara, W. B. Focke, P. Fortin, Y. Fukazawa, S. Funk, P. Fusco, F. Gargano, D. Gasparrini, N. Gehrels, S. Germani, N. Giglietto, F. Giordano, M. Giroletti, T. Glanzman, G. Godfrey, I. A. Grenier, M.-H. Grondin, J. E. Grove, L. Guillemot, S. Guiriec, M. Gustafsson, D. Hadasch, Y. Hanabata, A. K. Harding, M. Hayashida, E. Hays, S. E. Healey, A. B. Hill, D. Horan, X. Hou, G. Jóhannesson, A. S. Johnson, T. J. Johnson, T. Kamae, H. Katagiri, J. Kataoka, M. Kerr, J. Knödlseder, M. Kuss, J. Lande, L. Latronico, S.-H. Lee, M. Lemoine-Goumard, F. Longo, F. Loparco, B. Lott, M. N. Lovellette, P. Lubrano, G. M. Madejski, M. N. Mazziotta, J. E. McEnery, J. Mehault, P. F. Michelson, R. P. Mignani, W. Mitthumsiri, T. Mizuno, C. Monte, M. E. Monzani, A. Morselli, I. V. Moskalenko, S. Murgia, T. Nakamori, M. Naumann-Godo, P. L. Nolan, J. P. Norris, E. Nuss, T. Ohsugi, A. Okumura, N. Omodei, E. Orlando, J. F. Ormes, M. Ozaki, D. Paneque, J. H. Panetta, D. Parent, V. Pelassa, M. Pesce-Rollins, M. Pierbattista, F. Piron, G. Pivato, T. A. Porter, S. Rainò,

R. Rando, P. S. Ray, M. Razzano, A. Reimer, O. Reimer, T. Reposeur, R. W. Romani, H. F.-W. Sadrozinski, D. Salvetti, P. M. Saz Parkinson, T. L. Schalk, C. Sgrò, M. S. Shaw, E. J. Siskind, P. D. Smith, G. Spandre, P. Spinelli, D. J. Suson, H. Takahashi, T. Tanaka, J. G. Thayer, J. B. Thayer, D. J. Thompson, L. Tibaldo, O. Tibolla, D. F. Torres, G. Tosti, A. Tramacere, E. Troja, T. L. Usher, J. Vandenbroucke, V. Vasileiou, G. Vianello, N. Vilchez, V. Vitale, A. P. Waite, E. Wallace, P. Wang, B. L. Winer, M. T. Wolff, D. L. Wood, K. S. Wood, Z. Yang, and S. Zimmer. A Statistical Approach to Recognizing Source Classes for Unassociated Sources in the First Fermi-LAT Catalog. *ApJ*, 753:83, July 2012.

[10] M. Ackermann, M. Ajello, W. B. Atwood, L. Baldini, J. Ballet, G. Barbiellini, D. Bastieri, J. Becerra Gonzalez, R. Bellazzini, E. Bissaldi, R. D. Blandford, E. D. Bloom, R. Bonino, E. Bottacini, T. J. Brandt, J. Bregeon, R. J. Britto, P. Bruel, R. Buehler, S. Buson, G. A. Caliandro, R. A. Cameron, M. Caragiulo, P. A. Caraveo, B. Carpenter, J. M. Casandjian, E. Cavazzuti, C. Cecchi, E. Charles, A. Chekhtman, C. C. Cheung, J. Chiang, G. Chiaro, S. Ciprini, R. Claus, J. Cohen-Tanugi, L. R. Cominsky, J. Conrad, S. Cutini, R. D'Abrusco, F. D'Ammando, A. de Angelis, R. Desiante, S. W. Digel, L. Di Venere, P. S. Drell, C. Favuzzi, S. J. Fegan, E. C. Ferrara, J. Finke, W. B. Focke, A. Franckowiak, L. Fuhrmann, Y. Fukazawa, A. K. Furniss, P. Fusco, F. Gargano, D. Gasparrini, N. Giglietto, P. Giommi, F. Giordano, M. Giroletti, T. Glanzman, G. Godfrey, I. A. Grenier, J. E. Grove, S. Guiriec, J. W. Hewitt, A. B. Hill, D. Horan, R. Itoh, G. Jóhannesson, A. S. Johnson, W. N. Johnson, J. Kataoka, T. Kawano, F. Krauss, M. Kuss, G. La Mura, S. Larsson, L. Latronico, C. Leto, J. Li, L. Li, F. Longo, F. Loparco, B. Lott, M. N. Lovellette, P. Lubrano, G. M. Madejski, M. Mayer, M. N. Mazziotta, J. E. McEnery, P. F. Michelson, T. Mizuno, A. A. Moiseev, M. E. Monzani, A. Morselli, I. V. Moskalenko, S. Murgia, E. Nuss, M. Ohno, T. Ohsugi, R. Ojha, N. Omodei, M. Orienti, E. Orlando, A. Paggi, D. Paneque, J. S. Perkins, M. Pesce-Rollins, F. Piron, G. Pivato, T. A. Porter, S. Rainò, R. Rando, M. Razzano, S. Razzaque, A. Reimer, O. Reimer, R. W. Romani, D. Salvetti, M. Schaal, F. K. Schinzel, A. Schulz, C. Sgrò, E. J. Siskind, K. V. Sokolovsky, F. Spada, G. Spandre, P. Spinelli, L. Stawarz, D. J. Suson, H. Takahashi, T. Takahashi, Y. Tanaka, J. G. Thayer, J. B. Thayer, L. Tibaldo, D. F. Torres, E. Torresi, G. Tosti, E. Troja, Y. Uchiyama, G. Vianello, B. L. Winer, K. S. Wood, and S. Zimmer. The Third Catalog of Active Galactic Nuclei Detected by the Fermi Large Area Telescope. *ApJ*, 810:14, September 2015.

[11] M. Ackermann, M. Ajello, W. B. Atwood, L. Baldini, J. Ballet, G. Bar-

biellini, D. Bastieri, J. Becerra Gonzalez, R. Bellazzini, E. Bissaldi, R. D. Blandford, E. D. Bloom, R. Bonino, E. Bottacini, T. J. Brandt, J. Bregeon, P. Bruel, R. Buehler, S. Buson, G. A. Caliandro, R. A. Cameron, R. Caputo, M. Caragiulo, P. A. Caraveo, E. Cavazzuti, C. Cecchi, E. Charles, A. Chekhtman, C. C. Cheung, J. Chiang, G. Chiaro, S. Ciprini, J. M. Cohen, J. Cohen-Tanugi, L. R. Cominsky, J. Conrad, A. Cuoco, S. Cutini, F. D'Ammando, A. de Angelis, F. de Palma, R. Desiante, M. Di Mauro, L. Di Venere, A. Domínguez, P. S. Drell, C. Favuzzi, S. J. Fegan, E. C. Ferrara, W. B. Focke, P. Fortin, A. Franckowiak, Y. Fukazawa, S. Funk, A. K. Furniss, P. Fusco, F. Gargano, D. Gasparrini, N. Giglietto, P. Giommi, F. Giordano, M. Giroletti, T. Glanzman, G. Godfrey, I. A. Grenier, M.-H. Grondin, L. Guillemot, S. Guiriec, A. K. Harding, E. Hays, J. W. Hewitt, A. B. Hill, D. Horan, G. Iafrate, D. Hartmann, T. Jogler, G. Jóhannesson, A. S. Johnson, T. Kamae, J. Kataoka, J. Knödlseder, M. Kuss, G. La Mura, S. Larsson, L. Latronico, M. Lemoine-Goumard, J. Li, L. Li, F. Longo, F. Loparco, B. Lott, M. N. Lovellette, P. Lubrano, G. M. Madejski, S. Maldera, A. Manfreda, M. Mayer, M. N. Mazziotta, P. F. Michelson, N. Mirabal, W. Mitthumsiri, T. Mizuno, A. A. Moiseev, M. E. Monzani, A. Morselli, I. V. Moskalenko, S. Murgia, E. Nuss, T. Ohsugi, N. Omodei, M. Orienti, E. Orlando, J. F. Ormes, D. Paneque, J. S. Perkins, M. Pesce-Rollins, V. Petrosian, F. Piron, G. Pivato, T. A. Porter, S. Rainò, R. Rando, M. Razzano, S. Razzaque, A. Reimer, O. Reimer, T. Reposeur, R. W. Romani, M. Sánchez-Conde, P. M. Saz Parkinson, J. Schmid, A. Schulz, C. Sgrò, E. J. Siskind, F. Spada, G. Spandre, P. Spinelli, D. J. Suson, H. Tajima, H. Takahashi, M. Takahashi, T. Takahashi, J. B. Thayer, D. J. Thompson, L. Tibaldo, D. F. Torres, G. Tosti, E. Troja, G. Vianello, K. S. Wood, M. Wood, M. Yassine, G. Zaharijas, and S. Zimmer. 2FHL: The Second Catalog of Hard Fermi-LAT Sources. *ApJS*, 222:5, January 2016.

[12] M. Ajello, D. Gasparrini, R. W. Romani, and M. S. Shaw. The Cosmic Evolution of Fermi BL Lacertae Objects. In *American Astronomical Society Meeting Abstracts #224*, volume 224 of *American Astronomical Society Meeting Abstracts*, page 410.09, June 2014.

[13] W. B. Atwood, A. A. Abdo, M. Ackermann, W. Althouse, B. Anderson, M. Axelsson, L. Baldini, J. Ballet, D. L. Band, G. Barbiellini, and et al. The Large Area Telescope on the Fermi Gamma-Ray Space Telescope Mission. *ApJ*, 697:1071–1102, June 2009.

[14] C. A. L. Bailer-Jones, R. Gupta, and H. T. Singh. An introduction to artificial neural networks. *Proc. of the Workshop on Automated Data Analysis in Astronomy, IUCAA, Pune, India*, page 2000, October 2001.

[15] D. P. Bertsekas. Non Linear Programming. *Belmont,MA: Athena Scientific*, pages ISBN 1–886529–14–0, 1995.

[16] D. C.-J. Bock, M. I. Large, and E. M. Sadler. SUMSS: A Wide-Field Radio Imaging Survey of the Southern Sky. I. Science Goals, Survey Design, and Instrumentation. *Astronomical Journal*, 117:1578–1593, March 1999.

[17] R. Buccheri, M. Morini, and B. Sacco. On the nature of the galactic 2CG gamma-ray sources. *Royal Society of London Philosophical Transactions Series A*, 301:495–504, June 1981.

[18] R. Campana, E. Massaro, D. Gasparrini, S. Cutini, and A. Tramacere. A Minimal Spanning Tree algorithm for source detection in γ-ray images. *MNRAS*, 383:1166–1174, January 2008.

[19] P. A. Caraveo, G. F. Bignami, and J. E. Trümper. Radio-silent isolated neutron stars as a new astronomical reality. *A&A Rev.*, 7:209–216, 1996.

[20] J. J. Condon, W. D. Cotton, E. W. Greisen, Q. F. Yin, R. A. Perley, G. B. Taylor, and J. J. Broderick. The NRAO VLA Sky Survey. *Astronomical Journal*, 115:1693–1716, May 1998.

[21] S. Cutini, B. Lott, D. Gasparrini, S. Ciprini, E. Cavazzuti, and Fermi-LAT Collaboration. The Third Catalog of Active Galactic Nuclei Detected by the Fermi Large Area Telescope. In *American Astronomical Society Meeting Abstracts #223*, volume 223 of *American Astronomical Society Meeting Abstracts*, page 115.08, January 2014.

[22] F. Damiani, A. Maggio, G. Micela, and S. Sciortino. A Method Based on Wavelet Transforms for Source Detection in Photon-counting Detector Images. II. Application to ROSAT PSPC Images. *ApJ*, 483:370, July 1997.

[23] A. de Luca. Central Compact Objects in Supernova Remnants. In C. Bassa, Z. Wang, A. Cumming, and V. M. Kaspi, editors, *40 Years of Pulsars: Millisecond Pulsars, Magnetars and More*, volume 983 of *American Institute of Physics Conference Series*, pages 311–319, February 2008.

[24] M. de Naurois and D. Mazin. Ground-based detectors in very-high-energy gamma-ray astronomy. *Comptes Rendus Physique*, 16:610–627, August 2015.

[25] M. Doert and M. Errando. Search for Gamma-ray-emitting Active Galactic Nuclei in the Fermi-LAT Unassociated Sample Using Machine Learning. *ApJ*, 782:41, February 2014.

[26] C. E. Fichtel, R. C. Hartman, D. A. Kniffen, D. J. Thompson, H. Ogelman, M. E. Ozel, T. Tumer, and G. F. Bignami. High-energy gamma-ray results from the second small astronomy satellite. *ApJ*, 198:163–182, May 1975.

[27] J. D. Finke and C. D. Dermer. On the Break in the Fermi-Large Area Telescope Spectrum of 3C 454.3. *ApJL*, 714:L303–L307, May 2010.

[28] M. A. Forman, R. Ramaty, and E. G. Zweibel. The acceleration and propagation of solar flare energetic particles. In P. A. Sturrock, T. E. Holzer, D. M. Mihalas, and R. K. Ulrich, editors, *Physics of the Sun. Volume 2*, volume 2, pages 249–289, 1986.

[29] N. Gehrels and P. Michelson. GLAST: the next-generation high energy gamma-ray astronomy mission. *Astroparticle Physics*, 11:277–282, June 1999.

[30] H. Gish. A probabilistic approach to the understanding and training of neural network classifiers. *Proc. on Acoustic Speech and Signal Processing*, page 1361, 1990.

[31] H. Goldberg. Constraint on the photino mass from cosmology. *Physical Review Letters*, 50:1419–1422, May 1983.

[32] K. M. Górski, E. Hivon, A. J. Banday, B. D. Wandelt, F. K. Hansen, M. Reinecke, and M. Bartelmann. HEALPix: A Framework for High-Resolution Discretization and Fast Analysis of Data Distributed on the Sphere. *ApJ*, 622:759–771, April 2005.

[33] A. K. Harding, P. L. Gonthier, I. A. Grenier, and C. A. Perrot. Pulsar populations and unidentified γ-ray sources. *Advances in Space Research*, 33:571–576, 2004.

[34] R. C. Hartman, D. L. Bertsch, S. D. Bloom, A. W. Chen, P. Deines-Jones, J. A. Esposito, C. E. Fichtel, D. P. Friedlander, S. D. Hunter, L. M. McDonald, P. Sreekumar, D. J. Thompson, B. B. Jones, Y. C. Lin, P. F. Michelson, P. L. Nolan, W. F. Tompkins, G. Kanbach, H. A. Mayer-Hasselwander, A. Mücke, M. Pohl, O. Reimer, D. A. Kniffen, E. J. Schneid, C. von Montigny, R. Mukherjee, and B. L. Dingus. The Third EGRET Catalog of High-Energy Gamma-Ray Sources. *ApJS*, 123:79–202, July 1999.

[35] T. Hassan, N. Mirabal, J. L. Contreras, and I. Oya. Gamma-ray active galactic nucleus type through machine-learning algorithms. *MNRAS*, 428:220–225, January 2013.

[36] S. Hayakawa. Propagation of the Cosmic Radiation through Intersteller Space. *Progress of Theoretical Physics*, 8:571–572, November 1952.

[37] A. Hewish, S. J. Bell, J. D. H. Pilkington, P. F. Scott, and R. A. Collins. Observation of a Rapidly Pulsating Radio Source. *Nature*, 217:709–713, February 1968.

[38] J. Hinton. Gamma-ray Astronomy. *ArXiv e-prints*, December 2007.

[39] C. M. Hoffman, C. Sinnis, P. Fleury, and M. Punch. Gamma-ray astronomy at high energies. *Reviews of Modern Physics*, 71:897–936, July 1999.

[40] D. R. Hutchinson and M. L. Wiedenbeck. Reinvestigation of the Radioactivity of Sb^{124}. *Physical Review*, 88:699–700, 1952.

[41] G. Kanbach, D. L. Bertsch, C. E. Fichtel, R. C. Hartman, S. D. Hunter, D. A. Kniffen, B. W. Hughlock, A. Favale, R. Hofstadter, and E. B. Hughes. The project EGRET (Energetic Gamma-Ray Experiment Telescope) on NASA's Gamma-Ray Observatory (GRO). *Space Science Reviews*, 49:69–84, 1988.

[42] R. W. Klebesadel, I. B. Strong, and R. A. Olson. Observations of Gamma-Ray Bursts of Cosmic Origin. In *Bulletin of the American Astronomical Society*, volume 5 of *Bulletin of the American Astronomical Society*, page 322, June 1973.

[43] D. A. Kniffen, R. C. Hartman, D. J. Thompson, and C. E. Fichtel. SAS-2 Observations of Gamma Rays from the Galactic Plane. *ApJL*, 186:L105, December 1973.

[44] A. Kolmogorov. Sulla determinazione empirica di una legge di distribuzione. *G. Ist. Ital. Attuariale*, 4:83–91, August 1933.

[45] W. Kraushaar, G. W. Clark, G. Garmire, H. Helmken, P. Higbie, and M. Agogino. Explorer XI Experiment on Cosmic Gamma Rays. *ApJ*, 141:845, April 1965.

[46] W. L. Kraushaar, G. W. Clark, G. P. Garmire, R. Borken, P. Higbie, V. Leong, and T. Thorsos. High-Energy Cosmic Gamma-Ray Observations from the OSO-3 Satellite. *ApJ*, 177:341, November 1972.

[47] K. J. Lee, L. Guillemot, Y. L. Yue, M. Kramer, and D. J. Champion. Application of the Gaussian mixture model in pulsar astronomy - pulsar classification and candidates ranking for the Fermi 2FGL catalogue. *MNRAS*, 424:2832–2840, August 2012.

[48] Bishop C. M. *Neural Networks for Pattern Recognition*. 1995.

[49] N. Mandzhavidze and R. Ramaty. Gamma Rays from Pion Decay: Evidence for Long Term Particle Trapping in Solar Flares. In *American Astronomical Society Meeting Abstracts #180*, volume 24 of *Bulletin of the American Astronomical Society*, page 802, May 1992.

[50] N. Mandzhavidze and R. Ramaty. High-energy gamma-ray emission from pion decay in a solar flare magnetic loop. *ApJ*, 389:739–755, April 1992.

[51] J. R. Mattox, D. L. Bertsch, J. Chiang, B. L. Dingus, S. W. Digel, J. A. Esposito, J. M. Fierro, R. C. Hartman, S. D. Hunter, G. Kanbach, D. A. Kniffen, Y. C. Lin, D. J. Macomb, H. A. Mayer-Hasselwander, P. F. Michelson, C. von Montigny, R. Mukherjee, P. L. Nolan, P. V. Ramanamurthy, E. Schneid, P. Sreekumar, D. J. Thompson, and T. D. Willis. The Likelihood Analysis of EGRET Data. *ApJ*, 461:396, April 1996.

[52] J. R. Mattox, J. Schachter, L. Molnar, R. C. Hartman, and A. R. Patnaik. The Idenfication of EGRET Sources with Flat-Spectrum Radio Sources. *ApJ*, 481:95, May 1997.

[53] J. R. Mattox, J. Schachter, L. Molnar, R. C. Hartman, and A. R. Patnaik. The Idenfication of EGRET Sources with Flat-Spectrum Radio Sources. *ApJ*, 481:95, May 1997.

[54] P. A. Mazzali, J. Deng, N. Tominaga, K. Maeda, K. Nomoto, T. Matheson, K. S. Kawabata, K. Z. Stanek, and P. M. Garnavich. The Type Ic Hypernova SN 2003dh/GRB 030329. *ApJL*, 599:L95–L98, December 2003.

[55] S. Mereghetti. Recent results on magnetars. *ArXiv e-prints*, April 2009.

[56] P. Mészáros. The fireball shock model of gamma ray bursts. In S. S. Holt and W. W. Zhang, editors, *American Institute of Physics Conference Series*, volume 522 of *American Institute of Physics Conference Series*, pages 213–225, June 2000.

[57] P. Mészáros. Gamma-Ray Bursts: Accumulating Afterglow Implications, Progenitor Clues, and Prospects. *Science*, 291:79–84, January 2001.

[58] N. Mirabal, V. Frías-Martinez, T. Hassan, and E. Frías-Martinez. Fermi's SIBYL: mining the gamma-ray sky for dark matter subhaloes. *MNRAS*, 424:L64–L68, July 2012.

[59] J. E. Moody, S. J. Hanson, and R. P. Lippmann. The Effective number of parameters: An analysis of generalization and regularization in nonlinear learning systems. *Advances in Neural Information Processing Systems*, 4:847–854, 1992.

[60] P. Morrison. On gamma-ray astronomy. *Il Nuovo Cimento*, 7:858–865, 1958.

[61] I. V. Moskalenko and A. W. Strong. Diffuse γ-ray emission: lessons and perspectives. In T. Bulik, B. Rudak, and G. Madejski, editors, *Astrophysical Sources of High Energy Particles and Radiation*, volume 801 of *American Institute of Physics Conference Series*, pages 57–62, November 2005.

[62] R. J. Murphy, C. D. Dermer, and R. Ramaty. High-energy processes in solar flares. *ApJS*, 63:721–748, March 1987.

[63] W. S. Paciesas, C. A. Meegan, G. N. Pendleton, M. S. Briggs, C. Kouveliotou, T. M. Koshut, J. P. Lestrade, M. L. McCollough, J. J. Brainerd, J. Hakkila, W. Henze, R. D. Preece, V. Connaughton, R. M. Kippen, R. S. Mallozzi, G. J. Fishman, G. A. Richardson, and M. Sahi. The Fourth BATSE Gamma-Ray Burst Catalog (Revised). *ApJS*, 122:465–495, June 1999.

[64] A. Paggi, A. Cavaliere, V. Vittorini, F. D'Ammando, and M. Tavani. Flaring Patterns in Blazars. *ApJ*, 736:128, August 2011.

[65] T. Piran. Gamma-ray bursts and the fireball model. *Phys. Rep.*, 314:575–667, June 1999.

[66] R. Protassov, D. A. van Dyk, A. Connors, V. L. Kashyap, and A. Siemiginowska. Statistics, Handle with Care: Detecting Multiple Model Components with the Likelihood Ratio Test. *ApJ*, 571:545–559, May 2002.

[67] R. Ramaty and R. J. Murphy. Nuclear processes and accelerated particles in solar flares. *Space Science Reviews*, 45:213–268, 1987.

[68] R. Rando and for the Fermi LAT Collaboration. Post-launch performance of the Fermi Large Area Telescope. *ArXiv e-prints*, July 2009.

[69] J. J. Ruan, S. F. Anderson, R. M. Plotkin, W. N. Brandt, T. H. Burnett, A. D. Myers, and D. P. Schneider. The Nature of Transition Blazars. *ApJ*, 797:19, December 2014.

[70] J. M. Ryan and M. A. Lee. On the transport and acceleration of solar flare particles in a coronal loop. *ApJ*, 368:316–324, February 1991.

[71] W. S. Sarle. Neural Network Implementation in SAS Software, SAS Institute Inc. *Proc. of Nineteenth Annual SAS User Group International Conf., Cary, NC: SAS Institute*, page 1551, 1994.

[72] W. S. Sarle. Neural Networks and Statistical Models. *Proc. of Nineteenth Annual SAS User Group International Conf., Cary, NC: SAS Institute*, page 1538, 1994.

[73] W. S. Sarle. Stopped training and other remedies for over-fitting. *Proc. of the 27th Symp. on the interface of computing science and statistics*, page 352, 1995.

[74] V. Schönfelder. *The Universe in Gamma Rays*. 2001.

[75] P. Sreekumar, D. L. Bertsch, B. L. Dingus, J. A. Esposito, C. E. Fichtel, R. C. Hartman, S. D. Hunter, G. Kanbach, D. A. Kniffen, Y. C. Lin, H. A. Mayer-Hasselwander, P. F. Michelson, C. von Montigny, A. Muecke, R. Mukherjee, P. L. Nolan, M. Pohl, O. Reimer, E. Schneid, J. G. Stacy, F. W. Stecker, D. J. Thompson, and T. D. Willis. EGRET Observations of the Extragalactic Gamma-Ray Emission. *ApJ*, 494:523, February 1998.

[76] J.-L. Starck and M. Pierre. Structure detection in low intensity X-ray images. *A&AS*, 128:397–407, March 1998.

[77] A. W. Strong, I. V. Moskalenko, and O. Reimer. Diffuse Galactic Continuum Gamma Rays: A Model Compatible with EGRET Data and Cosmic-Ray Measurements. *ApJ*, 613:962–976, October 2004.

[78] B. N. Swanenburg, K. Bennett, G. F. Bignami, R. Buccheri, P. Caraveo, W. Hermsen, G. Kanbach, G. G. Lichti, J. L. Masnou, H. A. Mayer-Hasselwander, J. A. Paul, B. Sacco, L. Scarsi, and R. D. Wills. Second COS B catalog of high-energy gamma-ray sources. *ApJL*, 243:L69–L73, January 1981.

[79] M. Tavani, G. Barbiellini, A. Argan, M. Basset, F. Boffelli, A. Bulgarelli, P. Caraveo, A. Chen, E. Costa, G. De Paris, E. Del Monte, G. Di Cocco, I. Donnarumma, M. Feroci, M. Fiorini, L. Foggetta, T. Froysland, M. Frutti, F. Fuschino, M. Galli, F. Gianotti, A. Giuliani, C. Labanti, I. Lapshov, F. Lazzarotto, F. Liello, P. Lipari, F. Longo, M. Marisaldi, M. Mastropietro, E. Mattaini, F. Mauri, S. Mereghetti, E. Morelli, A. Morselli, L. Pacciani, A. Pellizzoni, F. Perotti, P. Picozza, C. Pittori, C. Pontoni, G. Porrovecchio, M. Prest, G. Pucella, M. Rapisarda, E. Rossi, A. Rubini, P. Soffitta, A. Traci, M. Trifoglio, A. Trois, E. Vallazza, S. Vercellone, A. Zambra, and D. Zanello. The AGILE mission

and its scientific instrument. In *Society of Photo-Optical Instrumentation Engineers (SPIE) Conference Series*, volume 6266 of *Society of Photo-Optical Instrumentation Engineers (SPIE) Conference Series*, July 2006.

[80] J. H. Taylor, R. N. Manchester, and A. G. Lyne. Catalog of 558 pulsars. *ApJS*, 88:529–568, October 1993.

[81] D. J. Thompson, D. L. Bertsch, C. E. Fichtel, R. C. Hartman, R. Hofstadter, E. B. Hughes, S. D. Hunter, B. W. Hughlock, G. Kanbach, D. A. Kniffen, Y. C. Lin, J. R. Mattox, H. A. Mayer-Hasselwander, C. von Montigny, P. L. Nolan, H. I. Nel, K. Pinkau, H. Rothermel, E. J. Schneid, M. Sommer, P. Sreekumar, D. Tieger, and A. H. Walker. Calibration of the Energetic Gamma-Ray Experiment Telescope (EGRET) for the Compton Gamma-Ray Observatory. *ApJS*, 86:629–656, June 1993.

[82] D. J. Thompson, G. A. Simpson, and M. E. Ozel. SAS 2 observations of the earth albedo gamma radiation above 35 MeV. *Journal of Geophysical Research*, 86:1265–1270, March 1981.

[83] C. M. Urry and P. Padovani. Unified Schemes for Radio-Loud Active Galactic Nuclei. *PASP*, 107:803, September 1995.

[84] Bourdes V. Advances in Artificial Neural Systems. *Article ID 309841*, 1995.

[85] J. van Paradijs, P. J. Groot, T. Galama, C. Kouveliotou, R. G. Strom, J. Telting, R. G. M. Rutten, G. J. Fishman, C. A. Meegan, M. Pettini, N. Tanvir, J. Bloom, H. Pedersen, H. U. Nørdgaard-Nielsen, M. Linden-Vørnle, J. Melnick, G. van der Steene, M. Bremer, R. Naber, J. Heise, J. in't Zand, E. Costa, M. Feroci, L. Piro, F. Frontera, G. Zavattini, L. Nicastro, E. Palazzi, K. Bennett, L. Hanlon, and A. Parmar. Transient optical emission from the error box of the γ-ray burst of 28 February 1997. *Nature*, 386:686–689, April 1997.

[86] S. Weinberg. Upper bound on gauge-fermion masses. *Physical Review Letters*, 50:387–389, February 1983.

[87] Wilks, S. S. The Large-Sample Distribution of the Likelihood Ratio for Testing Composite Hypotheses. *Annals of Mathematical Statistics*, 9:60–62, 1938.

[88] J.-H. Woo and C. M. Urry. Active Galactic Nucleus Black Hole Masses and Bolometric Luminosities. *ApJ*, 579:530–544, November 2002.

ACKNOWLEDGEMENTS

Thank you

I want to ackowledge all the people who support me and kindly share expertise and time during these three years of my study. Without them everything would have been much more difficult.
Thank you very much to: David Salvetti, Giovanni La Mura, Marcello Giroletti, Paola Grandi, Riccardo Rando, Sara Buson, Stefano Ciroi, Piero Rafanelli, Giovanni Busetto and Patrizia Caraveo.
Many thanks for the hospitality to : NASA Goddard Space Flight Center (Greenbelt MD USA), Institute of Space Astrophysics and Cosmic Physics (Milano) Istituto di Radioastronomia /INAF (Bologna), Osservatorio Astrofisico (Asiago). Acknowledgments to the Nordic Optical Telescope (NOT) observatory (La Palma, Canary Islands) and the Telescopio Nazionale Galileo observatory (La Palma, Canary Islands) Many thanks to the FERMI LAT Collaboration and in particular all the Members with them I developed and discussed my research
Special thanks to my advisor Professor Denis Bastieri and to the PhD School in Physics, University of Padova .

My biggest thanks goes to *David J Thompson* , Deputy Project Scientist for FERMI Gamma-ray Space Telescope, NASA. Thank you David for giving me your science, your comments and your time. Thank you for letting me to work in NASA with you and the most prestigious scientists in high energy astrophysics.

Most of all, I thank my wife Lorena, who has always stood by me, and supported me every day.